Robert Wimmer-Teubenbacher, Dipl.-Ing. BSc.

Development of Metal Oxide Nanomaterials for the Integration on Complementary Metal-Oxide-Semiconductor Gas Sensor Devices

DOCTORAL THESIS

to achieve the university degree of

Doktor der technischen Wissenschaften

submitted to

Graz University of Technology

Supervisor

Ao.Univ.-Prof. Dipl.-Ing. Dr.techn. Roland Resel

Institute of Solid State Physics

Graz, September 2019

AFFIDAVIT

I declare that I have authored this thesis independently, that I have not used other than the declared sources/resources, and that I have explicitly indicated all material which has been quoted either literally or by content from the sources used. The text document uploaded to TUGRAZonline is identical to the present doctoral thesis.

Date

Signature

Dedicated to my amazing family

Abstract

Increasing awareness to the issue of indoor air quality has led to a growing demand on reliable, cost-efficient and low-power consuming air quality monitoring systems. Air quality monitoring systems based on metal oxide gas sensors combine cost-effectiveness, low-power consumption and can be integrated on microelectromechanical systems (MEMS), called microhotplates, build in complementary metal oxide semiconductor (CMOS) technology. CMOS technology enables mass production. In this work, a carbon dioxide (CO_2) metal oxide gas sensor based on a thermally oxidized cupric oxide (CuO) thin film functionalized with gold nanoparticles has been developed. Additionally, tin dioxide, zinc oxide and cupric oxide thin films were deposited for gas sensor fabrication by an alternative method, called spray pyrolysis for their prospective application as volatile organic compounds (VOC) and carbon monoxide (CO) sensors. The process flow of all metal oxides is designed to enable integration on a CMOS platform. It is shown that the thermally oxidized CuO thin film gas sensor is sensitive to CO_2, prior to the nanoparticle functionalization. After the functionalization the sensors' sensitivity towards 2000 ppm of CO_2 at an operation temperature of 300°C is increased 13 fold compared to the non-functionalized sensor. Characterisations of the thermally oxidized CuO thin film by scanning electron microscopy (SEM), energy-dispersive x-ray spectroscopy and Raman spectroscopy indicate the oxidation state of the thin film and show the occurrence of gold nanoparticles on the sensor surface. In addition, the deposited tin dioxide, zinc oxide and cupric oxide thin films by spray pyrolysis are investigated by SEM, atomic force microscopy, x-ray reflectivity and x-ray diffraction method. The tin dioxide thin films are evaluated for gas sensing, especially for CO and VOCs and show viable sensitivities for both test gases in the respective concentration ranges for indoor air quality monitoring. First prototypes of this CO_2 gas sensor integrated on a CMOS based MEMS structure have been fabricated.

Acknowledgement

I would like to express my deep gratitude to Doz. Anton Köck, my supervisor at Materials Center Leoben Forschung GmbH (MCL). His continuous support, encouragement and advice during my thesis were a vital part for the success of my research.
My special thanks go to Prof. Roland Resel, my supervisor at Technical Universty Graz. His patient guidance and spot on critique always steered my ambitions in a more realistic direction.
I want to thank my colleagues at MCL for their support. Hereby, I want to thank Doz. Marco Deluca for the Raman measurements and evaluations done within this work. I want to thank Verena Perner for the implementation of the zinc oxide thin film deposition experiments within her intern ship. I want to thanks Bernhard Satory for his numerous scanning electron microscopy (SEM) investigations done for this work. I want to thank Eva Lackner and Johanna Krainer for their support in the integration of the metal oxide materials on a newly developed complementary metal oxide semiconductor (CMOS) platform for gas sensing. Additionally, I want to thank Eva Lackner for her help in the development of the carbon dioxide gas sensor. I want to thank Bernat Zaragoza Travieso for his extraordinary work on the automation of the gas measurement set-up and his patience with us, the software users. I want to thank Florentyna Sosada-Ludwikoska for the continuous advice in chemistry related questions and fruitful discussions on the topic of metal oxide gas sensing. Furthermore, I want to thank Franziska Frois for her support throughout my work.
I would also like to thank the staff at Austrian Institute of Technology (AIT, Techgate) for their help during my numerous stays. Especially, I want to thank Thomas Maier for his continuous lab support at AIT. I want to thank Giorgio Mutinati and Stephan Steinhauer for their introduction to the fabrication of thin film gas and the evaluation of gas sensors.
I would like to thank Prof. Joachim Krenn and his work-group at University

of Graz for their support and advice during my work at their electron beam lithography tool.
I would like to thank Birgit Kunert at the Institute of Solid State Physics at Graz University of Technology for doing the x-ray diffraction measurement shown in this work.
I would like to extend my thanks to the project partner Austrian Microsystems AG for providing the CMOS platform for gas sensor integration. I want to thank especially Karl Rohracher, Gregor Toschkoff and Martin Sagmeister for their continuous support.
I would also like to thank our project partner Siemens AG for their evaluation of our CMOS integrated gas sensors at their facility, namely Roland Pohle, Erhard Magori and Oliver von Sicard.
I would like to thank our project partner Fraunhofer Center for Applied Nanotechnology for their contribution of Au nanoparticles, namely Jan Steffen Niehaus.
I also want to thank Karl Voit for his development of an easy to use LaTex Template.
Special thanks should be given to my personal think tank at Plaka Beach, especially to Nikolaus Schwaiger.
Further special thanks should be extended to Eva and Darjan Kozic for their support, advice and friendship.
My deepest gratitude goes to my family, my grandparents, my sister, who is an integral part of my English education and moral support and my parents, who always supported and inspired me throughout my life.
Furthermore, I want to express my greatest gratitude to my wife Miriam even if words might not suffice. Without your moral support, scientific advice and understanding all this wouldn't be possible.
Finally, I want to thank the European Union as well as the Austrian Research Promotion Agency for the financial support to realize this dissertation (MSP Grant Agreement No. 611887).

Contents

Abstract 4

Acknowledegement 5

Abbreviations 10

I. Motivation 13

II. Fundamentals 18

1. Metal Oxide Materials for Gas Sensing 19

1.1. Fundamentals of metal oxides 19
1.2. Metal oxide gas sensors 27
1.2.1. Gas sensor quantities: 28
1.2.2. Ionosorption-Model 33
1.2.3. Nanowires 52
1.3. Metal oxide surface reactions 59
1.3.1. Interaction with gases 59
1.3.2. Interaction with humidity 66
1.3.3. Test gases 68
1.4. Sensitization: Enhancement of gas sensors characteristics . . . 73

III. Experimental 83

2. Sensor material fabrication 84
2.1. Thin films . . . 84
2.1.1. Spray pyrolysis technique . . . 84
2.1.2. SnO_2 . . . 97
2.1.3. CuO . . . 99
2.1.4. ZnO . . . 102
2.1.5. Thin film structuring . . . 104
2.2. Nanowire arrays . . . 106
2.2.1. Fabrication process of nanowire arrays . . . 106
2.2.2. CuO Nanowire Array . . . 109
2.2.3. ZnO Nanowire Array . . . 113

3. Gas sensor device fabrication 117
3.1. Silicon based Gas Sensors . . . 117
3.2. CMOS Integrated Gas Sensors . . . 124
3.2.1. CMOS integration . . . 124
3.2.2. CMOS: Process flow of the various materials . . . 129
3.3. Gas measurement set-up . . . 132

IV. Results 137

4. Thin film analysis 138
4.1. SnO_2 . . . 138
4.2. CuO thin film (spraypyrolysis) . . . 141
4.3. CuO thin film (thermal oxidation) . . . 150
4.4. ZnO . . . 155

5. Gas sensor device characterization 161
5.1. Measurement routine . . . 161
5.2. Standard Gas Sensors . . . 163
5.2.1. SB: CuO Measurements . . . 163
5.2.2. SB: ZnO Measurements . . . 169
5.3. MPW3: CMOS integrated SnO_2 Gas Sensors . . . 173

6. Discussion and Outlook **184**
6.1. Discussion 184
6.1.1. CuO thin film gas sensor 184
6.1.2. ZnO nanowire array gas sensor 189
6.1.3. SnO_2 thin film gas sensor 191
6.1.4. Spray pyrolysis of other metal oxides 193
6.2. Outlook 194

Appendix **203**

A. List of chemicals **203**

B. Materials and tools **205**

C. Instruments for characterization **207**

D. Scientific paper **209**

E. Patent **210**

Curriculum vitae **226**

Publication list **228**

Bibliography **230**

LIST OF ABBREVIATIONS

AFM Atomic Force Microscope
Au-NP Gold Nanoparicle
$BaTiO_3$ Barium Titanate
CCMOS Cambridge CMOS Sensors
CMOS Complementary Metal Oxide Semiconductor
CO_2 Carbon Dioxide
CO Carbon Monoxide
COCOA Chip On Chip technology to Open new Applications
Cu_2O Cuprous Oxide
CuO Cupric Oxide
CVD Chemical Vapor Deposition
DSC Differential Scanning Calorimetry
DTA Differential Thermal Analysis
DTG Differential Thermogravimetry
EBL Electron Beam Lithography
EDX Energy dispersive X-ray spectroscopy
ESD Electrostatic Discharge
eV Electron Volt
FELMI Forschungsverbund des Instituts für Elektronenmikroskopie und Nanoanalytik
FIB Focused Ion Beam
GMS Gas Measurement Set-up
H_2S Hydrogen Sulfide
HCMix Hydrocarbon Mixture
HVAC Heating, Ventilation and Air Conditioning
IUPAC International Union of Pure and Applied Chemistry
IDES Interdigitated Electrodes
IoT Internet of Things
IR Infrared

MBE Molecular Beam Epitaxy
MCL Materials Center Leoben Forschung GmbH
MEMS Microelectromechanical Systems
FBAR Film Bulk Acoustic Wave Resonator
MFC Mass Flow Controller
MOX Metal Oxide
MPW3 Multi Project Wafer (3rd generation)
MPW4 Multi Project Wafer (4th generation)
MSP Multi Sensor Platform for Smart Building Management
NP Nanoparticle
NW Nanowire
OLED Organic Light Emitting Diode
PCB Printed Circuit Board
PL Photolithography
PLD Pulsed Laser Deposition
PMMA Poly(Methyl Methacrylate)
POM Particulate Organic Matter
PPM Parts Per Million
PVD Physical Vapor Deposition
PVDF Polyvinylidene Fluoride
QMB Quartz Microbalance
RH Relative Humidity
RPM Revolutions Per Minute
SB Silicon Based
SCCM Standard Cubic Centimeters per Minute
SEM Scanning Electron Microscope
SMU Source Measure Unit
SnO_2 Tin Dioxide
SoC System on Chip
SVOC Semi Volatile Organic Compounds
TC Thermocouple
TEM Transmission Electron Microscopy
TG Thermogravimetry
TMO Temperature Modulated Operation
TPD Temperature Programmed Desorption
TRL Technology Readiness Level
TSV Through Silicon Via

TVOC Total Volatile Organic Compounds
UV Ultraviolet
VOC Volatile Organic Compounds
VVOC Very Volatile Organic Compounds
WHO World Health Organization
XRD X-Ray Diffraction
XRR X-Ray Reflectivity
ZnO Zinc Oxide

Part I.

Motivation

Serinus canaria, the canary bird, was the first "gas sensor" applied to monitor air quality for the occurrence of hazardous gases in mines. The dance and fall of the canary bird rescued countless coal miners from an invisible death. The deployment of canaries should have come to an end, when in 1815 the Davy lamp (safety lamp) was invented. This lamps flame is shielded by a steel mesh preventing the ignition of flammable gases in the ambient air. The steel mesh also allows ambient air to enter the air surrounding the flame. Flammable gases like carbon monoxide or methane would strength the flame, whereas gases like carbon dioxide would dampen or even extinguish it. Although, the Davy lamp was used around the globe, it didn't prevent the further use of canary birds. Their duty to the coal mine finally ended in the mid 80's of the 20^{th} century [1], [2].
Coal mines were the first confined space, where detection of flammable gases was of utmost importance. But ever since gas cookers and gas heating systems took part in our daily lives, indoor air quality monitoring grew more and more important on a broader scale. In 1962 Seiyama et al.[3] published their work on zinc oxide thin films for the detection of various gases. Following this was the founding of Figaro Engineering in 1968 and the commercialization of tin dioxide based gas sensors by Naoyoshi Taguchi [4].
Ever since the commercialization of the Taguchi type gas sensors, extraordinary vigour was invested, leading to the emergence of various new sensor types: thermocatalytic gas sensors [5], potentiometric gas sensors [6], optical gas sensors [7], acoustic wave gas sensors [7] and carbon nanotube gas sensors [6] to mention a few of them.
In general, these aforementioned sensors can be subdivided into direct and indirect gas sensors. In case of direct gas sensors a specific physical quantity is measured, which determines the gas species and gas concentration. An example would be an IR based gas sensor. Hereby the gas is illuminated by an IR source. Depending on the energy states of the gas molecules (e.g. carbon dioxide), certain wavelengths of the IR source excite these energy states, hence the wavelengths are absorbed. The comparison of the emitted and transmitted IR spectrum reveal the absorbed wavelengths. Since the absorbed wavelengths correspond to specific energy states of the gas molecule, the gas molecule can be identified qualitatively. The intensity of the absorbed wavelength can be used for quantitative identification, whereas a calibration with multiple known concentrations of the gas is necessary.

In case of indirect gas sensors the sensor materials' surface mediates or is part of a chemical reaction, which results in changes of the electronic state of the sensor material. An example for this kind of sensors are metal oxide based gas sensors. At the surface of metal oxide (MOX) gas sensors, ambient oxygen molecules are adsorbed. Upon adsorption the oxygen molecules draw electrons from the MOX material to establish a bond. Thereby, the base resistance of the MOX material is increased. In general, the exposure of this gas sensor to certain gas molecules results in a chemical reaction between the adsorbed oxygen and the gas molecules. After the reaction occurred, the formally drawn electrons are released back into the MOX material. The resistance decreases. For both qualitative and quantitative gas identification, a calibration under laboratory conditions has to be done for each reactive test gas separately. The reason for this separate test gas calibration is the fact that under ambient conditions multiple test gas species would react with the adsorbed oxygen at the same time. Therefore, the contribution of multiple test gases to the resistance cannot be distinguished without knowing their individual contribution to the resistance.
Two important requirements for a gas sensor to reach a mass market are: low power consumption and integrability into mass production fabrication methods like CMOS technology. CMOS is short for complementary metal-oxide-semiconductor. Herein n-type and p-type metal oxide semiconductor field effect transistors are fabricated on the same substrate. This enables the realization of integrated circuits with a low power consumption. CMOS technology is the primary fabrication technology in the semiconductor industry.
Metal oxide based gas sensors, despite their need for heating, can be integrated onto CMOS devices to satisfy the two requirements of low-power consumption and integrability. The heating issue of MOX materials in CMOS devices has already been addressed leading to the development of heatable microelectromechanical systems (MEMS) called microhotplates. Since temperatures up to 400°C are necessary for the operation of MOX gas sensors an effective thermal insulation is needed. This thermal insulation is provided by the microhotplate structure allowing the gas sensor operation at elevated temperatures without any heat dissipation to the CMOS side of the chip.
This work has been done within the framework of the "Multi Sensor Platform for Smart Building Management (MSP)" project. One of the main goals

of this project was the development of a platform, which would enable the 3D-integration of numerous sensors. The sensor integration is driven by introducing CMOS processes for sensor fabrication to reduce the overall cost and size of these sensors. Furthermore, this platform, based on CMOS technology, promotes the application of Through-Silicon-Via (TSV) technology to advance the integration density of the sensor system. TSV structures are electrically conducting vias through the CMOS chip connecting the front side to the backside. As a result no wire-bonding is necessary and the overall footprint of the chip is minimized to the chips own size.
The final demonstrator of this project included multiple gas sensors, a fine dust sensor, an IR sensor, an UV-A/B sensor, a light sensor and humidity and temperature sensors on an area of only 20 x 20 mm. Within the MSP project, the issue of indoor air quality monitoring for smart homes was to some extend addressed by the group at Materials Center Leoben. Monitoring of carbon dioxide (CO_2) levels and regulating the ventilation system to a certain safe CO_2 level would have a huge impact on the residents health and on the power consumption of heating, ventilation and air-conditioning (HVAC) systems. An overall reduction in power consumption of HVAC systems would lead globally, if applied, to a reduction of CO_2 emissions. Another important issue is carbon monoxide (CO) monitoring. Reports on accidents involving gas boilers causing injured or even deaths aren't a scarcity. A widely distributed access to cheap CO sensors, which is possible to achieve with CMOS integrated MOX gas sensors would possibly end such tragedies.
This work is structured in four parts: motivation, fundamentals, experimental and results. In the fundamentals part a broad overview of the topic, metal oxides for gas sensing, is given. Section 1 illustrates the gas sensing mechanism as described in the ionosorption model. Herein, specific questions like, "What are the basic gas sensor quantities?" or "What are the fields of application for metal oxides?" are answered. Detailed deliberations on specific interaction of the metal oxide surface with various gases and humidity are made. Additionally, ways to sensitize metal oxides for enhanced gas sensitivity or selectivity are discussed.
In the experimental part the techniques used for the fabrication process of each investigated gas sensing material are illustrated. Section 2 discusses the fabrication and structuring of thin films by spray pyrolysis. Furthermore, the fabrication of nanowire arrays via electron beam lithography is shown.

Section 3 addresses the different process flows of the gas sensitive materials of section 2 for integration on the silicon substrate and on a CMOS platform. Additionally, a detailed description of the gas measurement system used for gas sensor evaluation is given.
The results part is subdivided into three sections. Section 4 addresses the material investigations performed for all three gas sensitive materials. Section 5 provides the gas measurements of various sensor materials. Section 6 addresses and analyses the results of the gas measurements in section 5. Furthermore, an outlook concerning future development of these gas sensors is given.

Part II.

Fundamentals

1. Metal Oxide Materials for Gas Sensing

1.1. Fundamentals of metal oxides

Metal oxide materials are compounds comprised of one or more metal cation species and oxygen anions. Basically, the metal and the oxygen are bound by an ionic bond. For some metal oxides the metal oxygen bond has both ionic and covalent characteristics [8].
The domain of metal oxide materials can be arranged into two groups: non-transition metal oxides and transition metal oxides. The difference between these two groups is attributed to the metal part of the metal oxide compound. In non-transition metals the outer shell contains either s- or p-orbitals that are partially filled. Transition metals (transition elements) are defined by the IUPAC as follows:"An element whose atom has an incomplete d sub-shell, or which can give rise to cations with an incomplete d sub-shell [9]".
Metals and transition metals form various oxides [10]. Structural diversity of metal oxides result in electronic properties that range from insulator to semiconductor to metal [11]. Tuning the electronic property of a certain oxide material can be done by changing its structural geometry.
The interest in metal oxides increased rapidly around the year 2000. In figure 1.1 the annual scientific output concerning metal oxide topics is depicted for a period of 30 years (1988-2018) [12]. The usage of metal oxide materials ranges over multiple fields like: Microelectronics, sensors, solar cells, coatings and catalysts.
In the field of microelectronics metal oxides are used to fabricate new types of transistors. One example is vanadium dioxide. In this material a metal to insulator transition can be observed at $67°C$. The change of resistance at

this phase transition is of multiple magnitudes. Furthermore the switching frequency is in the range of 100 fs [13]. In the field of sensors, especially gas sensors metal oxides have already staked their claim. Metal oxides like SnO_2 [14] [15], ZnO [16], CuO [17] [18] and WO_3 [19] [20] are used in integrated solutions, which have been part of the market for some years now.
Another area, which is increasingly interested in metal oxides, is solar cell technology. Herein, two technologies show promising results: dye solar cells [11] and all oxide hetero-junctions [21]. In dye solar cells metal oxides are being used as photo-electrode material. In all oxide hetero-junctions metal oxides are fabricated to form a pn-junction.
In recent years the application of metal oxide coatings for surfaces has become the norm. Metal oxides are deposited on certain surfaces for scratch resistance, lotus effect cleaning, antistatic and corrosion protection [22].
In the field of catalysis metal oxides are being used to improve standard processes by increasing the efficiency of those processes. Some of those catalytic processes are: Fischer-Tropsch process, alkylation, transesterification reaction and environmental applications (catalytic oxidation of VOCs / catalytic reduction of NOx) [23]. In the following paragraphs the key parameters of SnO_2, CuO and ZnO will be given.

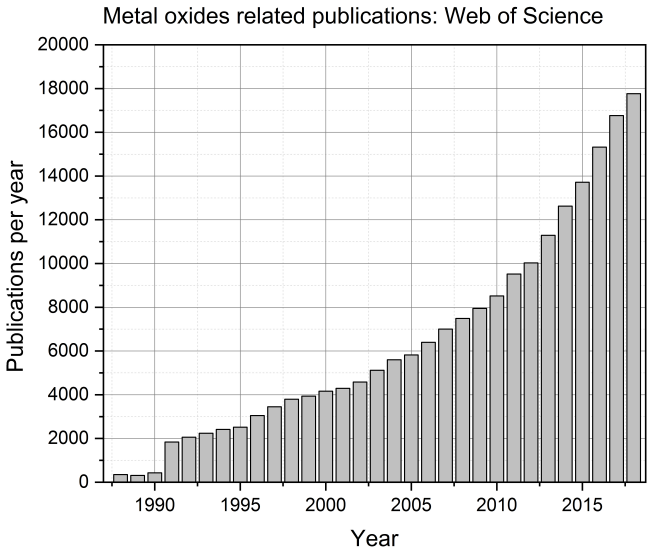

Figure 1.1.: Publication search on "metal oxides" on Web of Science. Period: 1988-2018 [12]

Table 1.1.: Typical metal oxide materials and morphologies used for gas sensing.

Material	**Morphology**
SnO_2	thin film [24], nanowires [25] , nanorods [26], nanoribbons [27], nanotubes [27]
CuO	thin film [28], nanowires [29], nanosheets [30]
ZnO	thin film [31], nanowires [32], nanorods [33],[34], nanoprims [33], [35]
WO_3	thin film [36], nanoplates [37], [38], nanowires [39]
NiO	nanoflakes [40]
Cr_2O_3	thin film [41], hollow spheres [42]
Co_3O_4	thick film [43], thin film [44]
La_2O_3	nanorods [45], nanoparticles-web [46]
V_2O_5	thin film [47], nanorods [48]

Tin(IV)dioxid SnO_2: Tin dioxide is a n-type metal oxide semiconductor [49] with a broad band gap of around 3.6 eV at room temperature [50] and a high electrical conductivity [51]. SnO_2 is a versatile material, that is applied in various fields. Some of them are: Electronics [52] [53], solar cells fabrication [54] [55], catalysis [56] [57] [58] [59] [60] [61] [62] [63] [64] and chemical sensors [14] [15].
In general, one can subdivide the properties of a material by its bulk properties and surface properties. For SnO_2 the difference between bulk and surface are defined by the dual valency of tin. The term dual valency attributes to the reversible reaction of stoichiometric tin cations (Sn^{4+}) into a non-stoichiometric tin cations (Sn^{2+}) [65]. This reversible reaction is dependent on the oxygen chemical potential of the material and the ambient atmosphere [66].
The interaction with the surface is also dependent on the geometry of the nanomaterial. Gas sensitive nanomaterials are fabricated as thin layers [15], nanoparticles [67], nanorods [26], nanotubes and nanowires [27].
The ways to synthesize SnO_2 materials are numerous. Typical processes are: hydro- and solvothermal synthesis [68] [69], vapor liquid solid synthesis [70], chemical vapour deposition (CVD) [71], sol-gel method [72], microemulsion method [73] [74], thermal evaporation [75], thermal oxidation [76] and spray pyrolysis [77] [78]. Table 1.2 shows the basic material properties and crystallographic parameters of SnO_2.

Table 1.2.: Material properties and crystallographic parameters of tin dioxide (SnO_2) [79] [50] [80].

Tin(IV)dioxide (SnO_2)	
Common tin oxides	SnO / SnO_2
Melting point	$1630°C$
Band gap	3.6 eV
Conduction mechanism	n-type (electrons)
Crystallographic parameters	
Crystal structure	tetragonal (rutile)
Density	6.85 $\frac{g}{cm^3}$
Space group	$P4_2/mnm$ [136]
Number of atoms per unit cell	6
a	4.737 Å
c	3.185 Å
$\alpha = \beta = \gamma$	90°

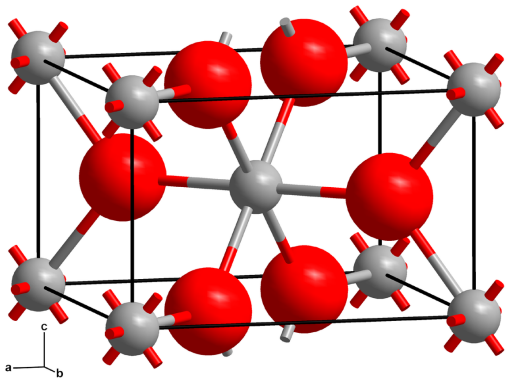

Figure 1.2.: Rutile crystal structure of tin dioxide (SnO_2). Taken from [81].

Cupric (II) Oxide CuO: Copper oxide [82] is found to have two primary oxides: cupric oxide CuO (tenorite) [83] and cuprous oxide Cu_2O (cuprite) [84]. Both oxides are a p-type semiconductor material. The band gap of

Cu_2O is 2.2 eV, whereas the band gap of CuO is only 1.2 eV [85]. Although Cu_2O exhibits a rather narrow band gap it has been shown that the usage of Cu_2O solar cells can yield energy conversion efficiency of 20% [86]. Furthermore, the p-type characteristic of Cu_2O allows the fabrication of hetero-junction solar cells reported in [87] and [86].
The applications of copper oxide materials aren't only limited to solar cell technology. Copper oxides are applied as antimicrobial material [88] [89], in electrochemical [90] [91] and electrochromic devices [92] [93], as part of OLEDs [94] [95], in photocatalysis [96] [97] and in gas sensing devices [17] [18].
The synthesis of CuO or Cu_2O can be done by various methods: direct current sputtering [98] [99], chemical vapour deposition (CVD) [100] [101], hydrothermal synthesis [102] [103], sol-gel method [104] [105], molecular beam epitaxy (MBE) [106] [107], pulsed laser deposition (PLD) [108] [109] and spray pyrolysis [28] [110]. Table 1.3 shows the basic material properties and crystallographic parameters of CuO.

Table 1.3.: Material properties and crystallographic parameters of cupric oxide (CuO) [79] [85] [111].

Copper(II) oxide (CuO)	
Common copper oxides	CuO / Cu_2O
Melting point	$1227^{\circ}C$
Band gap	1.2 eV
Conduction mechanism	p-type (holes)
Crystallographic parameters	
Crystal structure	monoclinic
Density	5.94 $\frac{g}{cm^3}$
Space group	C2/c [15]
Number of atoms per unit cell	6
a	4.6837 Å
b	3.4226 Å
c	5.1288 Å
$\alpha = \gamma$	90°
β	99.54°

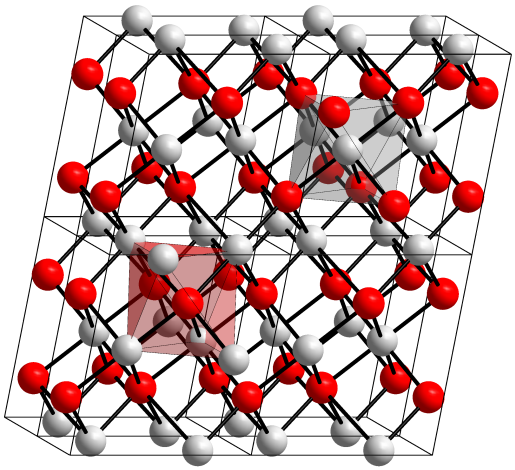

Figure 1.3.: Monoclinic crystal structure of copper (II) oxide (CuO). Taken from [111].

Zinc Oxide ZnO: Zinc oxide is a n-type metal oxide semiconductor with a band gap of 3.37 eV [112]. The crystalline structure of zinc oxide has two common polymorphs: hexagonal (wurtzite) and cubic (zinc blende) [112]. These two polymorphs have no inversion symmetry, hence no inversion centre. According to Tilley et al.[113] an inversion centre is defined as follows. For example the unit cell has an inversion centre at (0,0,0). In the unit cell an atom is positioned at (x,y,z). At the coordinates (-x,-y,-z) an atom of the same kind can be found. Therefore, the inversion centre is the point positioned equidistant between two atoms of the same kind [113]. Since both polymorphs have no inversion symmetry they are both piezoelectric. Furthermore, wurtzite ZnO has a spontaneous polarisation along the c-axis of the hexagonal structure and is therefore pyroelectric.
ZnO has many fields of application, which are as follows [114]: cosmetics [115], pharmaceutics [116], photocatalysis [117] [118], textile industry [119] [120], rubber industry [121] [122] and as gas sensors [16].
The methods to fabricate ZnO materials are: emulsion method [123], mechanochemical process [124], microemulsion method [125], precipitation process with [126] [127] or without surfactants [128] [129], sol-gel method [130], hydrothermal method [131] and microwave techniques [132]. Table 1.4 shows

the fundamental material properties and crystallographic parameters of ZnO (wurtzite).

Table 1.4.: Material properties and crystallographic parameters of zinc oxide (ZnO) [79].

Zinc oxide (ZnO)	
Common zinc oxide	ZnO
Melting point	$1974^{\circ}C$
Band gap	3.3 eV [112]
Conduction mechanism	n-type (electrons)
Crystallographic parameters	
Crystal structure	hexagonal (wurtzite)
Density	$5.1\ \frac{g}{cm^3}$
Space group	$C_{6v}{}^4$-$P6_3mc$
Number of atoms per unit cell	4
a	3.2495 Å
c	5.2069 Å
γ	120°
Formula unit Z	2

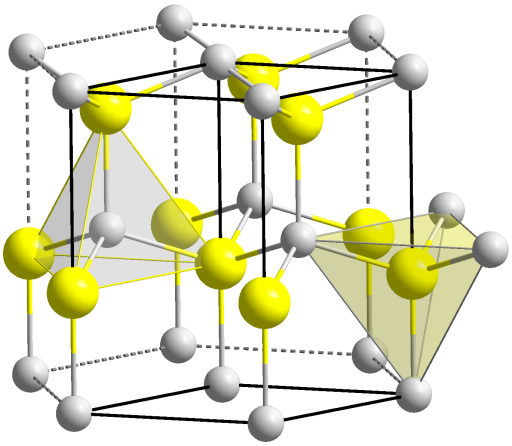

Figure 1.4.: Hexagonal (wurtzite) crystal structure of zinc oxide (ZnO). Taken from [133].

1.2. Metal oxide gas sensors

According to Eggins et al.[5] a sensor is a device that interacts with a physical quantity of its environment to return this interaction in the form of a specific signal. Before going into more detail concerning metal oxide gas sensors a general comparison of generic gas sensors and metal oxide gas sensors should be done to verify that the general characteristics are satisfied. What are the basic characteristics of a generic gas sensor? A generic gas sensor interacts with the ambient atmosphere and gives a feedback on its change. During this interaction the gas sensor recognizes an analyte. In this case the analyte is a specific target gas. The recognition is done by a reaction of the analyte with a receptor. A receptor is a feature of the sensor surface that specifically promotes the interaction with the target gas. The reaction of analyte and receptor can either lead to the change of a chemical or physical quantity, which can be measured.
These two cases are called chemical transduction and physical transduction. In the case of chemical transduction the reaction between analyte and receptor results in the change of a chemical quantity like pH value, which can be

measured and related to the analyte. In the case of physical transduction the reaction leads to the change of a physical quantity like the resistance, which again can be related to the analyte [5].
Are those two functions of a generic gas sensor to recept an analyte and transduce it as a measurable signal also found in a metal oxide gas sensor? Yamazoe et al.[134] shows these functions can be defined for a poly-crystalline metal oxide thin film gas sensor. A poly-crystalline MOX thin film consists of numerous crystallites or grains strung together. The sensing mechanism of MOX gas sensors is based on the adsorption of oxygen molecules from the ambient atmosphere to the surface of the MOX thin film, hence to the surface of the MOX grains. The oxygen adsorbed to the surface of a single grain results in the formation of a space charge layer at the surface of the grain. At the each grain boundary a double potential barrier (double Schottky barrier) is formed. In a simple picture the receptor of the MOX gas sensor is the adsorbed oxygen. Upon exposure to a reactive gas species (e.g.CO) the adsorbed oxygen reacts to the reactive gas species in a redox reaction. The conversion of a chemical signal, which is the interaction of the gas sensor surface with a reactive gas species (test gas), to a measurable signal is defined by the double potential barrier. The barrier height changes depending on the occurring surface reactions. These changes in the barrier height are reflected in the electrical resistance of the MOX material. The double potential barrier acts as the transducer of the MOX gas sensor. In the following subsection the gas sensing mechanism of MOX will be discussed in more detail.

1.2.1. Gas sensor quantities:

Sensitivity (S): The sensitivity of a gas sensor is the measure on its reactivity towards a specific gas at a given gas concentration. Sensitivity is a derived quantity of the gas sensor response, change of sensor signal, towards a gas pulse. A gas pulse is defined as a constant gas concentration over a specified time interval. In a standard lab set-up, the gas sensors' electrical resistance is measured continuously in a standard atmosphere. The gas sensor response to a certain test gas is evaluated by adding a gas pulse (test gas) to the standard atmosphere. The standard atmosphere is a gas mixture called

synthetic air, which contains 80% nitrogen and 20% oxygen. In general, test gases can be subdivided into two gas classes considering their effect on the gas sensors' resistance: reducing gases (e.g. CO) and oxidizing gases (NO_2). The behaviour of the n-type and p-type materials' electrical resistance at exposure to either oxidizing or reducing gases is reversed. Upon exposure to a reducing gas the electrical resistance of a n-type material decreases, whereas the electrical resistance of a p-type material increases. In case of an oxidizing gas the behaviour of the electrical resistance of n-type and p-type materials is reversed. The standard equations for the calculation of n-type and p-type gas sensors' sensitivities upon exposure to reducing and oxidizing gases are shown in equations 1.1 and 1.2. In those equations the reversing behaviour is reflected in the interchanging of numerator and denominator. The two resistance values R_{air} and R_{gas} are obtained from measurements similar to the one displayed in figure 1.5. The figure shows the electrical resistance of a n-type MOX gas sensor over time upon exposure to a reducing gas. Two vertical doted lines mark the onset and end of the test gas pulse. The resistance value before the gas exposure is the resistance value of the gas sensor in air (synthetic air) R_{air}. At the onset of the gas pulse the resistance of the gas sensor decreases strongly. After a certain time the resistance value reaches its saturation. The resistance value at the saturation is R_{gas}.

n-type [reducing gas] or p-type [oxidizing gas]:

$$S_n = \frac{R_{air}}{R_{gas}} \tag{1.1}$$

n-type [oxidizing gas] or p-type [reducing gas]:

$$S_p = \frac{R_{gas}}{R_{air}} \tag{1.2}$$

A more common form of the sensitivity is obtained by normalizing on the baseline of the gas sensors' electrical resistance (equation 1.3 and 1.4).

n-type [reducing gas] or p-type [oxidizing gas]:

$$S_n[\%] = \frac{|R_{air} - R_{gas}|}{R_{gas}} \cdot 100 \tag{1.3}$$

n-type [oxidizing gas] or p-type [reducing gas]:

$$S_p[\%] = \frac{|R_{gas} - R_{air}|}{R_{air}} \cdot 100 \tag{1.4}$$

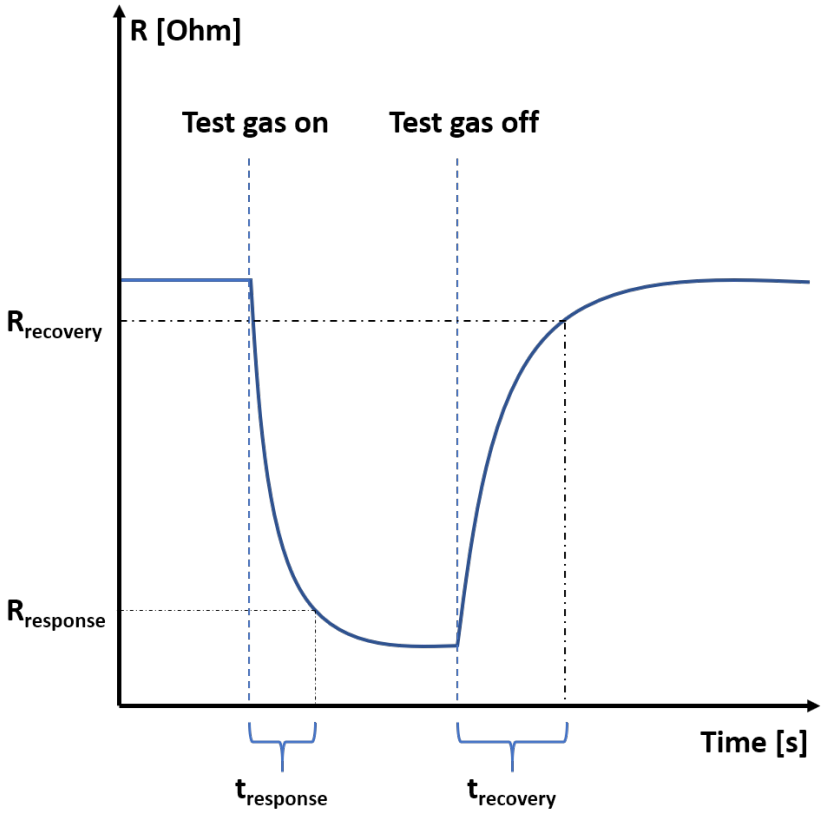

Figure 1.5.: Resistance change of an n-type metal oxide gas sensor upon exposure to a reducing gas. $R_{response}$ is 90% of the R_{gas} resistance value. $t_{response}$ is the time the gas sensor needs to reach $R_{response}$, after the onset of the gas pulse. $R_{recovery}$ is the resistance value 10% below the R_{air} resistance value. $t_{recovery}$ is the time the gas sensor needs to reach $R_{recovery}$, after the end of the gas pulse.

Selectivity (m): The term selectivity describes how sensitive a gas sensor is towards test gas i in contrast to test gas j. The gas sensor sensitivity is determined for a specific concentration of the test gas i and for the same concentration of test gas j. The following equation defines the selectivity quotient:

$$m_{ij} = \frac{S_i}{S_j} \tag{1.5}$$

The variable m_{ij} is the selectivity quotient defining whether a test gas i can be measured independently from a test gas j or not. S_i and S_j are the sensitivities towards test gas i and test gas j, respectively. The following six conditions arise:

- $m_{ij} \rightarrow$ not defined: One or both sensitivities S_i or S_j are equal to zero. If one of the sensitivities e.g. S_i is equal to zero, S_j is non zero, hence test gas j can be identified independently of test gas i. The opposite case exists is S_j is zero and S_i is non zero.
- $m_{ij} > 1$: The sensitivity S_j towards the test gas j is smaller than the sensitivity S_i to the test gas i. The two test gases cannot be measured independently.
- $m_{ij} < 1$: The sensitivity S_j towards the test gas j is larger than the sensitivity S_i to the test gas i. The two test gases cannot be measured independently.
- $m_{ij} = 1$: The sensitivities towards test gas i and test gas j are equal. The gas sensor cannot be used to measure those two gases in a mixture at all.
- $m_{ij} >> 1$: The sensitivity S_j towards the test gas j is much smaller than the sensitivity S_i to the test gas i. The gas sensor can measure test gas j with a small dependence to test gas i.
- $m_{ij} << 1$: The sensitivity S_j towards the test gas j is much larger than the sensitivity S_i to the test gas i. The gas sensor can measure test gas i with a small dependence to test gas j.

In general, if a gas sensor isn't only selective to a single test gas the gas sensor has so-called *cross-selectivity*.
In the two following paragraphs the response time as well as the recovery time will be explained. The explanations below are done for a n-type

MOX material. In case of a p-type MOX material the following explanations concerning the response to reducing and oxidizing gases have to be reversed to be valid for p-type materials.

Response time ($t_{response}$): For the definition of the response time figure 1.5 is used. The response time is defined by the resistance value $R_{response}$. Upon exposure to the gas pulse the gas sensors' electrical resistance decreases (reducing gas) or increases (oxidizing gas). For either reducing of oxidizing gas exposure the resistance of the gas sensor reaches a saturation level that is proportional to the gas pulse concentration, which is called R_{gas}. $R_{response}$ is 90% of the resistance value R_{gas}. The response time is the duration the resistance needs to reach the value $R_{response}$.

Recovery time ($t_{recovery}$): As for the response time figure 1.5 is used to define the recovery time. The recovery time is defined by the resistance value $R_{recovery}$. After the gas pulse has ended the gas sensors' electrical resistance increases (reducing gas) or decreases (oxidizing gas). The gas sensors' resistance returns to the resistance value, which it had before the gas exposure called R_{air}. $R_{recovery}$ is the resistance value 10% below (reducing gas) or above (oxidizing gas) of the R_{air} value. The time the gas sensor needs to reach the $R_{recovery}$ value starting after the gas pulse has been ended is called recovery time $t_{recovery}$.

Gas sensor drift: The base resistance value of a gas sensor is the resistance of the gas sensor at standard ambient air conditions (mixture of synthetic air and specific relative humidity level) at a specific operation temperature. During the operation of the gas sensor this base resistance value might change. The change in resistance is a result of irreversible chemical reactions at the sensor surface (sensor poisoning), diffusion of oxygen within the bulk and changes of the crystal structure of the thin film or thick film [135]. These changes have an impact on the long-term stability of the gas sensor and on the gas sensor's ability to produce reliable sensor data.

1.2.2. Ionosorption-Model

The ionosorption model is to date the most widely accepted model describing the MOX gas sensing mechanism. The first part of the ionosorption model considers the interaction of oxygen with the surface of the MOX material. Here, it is assumed that oxygen from the ambient atmosphere is adsorbed to the surface of the MOX material. The oxygen forms oxygen ion species, which react with reducing and oxidizing gases. The occurrence of the different oxygen ion species on the surface of the MOX is dependent on the temperature (see fig. 1.6). This temperature dependence directly influences the sensing mechanism, which will be discussed below. Figure 1.6 illustrates that the occurrence of oxygen ion species is split into two regions: molecular ionic species (O_2^-) and atomic ionic species (O^-, O^{2-}) [136]. At lower temperatures up to roughly 50°C ambient oxygen $O_{2(gas)}$ adsorbs surface sites S by physisorption forming $O_{2(phys)}$ oxygen species. From 100°C to 200°C molecular ionic oxygen O_2^- is the predominately found species. Around the transition temperature of 200°C both molecular ionic oxygen and single atomic ionic oxygen O^- can be found. In this direct competition O^- has more influence on the sensing mechanism than O_2^- as the former is more reactive. Reaching temperatures above roughly 450°C double atomic ionic oxygen O^{2-} is mainly found. O^{2-} is considered to have a minor influence as it is not stable [137].

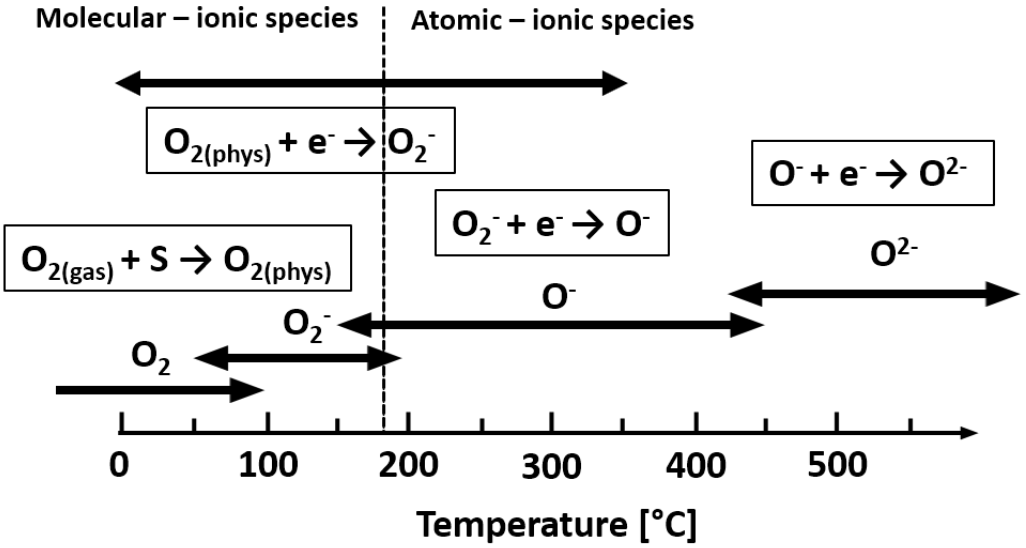

Figure 1.6.: Temperature dependent occurrence of oxygen ion species. Ambient oxygen $O_{2(gas)}$ adsorbs to surfaces sites S by physisorption forming $O_{2(phys)}$, which dissociates at higher temperatures. Below 200 °C molecular ionic oxygen species O_2^- is predominate. Above 200 °C atomic ionic oxygen species (O^-, O^{2-}) are mainly available. According to Barsan et al.[136].

The formation of these ionic oxygen species can be better understood by investigating the surface states of a semiconducting metal oxide (n-type material). Figure 1.7 shows the energy levels of a n-type semiconducting oxide. On the left side of the diagram the energy levels of the bulk material are shown: the conduction band $E_{C,b}$, the Fermi level E_F, the valence band $E_{V,b}$ and the vacuum energy level E_{vac}. Additionally, in this diagram χ is the electron affinity, Φ is the work function and $\Delta\Phi$ is the band bending. The right side of the diagram depicts the surface states. The energy levels of the vacuum energy and the Fermi level are the same. All other energy levels as conduction band $E_{C,S}$, donor level $E_{d,S}$ and valence band $E_{V,S}$ are shifted. The shift of the energy bands is a result of the following process. When oxygen adsorbs to the surface it draws electrons from the conduction band. These electrons start to fill up the surface states. The electrons in these surface states enter an ionic bond with the oxygen. The ionically bond oxygen species are depicted in figure 1.7 as $O_{\beta S}^{-\alpha}$, whereas the charge of

the surface states is Q_{SS}. Furthermore, the adsorption and desorption of physisorbed oxygen $O_{2(phys)}$ from ambient oxygen $O_{2(gas)}$ is shown by an incoming and outgoing arrow, which refers to the equilibrium state of the adsorption / desorption process. The dimension of the formed depletion layer as a result of the formation of the surface states is defined by the length z_0.
According to Barsan et al.[136] the reaction leading to the so-called ionosorption of oxygen is defined by equation 1.6:

$$\frac{\beta}{2} O_{2(gas)} + \alpha \cdot e^- + S \rightleftharpoons O_{\beta S}^{-\alpha} \tag{1.6}$$

In equation 1.6 β is a factor to differentiate between atomic ($\beta = 1$) and molecular ($\beta = 2$) oxygen, $O_{2(gas)}$ is a gaseous oxygen molecule, α is a factor to differentiate between single ionized oxygen ($\alpha = 1$) and double ionized oxygen ($\alpha = 2$), e^- is an electron, S is a site on the surface to which oxygen can adsorb and $O_{\beta S}^{-\alpha}$ is an ionosorbed oxygen molecule or atom.
The filling of the surface states leads to an accumulation of electrons at the surface. As a result of the growing number of negatively charged electrons at the surface states, a repulsive force is forming, which acts on any electron trying to fill the remaining surface states. This repulsive force is represented in the electronic band structure by bending of the conduction and valance band. This band bending continues until the potential energy to reach the surface states is higher as the kinetic energy of the electrons (equilibrium state). Furthermore, the band bending is accompanied by the formation of a space charge layer between the bulk and the surface. The space charge layer is also called depletion layer as the number of electrons in this region is reduced, due to the population of the surface states.
The formation of the space charge layer can also be seen as the formation of a potential between the bulk and the surface. This potential has a direct influence on the resistance (conductance):

$$R = R_0 \cdot \exp(\frac{qV_S}{k_B T}) \tag{1.7}$$

In equation 1.7, R is the resistance at the equilibrium state after exposure to oxygen, R_0 is the resistance without oxygen exposure, q is the elementary

charge, V_S is the surface potential, k_B is the Boltzmann constant and T is the temperature of the metal oxide layer. If the material is now exposed to a reducing gas (e.g. CO), the reactant reacts with the ionosorbed oxygen. This reaction leads to the removal of an ionosorbed oxygen, thereby releasing electrons back into the conduction band of the metal oxide material. The release of electrons would change the surface potential, which can be measured as a change in resistance of the material.

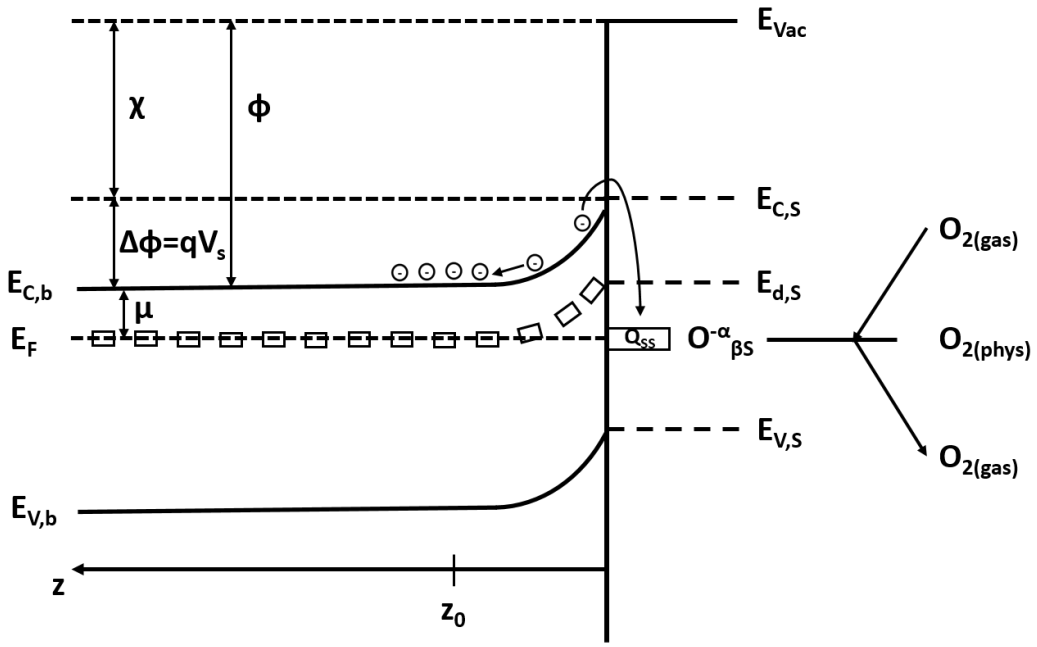

Figure 1.7.: Ionosorbed oxygen induces surface states on the n-type MOX surface resulting in a band bending of the electronic structure and formation of a depletion layer. Bulk: conduction band $E_{C,b}$, valence band $E_{V,b}$, χ electron affinity, ϕ work function, $\Delta\phi$ band bending. Surface: conduction band $E_{C,S}$, valence band $E_{V,S}$, donor level $E_{d,S}$, surface charge Q_{SS}, ionosorbed oxygen species $O^{-\alpha}_{\beta S}$, ambient oxygen $O_{2(gas)}$, physisorbed oxygen $O_{2(phys)}$. Bulk/surface: vacuum energy E_{vac}, Fermi level E_F. z_0 dimension of depletion layer. According to Barsan et al.[136].

The second part of the ionosorption model describes the dependence of the sensitivity on the surface geometry of the gas sensitive material. Apart of

one dimensional nanomaterials (nanowires, nanoribbons, nanobelts,...) the gas sensitive material of gas sensors mainly consist of thin or thick films. The base structures of thin or thick films are metal oxide crystallites or grains. The crystallite surface contributes to the gas sensitivity, as some surface atoms are part of the reactive surface sites that interact with gaseous species. The surface atoms differ from the bulk atoms by their coordination number. Therefore, surface atoms have unoccupied states that are available to form a bond, which contributes to the overall number of available surface sites. The number of surface atoms scales with the size of the crystallite. Assuming a spherically shaped crystallite the ratio of surface atoms to bulk atoms deceases with declining crystallite volume. Therefore, smaller crystallites result in a higher number of surface atoms (sites) calculated across the entire gas sensitive material. [138]. A higher number of reactive surface sites increases the sensors sensitivity.
Gas sensor layers, thin- or thick-films, consist of a large number of grains (crystallites). The grains are connected to each other by grain boundaries as well as structures called necks. Necks are formed during the crystallization process of the grains and connect neighbouring grains. These necks are made of the same material as the grains themselves. The dimension of the cross-sectional area of a neck defines the charge transport between two connected grains.
In general, the conduction of charges between grains is controlled by three effects that are directly dependent on the grain size. According to Yamazoe et al.[139] the three control mechanisms are:

1. grain boundary control
2. neck controls
3. grain control

All three effects are shown in figure 1.8 (c)-(e). The occurrence of each effect is defined by the relation of the grain size D to the thickness of the space charge layer L_d. The dimension of the space charge layer on the other hand is defined by the surface charge (ionosorbed oxygen) and the Debye length of the semiconducting material. These three effects can easily be differentiated by assuming a linear structure of grains (see fig. 1.8 (c)-(e)). Since in real polycrystalline material the number of necks supersedes the number of grain boundaries a heightened ratio is used for this simplistic structure of figure 1.8 (c)-(e).

In case of grain boundary control the condition states: $D >> 2L_d$ (fig. 1.8 (c)). The grain diameter is much larger than the space charge layer formed by the ionosorbed oxygen. Chemical reactions on the surface of the grain result in the change of the space charge layers thickness L_d. The majority of electric charges move through the neck structures. The cross-sectional area of the necks is rather large. Any change in the space charge layers thickness doesn't reduce the cross-sectional area of the necks to such an extend as to have a major impact on the conduction between neighbouring, neck-connected grains. Therefore, the grain boundaries are the sole contributor towards the conductance (resistance), hence the sensitivity. The influence of the grain boundaries on the conduction is shown in figure 1.8 (a). Herein, three consecutive grains are shown. The hatched area at the surface marks the space charge layer, which originates from the adsorbed oxygen. At the grain-boundaries a double Schottky barrier is being formed (see fig. 1.8 (b)). The height of the barrier relates to the thickness of the space charge layer. Chemical reactions of ionosorbed oxygen to test gas molecules lead to a change in height of the double Schottky barrier and therefore to the resistance (see eq. 1.7).
In case of neck control the condition states: $D \sim 2L_d$ (fig. 1.8 (d)). The space charge layer extends in such a way that the conduction of electrons through the neck is strongly influenced by chemical reactions at the surface. In other words, the diameter of the conducting pathway of the neck is either expanded or constricted. Although, there is a contribution of the grain boundaries, the number of neck structures exceeds them. Therefore, neck structures are the main contributors to the resistance, hence to the sensitivity.
In case of grain control the condition states: $D < 2L_d$ (fig. 1.8 (d)). The surface charge layer engulfs the whole grain. The grain is fully depleted of its electrons in the conduction band. The principle contributors to the resistance are the grains. In this condition the sensitivity is dependent on the size D of the grain. As already mentioned above, the smaller the grain size D the higher the reactivity of the surface as the surface-to-volume ratio increases. The highest gas sensitivity of a certain material can be achieved in this condition. Furthermore, at this conditions the material demonstrates a high resistance.

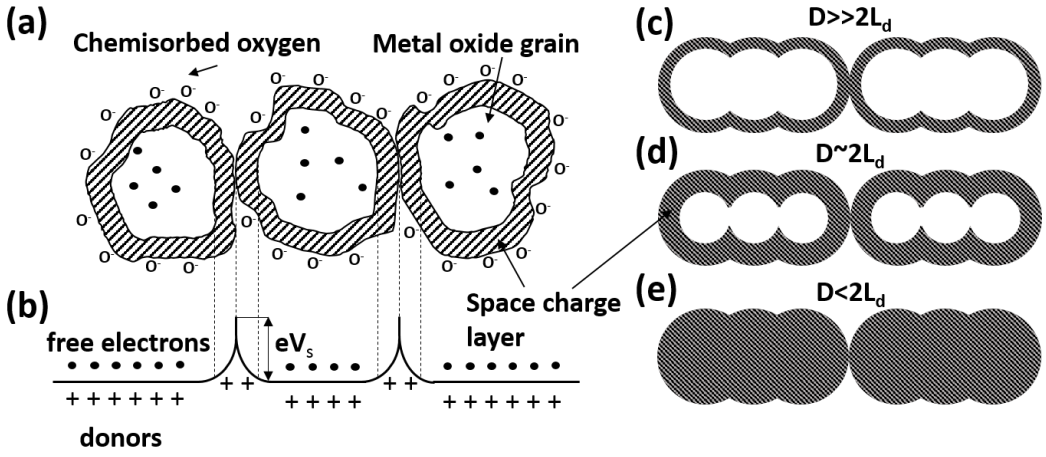

Figure 1.8.: (a) Space charge layers formed at the surface of three consecutive MOX grains as a result of ionosorbed oxygen. (b) At the grain boundaries of the three grains a Schottky double potential is formed. The height of the potential barrier is eV_S. The three control mechanisms for electron conduction through MOX materials: (c) grain boundary control $D >> 2L_d$, (d) neck control $D \sim 2L_d$ and (e) grain control $D < 2L_d$ (D grain size, L_d space charge layer thickness). According to Yamazoe et al.[139].

P-type metal oxide materials: Since p-type materials have different majority charge carriers some of the deliberations made above, concerning the ionosorption model have to be extended. In general, oxygen adsorbs in the same way on p-type MOX surfaces as it does on n-type MOX surfaces. A similar reaction equation to equation 1.6 can be given for the oxygen ionosorption on a p-type material surface [140]:

$$\frac{1}{2}O_{2(gas)} + S \rightleftharpoons O^-_{ad} + h^+ \tag{1.8}$$

In equation 1.8, $O_{2(gas)}$ is a gaseous oxygen molecule, S is a site on the surface to which oxygen can adsorb, O^-_{ad} is an ionosorbed oxygen atom and h is a hole. In contrast to n-type materials the majority charge carriers for p-type materials are holes. Figure 1.9 shows the energy band structure of a p-type material. In this figure the following energy levels are show: the vacuum energy E_{vac}, the conduction band E_C, the Fermi level E_F, the acceptor level

E_A and the valence band E_V. Furthermore, the electron affinity χ, the work function ϕ and the band bending $\Delta\phi$ are shown. The oxygen species bond by the surfaces states are titled as $O_{\beta S}^{-\alpha}$. The adsorption and desorption process of gaseous oxygen $O_{2(gas)}$ leading to the physisorption of oxygen $O_{2(phys)}$ is depicted by a energy level near the surface states. The dimension of the accumulation layer is defined by z_0. The process leading to the filling of the surface states proceeds as follows. Upon exposure to oxygen, electrons from the valence band are drawn into surface states. Within the valence band holes are formed. Accompanying the filling of the surface states is an energy band bending. Electrons continue to fill the surface states until the potential energy of the band bending supersedes the kinetic energy of the electrons.
The electrostatic attraction of the surface state electrons results in the formation of an hole accumulation layer beneath the surface (states). A major difference concerning the oxygen adsorption of p-type materials to n-type is the amount of adsorbed oxygen. According to [141] p-type materials adsorb more oxygen to their surface. Kim et al. states that as a result of the low stability of p-type oxides with multiple oxidation states the amount of oxygen that can be adsorbed is higher.
Equivalent to figure 1.8 for n-type materials figure 1.10 illustrates a double Schottky potential barrier formed between two consecutive p-type material grains. The hollow circles symbolize the accumulated holes at the potential barrier. Furthermore, the energy levels for the Fermi level E_F, the valance band E_V and the acceptor level E_A are shown.

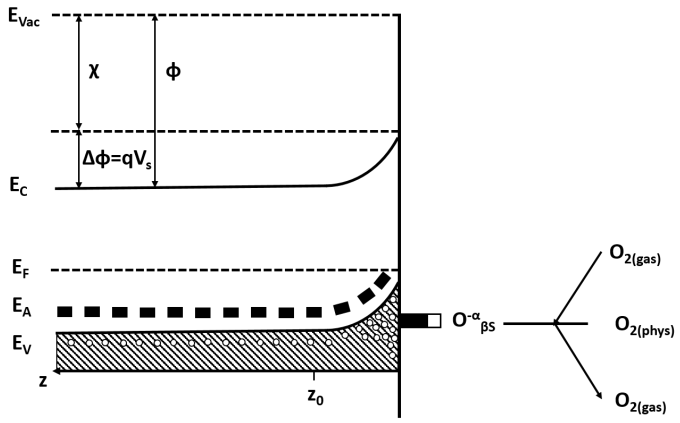

Figure 1.9.: Ionosorbed oxygen induces surface states on the p-type MOX surface resulting in a band bending of the electronic structure and formation of accumulation layer. Energy levels: vacuum energy E_{vac}, conduction band E_C, Fermi level E_F, acceptor level E_A, valence band E_V. χ is the electron affinity, ϕ the work function and $\Delta\phi$ is the band bending. The ionosorbed oxygen states are entitled as $O_{\beta S}^{-\alpha}$. The physisorption of gaseous oxygen $O_{2(gas)}$ to form physisorbed oxygen $O_{2(phys)}$ is marked by an arrow. z_0 defines the dimension of the accumulation layer. According to Barsan et al. [142].

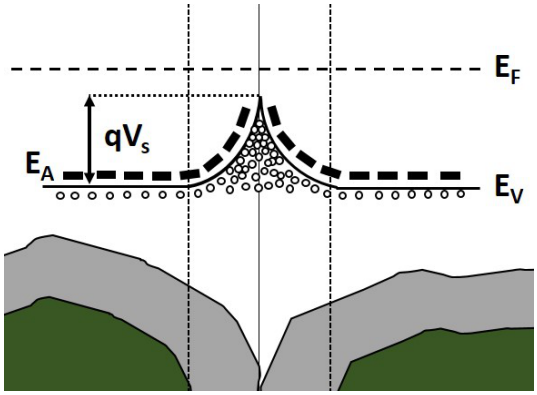

Figure 1.10.: Grain boundary of a p-type material depicting the double Schottky potential and the accumulation layer. qV_S is the barrier height of the double Schottky potential. The accumulation layer is shown as a highly concentrated hole area beneath the double Schottky potential. Energy levels: E_F is the fermi level, E_A is the acceptor level, E_V is the valence band. According to Barsan et al.[142].

Comparison of n-type and p-type metal oxide materials: The class of MOX materials contains both n- and p-type materials. In this paragraph the differences of n- and p-type MOX materials will be investigated. Furthermore, a direct comparison concerning their application as gas sensors will be done.
Figure 1.11 depicts a system of two consecutive grains for an n- and a p-type material. In figure 1.11 (a) two connected n-type MOX grains are shown. At the surface of each grain oxygen is ionically bound (ionosorption) to the surface. The oxygen molecules dissociate and each oxygen ion forms a separate ionic bond. Hereby, an electron is drawn from the MOX material to establish the bond. Multiple bonds to oxygen ions result in the formation of an electron depletion layer (shell) at the surface of the grains with a high electrical resistance. The remaining semiconducting core possesses a low electrical resistance compared to the shell. At the grain boundary a double Schottky potential is formed. Figure 1.11 (b) depicts two connected p-type MOX grains. Similar to the case of the n-type material, oxygen is adsorbed to the surface. The drawing of electrons from the p-type materials results in the formation of a hole accumulation layer at the surface of the grains. The hole accumulation layer (shell) possesses a low electrical resistance compared to the insulating core of the p-type grains. The formation of a double Schottky potential can also be observed for p-type materials at the grain boundaries.

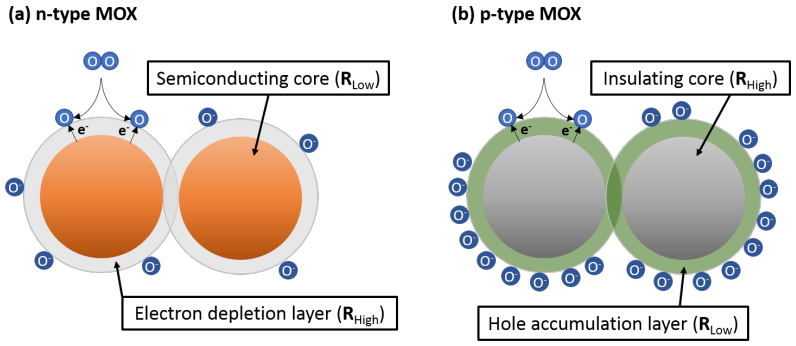

Figure 1.11.: (a) n-type MOX grains with electron depletion layer (grey) formed by ionosorption of oxygen. Electron depletion layer possesses a high electrical resistance R_{High}. The semiconducting core (orange) of the grains has a low electrical resistance R_{Low}. (b) p-type MOX grains with hole accumulation layer (green) formed by ionosorption of oxygen. Hole accumulation layer posseses a low electrical resistance R_{Low}. The insulating core (dark grey) has a high electrical resistance R_{High}. Between both n-type and p-type grains a double Schottky potential barrier is formed. According to Kim et al.[141]

Figure 1.12 (a) depicts the percolation path of the majority charge carriers (electrons) of a system of two connected n-type MOX grains, before and after gas exposure. On the right side of figure 1.12 (a) ionosorbed oxygen at the surface of the grains results in the formation of the electron depletion layer (space charge layer) at each grain and a double Schottky potential between the grains. The blue arrows in this figure represent the percolation path of the electrons. The electrons have to overcome two areas: the electron depletion layer (shell) and the semiconducting core of the grains. The electron depletion layer has a high electrical resistance, whereas the semiconducting core of the grains has a low electrical resistance. The bigger part of the resistance of the two grains can be attributed to the contribution of the electron depletion layer. On the left side of figure 1.12 (a) the system from the right side is depicted upon exposure to carbon monoxide (CO). The ionosorbed oxygen reacts with CO and forms CO_2. As a result of this chemical reaction an electron formally bound to the ionosorbed oxygen is released into the MOX material. A multitude of these reactions result in the decrease of the electron depletion layers' thickness and of its electrical resistance. The chemical reactions occurring at the grains surface have hardly any impact on the electrical resistance of the semiconducting core.

Figure 1.12 (b) shows an equivalent circuit of the core-shell system, which defines the total resistance. R_{core} is a constant value and remains unchanged over the entire process of ionosorption of oxygen and exposure to reactive gases. R_{shell} is marked with a green arrow, since it can change depending on ionosorption of oxygen or gas exposure [141].

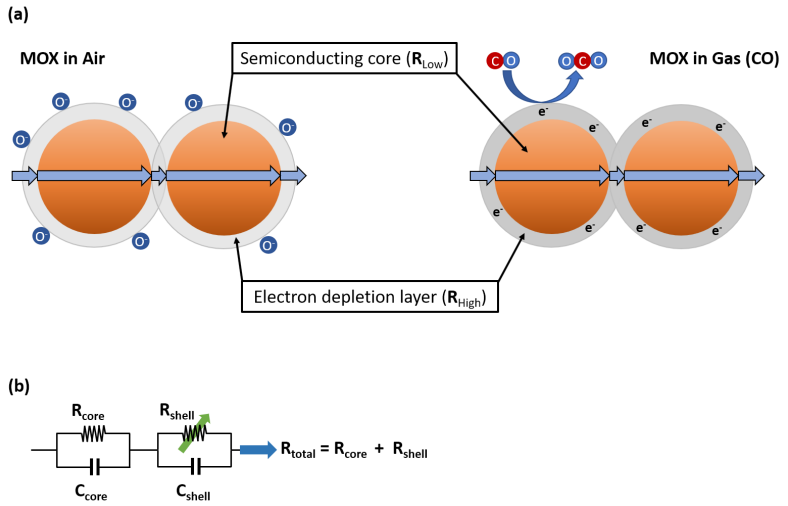

Figure 1.12.: (a) Percolation path of majority charge carrier (electrons) through two n-type MOX grains (blue arrow). Left side: Ionosorption of oxygen at the MOX surface leading to the formation of an electron depletion layer. Right side: Chemical reaction of ionosorbed oxygen O^- and CO resulting in CO_2, thereby changing the thickness of the electron depletion layer. (b) Equivalent circuit scheme depicting the total resistance as a serial circuit. The total resistance is the sum of the resistance of the electron depletion layer and the semiconducting core. According to Kim et al.[141]

Figure 1.13 (a) depicts the percolation path of the majority charge carriers (holes) of a system of two connected p-type MOX grains, before and after gas exposure. On the right side of figure 1.13 (a) the ionosorbed oxygen at the surface of the grains results in the formation of a hole accumulation layer (shell) at each grain and a double Schottky potential between the grains. As for the case of the n-type conduction the percolation path of the charge carrier is marked by a blue arrow. In contrast to the n-type conduction case the holes move only along the hole accumulation layer.

The hole accumulation layer has a low electrical resistance, whereas the insulating core of the grains has a high electrical resistance. On the left side of figure 1.13 (a) the two grains are exposed to CO. The ionosorbed oxygen chemically reacts with CO forming CO_2. The electron bound by the ionosorbed oxygen is released into the p-type MOX material. The electron recombines with a hole. A large number of CO reactions would result in the increase of the electrical resistance since the number of majority charge carrier, holes, is reduced by the recombination with electrons formally bond by the ionosorbed oxygen. Furthermore, the reduction of holes leads to a change of the hole accumulation layers thickness. Changes in the hole accumulation layer at the ionosorption of oxygen or gas exposure have only marginal impact on the resistance of the insulating core of the grains. In figure 1.13 (b) an equivalent circuit is shown. The resistance contributions of the core and of the shell are described via a parallel circuit. As for the n-type material the change of resistance is mainly done within the shell. Therefore, the resistance of the shell is marked with an green arrow as it will change at ionosorption of oxygen and gas exposure [141].

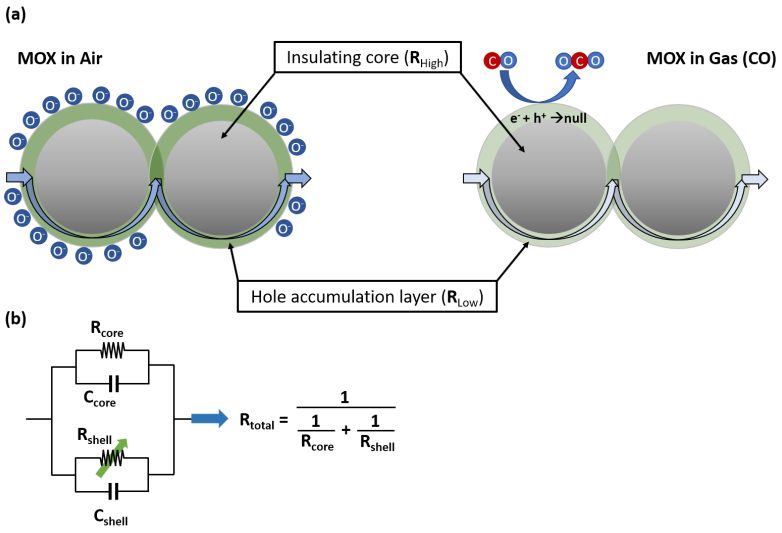

Figure 1.13.: (a) Percolation path of majority charge carrier (holes) through two p-type MOX grains (blue arrow). Left side: Ionosorption of oxygen at the MOX surface leading to the formation of a hole accumulation layer. Right side: Chemical reaction of ionosorbed oxygen O^- and CO resulting in CO_2, thereby changing the thickness of the hole accumulation layer. (b) Equivalent circuit scheme depicting the total resistance as a parallel circuit. The total resistance is the reverse sum of the reverse resistance of the hole depletion layer and the reverse resistance of the semiconducting core. According to Kim et al.[141]

As already stated above n-type materials behave differently for reducing or oxidizing gases compared to p-type materials. When n-type materials are exposed to reducing gases, their resistance drops. As explained above this is the result of the introduction of electrons into the conduction band originating from the chemical reaction of reducing gas and an ionosorbed oxygen. In p-type materials the same chemical reaction again leads to the introduction of electrons, but this time into the valence band. The electron recombines with a hole. This recombination lowers the number of charge carriers, hence holes. The resistances of the p-type material rises. In the case of oxidizing gases an inverse reaction occurs.
The sensitivity of n- and p-type materials is another issue to be investigated. The sensitivity is a relative measure of the change of resistance upon gas exposure. The change of both materials resistance can be lead back to the change of the double Schottky potential barrier height, hence the band

bending. By assuming an equal band bending the sensitivities of both materials can be compared. Hübner et al.[140] calculated the conductance for n- and p-type layers and reached the conclusion that if an equal band bending is assumed the materials transduce the chemical reaction at the double potential differently. This difference is a result of the conduction mechanism. A relationship between n- and p-type sensitivities ($S_{n,p}$) was derived by Hübner et al.[140] and is stated in equation 1.9 below.

$$S_p = \sqrt{S_n} \tag{1.9}$$

Since the sensitivity of a p-type material is only the square root of the sensitivity of a n-type material, n-type materials are more attractive for gas sensing when it comes to high sensitivities. However, the sensitivity of a material towards a test gas is also dependent on the material itself. Therefore, p-type materials can show sensitivities to test gases, where n-type materials are blind.

Derivation of gas sensor response and sensitivity: According to the ionosorption model ionosorbed oxygen is the main promoter for gas sensing reactions. The ionosorption of oxygen is only possible if electrons from the conduction band can be drawn to the surface states, thereby forming a depletion layer below the surface. The size of the depletion layer and its relation to the grain size will be discussed in the following section. However, in a case described by Williams [143] low bulk donor levels lead to a fully depleted grain. Hereby, the conduction mechanism is solely dependent on the surface states. Williams [144] extended this model by including a combination of bulk donor and acceptor states. The following considerations include various equilibrium conditions and are depicted according to Henshaw et al.[145]:

1. Thermal excitation of carriers $\longrightarrow$ X $\rightleftharpoons$ p + n

$$K_1 = N_C \exp\left(\frac{-\Delta E_G}{2k_B T}\right) = pn \tag{1.10}$$

K_1 ... equilibrium constant for X $\rightleftharpoons$ p + n
N_C ... density of states at the conduction band edge
ΔE_G ... band gap
p ... hole concentration
n ... electron concentration

2. Ionisation of donors $\longrightarrow$ D $\rightleftharpoons$ D^+ + n

$$K_2 = N_C \exp\left(\frac{-\Delta E_D}{k_B T}\right) = \frac{n f_D}{1 - f_D} \tag{1.11}$$

K_2 ... equilibrium constant for D $\rightleftharpoons$ D^+ + n
ΔE_D ... ionisation energy of donor states
f_D ... fraction of ionised donors states

3. Ionisation of acceptors $\longrightarrow$ S^- $\rightleftharpoons$ S + n

$$K_3 = N_C \exp\left(\frac{-\Delta E_S}{k_B T}\right) = \frac{n(1 - f_S)}{f_S} \tag{1.12}$$

K_3 ... equilibrium constant for S^- $\rightleftharpoons$ S + n
ΔE_S ... ionisation energy of surface acceptor states
f_S ... fraction of surface acceptor states with trapped electrons

4. Equilibrium of valence-band holes with surface oxygen
$\longrightarrow$ S $\rightleftharpoons$ S^- + p

$$K_4 = N_V \exp\left(\frac{-(\Delta E_G - \Delta E_S)}{k_B T}\right) = \frac{p f_S}{1 - f_S} \tag{1.13}$$

K_4 ... equilibrium constant for S $\rightleftharpoons$ S^- + p
N_V ... density of states at the valence band edge

5. Ionisation of bulk acceptors $\longrightarrow A^+ \rightleftharpoons A + p$

$$K_5 = N_V \exp\left(\frac{-(\Delta E_G - \Delta E_A)}{k_B T}\right) = \frac{p(1 - f_A)}{f_A} \tag{1.14}$$

K_5 ... equilibrium constant for $A^+ \rightleftharpoons A + p$
ΔE_A ... ionisation energy of bulk acceptor states
f_A ... fraction of ionised acceptors states

6. Charge balance

$$p + f_A N_A + f_D N_D = n + f_S N_S \tag{1.15}$$

N_S ... density of surface acceptor states
N_A ... density of bulk acceptor states
N_D ... density of bulk donor states

Since the premise in this derivation is that surface-trap limited conduction is predominant, the following assumption is valid: $N_S \ll N_D$ and $N_S \ll N_A$. As a result of this assumption the number of electrons n should be small and $K_1 \ll K_3 \ll K_2$ and $K_1 \ll K_3 \ll K_5$. This results in the energy states depicted in figure 1.14. Herein, the bulk donor states reside slightly below the conduction band, whereas the bulk acceptor states are slightly above the valence band. The energies of the surface acceptor states can be found between bulk donor and bulk acceptor states.

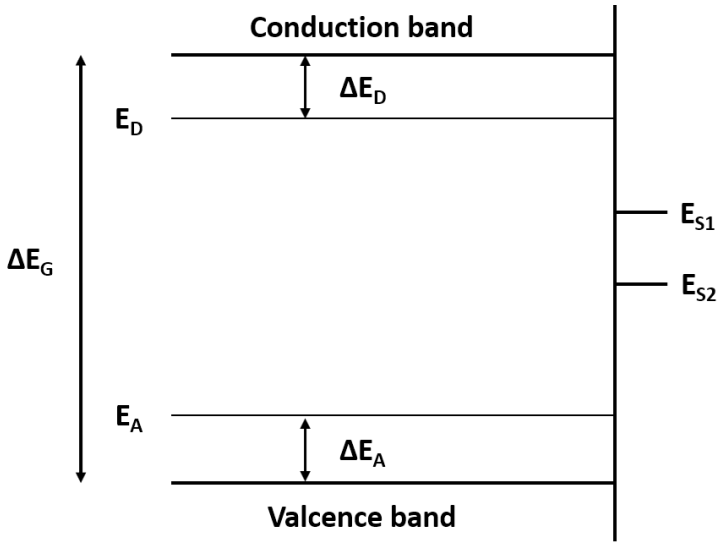

Figure 1.14.: Energy levels of two surface states. Energy levels: E_D bulk donor level, E_A bulk acceptor level, E_{S1} and E_{S2} surface acceptor levels. Energies: ΔE_G band gas energy, ΔE_D ionisation energy for donor levels, ΔE_A ionisation energy from bulk acceptor level. According to Henshaw et al.[145]

In the next step equations 1.10 - 1.15 are simplified and result in:

$$nK_1K_2K_3N_A + nK_1K_2K_3N_D - n^2K_1K_2N_S + n^2K_2K_3K_5N_D \approx 0 \tag{1.16}$$

As a consequence of this simplification the concentration of electrons and holes can be written as, with $K_4K_3 = K_1$:

$$n \approx \frac{K_3(N_A + N_D)}{N_S} \tag{1.17}$$

$$p \approx \frac{K_4N_S}{(N_A + N_D)} \tag{1.18}$$

In general the conductivity is given by:

$$\sigma = ne\mu_e + pe\mu_p \tag{1.19}$$

$\mu_{e,p}$ ... electron and hole mobility
e ... elementary charge

By using equation 1.17 and 1.18 the following equation is obtained:

$$\frac{\sigma}{e} = \frac{\mu_e K_3 (N_A + N_D)}{N_S} + \frac{\mu_p K_4 N_S}{(N_A + N_D)} \tag{1.20}$$

In n-type materials electrons are the majority charge carriers. The conductivity of this material is defined by the first term of equation 1.20. In p-type materials holes are the majority charge carriers. Therefore, the conductivity is defined by the second part of equation 1.20. Williams defines the sensitivity S as the dependence of the conductivity of the surface acceptor states concentration on the availability of reactive gas species in air. A first equation for the sensitivity is obtained by deriving equation 1.20 after N_S:

$$S = \frac{d(\sigma/e)}{dN_S} \left(\frac{1}{\sigma_0/e} \right) \tag{1.21}$$

σ_0 ... conductivity of material at ambient air (no reactive gas present)

Using equation 1.20:

$$S = \frac{1}{N_S} \left(\frac{\mu_p K_2 N_S/(N_A + N_D) - \mu_e K_1 (N_A + N_D/N_S)}{\mu_p K_2 N_{S,0}/(N_A + N_D) + \mu_e K_1 (N_A + N_D)/N_{S,0}} \right) \tag{1.22}$$

$N_{S,0}$ ... density of surface acceptor states at ambient air (no reactive gas present)

In case of changes in the surface trap state concentration are kept within bounds, it can be assumed that $N_S \approx N_{S,0}$. As a consequence S can be written as:

$$S \approx \frac{1}{N_S} \left(\frac{1-\alpha}{1+\alpha} \right) \tag{1.23}$$

with

$$\alpha = \frac{\mu_e K_1 (N_A + N_D)^2}{\mu_p K_2 N_S^2}.$$

As a result of the exposure to the test gas the density of surface acceptor states N_S decreases. The quantity α states which one of the conductivity types, n-type or p-type, is occurring. If $\alpha < 1$ the response of the material shows p-type behaviour (conductivity decreases). If $\alpha > 1$ the response of the material shows n-type behaviour (conductivity increases). The two quantities K_3 and K_4 depend on change in the surface acceptor energy ΔE_S. Since ΔE_S is in the exponent of K_3 and K_4 even small changes in E_S lead to large changes in K_3 and K_4, hence in the sensitivity.

1.2.3. Nanowires

Metal oxide nanowires are a 1D material exhibiting multiple properties, which are useful for the application in gas sensors. Kolmakov [146] states five reasons why MOX nanowire materials are interesting for gas sensing:

1. Nanowires have a high surface to volume ratio.
2. Chemical reactions on the surface have a strong influence on the bulk conductivity.
3. If the Debye length and the nanowire radius are of similar dimension the depletion zone spans over most or the entire nanowire volume.
4. Nanowires have the ideal morphology (high ratio of length to diameter) to be integrated into sensing devices.
5. The nanowire characteristics (crystallinity, morphology, composition,...) can be controlled by process technologies.

Since the nanowires described here are made of metal oxides the gas sensing mechanism is based on the ionosorption model (see section 1.2.2). MOX nanowires can be fabricated as single crystalline structures or as polycrystalline structures. Table 1.5 at the end of this section presents various MOX nanowire fabrication methods. For the polycrystalline case the sensing mechanism follows the deliberation made above for a thin or thick film. In general, single crystalline MOX nanowires are preferred for gas

sensing. The high crystallinity of such nanowires ensures better stability in operations over time compared to thin film materials [147]. The charge transport in nanowires will be discussed according to the model of n-type MOX nanowires. In general, MOX nanowires can be idealized as cylindrical structures, where the diameter is much smaller than the height. In MOX nanowires the charges are conducted along the longitudinal axis, which is parallel to the cylinders height. Figure 1.15 (a) shows the cross sectional view of a MOX nanowire. Here, the nanowire is shown without ionosorbed oxygen, hence no depletion zone. According to Miller et al.[148] the electrical resistance of the MOX nanowire can be described by equation 1.24.

$$R = \frac{\rho L}{\pi D_{channel}} \tag{1.24}$$

R is the electrical resistance of the nanowire. ρ is the electrical resistivity of the nanowire material. L is the length of the nanowire. $D_{channel}$ is the diameter of the conducting channel within the nanowire bulk. In the case of a pristine MOX nanowire without ionosorbed oxygen the conducting channel can be considered equivalent to the nanowire diameter.
In figure 1.15 (b) oxygen from the ambient atmosphere ionosorbs to the surface. During the adsorption process electrons from the conduction band of the MOX are drawn into surface states. As a result, equivalently to the grain of a thin film, a depletion layer (thickness L_d) is formed at the surface of the nanowire. The formation of the depletion layer causes a decrease of the conducting channel's diameter. The resistance of the nanowire increases. In figure 1.15 (c) the ionosorbed oxygen interact with a test gas (reducing gas). The surface reactions result in the removal of some ionosorbed oxygen ions from the surface and the reintroduction of electrons occupying surface states back into the material. The thickness of the depletion layer is reduced and the diameter of the conducting channel is increased, hence the resistance decreases.

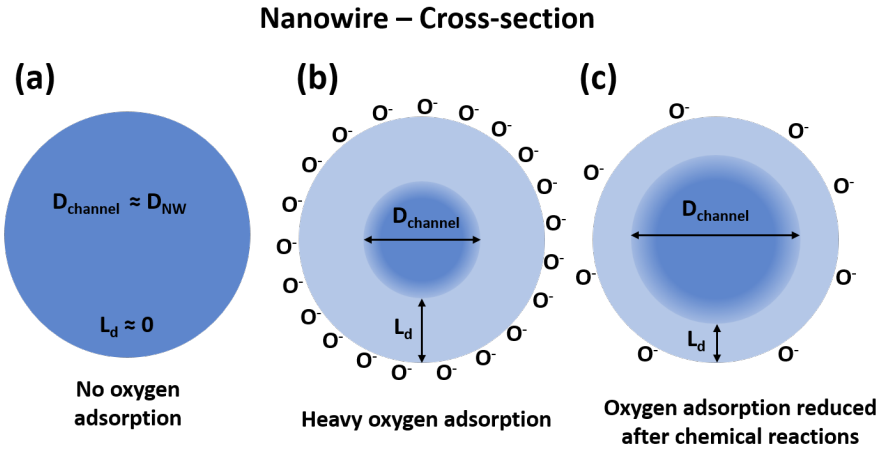

Figure 1.15.: Cross-section of a metal oxide nanowire with diameter D_{NW}. (a) No oxygen is adsorbed to the nanowire surface. The conduction channel diameter $D_{channel}$ is equal to the nanowire diameter. (b) Ambient oxygen is ionosorbed at the nanowire surface. At the surface a depletion layer is formed with thickness L_d. The diameter of the conduction channel is decreased as result of the formed depletion layer. (c) Upon exposure to a test gas (reducing gas) a chemical reaction between test gas and ionosorbed oxygen occurs, resulting in the increase of the conduction channels diameter. According to Miller et al.[148]

Since the fabrication of single nanowire devices for mass production is rather challenging other approaches have to be explored. Nanowire networks seem to be a more cost efficient way for nanowire device fabrication. Hereby, nanowires are either directly synthesised on an electrode system or deposited in a post processing step [149]. A high number of nanowires contained in a single device provide a large sensor surface.
Within a nanowire network the alignment of the nanowires is random to moderately order (template assisted growth) at best. The percolation line of a current through the entire network will pass along nanowires and across nanowire junctions. At these junctions separate nanowires are in contact with each other. These junctions are similar to the grain boundaries found in MOX films. Figure 1.16 shows a graphical representation of nanowire junctions. Herein, the nanowires have a diameter of D_{NW}. The conduction of the charges along the longitudinal axis of the nanowires is marked by a yellow line. The electrical resistance of a single nanowire along its lon-

gitudinal axis is calculated according to equation 1.24. At the nanowire junction a double Schottky potential barrier is formed. The contributions of the nanowire junction to the total resistance is calculated by equation 1.7. Both equations are presented in the figure 1.16. The total resistance of a nanowire network is predominantly defined by the potential barrier between separate nanowires [149].
The double Schottky potential barrier forming at the nanowire junctions is shown in figure 1.17 (a) at ambient air. Herein, V_{Air} is the potential of the barrier at ambient air, L_d is the thickness of the depletion layer, E_C is the conduction band, E_F is the Fermi level and E_V is the valance band. Figure 1.17 (b) depicts the potential barrier after the exposure to a reducing test gas. The value of the potential after gas exposure decreases to V_{Gas}. Furthermore, the thickness of the depletion layer is decreased accordingly.

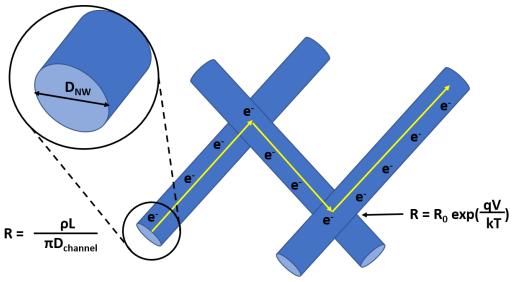

Figure 1.16.: Conduction path across multiple nanowires with diameter D_{NW}. The electrons move along the nanowires longitudinal axis as well as across nanowire junctions (yellow line). The two major contributions to the total electrical resistance are nanowire resistance (eq.1.24) and nanowire junction resistance (eq.1.7). According to Miller et al.[148]

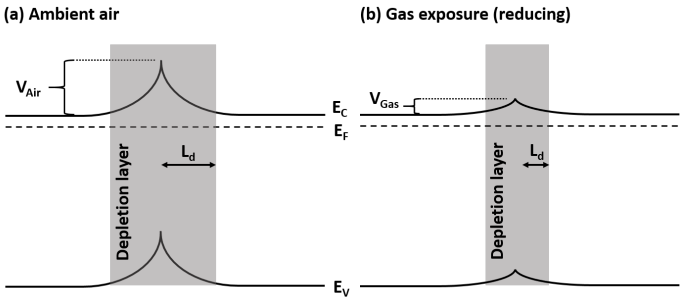

Figure 1.17.: (a) Double Schottky potential of a nanowire homo-junction (n-type MOX material) at ambient atmosphere V_{Air}. (b) Double Schottky potential after exposure to a reducing test gas V_{Gas}. The thickness of the depletion layer L_d at the nanowire junction is shown as a grey rectangle. Energy levels: E_C is the conduction band, E_F is the Fermi level and E_V is the valance band. According to Miller et al.[148]

Single nanowires or nanowire networks can be functionalized with nanoparticles to enhance each of their sensitivity towards a test gas. The influence of nanoparticles placed on the surface of a nanowire is shown in figure 1.18. Figure 1.18 (a) depicts a metallic nanoparticle M being placed on the surface of a single nanowire at inert gas conditions. There is no interaction between the system nanowire/nanoparticle to any gas molecule. The only occurring interaction is between the nanowire and the nanoparticle. Electrons from the nanowire are drawn by the metallic nanoparticle. As a result of this charge transfer an electron depletion layer is formed at the boundary between nanowire and nanoparticle extending into the nanowire. As already established above, electrons move parallel to the longitudinal axis of the nanowire within its conduction channel. The presence of the metallic nanoparticle M and the formation of the depletion layer results in a locally constriction of the conduction channel. A reduction in the conduction channels diameter leads to an increase in the electrical resistance. Figure 1.18 (b) and (c) depict the two main sensitization mechanisms occurring upon nanoparticle functionalization: electronic and chemical sensitization. Electronic sensitization describes the interaction of a test gas with the nanoparticle (fig.1.18 (b)). The test gas doesn't interact with the surface of the nanowire. At the surface of the metallic nanoparticle a chemical reaction is taking place. A charge transfer from the metallic nanoparticle

to the reactants takes place. Subsequently, these charges are replenished as they are drawn from the nanowire. Hereby, the electron depletion layer is extended, which can again be measured by an increase in resistance.
Chemical sensitization considers the nanoparticle as a catalyst. The nanoparticle dissociates the test gas and spills over the products to the nanowire surface. Consecutive reactions between the products and the nanowire surface lead to a charge transfer, resulting in the extension of the depletion layer. The spilled over reaction products extend the electron depletion layer. The extended area around the metallic nanoparticle resulted by the spilled over products is called spillover zone.
An example for this process is shown in figure 1.18 (c). Oxygen molecules are dissociated at the surface of the metallic nanoparticle and the oxygen ions are transported to the nanowire surface. The oxygen ions form an ionosorption bond with the nanowire surface resulting in the extension of the electron depletion layer and an increased electrical resistance of the nanowire [146]. More detailed information on these two sensitization mechanisms can be found in section 1.4.

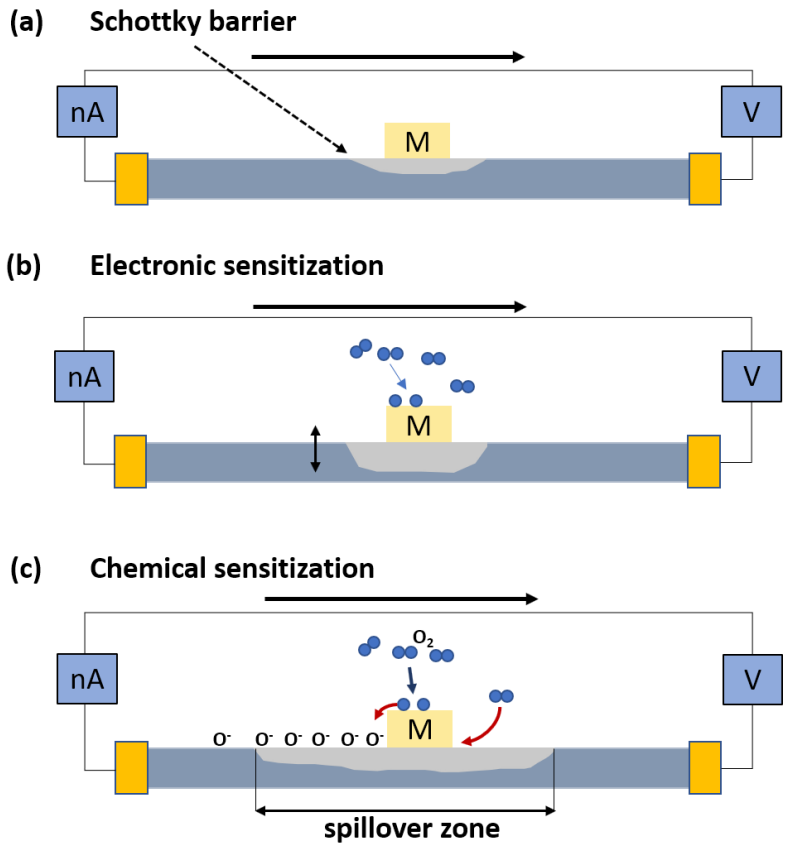

Figure 1.18.: Effect of nanoparticle functionalization on a nanowire surface. (a) Formation of an electron depletion layer at the boundary between nanoparticle and nanowire (Schottky barrier). (b) Electronic sensitization: the metallic nanoparticle M reacts with a test gas. Additional charges necessary for the chemical reaction are drawn from the nanowire. The depletion layer is extended (c) Chemical sensitization: the metallic nanoparticle M acts as a catalyst. Reaction products spill over to the nanowire surface. The spilled over products interact with the nanowire surface extending the electron depletion layer. The extension of the depletion layer is called spill over zone. According to Kolmakov[146]

Table 1.5.: Fabrication methods for metal oxide nanowires [150]:

Fabrication method	Materials
Physical vapour deposition (PVD)	copper oxide [151], tin oxid [152], tungsten oxide [153], zinc oxide [154] [155]
Chemical vapour deposition (CVD)	copper oxide [156], tin oxid [157] [158], tungsten oxide [159], zinc oxide [160] [161]
Thermal oxidation (TO)	copper oxide [162] [163] , tin oxid [164], tungsten oxide [165], zinc oxide [166] [167]
Electrospinning (ELS)	copper oxide [168] [169] , tin oxid [170] [171], tungsten oxide [172], zinc oxide [173]
Hydrothermal (HT)	tin oxide [68] [174], tungsten oxide [175] , zinc oxide [176] [74] [160]

1.3. Metal oxide surface reactions

1.3.1. Interaction with gases

In previous sections the classification of test gases interacting with the gas sensors' surface was divided into two groups: reducing and oxidizing gases. These two groups of gases are traditionally being used to describe the basic gas sensor mechanism, since those gases have an opposite effect on the gas sensor resistance. Following Krivetskiy et al.[177] in this section, the groups of interacting gases can be extended to eight groups.
Figure 1.19 presents these eight groups with some of the prime representatives. The gases shown in figure 1.19 vary in properties like: first ionization potential, electron affinity and proton affinity. Two general trends are being displayed within this figure. By going from left to right on figure 1.19 the proton affinity of the gases increases. In the same time the first ionization

potential decreases from left to right. Despite these differences the eight groups can be reduced according to similar properties to five groups listed below. Additionally, carbon dioxide will be revised as an independent group at the end of this subsection.

- **Group I**: oxidizing gases
- **Group II**: reducing gases
- **Group III**: strong acidic
- **Group IV - VI**: complex organic molecules
- **Group VII & VIII**: strong basic

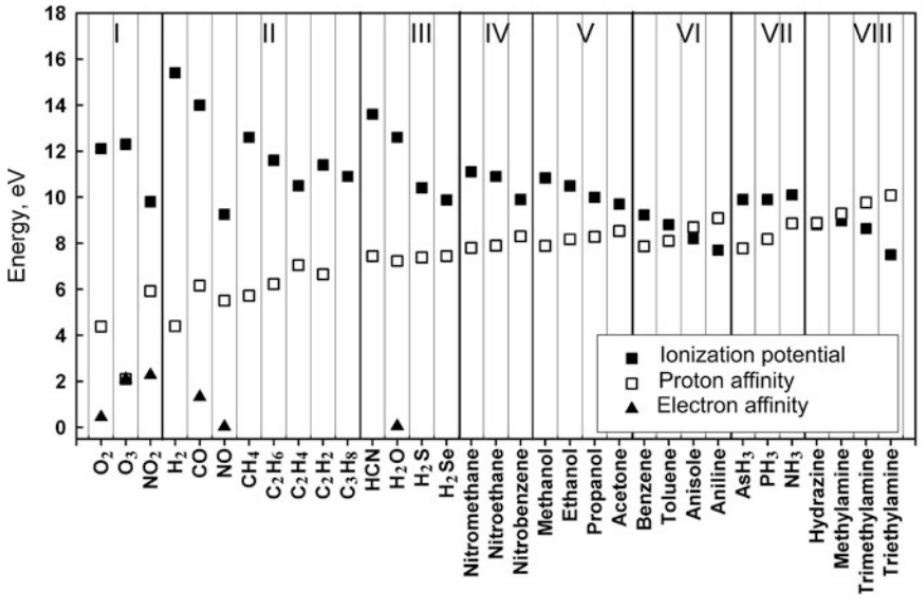

Figure 1.19.: Division of gases into eight groups according to their properties to interact with a sensor surface. Gases with similar surface reactions are grouped. Furthermore, the groups are classified by decreasing first ionization potential and increasing proton affinity. Taken from Krivetskiy et al.[177, chapter 3]

Group I (oxidizing gases): Nitrogen dioxide (NO_2) is the most prominent member of the group oxidizing gases. NO_2 interacts with a MOX surface on

two different paths according to Xu et al. [178]. The first path describes the immediate adsorption of the NO_2 molecule on the surface. The adsorption of NO_2 is similar to the adsorption of O_2.
In equation 1.25 the NO_2 molecule in gaseous form draws an electron from the MOX material and ionosorbs onto the surface. The second path considers the interaction of NO_2 with ionosorbed oxygen. As stated above (see section 1.2.2) oxygen can be found in two different forms on the surface of a MOX material: molecular ($O^-_{2(ad)}$) or atomic ($O^-_{(ad)}$). Therefore, NO_2 can react with both of them leading to the equations 1.26 (molecular oxygen) and 1.27 (atomic oxygen). Since the two oxygen ions are not equal NO_2 reacts with molecular oxygen to a ionosorbed NO_2 molecule. Whereas in the case of the interaction of NO_2 to atomic oxygen an ionosorbed nitrogen oxygen species is formed[177].

$$NO_{2(gas)} + e^- \rightleftharpoons NO^-_{2(ad)} \tag{1.25}$$

$$NO_{2(gas)} + O^-_{2(ad)} + 2e^- \rightleftharpoons NO^-_{2(ad)} + 2O^-_{ad} \tag{1.26}$$

$$NO_{2(gas)} + O^-_{(ad)} \rightleftharpoons NO^+_{(ad)} + 2O^-_{ad} \tag{1.27}$$

In equations 1.25 - 1.27 $NO_{2(gas)}$ is a nitrogen dioxide molecule in gaseous form, $NO^-_{2(ad)}$ is an ionosorbed nitrogen dioxide ion, $NO^+_{(ad)}$ is an ionosorbed nitrogen oxide ion, $O^-_{2(ad)}$ is an ionosorbed, molecular oxygen ion, O^-_{ad} is an ionosorbed, atomic oxygen ion and e^- is a captured electron from the MOX material.

Group II (reducing gases): A classic example of a reducing gas is carbon monoxide (CO). Depending on the temperature of the MOX surface CO can either show the property of an electron donor or acceptor. In case of low MOX surface temperatures CO interacts with metal cations. The CO and the metal cation form a molecular orbital [177]. At higher temperatures two possible reaction partners are available for the CO molecule, either an ionosorbed oxygen ion or a lattice oxygen. The interaction of CO with the ionosorbed oxygen results in the formation of a CO_2 molecule. Equation 1.28 shows the chemical reaction of CO with the ionosorbed oxygen [179].

In the special case of absent ambient oxygen, CO can directly interact with the MOX surface. Since there is no ionosorbed oxygen available at the MOX surface, CO reacts with lattice oxygen of the MOX material following the chemical reaction described in equation 1.29 [179].

$$CO + O_{ad}^{-} \rightleftharpoons CO_2 + e^{-} \tag{1.28}$$

$$CO + O_O \rightleftharpoons CO_2 + V_O^{++} + 2e^{-} \tag{1.29}$$

In equations 1.28 and 1.29 CO is a carbon monoxide molecule, O_{ad}^{-} is an ionosorbed oxygen ion, O_O is an oxygen of the MOX material, CO_2 is a carbon dioxide molecule, V_O^{++} is a double ionized lattice vacancy in the MOX material and e^{-} is an electron released into the MOX material. Since MOX gas sensors are operated in ambient conditions the latter chemical reaction is seldomly occurring.

Group III (reducing acids): Hydrogen sulphide (H_2S) combines two properties that define its reaction with MOX materials: reducing gas and Brønsted acid. The property of a reducing gas has already been discussed above in the example of CO. As a Brønsted acid H_2S can form a bond with a basic compound by transferring a proton in form of a H^{+} (proton donor). This property leads to multiple interactions with MOX material surface like the interaction to form sulphides, inhibition of acidic sites, reducing metal ions and the formation of sulphur oxides [177]. The last occurring reaction, the formation of sulphur oxides, is especially important for gas sensors, since this leads to the permanent damage of the sensing layer (sensor poisoning), hence reduction of overall sensitivity. Equation 1.30 is the general equation of the gas sensing mechanism of MOX material to H_2S.
Herein, The H_2S molecule reacts with ionosorbed oxygen and forms sulphur dioxide as well as water. This reaction is accompanied by a reduction (increase) of n-type (p-type) materials' resistance. As mentioned above the H_2S can react to metal ions of the MOX surface. An example is given in equation 1.31, where H_2S reacts to tungsten trioxide to form tungsten sulphide, sulphur dioxide and water. The result of this chemical reaction is a decrease in sensor resistance[170].

$$H_2S_{(gas)} + 3O^-_{(ad)} \rightleftharpoons SO_{2(gas)} + H_2O_{(gas)} + 3e^- \tag{1.30}$$

$$WO_3 + H_2S_{(gas)} \rightleftharpoons WS_2 + SO_{2(gas)} + H_2O_{(gas)} \tag{1.31}$$

In equation 1.30 $H_2S_{(gas)}$ is hydrogen sulphide in gaseous form, O^-_{ad} is an ionosorbed oxygen ion, SO_2 is sulphur dioxide, H_2O is water and e^- is an electron release into the MOX material.
In equation 1.31 WO_3 is tungsten trioxide, $H_2S_{(gas)}$ is hydrogen sulphide in gaseous form, WS_2 is tungsten sulphide, SO_2 is sulphur dioxide and H_2O is water.

Group V (complex organics): Acetone is a complex organic compound, whose interactions with a MOX surface results in the formation of various other compounds. A full oxidation of the molecule to CO_2 and H_2O is not the most likely reaction path. According to Krivetskiy et al.[177, chapter 3] the initial reaction between the MOX surface and the acetone molecule is occurring at the carbonyl group of the molecule. Consecutively, an enol species is formed. The enol dissociates by creating a propene-2-olate. One part of the propene-2-olate is bound to a metal ion, whereas a proton bounds to a lattice oxygen forming a hydroxyl group. As a consequence of this reactions acolein or acrylic acid can be formed.
Many of these products can react to adsorbed oxygen leading to partial oxidations or full oxidations. Galstyan et al.[180] describes three interactions of acetone with ionosorbed oxygen for the case of a ZnO surface at elevated temperatures. These three interactions are shown in equation 1.32, 1.33 and 1.34. All of the three reactions consequently lead to the release of an electron, which changes the resistance of the material.

$$CH_3COCH_3 + O^-_{(ad)} \rightleftharpoons CH_3COC^+H_2 + OH^- + e^- \tag{1.32}$$

$$CH_3COCH_3 + O^-_{(ad)} \rightleftharpoons CH_3C^+O + CH_3O^- + e^- \tag{1.33}$$

$$CH_3COCH_3 + 8O^-_{(ad)} \rightleftharpoons 3CO_2 + 3H_2O + e^- \tag{1.34}$$

In equations 1.32 CH_3COCH_3 is acetone in gaseous form, $O^-_{(ad)}$ is an ionosorbed oxygen species, $CH_3COC^+H_2$ is a carbanion, OH^- is an "adsorbed" hydroxyl group and e^- is an electron.

In equations 1.33 CH_3COCH_3 is acetone in gaseous form, $O^-_{(ad)}$ is an ionosorbed oxygen species, CH_3C^+O is an acetyl group, CH_3O^- is an methoxy group and e^- is an electron.

In equations 1.34 CH_3COCH_3 is acetone in gaseous form, $O^-_{(ad)}$ is an ionosorbed oxygen species, CO_2 is a carbon dioxide molecule, H_2O is a water molecule and e^- is an electron.

Group VII (reducing bases): Ammonia (NH_3) is a representative of the group of reducing bases. The adsorption of NH_3 onto a MOX surface without reacting with an ionosorbed oxygen species can follow three different paths [177, chapter 3]:

- A hydrogen atom of the NH_3 molecule bonds to a lattice oxygen atom or to an oxygen atom of a priorly adsorbed hydroxyl group on the MOX surface.
- The nitrogen atom of the NH_3 molecule bonds to the hydrogen of an existing hydroxyl group on the MOX surface.
- A metal ion of the surface bonds to the the NH_3 molecule via an coordinative bond.

At elevated temperatures ionosorbed oxygen ions form in the presence of ambient oxygen on the MOX surface. A chemical reaction of the ionosorbed oxygen and an NH_3 molecule is described by an oxidation process shown in equation 1.35. Herein, the ammonia is fully oxidized to nitrogen and water.

$$2NH_{3(gas)} + 3O^-_{(ad)} \rightleftharpoons N_{2(gas)} + 3H_2O + 3e^- \tag{1.35}$$

In equation 1.35 NH_3 is an ammonia molecule, $O^-_{(ad)}$ is an ionosorbed oxygen species, $N_{2(gas)}$ is a nitrogen molecule in gaseous form, H_2O is a water molecule and e^- is an electron.

Special group - Carbon dioxide (CO_2): Physisorption of carbon dioxide on a metal oxide surface is a rather common process. Freund et al.[181] described that at low temperatures CO_2 physisorption occurs on metal oxide surfaces like: BaO, CaO, Cr_2O_3, MnO, MgO, Na_2O, NiO, TiO_2 and ZnO. Especially for ZnO even chemisorption of CO_2 was shown. Hereby the CO_2 molecule forms a coordinate bond to a metal ion forming a carboxylate. Freund et al.[181] hypothesized that carboxylate can be formed by coordinate bonding to an oxygen atom too.
Baltrusaitis et al.[182] investigated the CO_2 adsorption at 296K on three different metal oxide nanoparticles: Fe_2O_3, γ-Al_2O_3 and TiO_2. Only on TiO_2 carboxylate structures were found. Additionally to the carboxylate structures, bicarbonate, monodentate and bidentate structures were found on TiO_2 as well. The formation of bicarbonate, monodentate and bidentate structures were also found on Fe_2O_3 and γ-Al_2O_3. Furthermore, Baltrusaitis et al.[182] showed a strong dependence of the CO_2 adsorption on adsorbed water.
In contrast to the gas sensing mechanisms based on the ionosorption of oxygen, structures formed upon CO_2 exposure like those described above most probably define the CO_2 gas sensing mechanism on the metal oxide surface. In the review by Fine et al.[183] various metal oxide materials (ITO, SnO2, La2O3, BaTiO3) were found to be sensitive towards CO_2, when applied as a resistive type gas sensor at elevated temperatures. Ishihara et al.[184] used a capacitive type CuO-$BaTiO_3$ gas sensor at elevated operation temperature. Hereby, the sensing mechanism is thought to be based on the carbonation of CuO, resulting in the change of the potenial barrier height between CuO and $BaTiO_3$.
Recently, Tanvir et al.[185] investigated CuO nanoparticles as CO_2 gas sensing material at room temperature by Kelvin probe measurements. Herein, they describe the mechanism for the CO_2 sensitivity to be related to the formation of the hydroxocarbonates: malachite and azurite. In equation 1.36 (malachite) and 1.37 (azurite) the chemical reaction between CuO and CO_2 to form the two hydroxocarbonates is shown. As mentioned above, the sensing mechanism is dependent on the water availability.

$$2CuO + CO_{2(gas)} + H_2O_{(l)} \rightleftharpoons Cu_2(OH)_2CO_3 \tag{1.36}$$

$$3CuO + 2CO_{2(gas)} + H_2O_{(l)} \rightleftharpoons Cu_3(OH)_2(CO_3)_2 \quad (1.37)$$

In equation 1.36 and 1.37 CuO is copper oxide, $CO_{2(gas)}$ is carbon dioxide in gaseous form, $H_2O_{(l)}$ is liquid water on the surface of the CuO nanoparticles, $Cu_2(OH)_2CO_3$ is the hydroxocarbonate malachite and $Cu_3(OH)_2(CO_3)_2$ is the hydroxocarbonate azurite.

1.3.2. Interaction with humidity

Since most metal oxide gas sensors are operated under ambient conditions the interaction with humidity is an important issue. In [136] Barsan et al. describes the occurrence of water species on a tin dioxide surface depending on the surface temperature. At low temperatures water is mainly found as molecular water bond to the metal oxide surface by physisorption or by the formation of hydrogen bonds [186]. If the operation temperature of a MOX gas sensor exceeds 200°C, water molecules are replaced by hydroxyl groups. A dissociation reaction of the water molecule occurs. The water molecule dissociates into an OH^- (hydroxyl group) and a H^+ (proton). These two products chemically interact with the MOX surface.
In Lewis' theory an acid is an electron acceptor, whereas a base is an electron donor. The OH^- molecule reacts as a Lewis base with a metal site (Sn) of the MOX surface, which acts as a Lewis acid. H^+ can either react with an oxygen of the MOX surface lattice or with an ionosorbed oxygen. In both cases H^+ acts as a Lewis acid and the oxygen reaction partner takes the role of a Lewis base.
According to Barsan et al.[136] three mechanism exist, which define the interaction of the MOX surface with water. These mechanisms, elaborated for the case of n-type MOX materials, result in the decrease of the total resistance of the MOX material. The first mechanism is shown in equation 1.38. The first species of the water dissociation, the OH^- molecule, bonds to a Sn cation of the MOX surface. As described above, this reaction is a Lewis acid/base reaction. The second species the proton (H^+) bonds to a lattice oxygen. Since the lattice oxygen is already saturated the resulting hydroxyl

group is positively charged. This hydroxyl group is called a rooted hydroxyl group as the oxygen atom of the group is part of the oxygen sub lattice.

$$H_2O_{(gas)} + Sn_{Sn} + O_O \rightleftharpoons (Sn^+_{Sn} - OH^-) + (OH)^+_O + e^- \tag{1.38}$$

The following variables are used in equation 1.38: $H_2O_{(gas)}$ water in gaseous form (vapour), Sn_{Sn} is a tin atom, which is part of the tin dioxide surface (metal site), O_O is an oxygen atom, which is part of the tin dioxide surface (oxygen sub lattice), Sn^+_{Sn} is an ionized tin metal site of the tin dioxide surface, OH^- is an hydroxyl group, OH^+_O is a routed hydroxyl group and e^- is an electron released at the formation of the routed hydroxyl group.
The second mechanism is shown in equation 1.39. At first the same reactions take place. The hydroxyl group binds to a Sn cation of the MOX surface and the proton binds to a lattice oxygen. During this process the lattice oxygen is removed from the lattice and a doubly ionized oxygen vacancy is formed. The newly formed hydroxyl group binds to another Sn cation of the surface. The generated vacancy can be filled up by an oxygen atom of the ambient atmosphere.

$$H_2O_{(gas)} + 2Sn_{Sn} + O_O \rightleftharpoons 2(Sn^+_{Sn} - OH^-) + (V)^{++}_O + 2e^- \tag{1.39}$$

Variables used in equation 1.39: $H_2O_{(gas)}$ water in gaseous form (vapour), Sn_{Sn} is a tin atom, which is part of the tin dioxide surface (metal site), O_O is an oxygen atom, which is part of the tin dioxide surface (oxygen sub lattice), Sn^+_{Sn} is an ionized tin metal site of the tin dioxide surface, OH^- is a hydroxyl group, $(V)^{++}_O$ is a doubly ionized oxygen vacancy of the MOX surface and $2e^-$ are two electrons released as a result of the doubly ionized oxygen vacancy formation.
The third mechanism focuses on the possibility of ionosorbed oxygen on the MOX surface being displaced by hydroxyl groups. The displacement would equally result in the decrease of the MOX' total resistance. Barsan et al.[136] considers this third mechanism to be an indirect mechanism. Furthermore, Barsan et al.[136] states that not only the surface displacement of oxygen by hydroxyl groups plays a role, but the surface topology matters as well. This includes surface steps, defects, dislocations and metal dopants (e.g. Ag, Pd) on the MOX surface.

1.3.3. Test gases

In course of this thesis three different test gases are applied for gas sensor evaluation: carbon monoxide (CO), carbon dioxide (CO_2) and a volatile organic compounds (VOC) substitute called hydrocarbon mixture (HCMix). All three gases are employed as they play an important role in the indoor air quality monitoring, which is a central issue of this thesis.

Carbon monoxide (CO): Carbon monoxide is a poisonous gas with the properties of being colourless and odourless. CO is a flammable gas and during its combustion it oxidises to CO_2 generating heat (blue flame).
In general, CO forms during incomplete combustion. Since combustion is the main driving force of an engine the formation of CO is an issue. The resolution of this issue is the usage of a catalyst. In engines platinum acts as a catalyst and reduces the reaction temperature for a total conversion to $400°C$ [10].
Outside of modern fuel engines carbon monoxide occurs in rather minuscule concentrations. In Earth's atmosphere the average concentration of CO is around 90 ppb [187]. In buildings the concentration can vary between 0.5 ppm and 5 ppm [188]. The full-time equivalent of CO is 30 ppm [10]. Since CO is formed at incomplete combustion the sources indoors are limited. In general, these sources are: gas heaters and stoves, fireplaces, tobacco smoke and outdoor contamination (e.g. car exhaust) [188]. Effects on the health of human beings are headache, dizziness and nausea. Prolonged exposure at high concentrations results in death [189]. A metal oxide gas sensor reacts in various ways with carbon monoxide. Below five possible reaction routes are displayed [190], [191]:

$$CO_{(ad)} \rightleftharpoons CO^{+}_{(ad)} + e^{-} \tag{1.40}$$

$$CO + O^{-} \rightleftharpoons CO^{-}_{2(ad)} \rightleftharpoons CO_{2(gas)} + e^{-} \tag{1.41}$$

$$CO + 2O^{-} \rightleftharpoons CO^{2-}_{3} \rightleftharpoons CO_{2(gas)} + O^{-} + e^{-} \tag{1.42}$$

$$CO + 2O^- \rightleftharpoons CO_3^{2-} \rightleftharpoons CO_{2(gas)} + \frac{1}{2}O_2 + 2e^- + V_O \tag{1.43}$$

$$CO + OH_{(ad)} \rightleftharpoons HCOO_{(ad)} \rightleftharpoons CO_2 + H_{(ad)} \tag{1.44}$$

In equations 1.40 - 1.44 following variables were used: $CO_{(ad)}$ is an adsorbed carbon monoxide molecule, $CO^+_{(ad)}$ is an ionosorbed carbon monoxide molecule, CO is a carbon monoxide molecule, O^- is an ionosorbed oxygen, $CO^-_{2(ad)}$ is a carboxylate, $CO_{2(gas)}$ is a carbon dioxide molecule in gaseous form, CO_3^{2-} is a bidententate carbonate, O_2 is an oxygen molecule, $OH_{(ad)}$ is an adsorbed hydroxyl group, $HCOO_{(ad)}$ is a formate, $H_{(ad)}$ is a hydrogen atom, V_O is a lattice vacancy and e^- is an electron.

Carbon dioxide (CO_2): Carbon dioxide is a colourless and odourless gas. CO_2 is not combustible and does not support combustion [10]. Furthermore, in sufficiently high amounts it suppresses combustion (fire extinguisher). The sources of CO_2 are numerous ranging from natural to artificial. Since all living organisms metabolising oxygen produce CO_2 as a by-product, CO_2 is a part of Earth's atmosphere. The amounts that can be found in the atmosphere (411 ppm, 22.05.2019,[192]) are just a part of the overall CO_2 content. CO_2 is naturally stored in the oceans and earth's crust (e.g. calcium carbonat $CaCO_3$, magnesium carbonat $MgCO_3$) [10]. Rising CO_2 levels in the atmosphere and oceans are attributed to man made sources.
In buildings the carbon dioxide level is dependent on the atmospheric levels. In Austria the value of the maximum concentration in the workplace (MAK) for CO_2 is set to a maximum peak value of 5000 ppm during a measurement period of one hour. According to Boos et al.[193] the indoor air quality can be divided into five classes ranging from special indoor air quality at low CO_2 concentrations of $\leq$ 400 ppm to very poor indoor air quality at high CO_2 concentrations of $\geq$ 1500 ppm. These concentrations are relative concentrations to the atmospheric concentrations. The defining source for CO_2 indoors are human beings and animals. Under normal conditions the effects on physical health are minimal. At elevated concentrations mild symptoms like fatigue, loss of focus and headaches can occur. Prolonged

exposure at high concentrations lead to loss of consciousness and subsequent death [193].
The interaction of carbon dioxide with metal oxide surfaces has been shown in the paragraph above, Special group - Carbon dioxide (CO_2). Figure 1.20 below shows the increase of the carbon dioxide concentration in Earth's atmosphere over the last ten years. The modulation of the CO_2 concentration over a single year is a result of the seasonal change in the CO_2 concentration in the atmosphere. Although the impact of atmospheric CO_2 levels on indoor air quality is not distinct it still shows an alarming trend.

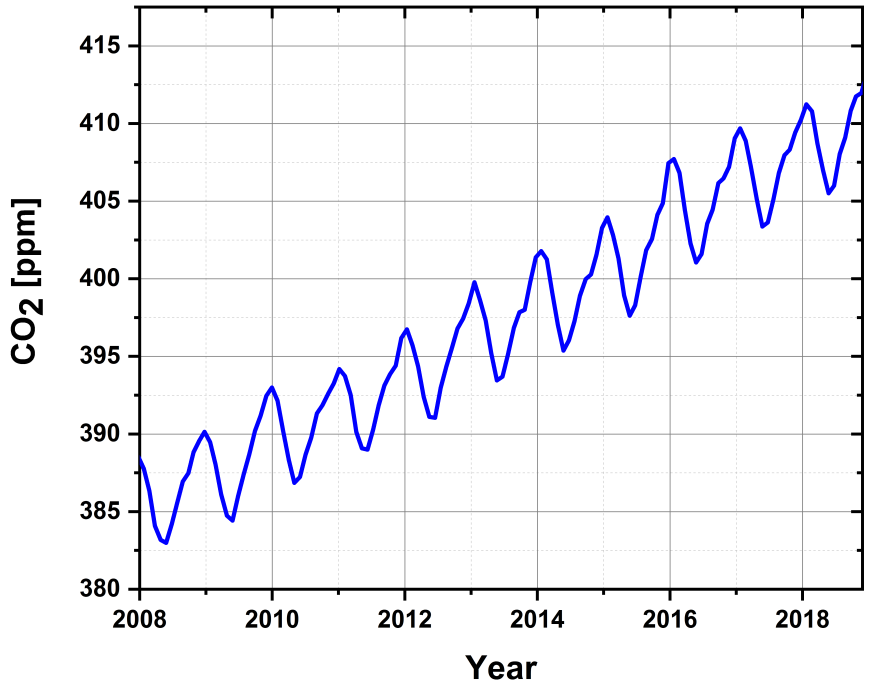

Figure 1.20.: Atmospheric carbon dioxide concentration over the last 10 years (May 2008 - April 2019)[192]. The modulation of the concentration over a single year is a result of the seasonal change of the CO_2 concentration in the atmosphere.

Total volatile organic compounds (TVOC): In contrast to carbon monoxide and carbon dioxide, the term volatile organic compounds (VOC) is not a single gas molecule but a class of compounds. A classification of the World Health Organisation (WHO) [194] consolidates numerous organic compounds in four classes: Very volatile organic compounds (VVOC), volatile organic compounds (VOC), semi-volatile organic compounds (SVOC) and organic compounds associated with particulate matter or particulate organic matter (POM).
These division into this four classes is done according to the boiling point of the compounds (see table 1.6). All classes combined are condensed in the term total volatile organic compounds (TVOC). TVOCs can be found in the atmosphere and within buildings. Some TVOC species in the atmosphere react photo-catalytically with NO_x or CO to form ozone. Therefore, extra effort has been made to reduce the exposure of Earth's atmosphere to those organic compounds [195].
The definition of a full-time equivalent for volatile organic compounds is difficult. Since the occurrence of those compounds is dependent on their sources a definite mixture cannot be defined. Following a long term survey Seifert [194] defined compound classes (alkanes, aromatics, terpene, chlorocarbon, ester, aldehyde and ketone) in their found concentration to form an overall TVOC concentration of 0.3 $\frac{mg}{m^3}$.
Despite this success new found compounds and changes in concentrations of already evaluated compound classes resulted in the change of the single compound class concentrations that were used to calculate the overall TVOC value. For now the TVOC value can be considered to be a guide value [194].
Sources of VOCs according to Mendell [196]:

- Solvent based paint
- Tobacco smoke
- Consumer products
- Adhesives
- Cleaning products
- PVC plastics
- Car exhaust
- Human beings (metabolism)

The impact on human health is still under investigation. Some investigations show that the exposure to mixtures of VOCs result in mucosal irritations

of eyes, nose and thorax. Others showed that probands with disposition of the respiratory system or allergies show stronger reactions to the exposure [194].
In respect to TVOC gas sensing since there are no generally accepted mixtures (to the knowledge of the author) for comparative analysis of different gas sensors, comparison to literature is mostly limited to single component gas analysis.
In this work a special mixture called HCMix (hydrocarbon mixture) is used as a test gas to evaluate VOCs. It consists in equal parts of acetylene, ethane, ethene and propene.

Table 1.6.: Organic compounds subdivided into four classes by WHO (Table according to Seifert [194]):

Classification	**Abbreviation**	**Example**	**Boiling point range** [°C]
Very volatile organic compounds	VVOC	formaldehyde, methanol [197]	<0 to 50-100
Volatile organic compounds	VOC	limonene, cyclohexanone [198]	50-100 to 250-260
Semivolatile organic compounds	SVOC	polychlorinated biphenyls [199]	250-260 to 380-500
Organic compounds associated with particulate matter or particulate organic matter	POM	pollen, spores [200]	>380

1.4. Sensitization: Enhancement of gas sensors characteristics

A gas sensing material's response towards a specific test gas concentration at a specific gas sensor operation temperature is defined by the characteristic quantities: sensitivity, response time and recovery time (see section 1.2). A change in concentration results in a change of these quantities. Equally to the concentration change would be the change of temperature. The chemical reactions underlying the gas sensing mechanism occur at specific rates. This reaction rates change with increasing temperature.
Yamazoe et al.[134] describes a quantity called utility factor, which connects the reactivity of the sensor surface to the entire available sensor surface. He considers thin film gas sensors. The entire available sensor surface is defined as the sum over all grain surfaces. By this consideration not all grains are part of the thin films surface. Grains below the thin film surface contribute to the gas sensor signal if the test gas diffuses into the thin film. Yamazoe et al.[134] concludes, as long as the reactivity of the surface is low enough to ensure test gas diffusion into the thin film, the majority of the grains surfaces will contribute to chemical reaction, hence to the gas sensor signal. If the reactivity increases the diffusion process is hindered. Only a part of the grains surfaces can contribute.
The reactivity of a MOX surface can be changed by increasing or decreasing the surface temperature. An optimum, operation temperature is found when the gas reactivity and the gas diffusion is in an equilibrium state. In this equilibrium state the measured sensitivities for any concentrations of a specific test gas are at their highest possible values. Therefore, for each test gas the optimum, operation temperature has to be determined to reach an equivalent equilibrium state to gain maximum sensitivities. If the optimum, operation temperature exceeds a specific temperature some MOX materials exhibit a process of grain growth. The grain growth can change the sensitivity, since the grain size has a direct influence on the sensing mechanism (see section 1.2), resulting in a decrease of long time stability and lifetime of the gas sensor.
Another issue would be that the optimum, operation temperature of two or more test gases is equivalent. In this case the gas sensor cannot differentiate amongst those test gases (cross-sensitivities). Therefore, not only gas sensor

sensitivity could be an issue, but also gas selectivity. These issues can be reduced by doping the MOX material or by deposition of nanoparticles onto the MOX surface.
In general, doping is the introduction of a foreign material into a host material to improve certain properties of the host material. As mentioned above, the reason for doping is the enhancement of the gas sensitive material in regard to its sensitivity, selectivity and lifetime (stability). In case of doping the enhancement can be achieved by either bulk doping or surface doping. The two paragraphs below will elaborate the possibilities of each kind of doping [137].

Bulk doping: In the bulk of a MOX material dopants (additives) are applied to enhance the quantities described above. According to Korotcenkov et al.[137] several possible dopants are listed below:

- Noble metals: Au, Pt, Ag, Pd, Rh
- Transition metals: Fe, Co, Cu
- Non metals: Se
- Alkaline earth metals: Mg, Ca, Ba, Sr
- Metalloids: B, Si

The materials mostly applied as dopants are from the noble metal group and the transition metal group. Bulk doping is done during the fabrication process of the gas sensitive material. The methods vary for thick film and thin film. In the case of thick films Korotcenkov [135, chapter 23] describes five methods to introduce dopants into the MOX material for the example of noble metal dopants. Thick film metal oxide materials are often fabricated from a powder.

1. The powder is mixed with a solution of a noble metal chloride and annealed to stabilize the material.
2. The dopants are introduced by adding noble metal colloids to the metal oxide powder.
3. The metal oxide material is mixed with a noble metal complex, which chemically reacts with hydroxyl groups on the surface of the metal oxide.

4. Sputtering a layer of the doping material onto the metal oxide material and a consecutive annealing step to ensure the diffusion of the sputtered material into the metal oxide.
5. A precise dopant profile can be achieved by ion implantation.

In the case of thin films various techniques can be applied to fabricate doped metal oxide materials. The list below includes four of the most common deposition methods:

1. Sol-gel method: Chloride precursor solution is mixed with a chloride compound in a certain amount of weight percentage. This is followed by a spin coating step and film annealing[201].
2. Pulsed layer deposition (PLD): The target used for deposition is prepared by mixing the metal oxide with the dopant material. The mixture is sufficiently stirred and consecutively pressed to form the target. The deposited film using the target as a material source has the same ratio of metal oxide to dopant[202].
3. Sputtering method: This method is similar to the PLD process. The sputtering target contains a mixture of the metal oxide and the dopant. The deposited films dopant content is dependent on the amount of dopant in the sputtering target [203].
4. Spray pyrolysis: Into the precursor solution a dopant is added. After stirring of the solution the spraying process is conducted. The ratio of metal oxide to dopant is dependent on the amount of dopant in the precursor solution [204].

The processes above show that there are various ways to fabricate a bulk doped thick or thin layer. But what are the implications of doping on the material in detail? Since foreign materials are introduced into the metal oxide matrix, changes in the microstructure take place. Some dopants influence the growth process of the grains during the annealing process. Annealing is a necessity to ensure crystal growth for amorphously deposited film and to promote stability.
For thick films fabricated from a powder material a sintering process at elevated temperatures is needed. Depending on the temperature and duration used for the sintering or annealing processes the diameter of grains can change. Not only the grain size can be modified when using dopants, but the morphology of the metal oxide crystallites changes as well.

Korotcenkov et al.[205], [135, chapter 23] shows that the doping of tin dioxide films (fab.: spray pyrolysis) with dopants Co, Fe, Ni, Cu with concentrations 0-16 at.% results in a decrease of the grain size for tin dioxide films doped with Cu, Ni and Fe. The grains of the doped materials also show twinning of the crystallites. Furthermore, a detailed analysis of larger structures of the material showed that these structures were formed by agglomeration of smaller crystallites [205].
Apart from a change of the microstructure, dopants can also result in modifications of the electrical properties of the material. A variation of the charge carrier concentrations leads to a change of the bulk conductance and to the change of thickness of the space charge layer. Changes of the space charge layer have effects on the resistance between adjacent grains and on the response towards a test gas.
Additionally, if changes are introduced to the donor and acceptor concentrations of the bulk material a shift of the Fermi level of the bulk occurs. As a result of this shift the gas adsorption and desorption process as well as the space charge layer are affected.
In general, bulk doping does not always increase the sensor performance. Although the micro-structural modifications can lead to better stability of the metal oxide material, the same modifications can also reduce the sensor's sensitivity towards a test gas. Therefore, the benefits of bulk doping should always be balanced to the detriment.

Surface doping: In contrast to bulk doping the deposition process of the dopants is done in a post-processing step [177]. The dopants (additives) are deposited on the surface by various methods like thermal evaporation, chemical vapour deposition (CVD) and electroless deposition [137, chapter 10] to mention a few. Since the interaction of a gas sensor and a test gas occurs on the surface of the sensor material, changes on the surface have a direct impact on sensitivity and selectivity. According to Korotcenkov [137, chapter 10] dopants on the sensor surface act as:

- inhibitors or activators to provide additional adsorption sites for gases (test gas and oxygen).
- catalysts to lower the activation energy for chemical reactions and thereby increasing the chemical reaction rate.

- promoters to enhance the effect of the catalyst and stabilize the sensor surface.

The main materials for surface doping are equivalent to the bulk doping materials: noble metals (Pt, Pd, Au, Ag, Ru, Rh) and transition metals (Fe, Cu, Ni, Co) [137, chapter 10]. Since surface dopants form particles of the size of a few nanometers on the sensor surface they will be refered to as nanoparticles from here on. The enhancement of the gas sensor by nanoparticles is attributed to two sensitization processes: chemical sensitization and electronic sensitization.

Chemical sensitization: The basic effect underlying chemical sensitization is the spillover effect (fig. 1.21). Ambient gas molecules (e.g. oxygen $O_{2(gas)}$) adsorb to the surface of a metallic nanoparticle. Dissociation of the adsorbed molecules occurs. The products of this dissociation are transported to the metal oxide surface, hence the term spillover. The metal oxide reacts with the products. This process is not only restricted to test gases for detection, but can also apply for the enhancement of oxygen replenishment. The size of the spillover zone shown in figure 1.22 has been investigated by Bennett et al.[206] for Pd nanoparticles on a TiO_2 surface for adsorbing oxygen molecules. The spillover zone is estimated to measure from 10 nm up to several tens of nanometres in diameter around the nanoparticles [207].
It has to be stated that the nanoparticles in case of chemical sensitization do not contribute directly to the change of conductance/resistance as a result of the test gas / MOX surface interaction. The change in conductance/resistance is only attributed to the interaction of the dissociation products and the MOX surface. The enhancement of the sensitivity is the result of an increased chemical reaction rate between the test gas and the MOX mediated by the nanoparticles. Therefore, the functionalized MOX gas sensor would show an equivalent sensitivity compared to a non-functionalized MOX gas sensor at a lower operation temperature.
In general, test gas molecules don't have to adsorb directly to the metal nanoparticles to be dissociated. If test gas molecules adsorb to the MOX surface without immediately reacting with the surface, they can be captured in an area around a nanoparticle that is called molecule-collection zone.

Within this zone the targt gas molecules will be transported to the metal nanoparticles, where the dissociation process and consecutive spillover takes place. This process is called inverse spillover effect [137].

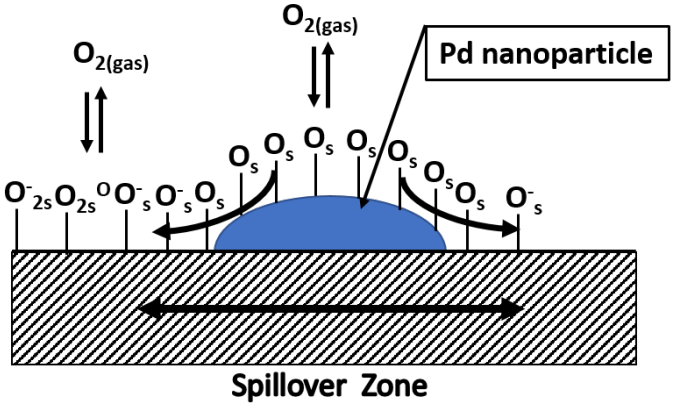

Figure 1.21.: Spillover process at the surface of a Pd metal nanoparticle by the example of oxygen dissociation. Gaseous oxygen ($O_{2(gas)}$) is dissociated at the Pd surface. The products (O_S) spill over to the MOX surface and form ionosorbed oxygen species (O_S^-, O_{2S}^-). According to Korotcenkov [208].

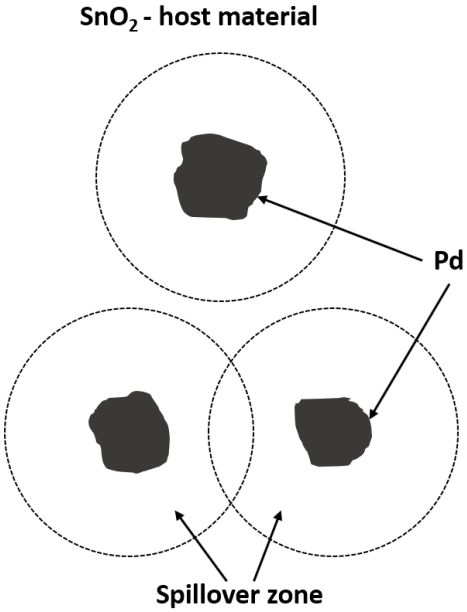

Figure 1.22.: Spillover zones encircling Pd metal particles on a tin dioxide surface. According to Korotcentkov et al. [209].

Electronic sensitization: In contrast to the chemical sensitization, where a chemical reaction between the products of a dissociated test gas (resulted by nanoparticles) and the MOX surface occurs, electronic sensitization is restricted to the interaction of the nanoparticles and the MOX surface only by electronic interactions [137].
A MOX gas sensor is operated at elevated temperatures. At room temperature the metal nanoparticles are in their metallic form. At specific, elevated temperatures the metal nanoparticles oxidize. The exception are gold nanoparticles, which don't oxidize under ambient conditions even at elevated temperatures. Charges needed for the oxidation are drawn from the MOX material. A space charge layer (depletion layer) is formed between the oxidized metal nanoparticle and the MOX surface. If the oxide nanoparticles are exposed to a reducing test gas the particles are reduced to their metallic state (receptor function [139]). During the reduction the formally acquired electrons from the MOX material are released back into MOX material. The change of the oxidation state results in a change of conductance/resistance

of the MOX material and the decrease of the space charge layer (transducer function [139]). Over this entire process no interaction between the reducing test gas and the MOX surface takes place.
At high nanoparticles concentration and high dispersion rates of the nanoparticles on the surface, the space charge layers of each of the nanoparticles could overlap. As a consequence the Fermi level will be defined by the oxidation state of the nanoparticles.
In figure 1.23 the example of an undoped and Pd-doped SnO_2 grain is illustrated. In the upper part of the figure the pristine tin dioxide is shown in air and exposed to a reducing test gas. In air a space charge layer is formed at the surface of the grain depending on the ionosorbed oxygen.
Upon reacting with the reducing test gas the oxygen ions are removed from the surface as a result of the chemical reaction. The space charge layer is strongly minimized and the resistance of the material is reduced. In the lower part of the figure the same process is depicted for a tin dioxide grain surface doped with Pd. In air the Pd is oxidized to PdO. A space charge layer is formed. As mentioned above the space charge layer is dependent on the PdO nanoparticles on the surface. Furthermore, the thickness of the layer is dependent on the PdO load. Upon exposure to the reducing test gas the PdO is reduced to Pd, consequently releasing electrons into the conduction band of the MOX material while decreasing its resistance [139].

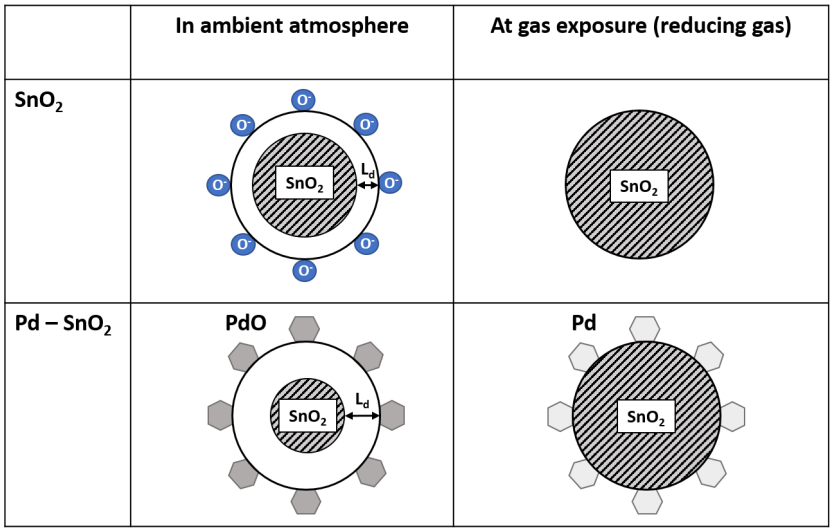

Figure 1.23.: Comparison of pristine and functionalized tin dioxide grain upon oxygen and test gas exposure. Upper: (Left) Pristine tin dioxide exposed to oxygen. The ionosorbed oxygen results in the formation of an electron depletion layer, with thickness L_d. The areas marked with dashed line represent the semiconducting core of the tin dioxide grain. (Right) After exposure to a reducing gas all ionosorbed oxygen species are removed. The electron depletion layer is gone. Lower: (Left) Tin dioxide functionalized with palladium exposed to oxygen results in a thicker depletion layer and the oxidation of Pd. (Right) After exposure to a reducing gas PdO is reduced to Pd and the electron depletion is gone. According to Yamazoe[139].

Nanoparticles: In the paragraph surface doping, the introduction of noble metal nanoparticles on top of the sensing layer was done by deposition of noble metal material and consecutive annealing step. In this annealing step the deposited material diffuses along the surface and agglomerates to form island structures with nanometre dimensions. Another approach is the independent fabrication of nanoparticles in a separate process. Methods for the fabrications of nanoparticles are [210]:

- Micro-wave method
- Co-precipitation method
- Hydrothermal method
- Selective catalytic reduction method
- Micro-emulsion method

The nanoparticles fabricated by these methods are stored in a solution. For most of the nanoparticles the storage in a solution is only possible if the particles are stabilized with a surfactant. These surfactants reduce the agglomeration of the nanoparticles in solution.

Part III.

Experimental

2. Sensor material fabrication

In this chapter techniques utilized to fabricate metal oxide materials for gas sensing are presented. These techniques are applied to fabricate thin films and nanowire arrays.
The deposition of thin films is done by spray pyrolysis technique. The structuring of the gas sensing layer is done by a following photolithography and physical etching step. The primary gas sensitive material deposited by spray pyrolysis is tin dioxide (SnO_2).
The process chain to fabricate SnO_2 thin films by spray pyrolysis has been developed within our group over the last years [191], [24]. In this work additional effort has been made to expand the material repertoire for gas sensitive materials to copper (II) oxide (CuO, cupric oxide) and zinc oxide (ZnO).
The fabrication of cupric oxide and zinc oxide nanowire arrays within this work is done by electron beam lithography, thermal evaporation, lift-off process and a consecutive thermal oxidation step to promote metal oxide nanowire growth. The process chain of nanowire arrays was developed in a previous work [29]. In this work the transfer of these structures onto a new CMOS device was achieved.

2.1. Thin films

2.1.1. Spray pyrolysis technique

Spray pyrolysis is a simple and cheap technique to deposit thin films and thick films of various materials on large areas. The most common materials that are being deposited as thin films by spray pyrolysis are: noble metals,

metal oxides, spinel oxides, chalcogenides and superconducting materials [211]. According to Pramond [211] spray pyrolysis has some advantages compared to other deposition methods, five of those advantages are mentioned below.

1. The primary material that is being deposited can easily be doped by adding the dopant material into the spraying solution.
2. Spray pyrolysis is done at ambient conditions. Therefore, no vacuum systems are required to reduce the influence of the ambient atmosphere.
3. The spray parameters determine the deposition of the material, which makes it possible to deposit various film thicknesses.
4. The deposition temperatures are rather low compared to CVD techniques.
5. Multilayer structures of different material compositions can be formed by using different spraying solutions.

In general, a spray pyrolysis apparatus consists of two parts: a spraying nozzle and a hotplate. A substrate, onto which the desired material is being deposited, is placed on top of the hotplate. The surface temperature on the substrates surface equalizes with the hotplate temperature. Basically, a spraying solution consists of a metal salt diluted in one or more solvents (e.g. tin(IV) chloride pentahydrate in ethyl acetate).
The spraying nozzle atomizes the spraying solution into small droplets. The fine mist of droplets is transported via a carrier gas (air, nitrogen) to the hotplate/substrate. The hotplate temperature is set to a specific temperature, which is adjusted to the chemicals used in the spraying solution. The dependency of the spraying process on temperature is shown in figure 2.1. The hotplate/substrate temperature leads to the definition of four processes classified by letters A to D, which correspond to different forms of deposition [212] [213].

- Process (A): On their way from the nozzle to the hotplate the solvent within the droplets is partly evaporated, thereby only reducing the size of the droplets slightly. Therefore, the droplets impinge on the substrate surface. After the droplet makes contact with the surface

the solvent evaporates. The resulting precipitate does not form an adherent layer on the substrate.

- Process (B): The solvent within the droplets is fully evaporated near the substrate surface. After evaporation a precipitate is formed. The precipitate impinges on the surface, where it decomposes. This process leads to the formation of non uniform distributed material deposition with only a slightly better adherence compared to deposition regime A.
- Process (C): Near the substrate surface the solvent of the droplets is evaporated and a precipitate is formed. The precipitate is melted and vaporized forming a vapour phase slightly above the substrate surface. The material in vapor phase reaches the surface, where it adsorbs, diffuses and chemically reacts on the surface (heterogeneous reaction). At this stage of the process a continuous deposition and conversion to the target material occurs. Deposition in regime C is equivalent to the chemical vapour deposition (CVD). The material deposited at this deposition regime shows the highest adherence compared to all the other three deposition regimes.
- Process (D): Deposition is performed at higher temperatures. Therefore, the evaporation of the solvent, vaporization of the resulting precipitate and its further chemical reaction to form the target material takes place near the surface (homogeneous reaction). The target material is deposited as a powder on the substrate surface. Therefore, the adherence of the material is low.

A standard spray pyrolysis process is done within Process C. In practice, numerous atomizing techniques are used to conduct a spraying process. A list of those techniques is given in table 2.1.

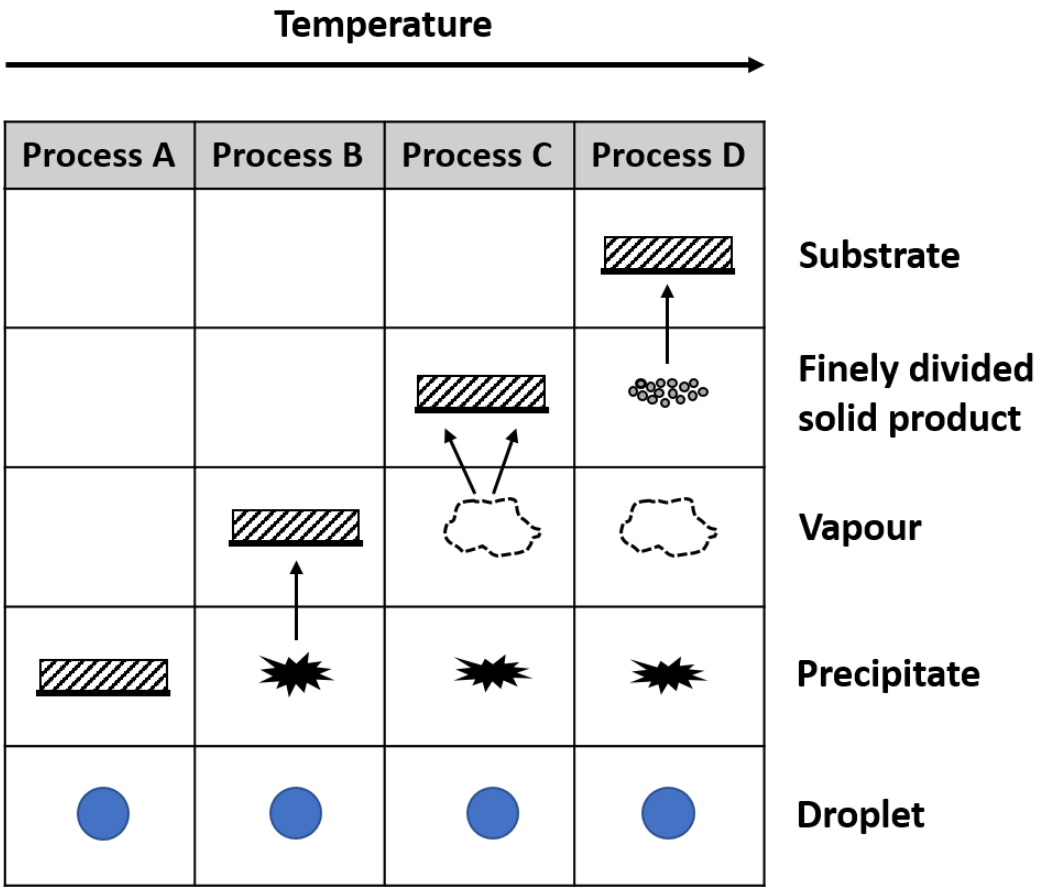

Figure 2.1.: Deposition of droplets as a function of increasing substrate temperature. Process (A): the droplets impinge on the substrate surface. Process (B) the precipitate impinges on substrate surface and decomposes (non uniform deposition). Process (C) the melted and vaporized precipitate chemically reacts with the substrate surface (continuous deposition). Process (D) the powdery target material is deposited on the substrate surface (low adhesion). According to Vigui et al.[212]).

Table 2.1.: List of various spray pyrolysis methods [212].

Method	Description	Reference
Pneumatic spray pyrolysis	Two fluid nozzle system to atomize the spraying solution.	[214] [213] [25]
Ultrasonic spray pyrolysis	Atomization of the solution is done by applying high frequency vibrations.	[215] [216] [217]
Flame spray pyrolysis	Atomization is done by a standard nozzle. Furthermore, no hotplate is needed as the droplets are converted to the target material by a flame adjacent to the nozzle.	[218] [219] [220]
Corona spray pyrolysis	Atomization is done by a standard nozzle or ultrasonic nozzle. The droplets are electro-statically charged and guided to the heated substrate by an electric field.	[221] [222]
Electrostatic spray pyrolysis	A high voltage is applied between the nozzle and the hotplate, whereon the substrate is placed. The droplets are positively charged and guided to the negatively charged heated substrate.	[223] [224]
Improved spray pyrohydrolysis	Atomization is done by a standard nozzle. A specific chamber provides size selection of the droplets transported to the hotplate.	[225]

Influences on droplets trajectory: A theoretical approach on the trajectory of a single droplet during the spraying processes is given by Sears et al.[226]. In this work the various forces acting on a single droplet are determined and evaluated for their contribution to the trajectory. Furthermore, the heating of the droplets as a result of the hotplate is investigated. The experimental set-up used by Sears et al., namely is a corona spray pyrolysis set-up, which differs from the two-fluid spray pyrolysis set-up used within this work. Despite that most of his deliberations can be applied for this spray pyrolysis set-up and only some adoptions have to be made.
The following deliberations are according to Sears et al.[226]. The first premise is that the droplets are moving within a laminar air flow. Droplets move from the nozzle parallel to the hotplate to an exhaust vent. A certain starting velocity of the droplets constitutes the laminar flow condition. Equation 2.1 depicts the forces act on the droplet on its trajectory.

$$F = F_g + F_t + F_S \tag{2.1}$$

Herein, F is the total force, F_g is the gravitational force, F_t is the thermophoretic force and F_S is the Stokes force. The thermophoretic force is a force, that acts on masses of a certain size, within a temperature gradient in a fluid (air). In the vicinity of a heated surface molecules in air are heated by the hot surface. Depending on their position relative to the hot surface, their kinetic energy is increasing. The molecules start to move away from the hot surface in perpendicular direction. The kinetic energy of the molecules is depending on the relative position to the heated surface. The nearer they are to the hot surface the more energy is passed to the molecules. A gradient is formed. Small masses moving into the gradient will be struck by these molecules. The molecules pass their kinetic energy to the smaller mass, which experiences a force action. This force on the small mass increases with decreasing distance to the hot surface.
Since the diameter of the droplets is within the micrometer range the mass of the droplets is rather small. Therefore, the contribution of the gravitational force is small and can be neglected. In case of the thermophoretic force the droplets experience a growing repulsive force the nearer they come to the surface. The thermophoretic force for a droplet with a radius much larger than the mean free path of a molecule is given in equation 2.2.

$$F_t = \frac{-9\pi K_a}{2K_a + K_d} \frac{\eta_a^2 R}{\rho_a T_a} \nabla T_a \tag{2.2}$$

In equation 2.2 K_a is the thermal conductivity of air, K_d is the thermal conductivity of a sprayed droplet, η_a is the dynamic viscosity of air, ρ_a is the density of air, R is the radius of a droplet, T_a is the temperature of air and ∇T_a is the thermal gradient at the hotplate surface of air.
The last force relevant for a two-fluid spray pyrolysis set-up is the Stokes force. Equation 2.3 defines the Stokes force acting on a single droplet.

$$F_S = -6\pi\eta_a R(v_d - v_a) \tag{2.3}$$

In equation 2.3 η_a is the dynamic viscosity of air, R is the radius of a droplet, v_d is the velocity of the droplet and v_a is the velocity of air.
The equilibrium state, where the total calculated force is equal to zero, is reached faster for small droplet radii. The two forces mainly defining the trajectory are the Stokes force and the thermophoretic force. In direct competition of these two forces, the thermophoretic force exceeds the Stokes force.
Therefore, small particles are deflected from the surface keeping it clean. Another effect that can be attributed to the thermophoretic force is that droplets start to evaporate on their way to the hotplate surface. The emerged vapour surrounds the droplets and shields them. As a result of this shielding the droplets cannot impact on the surface.
The last consideration above leads to the issue of droplet evaporation. The temperature of the droplets reaching the surface of the hotplate will increase up to their boiling point. Heat can be transferred to the droplet via: convection, conduction and thermal radiation. Heat transfer via thermal conduction can be neglected since air is a poor thermal conductor.
The impact of thermal radiation on the heat transfer between heat source and droplet is relevant as long as the radius of the droplet is larger than 100 μm. Below that value thermal radiation can be neglected as well. For small droplets convection is the only heat transfer process. The heat transfer by convection to a droplet is written in equation 2.4.

$$\Delta Q_c = 4\pi R K_a (T_a - T_d)\Delta t \tag{2.4}$$

In equation 2.4 ΔQ_c is the heat transfer by convection, R is the droplet radius, K_a is the thermal conductivity of air, T_a is the temperature of air, T_d is the temperature of the droplet and Δt is the time interval.
Depending on the temperature of the droplet prior to the heat transfer two cases can be defined.

1. The droplet temperature is below the boiling point: the transferred heat increases the droplet temperature up to the boiling point.
2. The droplet is boiling: the transferred heat vaporizes parts of the droplet (mass change).

As a result of the second point a change of mass of the droplet leads to change of its trajectory. As already mentioned in the paragraph above different hotplate temperatures define the regime of deposition, hence the thermal gradient defining the change of the droplets temperature.
The interaction of the droplets with the heated surface leading to film growth is shown in figure 2.2. In general, the deposition shown in this figure can be divided into film deposition and powder deposition. In cases when droplets hit or splatter on the surface or are fully converted above the surface (hydrolysis reaction) the deposition leaves a powdery residue. Only in the case when deposition of the material occurs from the vapour phase a film deposition is achieved.

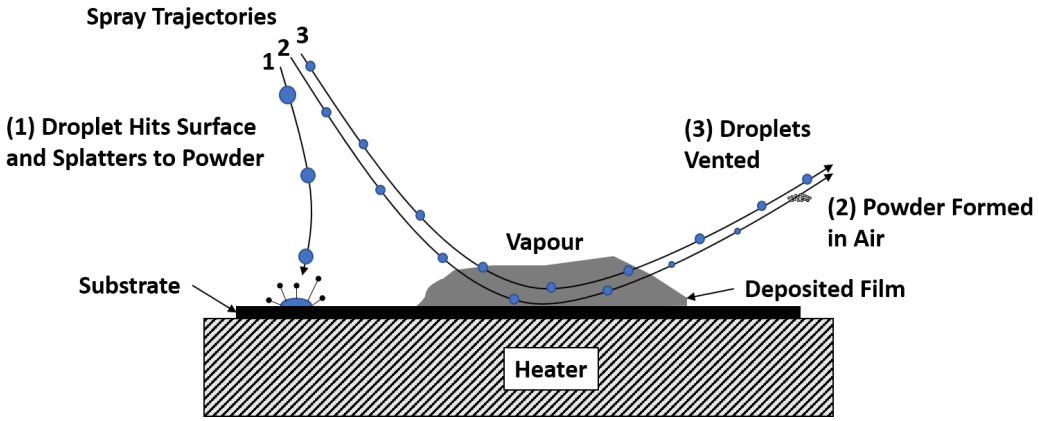

Figure 2.2.: Spray pyrolysis: Three possible trajectories during film growth. (1) Direct impact of droplets onto the substrate surface. A part of the droplets contribute to the film formation. The other part of the droplets is either formed to powder after passing the deposition area (2) or vented (3). According to Sears et al.[226])

Spray pyrolysis set-up: Figure 2.3 shows a schematic representation of the two-fluid spray pyrolysis set-up used within this work. The set-up consists of an air atomizing nozzle, a pressure system and a hotplate.

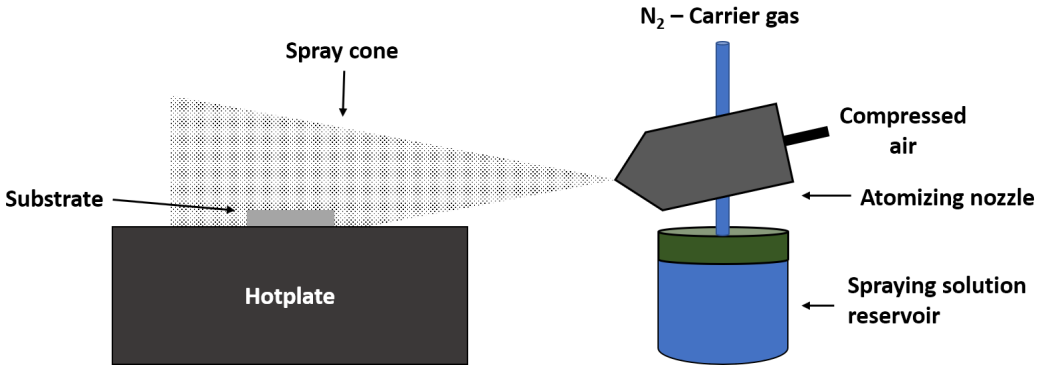

Figure 2.3.: Set-up of a two-fluid spray pyrolysis set-up. Right side: Hotplate with the substrate on top. Left side: Spraying nozzle has three feeds for N_2 carrier gas, compressed air and spraying solution reservoir. The flow from the carrier gas and spraying solution reservoir are mixed in the nozzle. The compressed air is used to start and stop the spraying process. According to Mutinati [24])

Air atomizing nozzle: The air atomizing nozzle applied in this set-up is of the model Quickmist 1/4QMJ from the company Spraying Systems Co. Figure 2.4 shows a cross-section of the air atomizing nozzle before starting the spraying process (a) and during the spraying process (b). In general, the nozzle consists of an air cap, a fluid cap, two inlets for liquid (spraying solution) and air (carrier gas) and a pressure inlet (compressed air, not shown in fig. 2.4). The retainer cap retains the fluid and air cap at their position and seals the area between fluid cap and the main body. The air cap and the fluid cap define the form of the spraying pattern and partially the spraying rate. The spraying rate is mostly defined by the ratio of applied liquid and air pressure. Before the spraying process is started a pressure is applied to the bottle containing the spraying liquid and to the air inlet. In both cases nitrogen is used for pressurization.
Figure 2.4 (a) depicts the conditions before the spraying process is initiated. The liquid is pushed into the liquid inlet (green area). A needle positioned in the fluid cap blocks the entrance for the liquid. At the air inlet nitrogen is flowing into the area between retainer cap and fluid cap (blue area). A small opening in the fluid cap (blue dot) allows the nitrogen to pass into the air cap. At the air cap the gas is vented from the nozzle in spraying direction (blue cone).
Figure 2.4 (b) shows the conditions during the spraying process. Upon applying pressure to the compressed air inlet of the nozzle, the needle blocking the liquid flow, is retracted. The liquid is pushed into the fluid cap (green arrow). In the fluid cap the liquid is mixed with the nitrogen flow. At the opening of the air cap the liquid is atomized and vented in spraying direction (green/blue cone). The spraying process is stopped, when the pressure at the compressed air inlet is depressurized and the needle is extended into its initial position.
Figure 2.5 (a) shows a flat air cap, whereas in figure 2.5 (b) a round air cap is shown. Both air caps have a specific fluid cap. The difference between the two air caps is the form of the resulting spraying pattern. The flat air cap produces a spraying pattern of a plane like geometry. The round air cap produces a cone shaped spraying pattern. At the same pressure conditions the flat configuration shows a much higher mass transport compared to the round configuration.

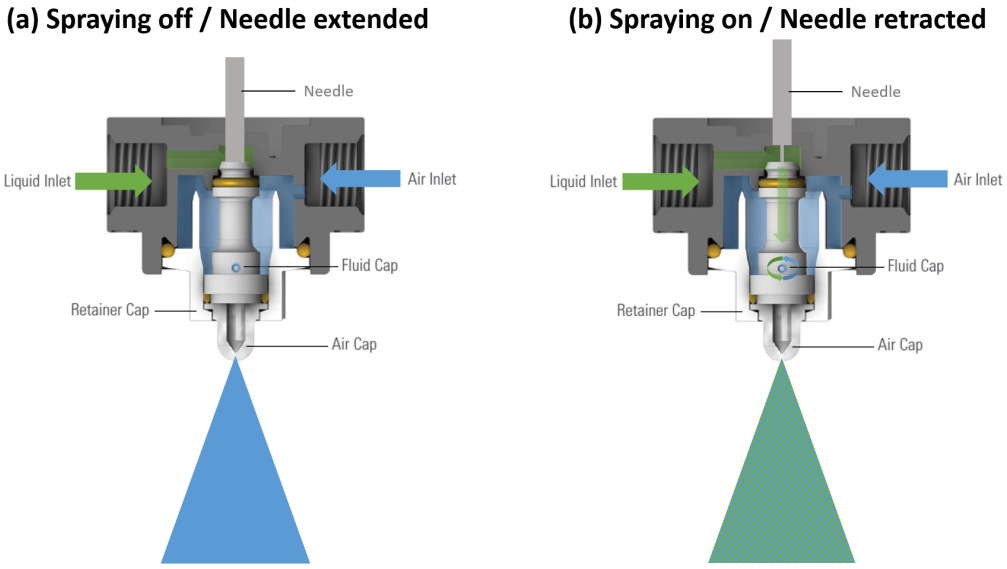

Figure 2.4.: Cross-section of an air atomizing nozzle from Spraying Systems Co. / model: Quickmist 1/4QMJ [227] before (a) and during the spraying process (b). In (a) the needle blocks the flow from the liquid inlet into the fluid cap. Only nitrogen from the air inlet can pass through the nozzle exit (blue cone). In (b) the needle is retracted leading to the mixture of spraying liquid and nitrogen in the fluid cap and an atomization of the mixture through the nozzle exit (green/blue cone).

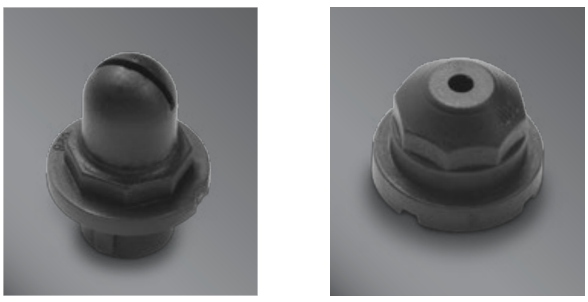

(a) Type: round / model: SUQF130

(b) Type: flat / model: SUQR220B

Figure 2.5.: Air cap types for the air atomizing nozzle Quickmist 1/4QMJ [227].

Pressure system: The two-fluid nozzle is operated by applying pressurized gas to the solution bottle, the air inlet (carrier gas) and the compressed air inlet.
The solution bottle and the air inlet are fed by pressurized nitrogen. Compressed air is applied at the compressed air inlet. The ratio of the pressure applied at the solution bottle and the air inlet defines the size of the droplets of the spraying process and the amount of spraying solution that is being used. The nitrogen pressure at the solution bottle and the air inlet is set by two independent manometers, since the two pressures vary strongly to each other. The compressed air is adjusted by a separate manometer as well.
In addition, a pressure relief valve is installed between the manometer and the compressed air inlet. The compressed air is used to retract the needle to initiate the spraying process. After the spraying process closing the manometer feeding the compressed air inlet will not stop the process. A constant pressure is retained between the compressed air manometer and the compressed air inlet. Therefore, opening the pressure relief valve de-pressurizes the compressed air inlet and the spraying process is stopped.

Standard pressure conditions are:

- Solution bottle pressure: 0.35 bar
- Air inlet pressure: 1.8 bar
- Compressed air inlet pressure: $>$ 2.5 bar

The spraying pattern provided by the air/fluid cap of the air atomizing nozzle starts to exhibit turbulent behaviour after exceeding a certain distance from the nozzle (round air cap: max 56 cm / flat air cap: max 36 cm) [227]. To ensure a steady non turbulent behaviour the distance nozzle to hotplate is set around 30 cm.

Hotplate: The hotplate used in the two-fluid spray pyrolysis set-up is fabricated by the company Harry Gestigkeit GmbH. It consists of two parts: the hotplate (fig. 2.6 (a)) and the controlling unit (fig. 2.6 (b)). The heated area of the hotplate is made of titanium. Titanium is used, since it is resilient to corrosion caused by chemical by-products of the spray pyrolysis process. The maximum temperature of the hotplate is 600°C with a temperature

distribution on the surface of $\pm 2°C$. With an area of 230 mm x 160 mm large samples can be coated. The control unit provides a constant temperature ensured by a thermocouple controlled feedback loop. In addition, the control unit provides various heating ramps and the possibility to program individual heating schemes [228].

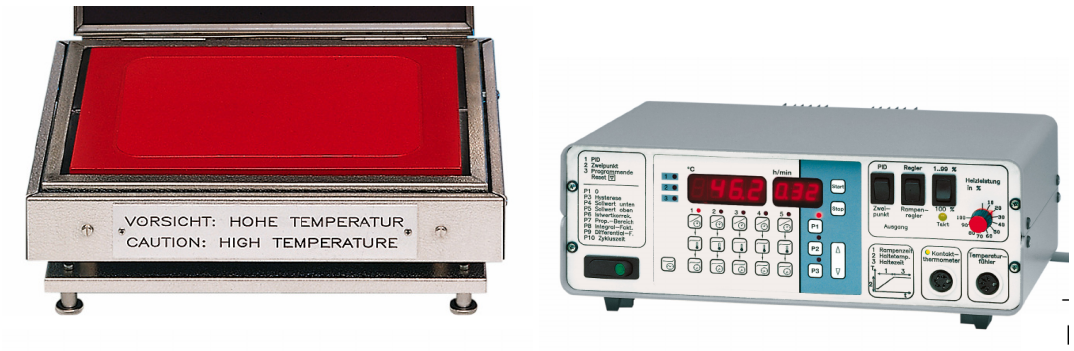

(a) Titianium hotplate (PZ 28-3TD) (b) Control unit (PR 5-3T)

Figure 2.6.: PRÄZITHERM High temperature hotplate with control unit [228]

Single spraying cycle: Figure 2.7 shows the procedure applied for a single spray pyrolysis cycle. Before initializing the spraying cycle the hotplate has to be set to a specific process temperature. Since the thermal mass of the hotplate is rather large a sufficient amount of time has to pass for the hotplate to reach a stable temperature.
After the hotplate is at a stable operation temperature the substrate can be put on the hotplate. The surface temperature on the substrate should reach the hotplate temperature in a couple of minutes, since all substrates used in the spraying experiments have a small thermal mass.
The spraying cycle continues by applying pressure first at the precursor solution bottle and then at the air inlet (carrier gas). The process is started when compressed air is applied to the compressed air inlet. The layer thickness is proportional to the spraying duration. Before each spraying process the relationship of layer thickness to spraying duration is empirically determined by spraying test samples at varying spraying durations.
After measuring the thickness of the layers (white light reflectometer) the

spraying duration can be associated with a specific layer thickness. This empirical determination of the relation between spraying duration and layer thickness is dependent on the precursor solution. For every precursor solution with a varying concentration this determination has to be repeated. After a specific layer thickness is reached the pressure at the compressed air inlet is relieved and the process is completed. In case of multiple cycles a new spraying cycle can be initiated by applying pressure to the compressed air inlet, as long as the pressure at the precursor solution bottle and air inlet is still applied. To end the entire process the pressure at the compressed air inlet has to be relieved followed by the pressure at the air inlet and the solution bottle. The coated substrate can be removed from the hotplate.

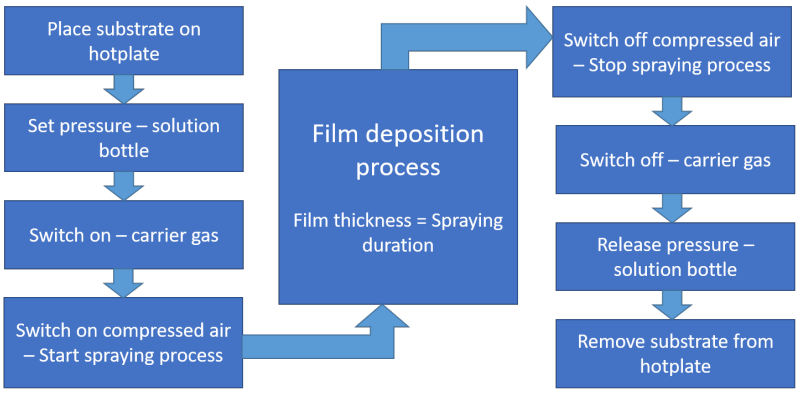

Figure 2.7.: Schematic representation of a full spray pyrolysis cycle. (Left) Procedure applied to start the MOX deposition on a substrate. (Center) MOX deposition of thin film. (Right) Procedure followed after the MOX deposition.

2.1.2. SnO_2

Set-up: Figure 2.4 shows a schematic representation of the spray pyrolysis set-up, that has been used for the deposition of the tin dioxide thin films. Herein, the air atomizing nozzle is equipped with a flat air cap system (see figure 2.5 (a)). Table 2.2 shows the parameters applied for the spray pyrolysis process.

Table 2.2.: Parameters of spray pyrolysis set-up for SnO_2 thin film deposition.

SnO_2 spraying conditions	
Carrier gas pressure	1.8 bar
Spray solution bottle pressure	0.35 bar
Compressed air pressure	2.5 bar
Nozzle type	flat
Hotplate temperature (surface temperature)	400°C
Solution	$SnCl_4 \cdot 5H_2O$ in ethyl acetate
Molarity of solution	0.28 molar

Precursor solution preparation: The solution is prepared according to [24]. Tin(IV) chloride pentahydrate ($SnCl_4 \cdot 5H_2O$) (see tab.:A.1 (1)) is dissolved in ethyl acetate ($CH_3COOC_2H_5$) (see tab.:A.1 (2)) to obtain a solution with a molarity of 0.28 molar. The solution is stirred for an hour. After the tin tetrachloride pentahydrate is dissolved in ethyl acetate the solution is left aside over night. It is reported in [229], that this waiting period of several hours stabilizes the solution to obtain more comparable tin dioxide thin films.

Chemical reaction: The model chemical reaction for the deposition of tin dioxide from a tin tetrachloride based solution is shown in equation 2.5 [230].

$$SnCl_4 + 4H_2O \rightleftharpoons SnO_2 + 4HCl_{(gas)} \tag{2.5}$$

In this equation the entire precursor solution is converted into the two products tin dioxide and hydrochloric acid. It is a common fact that a film consisting of pure SnO_2 would be an insulator. Since SnO_2 fabricated by spray pyrolysis shows no insulator behaviour, impurities of some sort must introduce additional charge carriers. According to Arai [230] the increase in conductance can be attributed to an oxygen deficiency and chlorine ion

impurities resulted by the spraying process. Equation 2.6 describes the case of oxygen deficiency in the resulting thin film. In equation 2.7 the impurities introduced by the spray pyrolysis process are considered.

$$2SnCl_4 + 4H_2O \rightleftharpoons SnO_2 + SnO + 8HCl + \frac{1}{2}O_2 + 2e^- \tag{2.6}$$

$$2SnCl_4 + 4H_2O \rightleftharpoons SnO_2 + SnO + 7HCl + \frac{1}{2}H_2 + \frac{1}{2}O_2 + \frac{1}{2}Cl_2 + e^- \tag{2.7}$$

Both processes introduce additional charge carriers into the conduction band of the resulting material. Furthermore, it should be considered that both reactions occur simultaneously. Although Arai [230] investigated which of the processes dominates no conclusive answer could be given.

2.1.3. CuO

Set-up: The set-up used to fabricate copper oxide thin films is the same as for tin dioxide except for the air atomizing nozzle. For each process a new nozzle was used. The spray pyrolysis process of various precursor solutions is tested with both round (fig.: 2.5 (a)) and flat (fig.: 2.5 (b)) air cap systems. The spray pyrolysis process for copper oxide is investigated for its application in the gas sensor fabrication process flow of our group. The parameters of the best copper oxide spray pyrolysis process are shown in table 2.4. In contrast to tin dioxide the spraying rate is decreased by reducing the compressed air pressure at the pressure inlet of the nozzle.

Precursor solution preparation: In the process of finding the optimal precursor solution three copper salts are investigated. In table 2.3 the copper salts with the tested solvents are shown. In the case of copper chloride and acetate the molarity of the solutions are varied between 0.1 to 1 molar. After weighing the precursor powder of the corresponding copper salt, the powder is mixed with the solvent. The obtained solution is stirred for an hour at ambient temperature. Within that time the copper salt is completely

dissolved in the solvents stated in table 2.3.
This process is true for either copper chloride and acetate. In the case of copper nitrate the solution was prepared according to Abdelmounaim et al.[231]. The solvent used in this paper is water. To investigate the impact of the solvent on the spraying process an additional solvent, namely ethanol, was chosen. Both nitrate based solutions are fabricated by weighing the precursor powder, mixing and stirring it within water or ethanol for around an hour.

Table 2.3.: Different copper salts and solvents investigated for applicability of spray pyrolysis process for CuO.

Copper salt	**Solvents**
$CuCl_2 \cdot 2H_2O$ [tab.:A.1 (3)]	ethanol[tab.:A.1 (6)], water, aceton[tab.:A.1 (7)]
$Cu(COOH_3) \cdot H_2O$ [tab.:A.1 (4)]	ethanol[tab.:A.1 (6)], water, aceton[tab.:A.1 (7)]
$Cu(NO_3)_2 \cdot 3H_2O$ [tab.:A.1 (5)]	water, ethanol[tab.:A.1 (6)]

The deposition of the solutions based on the two salts, copper chloride and copper acetate, was conducted at hotplate temperatures of 300°C - 400°C. Two kind of substrates are tested for deposition: silicon + native silicon oxide and silicon + thermally oxidized silicon oxide. On both surfaces the deposition is possible, although no continuous layers are formed.
The resistance of the layers is measured by a two point measurement on the surface. Both materials show resistance values in the Giga-Ohm regime. Furthermore, the layers are rather thick, rugged and show bad adhesion. The adhesion has been tested by applying an adhesive tape, which resulted in the partial delamination of the layer (tape-test). Therefore, the application of these two salts for the fabrication of thin films is disregarded.
The salt copper nitrate showed promising results. Therefore, copper nitrate based solutions are the main focus for the deliberations of the following paragraphs.

Chemical reaction: Ghose et al.[232] investigated the decomposition of $Cu(NO_3)_2 \cdot 3H_2O$ powder via differential thermal analysis (DTA), difference thermo analysis (DTG), thermogravimetry (TG) and x-ray diffraction (XRD). The copper nitrate used for the fabrication of the copper nitrate solutions is $Cu(NO_3)_2 \cdot 3H_2O$ in powder form. Although copper nitrate is dissolved to fabricate the precursor solution, during the spray pyrolysis process the solvent of a droplet is evaporated prior to decomposition of the containing material. Therefore, it can be assumed that the results of the decomposition of $Cu(NO_3)_2 \cdot 3H_2O$ powder produced by Ghose et al.[232] is equivalent to the spray pyrolysis reaction occurring during deposition of cupric oxide.
The investigation of Ghose et al.[232] confirms the decomposition of copper nitrate occurring in a two step reaction. In equation 2.8 decomposition of the base material and the formation of an intermediate compound (copper nitrate hydroxide) is shown. As Ghose et al.[232] states this reaction takes place at a temperature of roughly 205°C. The copper nitrate hydroxide is decomposed into cupric oxide (CuO) and nitrogen dioxide (NO_2), water (H_2O) and oxygen (O_2) at a temperature of roughly 310°C.

$$Cu(NO_3)_2 \cdot 3H_2O \rightleftharpoons \frac{1}{4}[Cu(NO_3)_2 \cdot 3Cu(OH)_2] + \frac{3}{2}HNO_3 + \frac{3}{2}H_2O \quad (2.8)$$

$$\frac{1}{4}[Cu(NO_3)_2 \cdot 3Cu(OH)_2] \rightleftharpoons CuO + \frac{1}{2}NO_2 + \frac{3}{4}H_2O + \frac{1}{8}O_2 \quad (2.9)$$

These two temperatures concerning the decomposition reaction seem to be true for the powder process but not for the spray pyrolysis process. Since cupric oxide layers are fabricated at hotplate temperatures of 300°C - 400°C the temperature for the second decomposition reaction must be lower for the spray pyrolysis process. Further investigations have to be made to determine proper decomposition temperatures for this cupric oxide deposition process.

Table 2.4.: Final parameters of spray pyrolysis set-up for CuO thin film deposition.

CuO spraying conditions	
Carrier gas pressure	1 bar
Spray solution bottle pressure	0.15 bar
Compressed air pressure	2 bar
Nozzle type	round
Hotplate temperature (surface temperature)	300°C - 400°C
Solution	$Cu(NO_3)_2 \cdot 3H_2O$ in H_2O
Molarity of solution	0.05 molar

2.1.4. ZnO

Set-up: The same set-up as for the previous materials is used to test spray pyrolysis deposition of zinc oxide (ZnO). For each process a new nozzle was used. Again both types of air cap systems are investigated.
In table 2.5 the parameters of the optimal zinc oxide spraying process are shown. A parameter set for a spraying process is assumed to be optimal, when uniform deposition of a smooth thin film (low roughness) is achieved. The uniformity of the film is verified by film thickness measurements (white light reflectometer). The roughness is investigated by AFM measurements. As with the cupric oxide spray pyrolysis the compressed air pressure is reduced to decrease the spraying rate.

Table 2.5.: Final parameters of spray pyrolysis set-up for ZnO thin film deposition.

ZnO spraying conditions	
Carrier gas pressure	1 bar
Spray solution bottle pressure	0.15 bar
Compressed air pressure	2 bar
Nozzle type	round
Hotplate temperature (surface temperature)	400°C
Solution	$Zn(COOCH_3)_2 \cdot 2H_2O$ [tab.:A.1 (8)] in H_2O & ethanol [tab.:A.1 (6)] mixture (ratio 1:3)
Molarity of solution	0.1 molar
Additive	0.5 ml hydrochloric acid (HCl) [tab.:A.1 (9)]

Precursor solution preparation: Edinger et al.[215] employs zinc acetate in aqueous solution to deposit thin films by an ultra sonic spray pyrolysis technique. The solution proposed in this publication is being used as a starting point for the application in our two-fluid spray pyrolysis set-up.
Since the atomizing process for ultra sonic spray pyrolysis and two-fluid spray pyrolysis is different three different solvents are tested. The solvents used for fine tuning the process are: water, a mixture of water and ethanol (ratio 1:3) and ethanol. The molarity of all solutions is set to 0.1 molar. As proposed by Edinger et al.[215] hydrochloric acid (HCl) is added to prevent hydrolysis of the solution. In each of the solutions an amount of 0.5 ml HCl is added.

Chemical reaction: Lin et al.[233] investigated the formation of zinc oxide nanowires from a zinc acetate powder ($Zn(CH_3COO)_2 \cdot 2H_2O$) during heat treatment and analysed the decomposition of the zinc acetate powder via TGA, DSC and MS.
The spray pyrolysis process of zinc acetate solution is assumed to be similar to the decomposition process. The first step of the decomposition of

zinc acetate powder is shown in equation 2.10. Herein, the zinc acetate is deprived of its water content. This occurs at a temperature of around 50°C. The chemical reactions shown in equation 2.11 - 2.13 take place in the temperature range of 200°C - 285 °C.
In equation 2.11 the formation of zinc oxyacetate and acetic acid from zinc acetate and residual water is shown. The formed zinc oxyacetate is further decomposed to zinc oxide, acetone and carbon dioxide in equations 2.12 and 2.13.

$$Zn(CH_3COO)_2 + 2H_2O \rightleftharpoons Zn(CH_3COO)_2 + 2H_2O_{(gas)} \tag{2.10}$$

$$4Zn(CH_3COO)_2 + 2H_2O \rightleftharpoons Zn_4O(CH_3COO)_6 + 2CH_3COOH_{(gas)} \tag{2.11}$$

$$Zn_4O(CH_3COO)_6 + 3H_2O \rightleftharpoons 4ZnO + 6CH_3COOH_{(gas)} \tag{2.12}$$

$$Zn_4O(CH_3COO)_6 \rightleftharpoons 4ZnO + 3CH_3COCH_{3(gas)} + 3CO_{2(gas)} \tag{2.13}$$

This decomposition process described in Lin et al.[233] can only be seen as similar process. A small amount of hydrochloric acid (HCl) is added to stabilize the precursor solution. The influence of the hydrochloric acid is not taken into account. Nevertheless, the basic reaction process during spray pyrolysis should be similar.
All chemical compounds used in the fabrication of all spray pyrolysis experiments are shown in the appendix section A.

2.1.5. Thin film structuring

The structuring of spray pyrolysed metal oxide thin films for gas sensor fabrication is done by photolithography and physical etching. The two processes will be described in the paragraphs below.

Photolithography: Photolithography is used for the structuring of the gas sensitive layers of the gas sensors. Hereby, the substrate fully coated with a metal oxide thin film is spin-coated with a photo-resist. The photo-resist applied for structuring is a positive photo-resist. Illuminated areas of the positive photo-resist are removed from the substrates surface after being developed. After spin-coating the resist is annealed for a specific time to remove residual solvents from the resist.
Prior to the illumination step a photo-mask has to be fabricated. The photo-mask contains the desired structure in a ratio of 1:1. The mask itself is transparent for UV light, whereas the structures on the mask are made of a chromium layer which reflects UV light.
The illumination of the photo-resist coated substrate is done with a EVG 620 mask aligner (EVGroup). The development of the illuminated photo-resist is done by submerging the substrate in a developer. After a specific time the substrate is removed from the developer and submerged in deionized water to stop the developing process. After being removed from the deionized water the substrate is rinsed with water for a couple of minutes and blown dry with nitrogen gas. This process results in a photo-resist structure on top of the substrate, which defines the area of the gas sensitive layers. In table 2.6 standard parameters for the applied photo-resist are stated.

Physical etching (Ar-Ion etching): The physical etching process follows the successful execution of the photolithography step. Within this process the entire surface of the substrate is physically etched by argon ions. The process is conducted with an IonSys 500 by Roth & Rau AG. The argon ion etching process is done under vacuum conditions. The stage on which the substrate resides is tilted in a specific angle to ensure the removal of the entire excess material even when the substrate has a non planar surface geometry. The duration of the etching process depends on the material, the thickness of the layer and the kinetic energy of the ions.
After the etching process is completed the metal oxide layer not covered by a previously fabricated photo-resist is removed from the substrate completely. Below the photo-resist structures, patterned metal oxide structures are present. The removal of the photo-resist can either be done by submerging the substrate in acetone for a couple of hours or by exposing the substrate to an oxygen plasma.

Table 2.6.: Parameters of a standard photolithography resist.

Photolithography	
Resist	AZ®MIR701 (Microchemicals GmbH)
Spin speed [rpm]	4000
Spin duration [s]	35
Annealing temperature [°C]	90
Annealing duration [s]	60
Developer	AZ®MIF726 (Microchemicals GmbH)
Development [s]	30
Stopper	deionized water
Stopper duration [s]	120

2.2. Nanowire arrays

Metal oxide nanowire arrays used in this work are based on a previous work done by Steinhauer [29]. These kind of metal oxide nanowire arrays are fabricated by depositing a structured metal layer and a consecutive thermal oxidation to promote metal oxide nanowire growth. The structure of the metal layer is comprised of multiple metal stripes or squares with a defined gap spacing in between. During the thermal oxidation process metal oxide nanowires are formed. These nanowires grow until the gaps between the structures, stripes or squares, are bridged. Before the oxidation process the metal structures were isolated from each other. After the oxidation the entire, now metal oxide structure, was connected by the bridging metal oxide nanowires.

2.2.1. Fabrication process of nanowire arrays

The fabrication process of cupric and zinc oxide nanowire arrays is done similarly. The difference between the two materials is the growth mechanism

of the metal oxide nanowires. A closer look will be taken on the two growth mechanisms in the section 2.2.2 and 2.2.3.

Electron beam lithography: Electron beam lithography (EBL) is applied to fabricate a structured poly methyl methacrylate (PMMA) mask on top of a substrate (silicon or CMOS wafer piece). This structured mask is used in a consecutive process step to obtain a structured metal layer.
The PMMA mask is fabricated by spin-coating of a PMMA resist on a substrate. In this work positive PMMA resist is employed. Therefore, areas exposed by an electron beam are cut out of the mask. The spin-coating parameters are depending on the PMMA resist that is employed as well as on the desired thickness of the resulting PMMA mask. The spin-coating process is carried out on a make-shift spin-coater.
First, the spin-coating parameters, rotation speed and spin-coating duration are set at the spin-coater. Second, the substrate is placed in the spin-coater and fixed by a vacuum pump. Third, the surface of the substrate is cleansed of dust in the ambient atmosphere by applying a stream of nitrogen gas. As a fourth step a specific volume of the PMMA resist is deposited on the substrate surface via an Eppendorf pipette. Finally, the spin-coating process is activated. After the process is completed the substrate is removed from the spin-coater and placed on a hotplate for annealing. During annealing residual solvents in the PMMA resist evaporate.
The EBL step is carried out on a Raith eLine plus tool. Placed in the EBL tool either copper (fig.2.8) or zinc (fig.2.9) structures can be drawn into the PMMA resist by electron beam exposure. After exposure the substrate is removed from the EBL tool and developed. Hereby, the substrate is submerged in a developer for a specific time. The developing process is stopped by submerging the substrate into a stopping agent.

Figure 2.8.: Electron beam lithography design of copper oxide nanowire array [29].

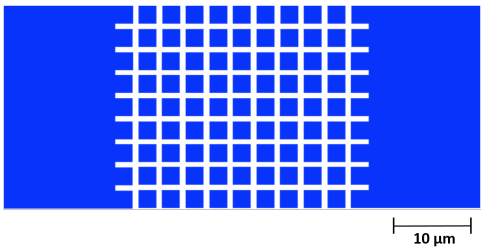

Figure 2.9.: Electron beam lithography design of zinc oxide nanowire array [29].

Thermal evaporation: The deposition of metal onto the PMMA mask is done by thermal evaporation. For this purpose, a thermal evaporation tool is employed. This tool contains two metal boats that are resistively heated under vacuum conditions to evaporate their content.
Depending on which kind of nanowire arrays is being fabricated copper or zinc is loaded into the first boat. The second boat is loaded with titanium. A thin layer of titanium of around 5 nm promotes adhesion between the substrate and the copper or zinc metal layer. The thickness of the evaporated metal layers is determined by a crystal oscillator. The layer thickness for copper and zinc under standard conditions is 500 nm and 250 nm respectively.
After the deposition of the titanium and copper or zinc the substrate is removed from the thermal evaporation chamber. The substrate is placed in acetone for 4 hours, where the lift-off process takes place. Hereby, the metal layers on top of the PMMA resist areas are lifted from the substrate,

whereas the metal layers directly in contact with the substrate remain. As a result, the structures of figure 2.8 and 2.9 are obtained depending on which material system (copper or zinc) is prepared.

Thermal oxidation: The substrate containing the prepared metal structures is thermally oxidized to promote the growth of metal oxide nanowires. The gas sensors employed in this work are integrated onto a test circuit structure capable of setting the sensor's temperature and measuring the sensor's temperature at the same time. Therefore, the metal structure is thermally oxidized on the test circuit structure.
The test circuit structure is placed in our gas measurement set-up, which allows the performance of the thermal oxidation at specific atmospheric conditions. The nanowire growth of these two materials (Cu, Zn) is dependent on the thermal oxidation temperature and of the relative humidity level in the artificially provided atmosphere. In section 2.2.2 and 2.2.3 the precise oxidation parameters are given.

2.2.2. CuO Nanowire Array

In the previous section a general description of the fabrication of a nanowire array has been given. In this section the growth mechanism of a cupric oxide nanowire array will be discussed. The thermal oxidation of a copper metal layer results in the formation of a multilayer system comprised of a residual metallic copper layer at the bottom, a cuprit oxide layer (Cu_2O) in the middle and a cupric oxide (CuO) layer on top. These three copper phases differ each in their volume. Copper has the lowest volume followed by cuprit oxide and cupric oxide.
Therefore, stress is induced at the boundaries between the phases. At the boundary between copper and cuprit oxide a compression force is acting on cuprit oxide, whereas on the boundary between cuprit oxide and cupric oxide a tensile force is acting on cuprit oxide. A similar observation can be made for cupric oxide. On the boundary of cuprit oxide to cupric oxide, cupric oxide experiences a compression force resulted by the cuprit oxide. Since no further phase is on top of the cupric oxide no stress is induced at its surface. The compression and tensile forces result in the formation of a

stress gradient. The stress gradient induces a particle flux in the direction of the compressed area to the tensioned area. Copper ions start to diffuse along the gradient. According to Xu et al.[234] three different diffusion paths occur. Each diffusion path dominates in a certain oxidation temperature range.

- Range 1: the oxidation is done at temperatures $\leq$ 300 °C. The material transport during oxidation is mainly defined by grain boundary diffusion (fig.2.10(a)).
- Range 2: the oxidation is performed between the temperature of 400°C - 700°C. In this temperature range the material transport during oxidation is promoted by sub-boundary diffusion (dislocations, fig.2.10(b)).
- Range 3: the oxidation is done at temperatures $\geq$ 800 °C. Hereby, the material transport during oxidation is mainly defined by lattice diffusion (fig.2.10(c)).

Each of this oxidation ranges result in different morphologies. Xu et al.[234] defines the conditions of range 2 as suitable for nanowire formation. Chen et al.[235] observes a higher number density of nanowires in the oxidation temperature range of 300°C - 400°C.
Nevertheless, the copper ions which diffused to the surface continue to diffuse parallel to the surface until reaching surface sites where cupric oxide nanowire nucleation and growth takes place. Figure 2.11 depicts the path of copper ions along their diffusion path. Arriving at the surface the ions can either initiate a nanowire nucleation or the ions can move along the surface of an already existing nanowire, oxidise and assist in the continuous growth of this nanowire. The copper ion diffusion along an existing cupric oxide nanowire and oxidation explains the continuous increase of cupric oxide nanowire diameters over oxidation time.
Furthermore, this also explains the morphology of cupric oxide nanowire, which shows a larger diameter at the nanowire base compared to the nanowire tip. Nanowires grown by thermal oxidation process are single crystalline. As a result of their crystallinity CuO nanowires used as a sensor material in gas sensors, exhibits a higher stability over time during gas sensor operation. In table 2.7 the process flow parameters for cupric oxide nanowire array fabrication are given.

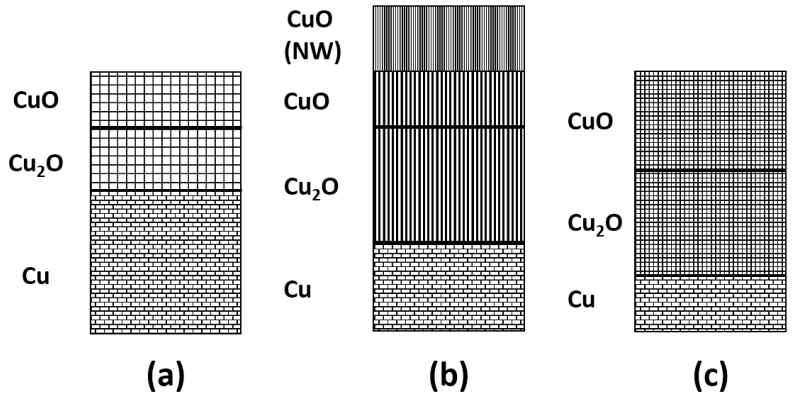

Figure 2.10.: Multilayer system formed during the thermal oxidation of a copper foil. (a) $T_{oxidation}$ $\leq$300°C growth promoted by grain boundary diffusion. (b) $T_{oxidation}$ $\approx$400°C - 700°C growth promoted by sub-boundary diffusion. (c) $T_{oxidation}$ $\geq$800°C growth promoted by lattice diffusion. According to Xu et al.[234]

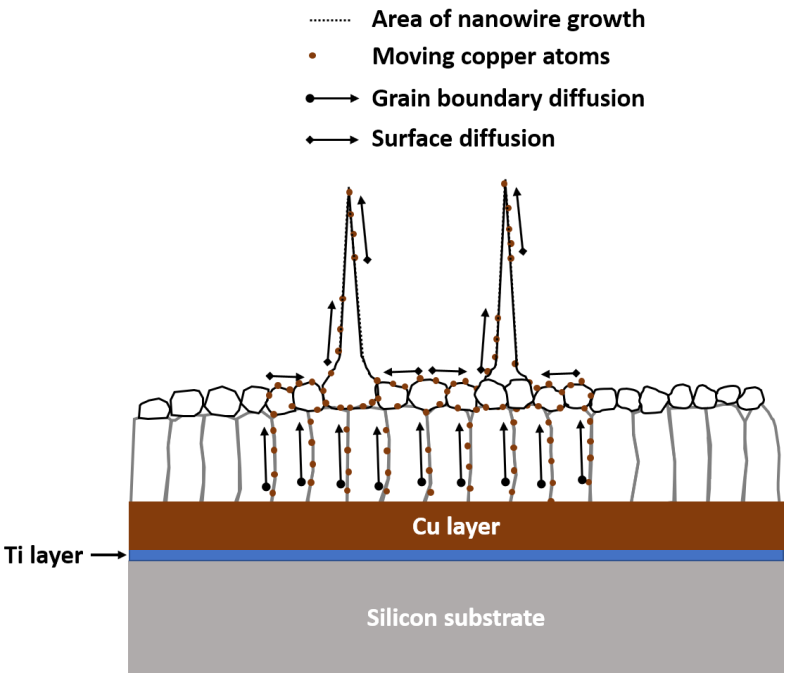

Figure 2.11.: Growth mechanism of copper oxide nanowires during thermal oxidation. Formation of a multilayer system of Cu, Cu_2O, CuO and CuO nanowires. The nanowire growth is driven by diffusion of copper ions (red dots) along the grain boundaries of Cu_2O and CuO. On the CuO surface CuO nanowires are formed. A continuous flux of copper ions ensures the further growth of the CuO nanowires with oxygen from the ambient atmosphere. According to Chen et al.[235]

Table 2.7.: Parameters for cupric oxide nanowire array or cupric oxide thin film fabrication.

(1) Electron beam lithography (EBL)	
PMMA resist	AR-P 672.08 (ALLRESIST)
Spin speed [rpm]	2000
Spin duration [s]	60
Annealing temperature [°C]	180
Annealing duration [s]	300
Developer	AR600-55 (ALLRESIST)
Development [s]	15
Stopper	AR600-60 (ALLRESIST)
Stopper duration [s]	60
(2) Thermal Evaporation	
metal 1	titanium
metal 1 thickness [nm]	5
metal 2	copper
metal 2 thickness [nm]	500
(3) Lift-off	
Solvent	acetone
Duration [h]	4
(4) Thermal Oxidation (nanowires)	
Oxidation temperature [°C]	335
Oxidation duration [h]	5
Relative humidity [%]	≈ 4
(5) Thermal Oxidation (thin film)	
Oxidation temperature [°C]	400
Oxidation duration [h]	6
Relative humidity [%]	50

2.2.3. ZnO Nanowire Array

The growth mechanism of zinc oxide nanowires by thermal oxidation is similar to the oxidation process of cupric oxide nanowire. A stress induced

diffusion of zinc ions results in the formation of zinc oxide nanowires.
According to Zhao et al.[236] the growth process can be described as depicted in figure 2.12. Herein, the oxidation temperature is rising up to an upper temperature level. The initial state before oxidation is a zinc film with a hexagonal crystal structure (fig.2.12(a)). The zinc layer is closely packed. During the thermal oxidation the grains start to oxidise at the edges, which is attributed to the edge-enhanced oxidation effect as it is called by Zhao et al.[236]. A tight zinc oxide layer is formed at the surface, preventing a further rapid oxidation of the entire zinc metal layer. At the grain boundaries of the surface zinc oxide layers stress is generated. The stress induces the formation of zinc oxide nanowire seeds at grain-grain-boundaries (fig.2.12(b)). By increasing the oxidation temperatures further, metallic zinc grains below the zinc oxide surface layer reach their melting point. As a result, agglomeration of the metallic zinc grains occurs forming larger grains. The zinc oxide nanowires formation initiates at the seed structures. For continuous nanowire growth a steady supply of zinc ions is needed. At even higher temperatures the already molten zinc transitions into the vapour phase.
Zinc ions in the vapour phase diffuse along the grain boundaries to fuel zinc oxide nanowire growth. The hexagonal structure of zinc allows the formation of zinc oxide nanowire with a twin boundary structure. The twin boundary structure is formed at the grain boundary, where a crystallisation can occur in two different direction (indicated by the two arrows at the base of the nanowire in fig. 2.12 (c)). Therefore, a crystalline structure with two crystallites can be formed. Furthermore, zinc ions can either diffuse along the grain boundaries of the zinc oxide layer or the twin boundaries within the zinc nanowire. Diffusion along the twin boundaries as well as the ZnO nanowire surface results in the growth of the zinc nanowire.
As stated above the diffusion process promoting the nanowire growth is stress induced. The growth of zinc oxide grains at the surface of the zinc layer introduces stress into the material. The diffusion of zinc ions and the growth of zinc oxide nanowires as seen in figure 2.12 (c) is a mechanism to relieve stress in the zinc / zinc oxide layer structure. In table 2.8 the process flow parameters for zinc oxide nanowire array fabrication are provided.

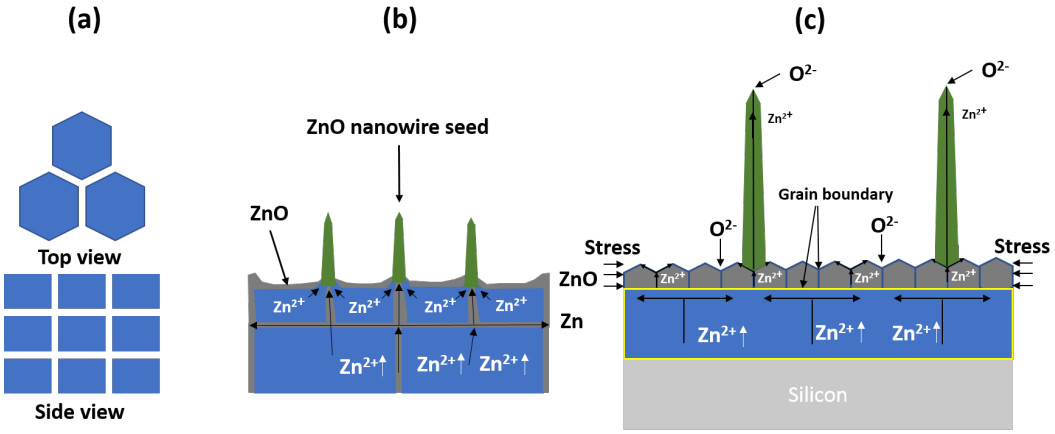

Figure 2.12.: Growth mechanism of zinc oxide nanowires during thermal oxidation. (a) Hexagonal crystal structure of metallic zinc layer before oxidation (top view and side view). (b) Formation of zinc oxide layer and zinc oxide nanowire seeds during thermal oxidation. (c) The zinc oxide nanowire growth is fed by a flux of zinc ions from the subsiding zinc layer to the surface, where the oxidation occurs. According to Zhao et al.[236]

Table 2.8.: Parameters for zinc oxide nanowire array fabrication.

(1) Electron beam lithography (EBL)	
PMMA resist	AR-P 679.04 (ALLRESIST)
Spin speed [rpm]	1000
Spin duration [s]	60
Annealing temperature [°C]	150
Annealing duration [s]	180
Developer	AR600-56 (ALLRESIST)
Development [s]	20
Stopper	AR600-60 (ALLRESIST)
Stopper duration [s]	30
(2) Thermal Evaporation	
metal 1	titanium
metal 1 thickness [nm]	5
metal 2	zinc
metal 2 thickness [nm]	250
(3) Lift-off	
Solvent	acetone
Duration [h]	12
(4) Thermal Oxidation	
Oxidation temperature [°C]	400
Oxidation duration [h]	3-5
Relative humidity [%]	50

3. Gas sensor device fabrication

In this chapter the process flow of the gas sensor fabrication is described. Gas sensors employed in this work are either integrated on a test circuit structure or on a CMOS structure. From here on gas sensors integrated on a test circuit are called silicon based (SB) gas sensors.

3.1. Silicon based Gas Sensors

SB - Process flow of the various materials: The gas sensors fabricated on test circuit structures are called silicon based gas sensors, since the deposition of the metal oxide sensor material is done on a silicon substrate. The substrates used in this work were fabricated by Siegert Wafer GmbH. The substrates are purchased in wafer form, which are cut in 20 by 20 mm pieces. The thickness of a wafer piece is around 675 μm. The surface layer of the substrate consists of a thermally oxidized silicon oxide with a thickness of roughly 300 nm. This silicon oxide layer provides insulation for multiple gas sensors fabricated in parallel on the same silicon substrate.
For each silicon based gas sensor, either thin film or nanowire array, a standard electrode system to provide four wire measurement is fabricated. In figure 3.1 the process steps for the fabrication of the electrode system is shown. In step 1 a photoresist (AZ Mir701) is spin-coated onto a silicon substrate.
In steps 2 and 3 the photolithography and photoresist development for electrode system pattering is done. The photomask utilized to expose the photoresist contains of multiple electrode systems, wherein each electrode system can be employed for the fabrication of a single gas sensor.
In step 4 the electrode material is deposited onto the patterned photoresist. A 5 nm thin film of titanium is deposited as an adhesive layer followed by a

200 nm gold thin film as the primary electrode material.
In step 5 the lift-off process is done. The processed silicon substrate contains multiple electrode systems.

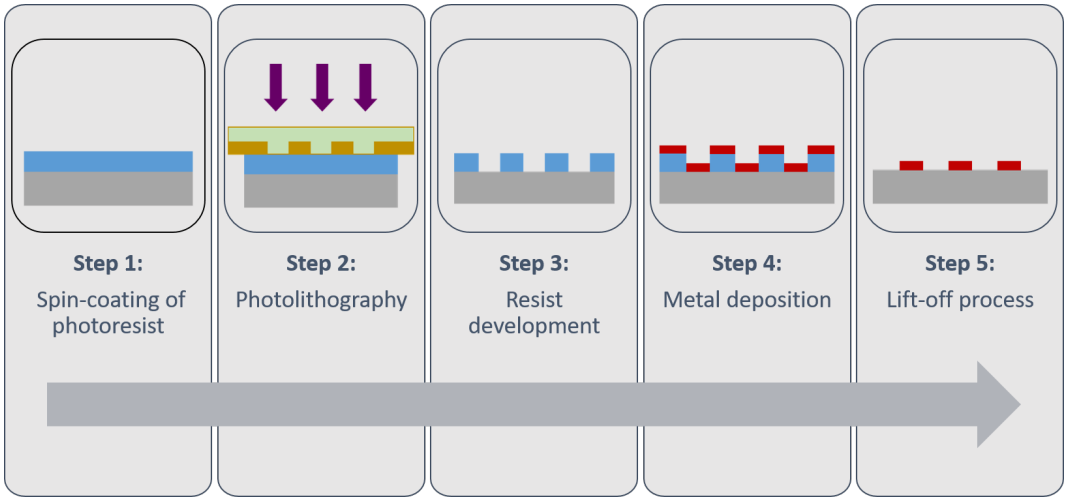

Figure 3.1.: Process steps for electrode system fabrication.

Thin films: The process flow for thin film fabrication on silicon based gas sensors is depicted in figure 3.2. Firstly, the electrode system is fabricated on a silicon substrate. This process has already been discussed above.
Secondly, the metal oxide material is deposited on the entire substrate surface. The deposition is done by spray pyrolysis technique. After the MOX layer is deposited an annealing step is needed to convert the amorphous layer into a polycrystalline layer.
Thirdly, the metal oxide material on top of the electrode system is patterned to form the gas sensitive area of the gas sensor. Hereby, the form of the gas sensitive area is defined by a photo-resist mask fabricated by photolithography. After fabrication of the photo-resist mask the entire substrate is uniformly etched via a physical etching process (Ar ion etch). Areas not covered by photo-resist are etched. As a result multiple MOX areas following the photo-resist mask pattern are obtained. Residual photo-resist has to be removed. This is done by dissolving the photo-resist in acetone or by exposing the sample to an oxygen plasma.

Fourthly, the gas sensor is assembled. Since the silicon substrate contains multiple pairs of electrode system and gas sensitive layer the silicon substrate has to be cleaved to obtain single structures. Each of these single structures is merged with a heater and a thermocouple to ensure precise heating during gas sensor operations. This so-called sensor stack is soldered and wire bonded to a gas sensor evaluation PCB, which can be used within our gas measurement set-up. The entire assembly procedure is reviewed in the paragraph gas sensor assembly below.

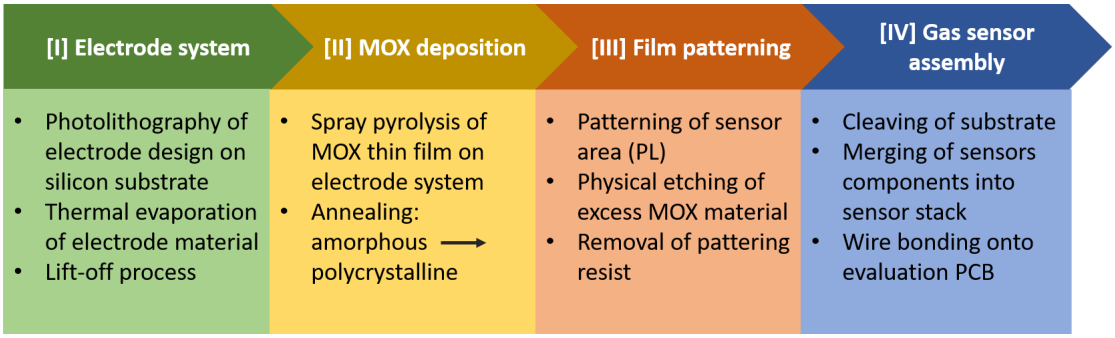

Figure 3.2.: Process flow for thin film gas sensor fabrication for silicon based gas sensors.

Nanowire arrays: The process flow for nanowire array fabrication for silicon based gas sensors is similar to the process flow for thin films. Firstly, the electrode system on a silicon substrate is fabricated.
Secondly, the metal layer structures, which are the precursor structures for nanowire growth are deposited. The pattering of the metal layer structures is done by EBL. Hereby, an electron beam resist is spin-coated on a silicon substrate and consecutively annealed. The design, which is used to pattern the electron beam resist is dependent on the applied material (Cu or Zn, see section 2.2). After the patterning the electron beam resist is being developed. Two metal layers are thermally evaporated onto the patterned resist: an adhesive layer (Ti) and sensor precursor metal layer (Cu or Zn). The lift-off process concludes the metal deposition resulting in metal layer structures corresponding to the patterning design. Equally to the thin film case multiple metal layer structures are deposited on different electrode systems.
Thirdly, the gas sensor assembly is done. The silicon substrate is cleaved

to obtain a single electrode system / metal layer structure. After merging the silicon substrate to a heater, a thermocouple and consecutive soldering and bonding it to an evaluation PCB the final step of the nanowire array fabrication can be done.
Fourthly, the in-situ thermal oxidation is done. Hereby, the operation temperature and the atmosphere in the gas measurement set-up are adjusted to the optimal growth conditions for the metal oxide nanowire arrays. After several hours (see section 2.2) the fully bridged nanowire array is formed.

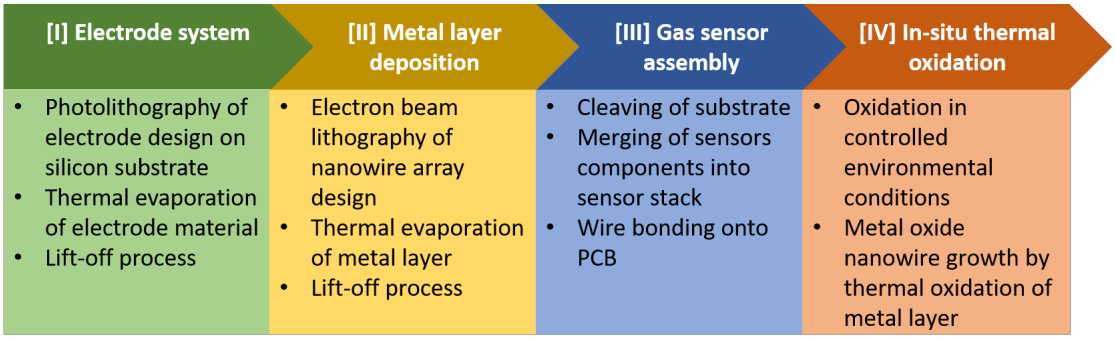

Figure 3.3.: Process flow for nanowire array gas sensor fabrication for silicon based gas sensors.

Thin films based on nanowire array process: The process described in the above paragraph (Nanowire arrays) can also be used to fabricate continuous films. In the case of copper, the striped metallic structure is the base for this thin film (see section 2.2). The fabrication process is done identically up to the oxidation step. By changing the oxidation temperature the formation of CuO nanowires is not favoured. The oxidation results in the formation of a continuous CuO film. This CuO thin film is the base sensing layer for the CO_2 gas sensor described in this work.

Gas sensor assembly: The five steps of the silicon based gas sensor assembly is shown in figure 3.4. The first step is done after gas sensitive layers or precursor metal layers are properly patterned on top of various electrode systems. An array of multiple, yet singular gas sensors, separated by sufficient spacing to each other are obtained. The array of gas sensors is

cleaved to obtain single gas sensors.
In the second step the silicon substrate containing the electrode system and the gas sensitive layer (or precursor metal layers) is merged with a heater (Pt6.8), a thermocouple (Pt100) and glued to a carrier silicon substrate. The heater applied for gas sensor fabrication consists of two Pt6.8 elements operated in serial to provide an bigger area with a stable temperature distribution, whereas for the thermocouple a single element is sufficient. The merging of the three elements sensor, heater and thermocouple onto the silicon substrate is done via a thermoconductive adhesive. The adhesive paste is processed at ambient conditions and cured at 100°C for an hour.
In the third step the sensor stack is soldered to an evaluation PCB.
In the fourth step the electrode system of the gas sensor is wire bonded with gold wires to the evaluation PCB.
In the fifth step the readily prepared gas sensor is evaluated in the gas measurement set-up. In the case of nanowire array gas sensors the in-situ nanowire growth is conducted before evaluation. Figure 3.5 (a) shows a camera picture of the final product of the gas sensor assembly. Herein, the evaluation PCB with the attached gas sensor stack is shown. Figure 3.5 (b) shows a magnified gas sensor on the sensor stack featuring its wire bonded electrode system and gas sensitive material (CuO thin film).

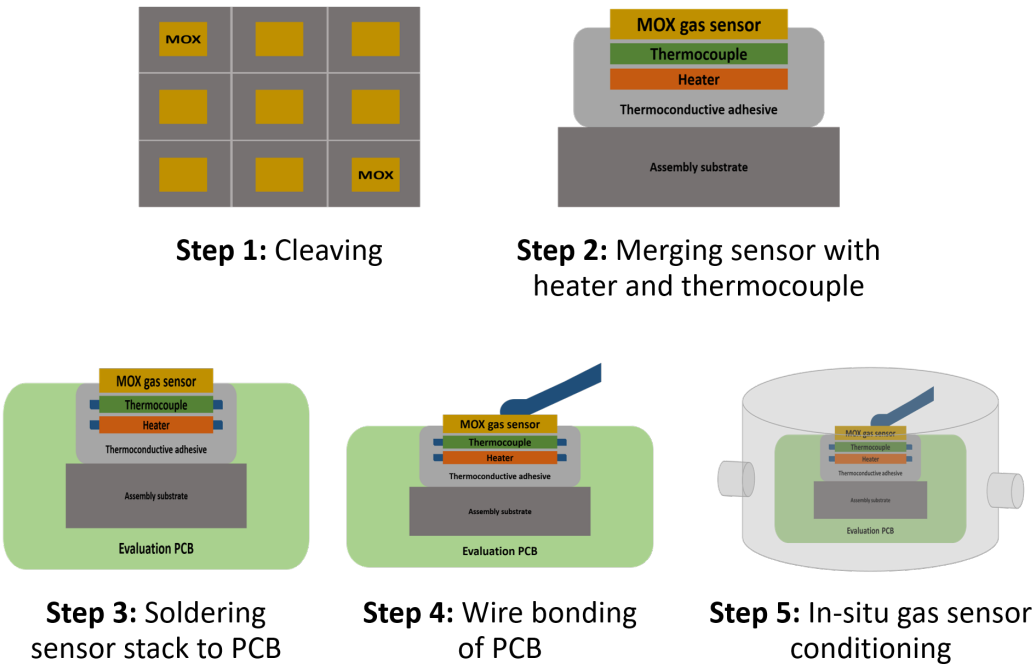

Figure 3.4.: The five process steps of gas sensor assembly and conditioning.

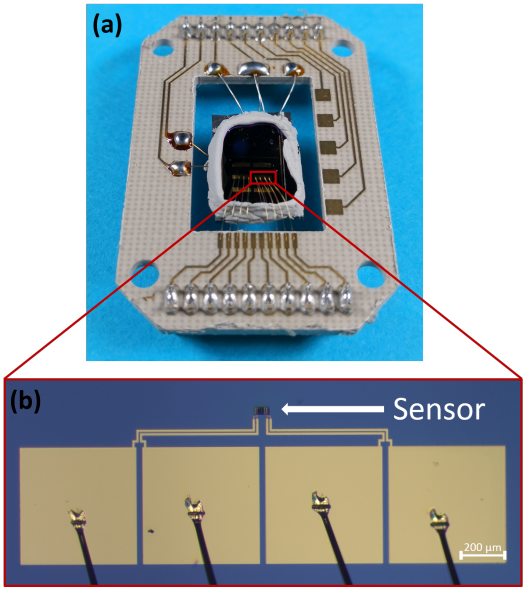

Figure 3.5.: Final product of silicon based gas sensor fabrication. (a) Camera picture of the evaluation PCB with the attached gas sensor stack. The gas sensors itself are wire bonded (Au wires) to the PCB. (b) Optical microscope picture of a single gas sensor on the sensor stack. The gas sensor is made of the electrode system and the gas sensitive material (CuO thin film).

Gold (Au) nanoparticles functionalisation: The functionalization process step is done at the end of the process flow. Hereby, the fully assembled and operable gas sensor is functionalized with gold (Au) nanoparticles. For these silicon based gas sensors drop coating is employed to deposit the nanoparticles from solution.
The NPs solution used within this work is provided by Fraunhofer IAP-CAN. The Au-NPs (CANdot®series G, c = 100 μg Au/ml) are stabilized in the aqueous solution by sodium citrate, which prevents agglomeration of the NPs in the solution.
A volume of 40 μL is applied onto the sensor surface by a pipette. During the deposition process the gas sensor is operated in ambient conditions and the sensor is heated to 85°C. The aqueous Au-NPs solution is drop coated onto the sensors surface in steps of 5 μL. Since the solution leads to a cooling of the sensor, each consecutive drop coating step is done after the sensor temperature has reached the initial 85°C.

Following the deposition of the 40 μL of the Au-NPs solution is an annealing step for 12 hours. The annealing temperature is set to 400°C to burn of the surfactants.

3.2. CMOS Integrated Gas Sensors

3.2.1. CMOS integration

In this work the integration of metal oxide gas sensor materials is done on two separate CMOS chips, called MPW3 and MPW4. The abbreviation MPW stands for multi project wafer, a fabrication procedure, where multiple users can split the costs of a single wafer by fabricating multiple designs on the same wafer. The MPW3 CMOS chip was developed in a previous project called Chip On Chip technology to Open new Applications (CO-COA), whereas the MPW4 CMOS chip has been developed within the Multi Sensor Platform (MSP) project.
The integration of thin films onto MPW3 chips used in this work is done according to a process flow developed by Mutinati [24]. The integration of nanowire arrays (designs based on by Steinhauer [29]) onto MPW4 chips has been developed within this work.
Both chips contain MEMS structures called microhotplates (see paragraph microhotplate below), which are employed to provide the operation temperature of the metal oxide gas sensitive materials integrate on a CMOS chip.

Microhotplate: The microhotplate is a microelectromechanical system (MEMS) that is being used to provide the operation temperature for the metal oxide gas sensing material as well as thermal insulation to the rest of the silicon chip.
In figure 3.6 a scanning electron microscope (SEM) picture of a microhotplate is shown (MPW4 microhotplate). The centre structure is a thin membrane with dimensions of 70 μm x 70 μm and thickness of roughly 8 μm. The membrane is connected via four arms to the adjacent chip, which is why this structure is called a spider structure. The microhotplate is heated by a

heating filament built into the centre of the membrane. The electrical supply lines for the heater are built into the arms of the microhotplate. Below the membrane a cavity is etched into the silicon, insulating the membrane and the arms from the silicon. As a result of this insulation, temperatures of up to 400°C can be reached without heating the adjacent chip.
On the membrane up to two gas sensing layers are deposited. The electrodes system vary from MPW3 to MPW4 (see paragraphs below). In figure 3.7 a cross-section of a schematic microhotplate membrane is depicted. Going from top to bottom the top layer is the MOX gas sensing layer.
Right below this layer is the electrode system for resistive measurement evaluation. Electrode system and MOX layer are insulated by a silicon dioxide layer. Below the insulating layer is a heat spreader. This layer ensures a precise temperature distribution along the entire membrane surface. The final functional layer is the heater, a poly-silicon structure which provides heating. The stack is closed at the bottom by a silicon dioxide layer as insulation. A thermocouple is applied for temperature control.
The entire structure is optimized for low power consumption. At a temperature of 400°C the power consumption is at roughly 17 mW. In addition to low power consumption fast heating cycles can be applied. The microhotplate's rise time from room temperature to 400°C is around 10 ms. The fall time going from 400°C to room temperature is roughly equivalent to 10 ms.

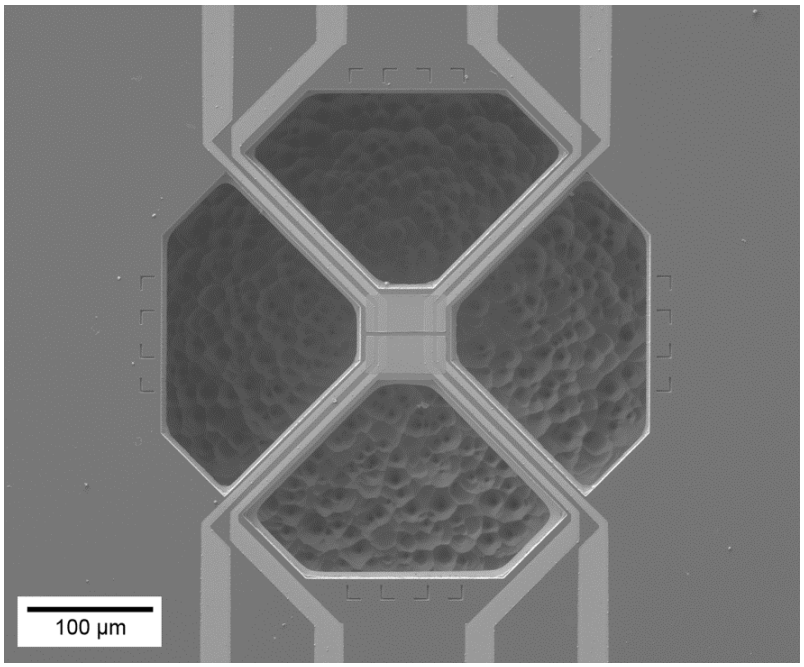

Figure 3.6.: Scanning electron microscope picture of a microhotplate showing the spider structure and the etched cavity beneath it. This mircohotplate is part of a MPW4 CMOS chip. The two rectangles on the membrane are two gas sensing layers (SnO_2). Each gas sensing layer is contacted with four electrodes enabling a 4 wire measurement.

Figure 3.7.: Schematic representation of a cross-section of the membrane stack with its general layer composition.

MPW3: The MPW3 CMOS chip contains two microhotplate structures of different sizes. These two sizes were defined in previous projects to evaluate the influence of the size on the stability of the MEMS structure during sensor operations. Both microhotplates contain the same membrane with dimensions of 70 μm x 70 μm and thickness of 8 μm. The difference between the microhotplates is the length of their four arms. The large microhotplate has an arm length of 150 μm, whereas the small microhotplate has an arm length of 50 μm. In both configurations the arm width is 12 μm. As a result of the longer arm length the thermal insulation of the larger microhotplate is better compared to the smaller microhotplate.
A special feature of both microhotplates is the fabrication of the electrode system. Since the electrodes are made of tungsten, they can be fabricated directly within the CMOS fabrication process. Each of the four electrodes used for the four wire measurement are made of multiple tungsten bars, called tungsten plugs. These tungsten plugs protrude from the membrane surface. The electrical wiring for electrical evaluations leads from the tungsten plugs through the membrane stack inside the microhotplate arms to the bond pads on the edges of the CMOS chip.
The bond pads are integrated with an electric discharge (ESD) protection. For gas sensor measurements this protection has to be disabled. Therefore, a voltage is applied at a specific pad on the MPW3 CMOS chip to disable the protection. A total of four gas sensors can be implemented on the MPW3 CMOS chip.

MPW4: The MPW4 CMOS chip contains eight microhotplate structures. The dimensions of these microhotplates is similar to the large microhotplate of the MPW3 CMOS chip. The membranes have the same dimensions of 70 μm x 70 μm and thickness of 8 μm. Furthermore, the microhotplate arms have the same length of 150 μm as well. The difference is the width of the arms, which is 20 μm. A major difference between MPW3 and MPW4 is the applied electrode system.
Since the MPW3 microhotplates' tungsten electrodes start to oxidise at elevated temperatures, resulting in the expansion of the tungsten electrodes and subsequently in the cracking of the MPW3 microhotplate membrane an alternative electrode material had to be found. For the MPW4 microhotplates a simple gold electrode system had been chosen. The fabrication of the gold

electrodes is being done in a post-processing step outside of the CMOS fab. The change of the microhotplates arm width is a direct consequence of the alternative gold electrode system, since the electrode wiring cannot be integrated into the microhotplate membrane and the microhotplate arms. Figure 3.6 shows a SEM picture of the gold electrode system on the MPW4 microhotplate.
To improve the temperature measurement on the microhotplates the thermocouple positions are altered. The thermocouple position at high temperature is shifted onto the microhotplate membrane. The thermocouple position at low temperature is shifted further away form the microhotplate structure. Additionally, a temperature sensor to measure the CMOS chip temperature is directly integrated into the chip (Celsius, ams AG). This temperature sensor is applied to gauge the microhotplate thermocouple, leading to a higher accuracy. A total of 16 gas sensors can be implemented on the MPW4 CMOS chip.
A special feature of the MPW4 CMOS chip is the possibility to 3D integrate this multi gas sensor chip via through silicon via technology (TSV).

Differences MPW3 / MPW4: In table 3.1 the a direct comparison of both CMOS chips, MPW3 and MPW4, described above is shown. Since MPW4 is a further development of MPW3 some aspects had to be changed. The biggest change is the electrode system. The tungsten plugs used in the MPW3 chips reduced the work needed during post processing, since the electrodes were made during the initial CMOS fabrication process. During operation at temperatures up to 400°C the tungsten electrodes started to oxidize, expand and finally cracking the membrane. Therefore, an alternative electrode fabrication was chosen for the MPW4 chip. The electrodes are deposited in a post processing step by photolithography and sputtering of the electrode material. Another big change is the usage of a single sized microhotplate. Investigations done at prior projects showed that the large microhotplate structure of the MPW3 chip has a higher mechanical stability. Therefore, this size was chosen for the MPW4 chip.
A further improvement is the implementation of an additional temperature sensor, which is part of the MPW4 chip. The temperature sensor allows the calibration of the low temperature side of the thermocouples to the MPW4 chip temperature, hence ambient temperature. This enables a more

precise temperature measurement of the microhotplates' temperature by the thermocouples. Furthermore, the MPW4 chip is equipped with through silicon via technology, which allows 3D stacking of this chip.

Table 3.1.: Direct comparison of both CMOS chips MPW3 and MPW4.

Property	**MPW3**	**MPW4**
Number of microhotplates	2	8
Sizes of microhotplates	two (small & large)	single
membrane dimensions [μm x μm]	70 x 70	70 x 70
arm length [μm]	50 (small) / 150 (large)	150
arm width [μm]	12	20
Type of electrode system	integrated (tungsten plugs)	post processed
Electrode material	tungsten	platinum or gold
Connectivity	bond pads	bond pads & through silicon vias (TSV)
Microhotplate temperature measurement	thermocouple	thermocouple & reference sensor on CMOS chip

3.2.2. CMOS: Process flow of the various materials

In this work the fabrication of thin films is done on MPW3 CMOS chips, whereas the nanowire array fabrication is done on MPW4 CMOS chips.

Thin films: In figure 3.8 (a) depicts the process flow for CMOS integrated thin films on MPW3 CMOS chips. The base material for the process flow are wafer pieces of the dimensions 20 mm x 20 mm containing multiple CMOS chips. Two of those CMOS chips are of the MPW3 CMOS chip type.
The first process step is the deposition of the thin film on a wafer piece.

Hereby, a thin film of SnO_2 is deposited via spray pyrolysis. Following the deposition is an annealing step to transition the amorphous film to a polycrystalline film.
In the second process step the gas sensitive area on the microhotplate membrane is patterned. The pattering is done by photolithography. The photolithography step results in a patterned photoresist on top of the SnO_2 layer. Via a physical etching method (argon ion etching) SnO_2, which isn't covered by photoresist, is removed from the surface of the wafer piece. Consequently, the photoresist is removed from the surface (acetone submersion or oxygen plasma) as well, leaving structured SnO_2 layers on the electrode system of the MPW3 microhotplate membranes.
The third process step is optional. Hereby, a thin layer of gold is structured directly on the SnO_2 layers. This is done by a photolithography step followed by thermal evaporation of gold (5 nm) and lift-off process. This thin gold layer is used to fabricate gold nanoparticles on the surface of the SnO_2 layer during a conditioning step in the gas measurement set-up. At 400°C the thin gold layer on top of the SnO_2 layer starts to form gold islands, which are in the nanometre regime, hence gold nanoparticles.
In the fourth process step a protection layer is fabricated on top of the microhotplate membranes covering both sensor layers. The protection layer consisting of a photoresist made by photolithography. The purpose of the protection layer is to protect the SnO_2 layers from the xenon difluoride (XeF_2) etchant during the release etch of the microhotplates.
In the fifth process step the wafer piece is diced via saw dicing. Two MPW3 CMOS chips are obtained.
In the sixth process step the release etch is conducted. A XeF_2 release etch detaches the spider structure from the silicon beneath it. During this etching process, described by equation 3.1, the silicon beneath the CMOS stack is partly etched. The etchant can access the silicon from the frontside (sensor side of the substrate) through openings in the CMOS stack, which are the areas between the microhotplate arms (see figure 3.6). The anisotropic etch forms a cavity below the spider structure shaped hemispherical. Equation 3.1 shows that XeF_2 reacts with silicon (Si) to form gaseous xenon ($Xe_{(gas)}$) and silicon tetrafluoride ($SiF_{4(gas)}$). The etching process is controlled by monitoring the silicon tetrafluoride content in the exhaust.

$$2XeF_2 + Si \rightleftharpoons 2Xe_{(gas)} + SiF_{4(gas)} \tag{3.1}$$

In the seventh process step the protection resist is removed (acetone submersion or oxygen plasma) and the MPW3 CMOS chips are aluminium wedge bonded to an evaluation PCB.

Nanowire arrays: Figure 3.8 (b) depicts the process flow for CMOS integrated nanowire arrays on MPW4 CMOS chips. As for the case of MPW3 CMOS chips the base material for the process flow are wafer pieces of the dimensions 20 x 20 mm containing multiple CMOS chips. Six CMOS chips are of the MPW4 CMOS chip type.
In the first process step the metal layer structure (Cu or Zn) acting as precursor materials of the MOX nanowire array is deposited. Hereby, either the copper or the zinc structure is written into a PMMA resist by EBL. After development of the electron beam resist the metal is deposited. First an adhesive layer of titanium (5 nm) is thermally evaporated, followed by copper (500 nm) or zinc layer(250 nm). After the lift-off process metal layer structures are obtained on multiple chips of the wafer piece.
In the second process step the protection layer is deposited covering both sensor areas at each microhotplate of the wafer piece (photolithography).
In the third process step the release etch of the spider structure is conducted (see above thin films).
In the fourth process step the wafer pieces are diced into the MPW4 CMOS chips. Since the MPW4 CMOS chip can be 3D integrated the thickness of the chip itself and the wafer is around 200 μm. Ensuring a precise and crack free dicing, stealth dicing is employed.
In the fifth process step the protection layer is removed (acetone submersion) and the MPW4 CMOS chips are aluminium wedge bonded onto an evaluation PCB. In the sixth process step the nanowire growth is conducted. The bonded MPW4 CMOS chips are operated in a gas measurement set-up, where the environmental conditions can be set. The metal layers on the microhotplates are thermally oxidized in-situ promoting nanowire growth. After several hours at nanowire synthesis conditions a fully bridges nanowire array is obtained (CuO or ZnO).
The seventh process step is optional. Hereby, the nanowire array is functionalized with nanoparticles. Two methods are employed for nanoparticles functionalization: drop-coating or ink-jet printing. Both methods require nanoparticles in solution. Since ink-jet printing shows a higher accuracy for

the positioning, better results can be expected.

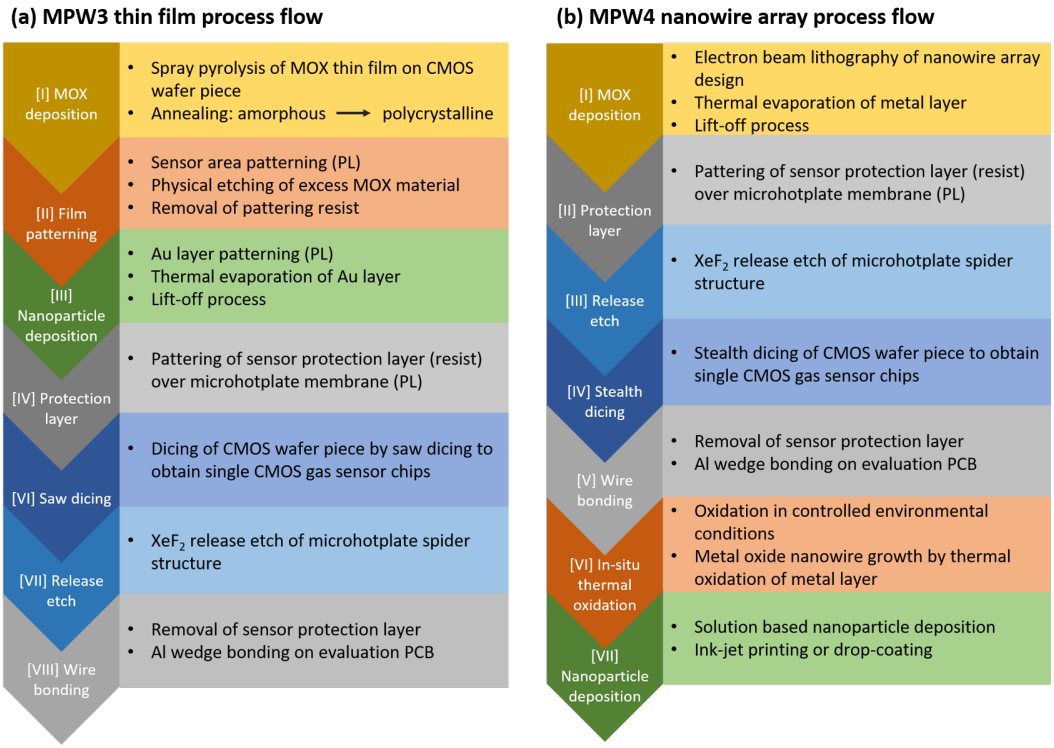

Figure 3.8.: Process flow of (a) thin film gas sensor fabrication on MPW3 CMOS chip and (b) nanowire array gas sensor fabrication on MPW4 CMOS chip.

3.3. Gas measurement set-up

The evaluation of both gas sensor types, silicon based gas sensors and CMOS gas sensors, is done by a self-built gas measurement set-up. The gas measurement set-up (GMS) can be divided into two systems: the gas system and the electrical system. The gas system provides a specific gas atmosphere for gas sensor testing. The electrical system measures the resistance of the gas sensor, voltage of the thermocouple and provides the current for the heater. Both systems are combined by a python based program on a standard personal computer.

The gas system provides the capability to precisely adjust the concentration of two test gases in a relative humidity controlled background gas (see figure 3.9). For each of the two test gases a set of three mass flow controllers is applied to mix the precise concentration. As depicted in figure 3.9 the mass flow controllers of each set are marked with ”low”, ”mid” or ”high”. The range of each of those three MFCs is calibrated on a specific concentration range. Within this concentration range the precision of the MFC is high. The subdivision into three separate concentration ranges ensures the precise adjustment of a wide range of test gas concentrations.
The background gas, synthetic air consisting of nitrogen (80 %) and oxygen (20 %), is controlled by two MFCs. In figure 3.9 the two MFC of the background gas are marked with dry air and wet air. The dry air MFC supplies the gas system with pure synthetic air. The wet air MFC introduces humid air into the gas system by conducting a stream of synthetic air through a bottle filled with deionized water. By mixing the dry air and wet air concentrations the relative humidity level in the test chambers atmosphere can be set. The mixing of dry and wet air is controlled by a relative humidity sensor placed prior to the test chamber. Via a feedback loop the precise level is set.
The volume flowing through the test chamber, consisting of the contributions of the background gas and test gas 1 and 2, is set to a constant value of 1000 sccm (standard cubic centimetres).

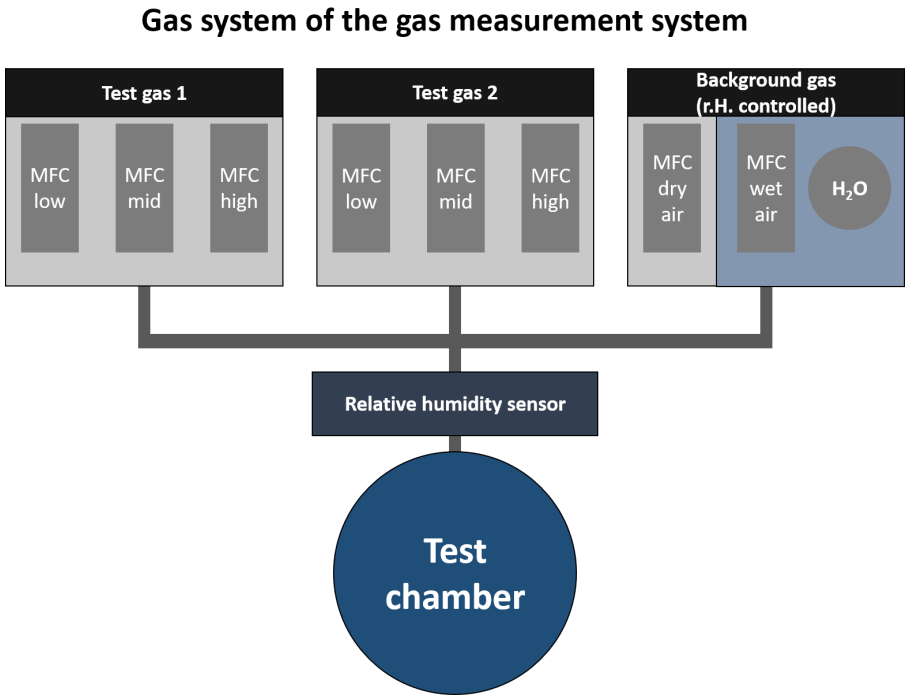

Figure 3.9.: Schematic representation of the gas system of the gas measurement set-up. The upper three blocks define the gas intake. Two test gases can be set individually. Each test gas block is made of three mass flow controller to provide precise test gas concentrations. The block background gas defines the overall adjustment of the relative humidity level by mixing dry and water enriched air. A relative humidity sensor positioned before the test chamber is used in a feedback loop configuration with the background gas to ensure precise relative humidity levels.

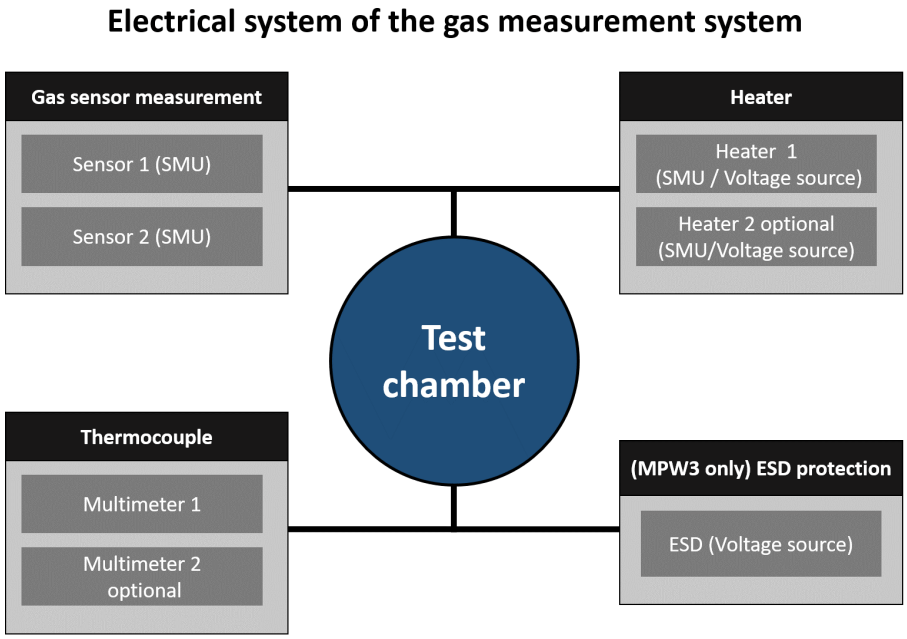

Figure 3.10.: Schematic representation of the electrical system of the gas measurement set-up. The four blocks surrounding the test chamber define different measurement devices needed to measure the gas sensors resistance, to apply voltage to the heater and to measure the heaters temperature via thermocouple. In the case of the MPW3 chip an additional device is needed to release the ESD protection.

The electrical system used for the gas sensor evaluation consists of multiple measurement devices. Since both types of sensors, silicon based gas sensors and CMOS gas sensors, can be evaluated in the GMS the configuration of measurement devices has to be adapted to each sensor type. In figure 3.10 a schematic representation of the electrical system is shown.
The measurement of the gas sensors resistance (silicon based gas sensors or CMOS gas sensors) is done via Keithley 2400 (Tektronix Inc.) source measure units (SMU). Depending on the number of evaluated gas sensors multiple SMUs are applied.
The devices used for heater operation of silicon based and CMOS gas sensors vary. In the case of silicon based gas sensors a voltage source from the company Thurlby Thandar Instruments of the model PL330P is used. In

the case of CMOS gas sensors a Keithley 2400 SMU is used. The voltage of the thermocouple is measured by a 34401A digital multimeter from Keysight technologies. This instrument is applicable for both sensor types. For CMOS gas sensors multiple thermocouples can be measured. Therefore, multiple digital multimeter are employed. In the special case of the MPW3 CMOS gas sensor an additional SMU (Keithley 2400) is needed to disable the ESD protection.

Part IV.

Results

4. Thin film analysis

4.1. SnO_2

Tin dioxide is the standard material in our group for thin film gas sensor fabrication. Therefore, the tin dioxide material has been thoroughly investigated by Mutinati [24] and Zima [191].
The first step of the thin film investigation is an optic inspection of the surface of the thin film. Figure 4.1 (a) shows a picture of a silicon substrate coated with a tin dioxide thin film. The topmost layer of the silicon substrate (dimensions: 20 x 20 mm) is a thermal oxide (SiO_2) layer of around 300 nm. The tin dioxide layer is deposited onto the substrate by spray pyrolysis. A first glance of the sample reveals a rather homogeneous deposition. Although this seems to be quite subjective a follow up atomic force microscope (AFM) and x-ray reflectivity (XRR) measurement supports this initial assumption. The AFM and XRR investigation are done for SnO_2 thin film that are deposited on a silicon substrate, of the same size as described above, but without a thermal oxide layer. Only a native oxide layer formed at ambient conditions is present. Figure 4.1 (b) displays an AFM measurement of a SnO_2 thin film on a silicon substrate. The roughness of this film is around 0.45 nm. The XRR measurement is shown in figure 4.2. A silicon substrate with native oxide is used as a base material upon which the SnO_2 thin film is deposited. The XRR measurement shows that the investigated film has a thickness of 43.3 nm and shows a surface roughness of 0.56 nm. The difference between the AFM and the XRR measurement concerning the surface roughness is attributed to the different area which is been investigated. Despite that the surface roughness measurement of AFM and XRR are in good agreement.

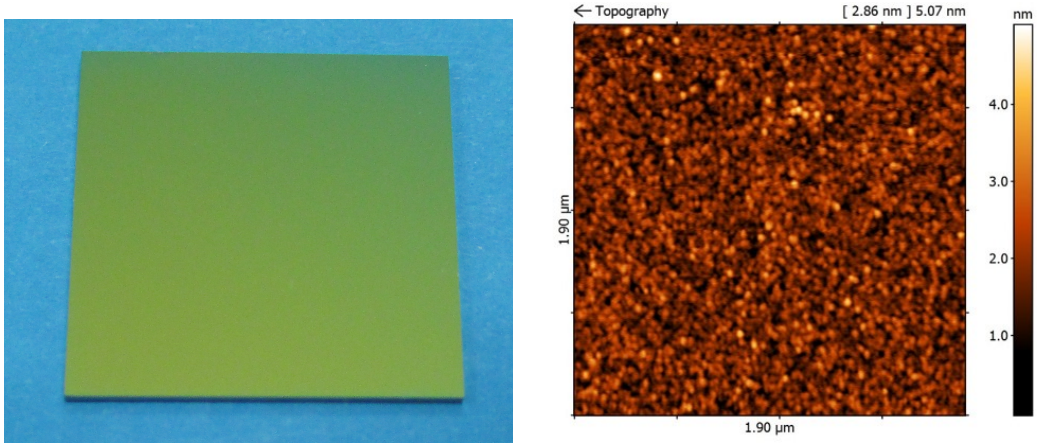

(a) Camera picture of a 2 x 2 cm SiO_2 wafer piece coated with a SnO_2 thin film.

(b) AFM measurement of a SnO_2 thin film (area 1.9 x 1.9 μm).

Figure 4.1.: Camera picture and AFM measurement of a SnO_2 thin film sample.

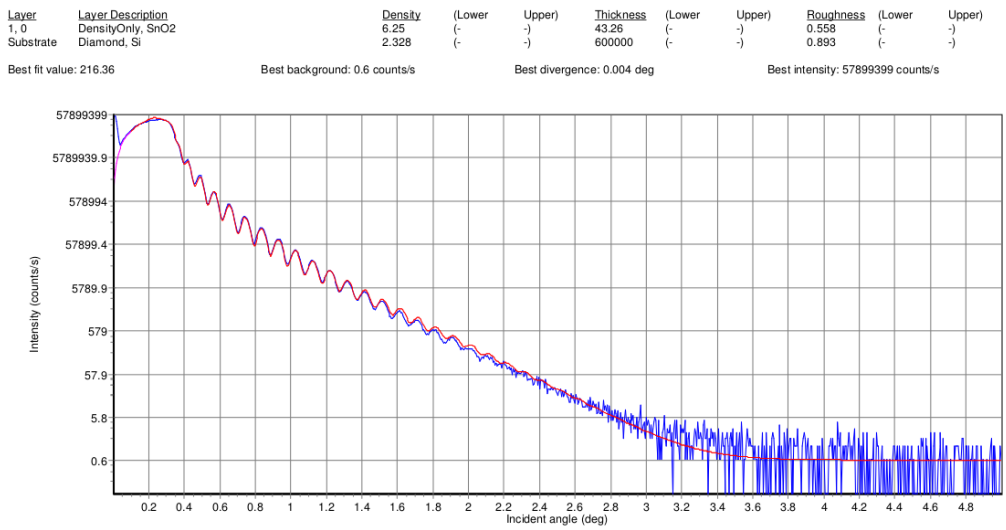

Figure 4.2.: X-ray reflectivity measurement of a SnO_2 thin film.

The second step is the investigation of the structure of the thin film. This is done via a transmission electron microscopy (TEM) investigation at the

Austrian Centre for Electron Microscopy and Nanoanalysis (FELMI). In figure 4.3 (a) a TEM lamella of a MPW3 CMOS integrated SnO_2 thin film is shown. The surface layer of the MPW3 CMOS chip at the microhotplate has a higher roughness, which is a result of an etching step. The tin dioxide thin film adopts the roughness of the substrate. Figure 4.3 (b) shows a TEM picture of a SnO_2 thin film on a silicon substrate after being annealed. This picture depicts numerous areas with different crystalline orientation, which confirms the polycrystalline structure of the SnO_2 thin film.

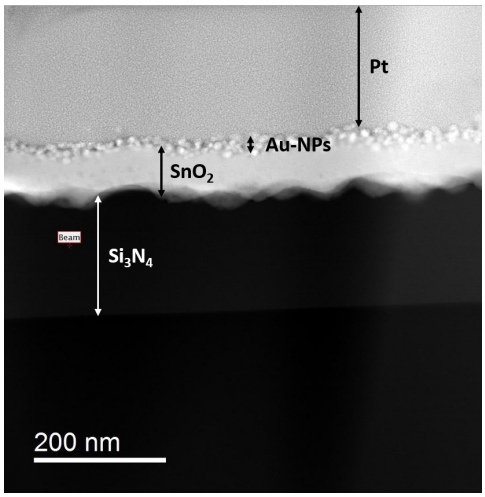

(a) Cross-section of a MPW3 CMOS chip SnO_2 thin film. Layers from bottom to top: Si_3N_4 is the top layer of the MPW3, SnO_2 layer deposited by spray pyrolysis, Au-NPs deposited by thermal evaporation and consecutive annealing for nanoparticle formation, Pt deposited before the focused ion beam process for the TEM lamella preparation.

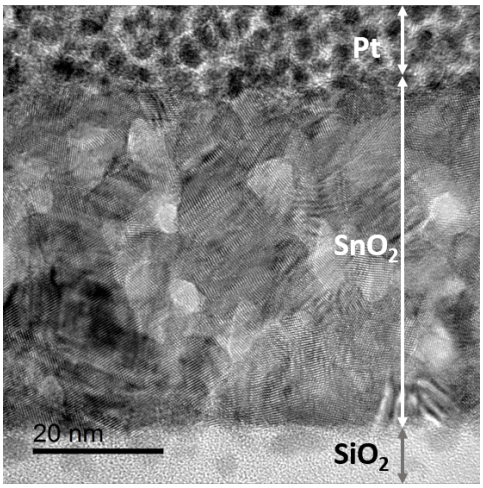

(b) SnO_2 thin film prepared on a silicon substrate after annealing. Layers from bottom to top: thermally oxidized SiO_2 is the top layer of the silicon subrate, SnO_2 deposited by spray pyrolysis, Pt layer deposited before the focused ion beam process for the TEM lamella preparation. In the SnO_2 layer multiple crystallites can be seen indicating the polycrystalline structure of the layer.

Figure 4.3.: Transmission electron microscope investigation of SnO_2 thin films on a CMOS microhotplate (left) and on a silicon substrate (right).

4.2. CuO thin film (spraypyrolysis)

Thin films of cupric oxide (CuO) are fabricated by spray pyrolysis method. In section 2.1.3 three different precursor solutions based on the following copper salts are stated: copper chloride, copper acetate and copper nitrate. The goal of this experiments was the deposition of a homogenous thin film of CuO for gas sensor fabrication. Although, the deposition of solutions based on all three salts was feasible, only the solution based on copper nitrate resulted in an adherent thin film. In these initial experiments the application of copper chloride and copper acetate based solutions lead to films with bad adhesion. As a result of time constrains copper nitrate was chosen to be further investigated for gas sensor fabrication.
Since only solutions based on copper nitrate lead to suitable thin films, the main emphasis is set on these kind of precursor solutions. The precise precursor details for copper nitrate solutions can be found in section 2.1.3. Figure 4.4 shows a picture of an as-deposited cupric oxide thin film. In contrast to tin dioxide thin films presented above, the CuO layer shows a colour gradient from left to the right. This is an indicator of a non homogeneous deposition. Furthermore, dot like structures are present at the surface of the layer. These dots are bulky pillars with diameters and heights in the micron range. In between these pillars a thin film is found. Figure 4.5 shows a SEM picture of a cupric oxide thin film at 300x magnification. Herein, these bulky pillars can be seen, randomly distributed on the surface of the CuO layer. Further magnification between the pillars shows the surface structure of the thin film. Figure 4.6 shows a SEM picture at 3000x magnification. This picture shows the granular structure of the cupric oxide surface undisturbed by the pillar structures.

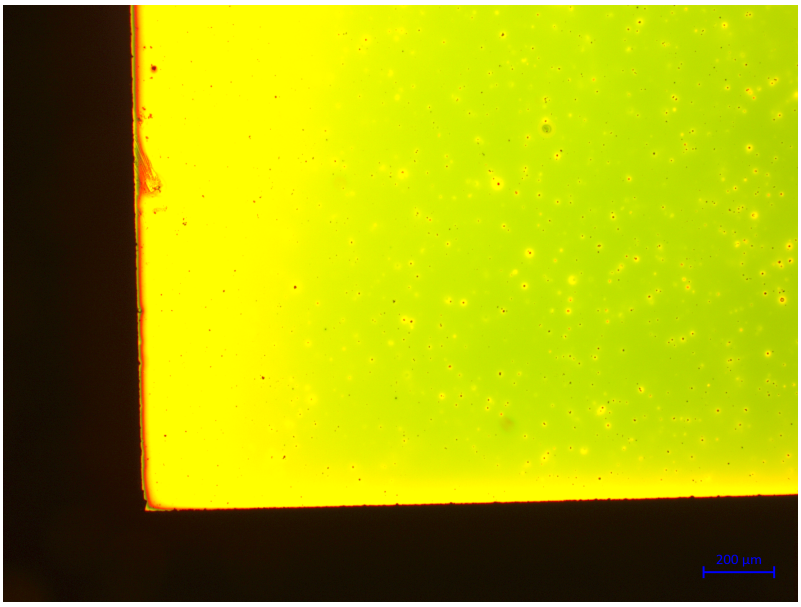

Figure 4.4.: Microscope picture of a silicon substrate coated with a cupric oxide thin film. The CuO thin film was deposited at a deposition temperature of 400°C.

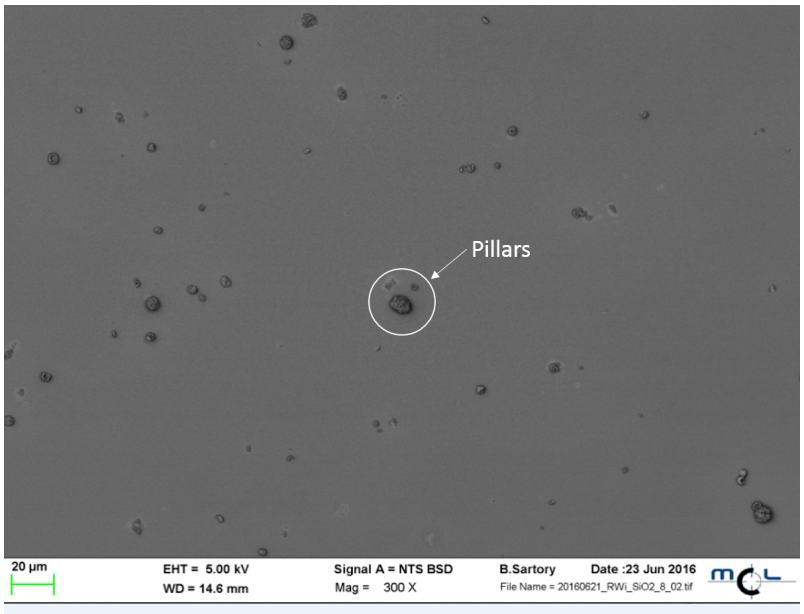

Figure 4.5.: Scanning electron microscope picture of a cupric oxide thin film at 300 x magnification. A single pillar structure (height, width: several μm) is marked with a white circle.

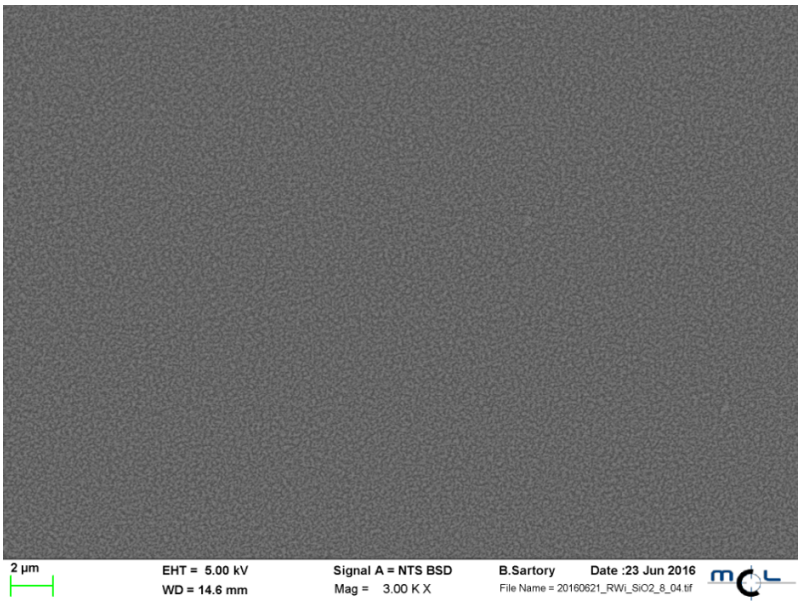

Figure 4.6.: Scanning electron microscope picture of a cupric oxide thin film at 3000x magnification.

An EDX (energy-dispersive x-ray spectroscopy) provides an elemental analysis of the cupric oxide film. In figure 4.7 the EDX spectrum of the thin film is shown. As can be expected copper as well as oxygen is found. The origin of nitrogen can be attributed to the copper nitrate precursor solution. The appearance of nitrogen in the EDX spectrum hints an incomplete chemical conversion. Furthermore, this incomplete conversion explains the size of the oxygen peak as well. Since copper nitrate salt consists of oxygen a part of this peak can be attributed to remaining copper salt in the layer. The silicon peak as well as part of the oxygen peak can be attributed to the silicon substrate, since it consists of silicon and silicon dioxide (top layer). The gold peak originates from a sputtering process done before imaging. A thin layer of gold reduces the charging of the investigated surface. The carbon peak probably originates from contaminations during sample preparation.

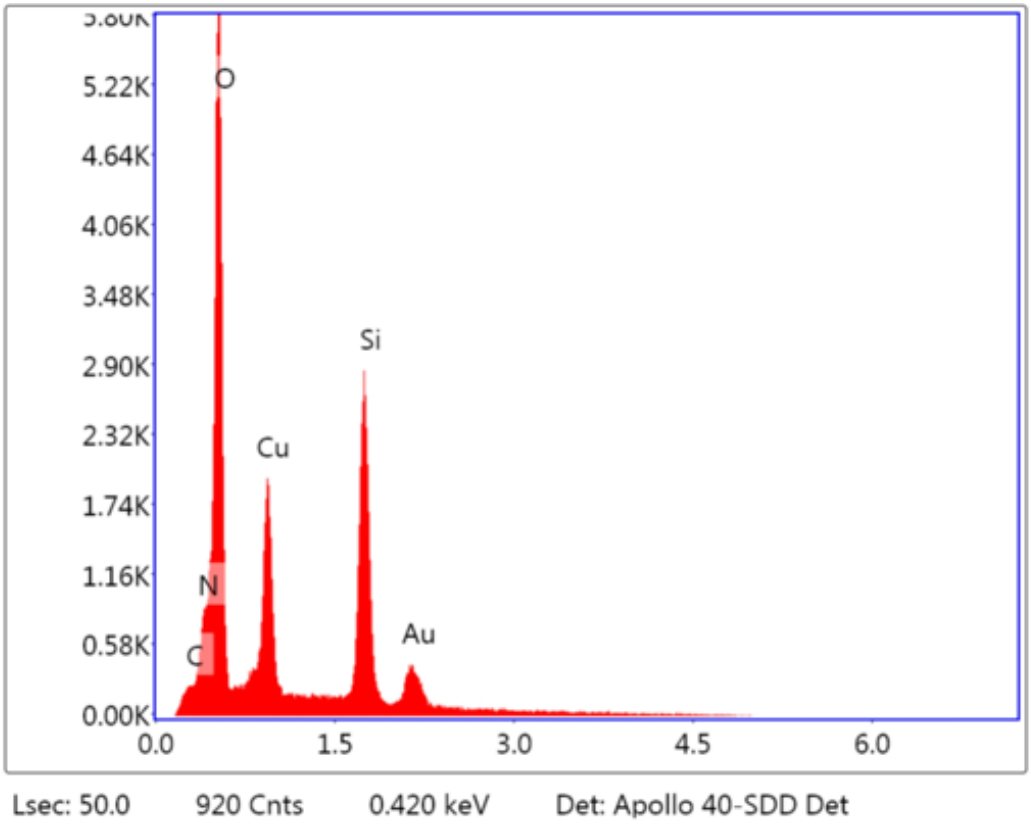

Figure 4.7.: Energy-dispersive x-ray spectrum of the cupric oxide thin film fabricated at a deposition temperature of 400°C.

The EDX measurement above only confirms the presence of copper and oxygen. There is still a possibility that the deposited layer is made of cuprite oxide or a mixture of cuprite and cupric oxide. In figure 4.8, a x-ray diffraction (XRD) pattern of the proposed CuO layer (black pattern) is shown. The blue pattern shows a reference pattern of cupric oxide taken from the Inorganic Crystal Structure Database (ICSD) with the reference code 01-080-0076. The reference pattern shows the Miller indices referencing the crystallographic lattice planes found within the cupric oxide reference sample. The peaks of the measured thin film match the reference pattern. Additionally, the measured XRD pattern shows two peaks of the lattice plane (400) of silicon. This can be attributed to the silicon substrate onto

which the cupric oxide is deposited.

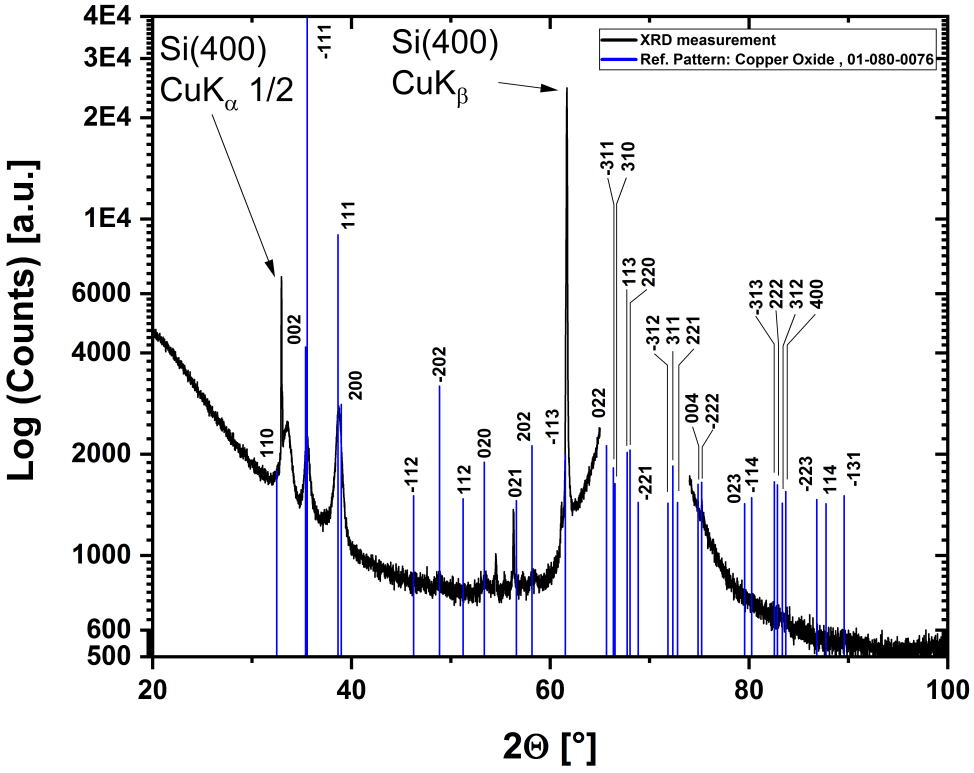

Figure 4.8.: X-ray diffraction pattern of a CuO thin film prepared by spray pyrolysis. The black pattern shows the measured pattern. The blue pattern is the reference pattern taken from the Inorganic Crystal Structure Database (ICSD) of cupric oxide with the reference code 010-080-0076. The reference pattern is marked with the Miller indices of crystallographic lattice planes found for cupric oxide. The two silicon peaks from the lattice plane (400) are attributed to the silicon substrate.

Figure 4.9 (a) shows the surface of a CuO layer deposited by spray pyrolysis at a deposition temperature of 400°C. The inset in figure 4.9 (a) depicts a magnified view of a single pillar structure. It can be seen that this structure

is hollow. The EDX spectrum (fig.4.9 (b)), recorded from the area marked by a red dot, indicates that the pillars themselves are made of cupric oxide (CuO).

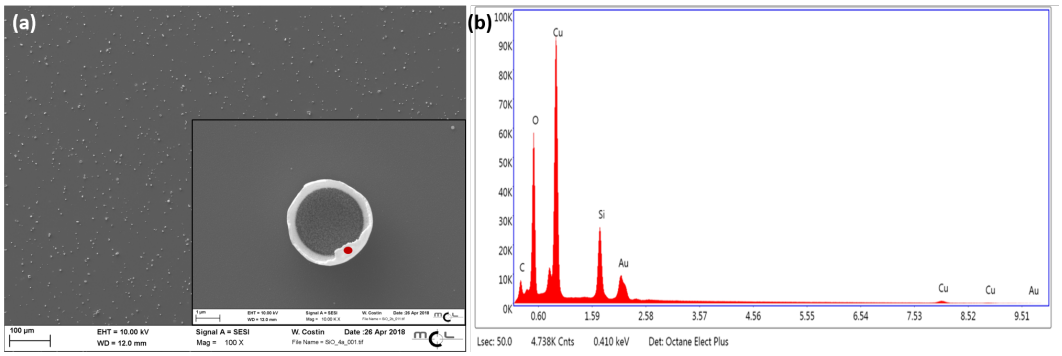

Figure 4.9.: (a) Magnified CuO pillar structure (inset) on CuO thin films deposited by spray pyrolysis. (b) EDX spectrum of the area marked by the red dot on the pillar structure.

A further investigation of the cupric oxide layer is done by AFM measurement. The samples investigated above are fabricated at a deposition temperature of 400°C. In figure 4.10 and 4.11 AFM measurements of two CuO layers fabricated at 300°C and 400°C respectively are shown. The surface roughness of the CuO layer in figure 4.10 is 6.5 nm, whereas the surface roughness of the CuO layer in figure 4.11 is 3 nm. Therefore, it can be assumed that a higher deposition temperature leads to a smoother surface. The formation of the bulky pillar structures can not be reduced by increasing the deposition temperatures. At both temperatures these structures can be observed.

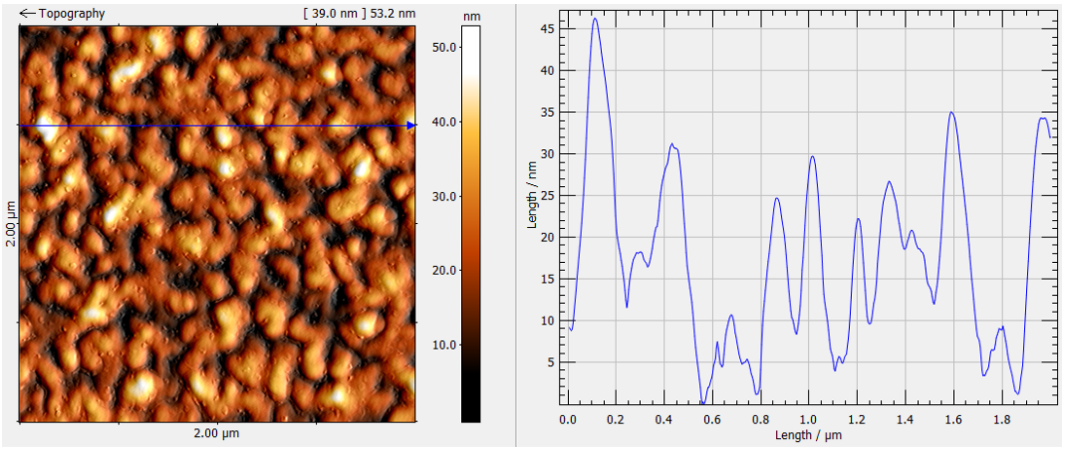

Figure 4.10.: AFM measurement of a cupric oxide thin film deposited by spray pyrolysis at a deposition temperature of 300°C. (Right) Topography of an area of 2 x 2 μm. (Left) Linescan over a length of 2 μm marked by blue arrow in picture.

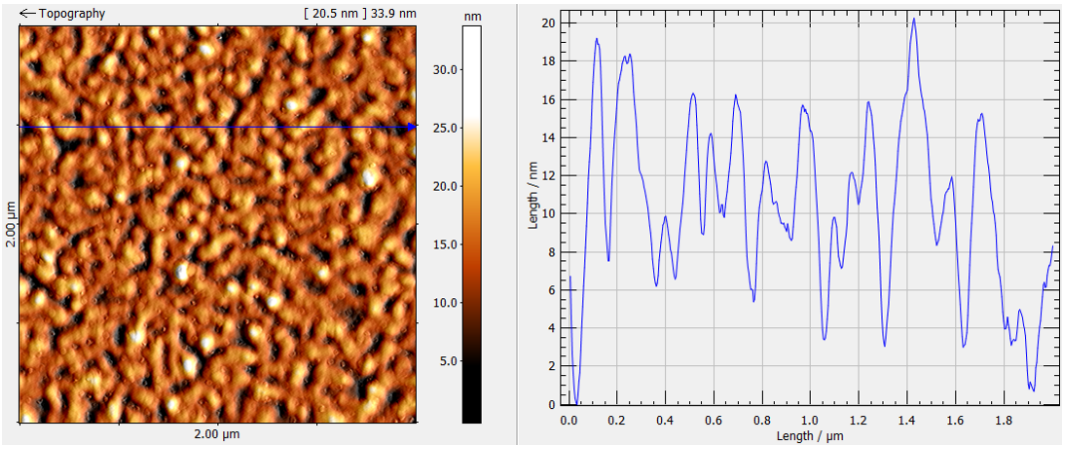

Figure 4.11.: AFM measurement of a cupric oxide thin film deposited by spray pyrolysis at a deposition temperature of 400°C.(Right) Topography of an area of 2 x 2 μm. (Left) Linescan over a length of 2 μm marked by blue arrow in picture.

The thickness of the deposited CuO layers at the areas between the pillar structures is determined by a focussed ion beam (FIB) cut and SEM investigations. Figure 4.12 (a) shows a SEM picture of a FIB cut of a silicon

substrate with a thermally oxidized silicon layer (thickness: ∼300 nm, according to manufacturer) coated with a CuO layer. Prior to the FIB cut a layer of platinum is deposited directly at a specific area on top of the CuO by in-situ Pt deposition to obtain a smoother cutting edge. During the FIB cut a trench is cut into the sample. Hereby, the material is removed layer by layer within an previous defined area. The depicted edge in figure 4.12 (a) shows the layers of the sample. The layer stack starting at the top is as follows: platinum, cupric oxide, silicon dioxide and silicon. The layout of the layer stack wasn't investigated and is therefore an assumption based on the manufacturers informations. By means of a virtual measurement tool the thickness of silicon dioxide layer and cupric oxide layer was measured. Figure 4.12 (b) shows a magnified SEM picture of the same layer system. The higher magnification is used to measure the layer thickness of the CuO layer more precisely and is determined to be 83.4 nm. The layer thickness of silicon dioxide is determined to be 255 nm. Hereby, a deviation from the manufacturers information (∼300 nm) is seen. Since the layer thickness measurement is done with a virtual tool a certain error has to be assumed.

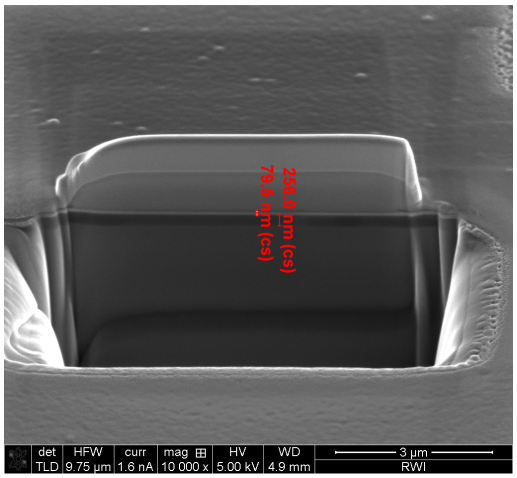

(a) Focussed ion beam trench of a CuO layer on a silicon substrate with thermally oxidized silicon oxide layer. Layer stack starting from the top: platinum, cupric oxide 79.5 nm, silicon dioxide 256 nm and silicon. The platinum layer is applied prior to the cutting process by an in-situ deposition method.

(b) Magnified layer system for thickness determination. The layer thicknesses measured by an image processing tool are: cupric oxide 83.4 nm and silicon dioxide 255 nm.

Figure 4.12.: Focussed ion beam cut of a cupric oxide layer deposited on silicon substrate with an silicon dioxide layer on top. SEM pictures of the layer system with additional layer thickness measurement of CuO and SiO_2 layers.

4.3. CuO thin film (thermal oxidation)

In a parallel development process thin films of CuO were fabricated by thermal oxidation of copper metal structures. These structures normally used to promote CuO nanowire arrays can be used to form continuous layers too. Therefore, the structures described in section 2.2 (copper nanowire arrays) are fabricated. The fabrication as stated in this section is done by EBL, thermal evaporation of copper and lift-off process. These metallic copper structures are deposited onto the silicon based gas sensor platform described in section 2.2. Onto this platform the copper structures are thermally oxidised in our gas measurement set-up (section 3.3). For the oxidation

process relative humidity within the gas measurement set-up is set to 50%. At an oxidation temperature of 400°C the copper structures are oxidised for 6 hours. After this oxidation period a continuous copper oxide film is formed. Figure 4.13 shows the oxidised copper structure. The as formed oxide bridges the gaps between the previously separated structures. The vertical lines in the pictures hint the stripped copper structure prior to the oxidation. Before continuing the fabrication process the oxidation state of the copper oxide is determined by Raman spectroscopy. Figure 4.14 depicts the Raman spectrum of the copper oxide surface. In general copper can be oxidised to CuO (cupric oxide) or Cu_2O (cuprous oxide). In its primitive cell CuO incorporates four atoms, which result in 12 phonon modes. A factor group analysis results in the formula [237]:

$$\Gamma_{vibr} = A_g + 2B_g + 4A_u + 5B_{u'} \tag{4.1}$$

Herein, only three modes are Raman-active: A_g mode and two B_g modes. In the Raman spectrum (fig. 4.14) these three active modes are shown: A_g at 296 cm^{-1} and B_g at 346 cm^{-1} and 631 cm^{-1}. All three modes are linked to the vibration of the oxygen atoms: the A_g mode describes the vibration of the oxygen atoms in direction of the b-axis of the unit cell, the two B_g modes describe the vibration of the oxygen atoms perpendicular to the b-axis [237]. These Raman modes shown in figure 4.14 indicate the copper oxide species CuO. No other modes matching Cu_2O can be found, thereby excluding the presents of Cu_2O.

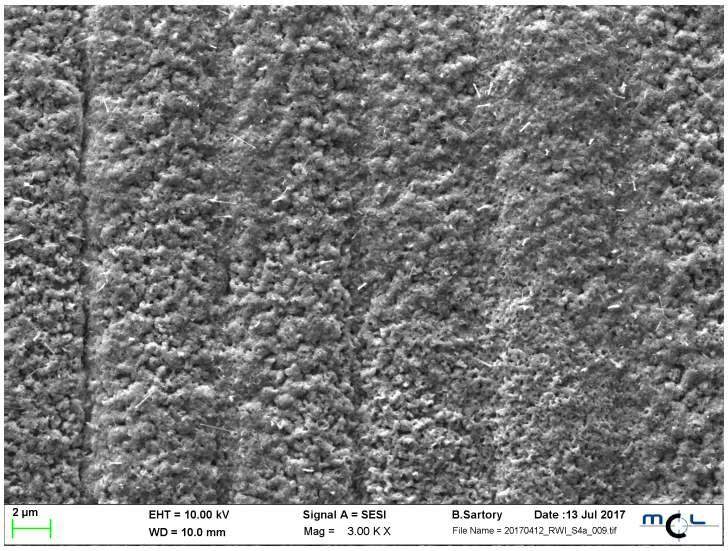

Figure 4.13.: SEM picture of the thermally oxidised copper structures. Oxidation temperature 400°C.

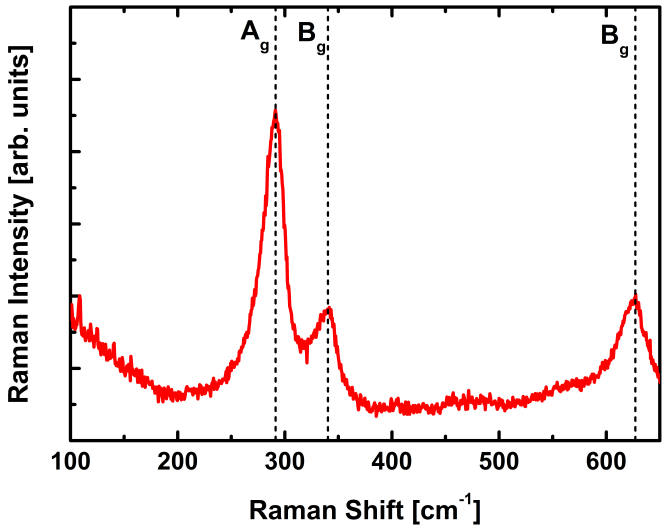

Figure 4.14.: Raman spectrum of the thermally oxidised copper structures forming a continuous copper oxide layer (see fig.4.13). The copper structures are oxidized at 400°C.

After the oxidation state of the CuO thin film is determined the gold nanoparticles functionalization is done according to the process flow described in chapter 3. The validation of the Au-NPs functionalization of the CuO surface is done by SEM investigation. In figure 4.15 the surface of the CuO thin film is shown decorated with Au-NPs. The insert shows a TEM image of a Au-NP. This TEM image has been done in a separate investigation to determine the size of a single Au-NP, which is claimed by the manufacturer to be 20 nm. The verification of the NPs on the CuO surface is done by energy dispersive x-ray (EDX) spectrography. In figure 4.16 an EDX map of the area shown in figure 4.15 is done. Hereby, an EDX spectrum is measured for each pixel of the map. The elemental information of each EDX spectrum is split into single EDX maps. Thereby, the spatial distribution of each containing element can be shown. In figure 4.16 four different elements can be seen: (a) Au, (b) Cu, (c) O and (d) Si. Bright areas in each of these EDX maps show the occurrence of the corresponding element, whereas dark areas are areas with no occurrence of the element. The comparison of fig.4.15 and fig.4.16 (a) shows that the bright nanoparticles in fig.4.15 corresponds to Au distribution of the fig.4.16 (a). In fig.4.16 (b) and (c) dark areas at the same positions indicate no occurrence. Therefore, it can be assumed that these nanoparticles are made of gold. Supporting this assumption is fig.4.17, which depicts a EDX spectrum of a single nanoparticle. Hereby, an EDX spectrum is recorded from a spot, defined by the measurement tool, on the surface of a nanoparticle found on the surface of the CuO layer. The spectrum shows the occurrence of gold. Furthermore, silicon is found in the elemental map fig.4.16 (d) as a result of silicon diffusion during the annealing processes.

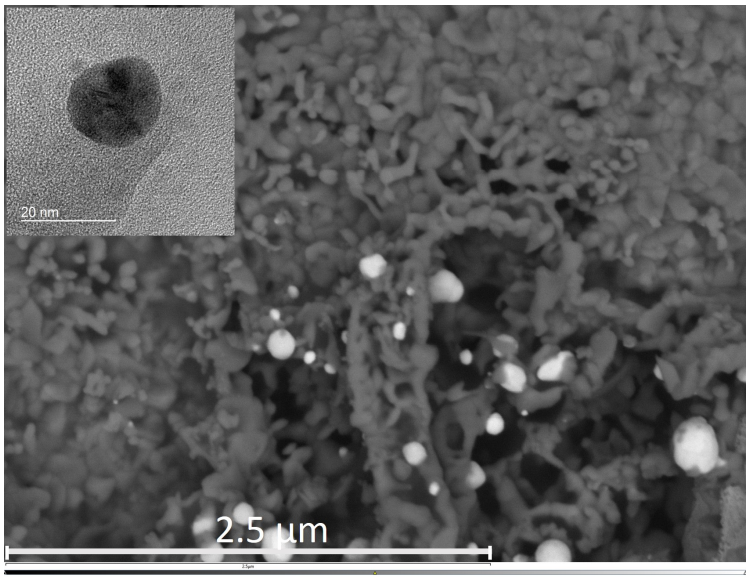

Figure 4.15.: SEM investigation of CuO surface decorated with gold nanoparticles. The insert shows a TEM image of a single gold nanoparticle.

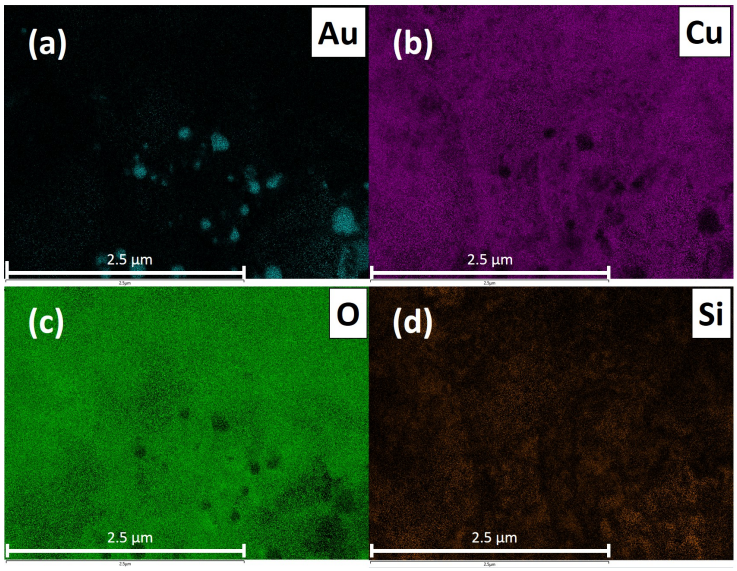

Figure 4.16.: Elemental mapping of the CuO surface decorated with Au nanopartilces (Area 4 μm x 4μm / E = 5 keV). (a) Au elemental map, (b) Cu elemental map, (C) O elemental map and (d) Si elemental map.

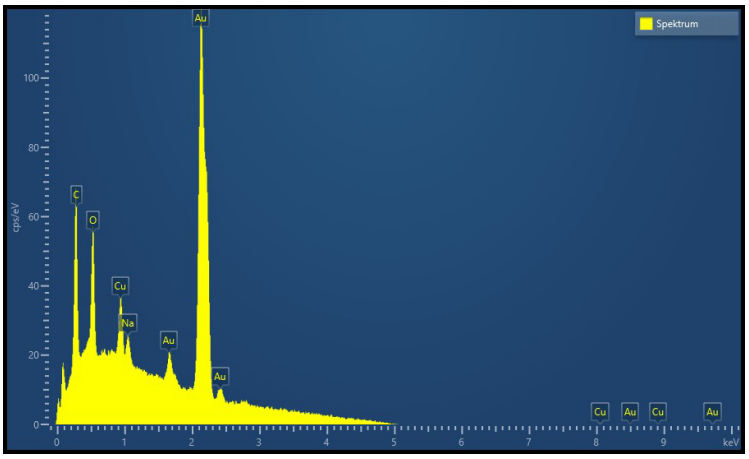

Figure 4.17.: Energy-dispersive x-ray spectrum of a single Au nanoparticle on the CuO surface recorded at 5 keV.

4.4. ZnO

In section 2.1.4 the basic spraying parameters for zinc oxide thin film deposition by spray pyrolysis are given. In contrast to the cupric oxide deposition only one zinc salt, zinc acetate, is investigated. As already mentioned in section 2.1.4 three spraying precursor solutions are tested for their usefulness: ethanol, water and a mixture of water and ethanol (ratio 1:3). Additionally, all solutions are mixed with hydrochloric acid to prevent hydrolysis. In figures 4.18 (ethanol), 4.19 (water) and 4.20 (water/ethanol mixture) zinc oxide films deposited onto a silicon substrate with thermally oxidised silicon oxide are shown at the same magnification (10x). The deposition temperature during spray pyrolysis is set to 400°C. The duration of the spraying process for these samples is set to 90 seconds. In the case of the spraying precursor solution zinc acetate in ethanol figure 4.18 shows various randomly distributed structures. No continuous layer is formed. The spraying precursor solution zinc acetate in water figure 4.19 shows a continuous layer. In comparison to figure 4.18 the number of randomly distributed structures is strongly reduced. Figure 4.20 shows a layer fabricated from the spraying precursor solution of zinc acetate in mixture of water and ethanol (1:3). A

continuous layer is formed. Despite still having structures on top of the layer this spraying solution seems to be most promising.

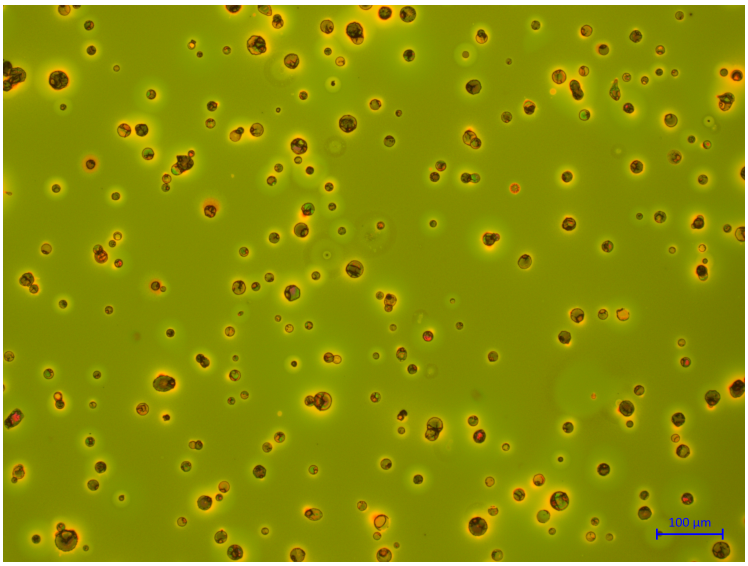

Figure 4.18.: Light microscopy picture of zinc oxide thin film deposited by spray pyrolysis at 400°C. Precursor solution: zinc acetate in ethanol.

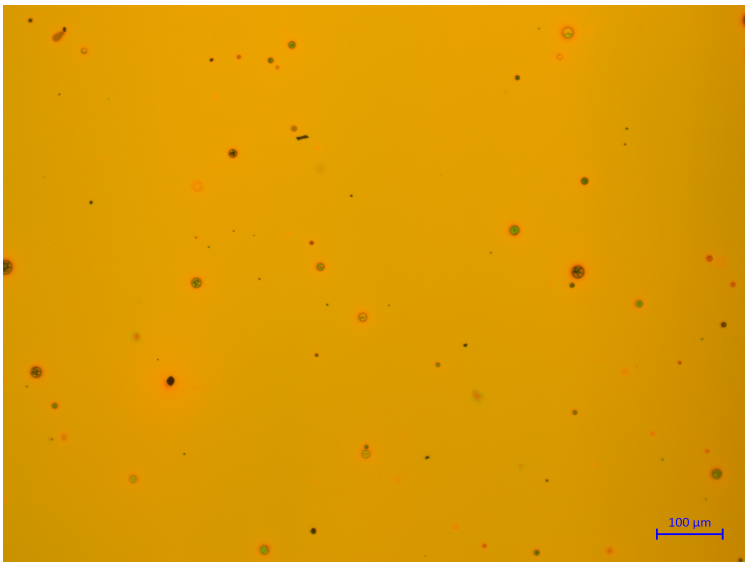

Figure 4.19.: Light microscopy picture of zinc oxide thin film deposited by spray pyrolysis at 400°C. Precursor solution: zinc acetate in water.

Figure 4.20.: Light microscopy picture of zinc oxide thin film deposited by spray pyrolysis at 400°C. Precursor solution: zinc acetate in mixture of water and ethanol (1:3)

A SEM investigation of the zinc layer deposited by the precursor solution based on the water and ethanol mixture is done. In figure 4.21 the zinc layer is depicted at 300x magnification. The structures previously observed in the light microscope can be distinguished mostly in three types. On the top edge of figure 4.21 a lighter circular structure can be seen, herein denoted dot. This structure, which has already been seen in the light microscope image shows a density variation. The structure below the dot structure is a pin hole. On the lower left two bulky structures can be seen, denoted mounds. These mounds are either fragments of the layer or structures emerged from a locally inhomogeneous growth process. In figure 4.22 the fine structure of the layer is shown. The zinc layer consists of close packed elongated islands.

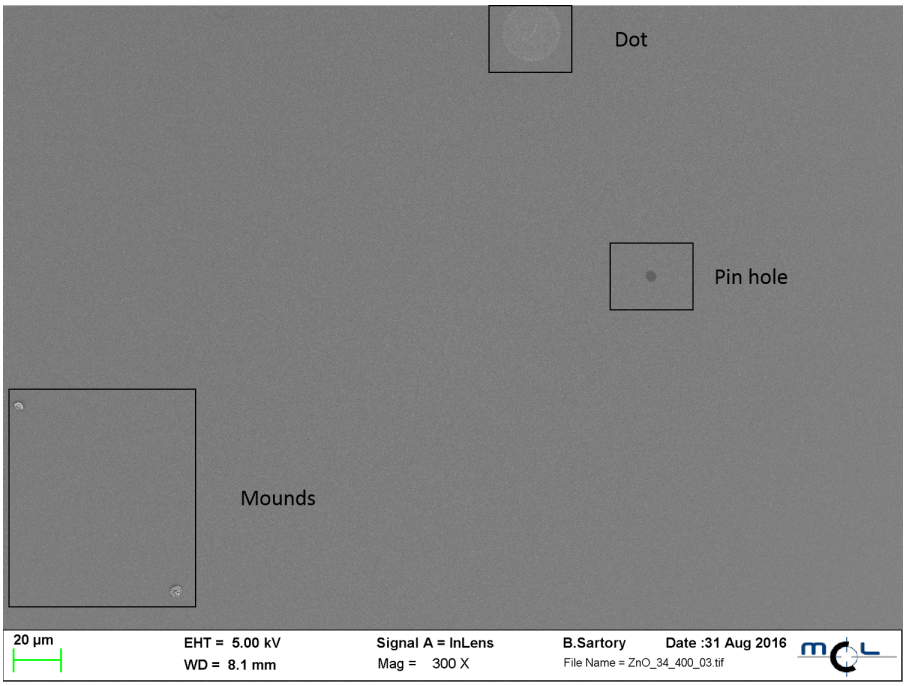

Figure 4.21.: SEM picture of a zinc oxide layer at a magnification of 300x. Precursor solution: zinc acetate in water/ethanol mixture. Deposition temperature: 400°C. Structures visible on picture: a dot like structure showing a density variation, a pin hole and mounds. The mounds are either fragments of the layer or areas of extended growth.

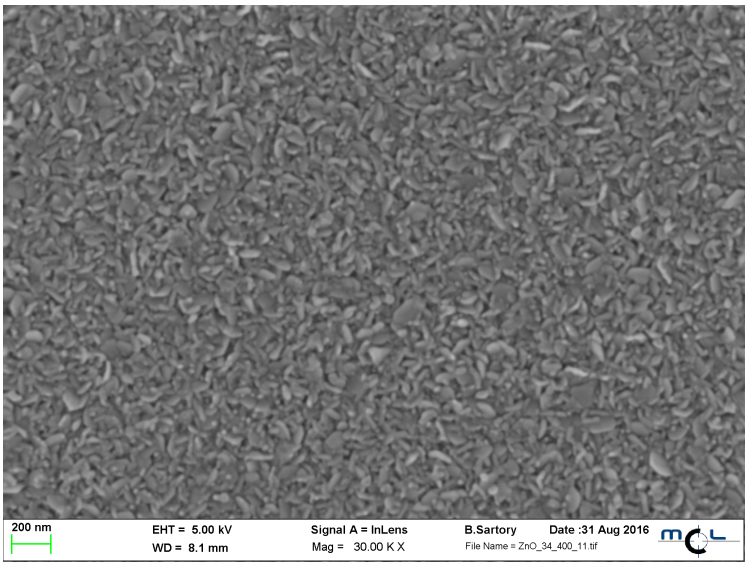

Figure 4.22.: SEM picture of a zinc oxide layer at a magnification of 30000x. Precursor solution: zinc acetate in water/ethanol mixture. Deposition temperature: 400°C. The fine structure of the layer consists close packed elongated islands.

The composition of the layer is investigated by EDX measurement. Figure 4.23 shows the EDX spectrum of the zinc oxide layer. Four elements are found: zinc, oxygen, silicon and gold. Since a deposition of zinc oxide is the goal of the deposition zinc and oxygen are expectable. Silicon is being used as the substrate for the zinc oxide layer. The gold peaks are a result of the sputter thin gold layer, which is applied to reduce charging effects during imaging. Since no other material is found the conversion of the precursor solution seems to be complete.
In figure 4.24 the topography of the zinc oxide layer is measured. The surface roughness of the zinc oxide layer investigated here is 3.7 nm.

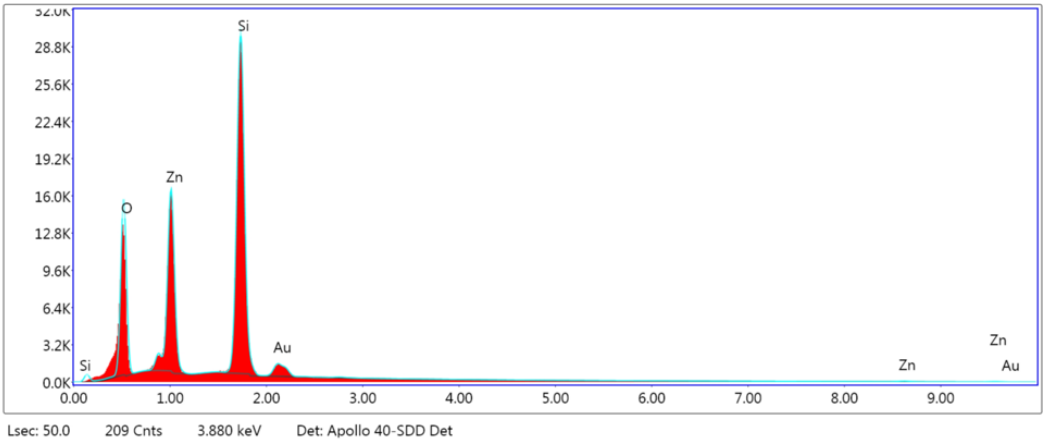

Figure 4.23.: Energy-dispersive x-ray spectrum of the zinc oxide thin film on a silicon / silicon dioxide substrate (top layer, thickness: 300 nm). Layer composition: zinc, oxygen and silicon.

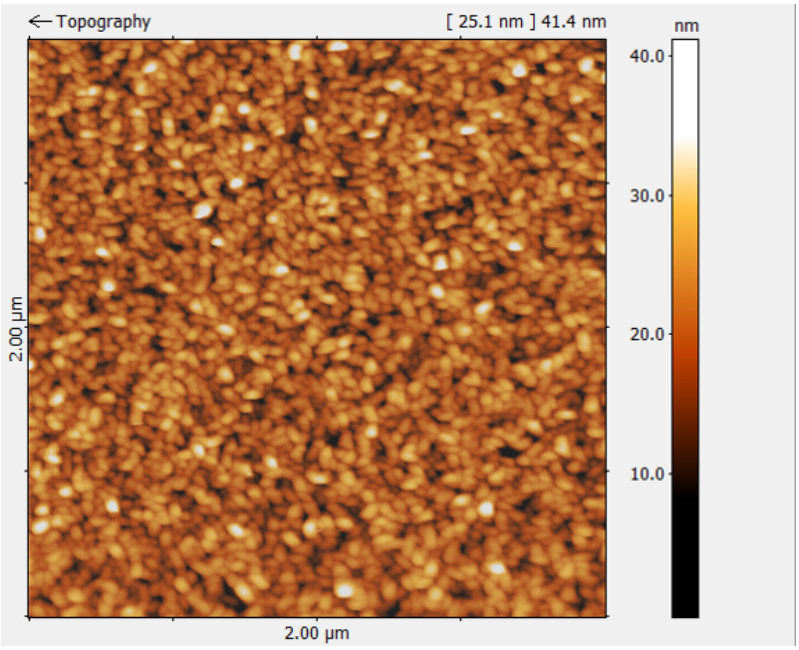

Figure 4.24.: AFM measurement of a zinc oxide thin film deposited by spray pyrolysis at 400°C. Topography of an area of 2 μm x 2 μm.

5. Gas sensor device characterization

5.1. Measurement routine

All gas sensors are evaluated for their sensitivity towards a certain target gas by following a predefined measurement routine. This routine includes multiple operation temperatures and multiple relative humidity levels. A default measurement routine is shown in figure 5.1. In part (I) of figure 5.1 the change of the operation temperature over time is shown. The operation temperature of a gas sensor is dependent on the gas sensitive material. To find the optimal operation temperature three previously selected temperature levels are chosen. These levels are determined a by single gas pulse test at various temperatures. Since the MOX sensors evaluated in this work should be integrated onto a CMOS platform the highest operation temperature cannot supersede 400°C. The dependence of the gas sensor towards humidity is evaluated by applying three relative humidity levels (25 %, 50 % and 75 %) at each operation temperature (fig. 5.1 (II)). The gas sensors sensitivity towards a target gas is tested by applying four different gas concentrations. Each gas concentration is applied as a gas pulse. These gas concentrations are adjusted according to the target gas (fig. 5.1 (III)). The number of gas pulses applied at each temperature and relative humidity level sums up to 36. This measurement routine ensures an accurate evaluation of the gas sensors gas sensing capabilities.

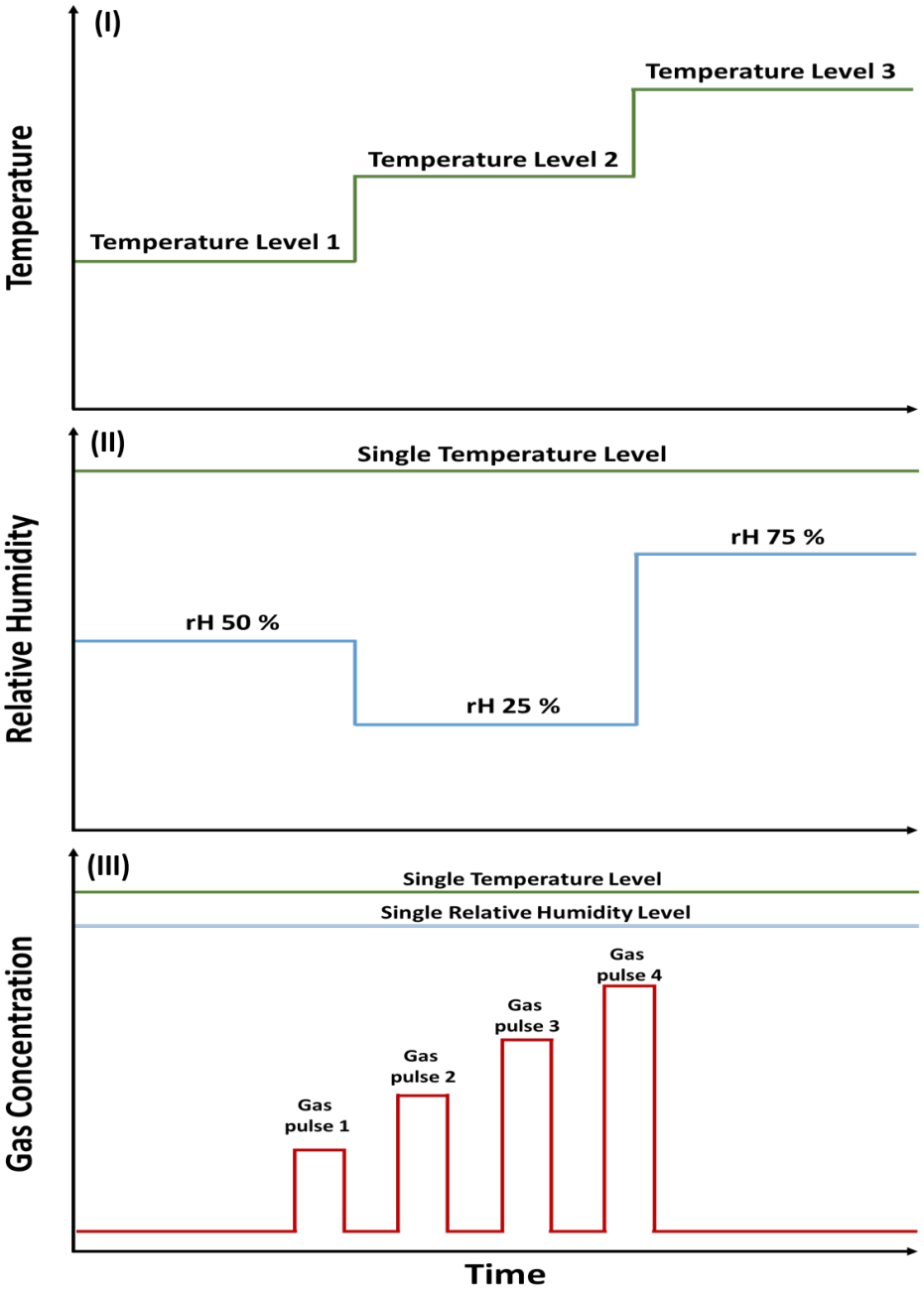

Figure 5.1.: Measurement routine for gas sensor evaluation. (I) Three different operation temperature levels are applied. At each operation temperature (II) three relative humidity (rH) levels are set and at each rH level (III) four different gas concentrations are applied.

5.2. Standard Gas Sensors

5.2.1. SB: CuO Measurements

The CuO thin film gas sensor fabricated as described in 4.3 (process parameters: tab.2.7) is evaluated for its sensitivity towards carbon dioxide (CO_2) and carbon monoxide (CO). The measurement sequence is done accordingly to previous section 5.1. The operation temperatures used for the evaluation are chosen to be 300°C, 350°C and 400°C. The relative humidity levels are 25%, 50% and 75%. The applied gas concentrations depend on the evaluated test gas. This section is based on the paper [238].

CO_2 measurements

In the first step the CuO thin films are evaluated for their sensitivity towards CO_2 without an Au-NPs functionalization. The gas pulse concentrations chosen for all CO_2 measurements are as follows: 250 ppm, 500 ppm, 1000 ppm, 1500 ppm and 2000 ppm. These CO_2 gas concentrations are chosen to match indoor air CO_2 concentrations. Figure 5.2 shows the resistance of the CuO thin film gas sensor with (red) and without (black) Au-NPs functionalization in dependence of the CO_2 concentrations and relative humidity levels. The operation temperature used in this measurement is 300°C, which will be shown is the optimal operation temperature for this gas sensor. Figure 5.2 shows that the base resistance of the CuO thin film drops by a factor of 2 after the Au-NPs functionalization. Furthermore, in its pristine form the CuO gas sensor shows a rather low sensitivity towards CO_2 with a maximum of around 28% for the highest CO_2 concentration of 2000 ppm. In direct comparison the Au-NPs functionalized CuO gas sensor shows a 13 times higher sensitivity towards the same CO_2 concentrations resulting in a sensitivity value of 365%.

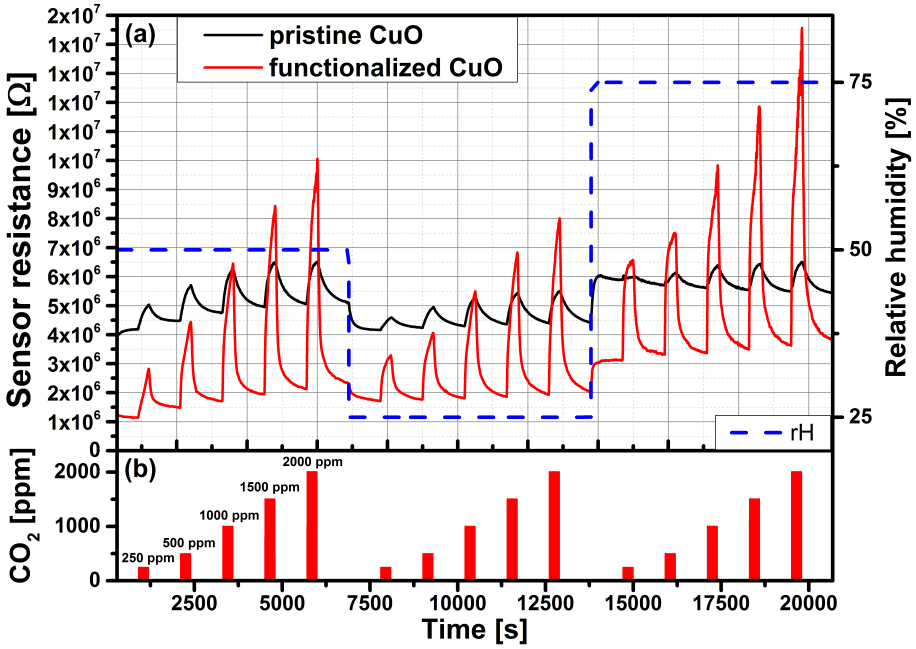

Figure 5.2.: (a) CO_2 measurements of pristine and Au-NPs functionalized CuO thin film gas sensors at an operation temperature of 300°C and rH levels of 25%, 50% and 75%. (b) CO_2 gas concentrations: 250 ppm, 500 ppm, 100 ppm, 1500 ppm and 2000 ppm.

The process to find the optimal operation temperature of the CuO gas sensor for CO_2 measurement is shown in figures 5.3 and 5.4. Both figures show the normalized sensitivities of the gas sensor towards the highest CO_2 concentration (2000 ppm) at each operation temperature (300°C, 350°C, 400°C) and each relative humidity level (25%, 50%, 75%). The sensitivity is calculated according to equation 1.4.
Figure 5.3 (b) depicts the CO_2 measurement of the pristine CuO thin film gas sensor. Herein, the response to the sensor towards a single CO_2 gas concentration of 2000 ppm is shown. All three operation temperatures of the gas sensor are shown at constant relative humidity levels of (a) 25%, (b) 50% and (c) 75%. The CO_2 gas pulse is shown in figure 5.3 (d). Figure 5.3 shows the maximum sensitivity of the pristine CuO gas sensor at 32%. The operation temperature is at 350°C and a relative humidity level of 50%.

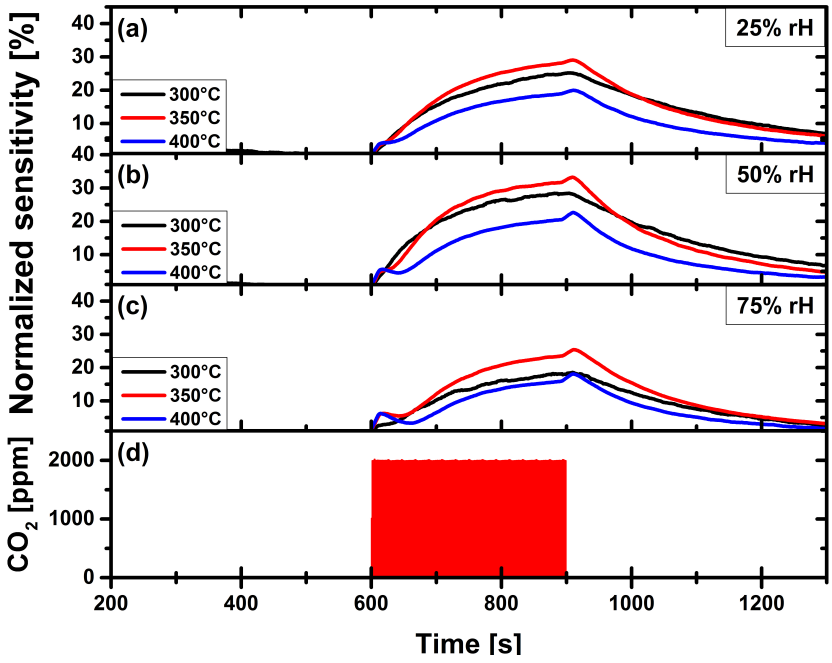

Figure 5.3.: CO_2 measurement of pristine CuO thin film gas sensor at operation temperatures of 300°C, 350°C and 400°C and relative humidity levels of: (a) 25% (b) 50% (c) 75%. (d) CO_2 gas pulse with a concentration of 2000 ppm.

Figure 5.4 depicts the sensitivities of the Au-NPs functionalized CuO gas sensor. The direct comparison of figure 5.3 and 5.4 shows that the sensitivity scale in the case of the Au-NPs functionalized sensor is up-scaled by a factor of 10. The maximum sensitivity of the Au-NPs functionalized is drawn from figure 5.4 (b). At an operation temperature of 300°C and a relative humidity level of 50% the sensitivity reaches a value of 365%. The pristine and the Au-NPs functionalized CuO gas sensor differ in their optimal operation temperature. Therefore, at each of the sensors optimal operation temperature the Au-NPs functionalized CuO gas sensor is 11 time more sensitive than the pristine CuO gas sensor. An additional trend concerning the temperature dependence of the Au-NPs functionalized CuO gas sensor can be seen in figure 5.4. The higher the operation temperature the less sensitive the sensor gets towards the same CO_2 concentration. After reaching an operation temperature of 350°C the sensitivity drops strongly up to reaching 400°C.

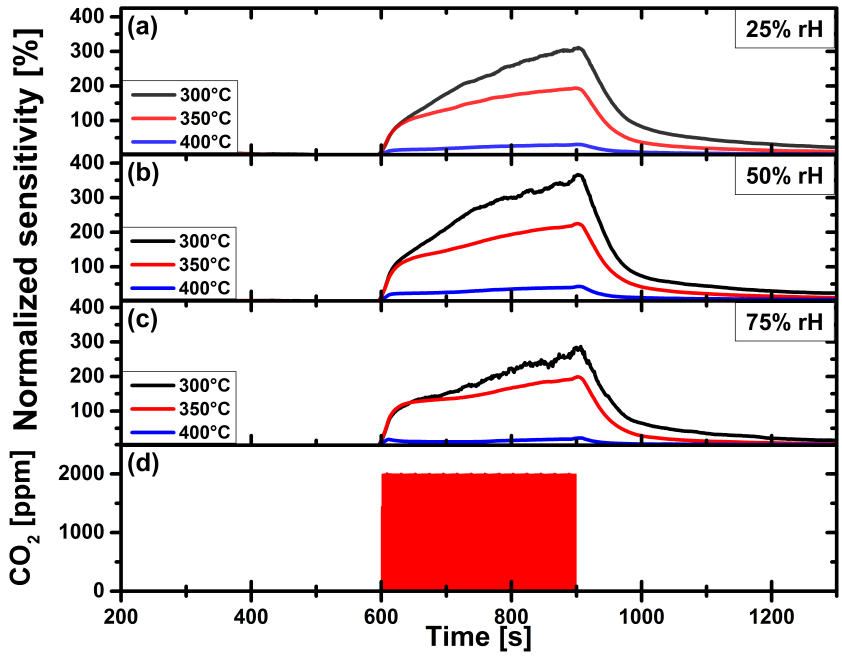

Figure 5.4.: CO_2 measurement of Au-NPs functionalized CuO thin film gas sensor at operation temperatures of 300°C, 350°C and 400°C and relative humidity levels of: (a) 25% (b) 50% (c) 75%. (d) CO_2 gas pulse with a concentration of 2000 ppm.

Figure 5.5 depicts the comparison of the sensitivities of both sensors, pristine and Au-NPs functionalized, depending on the three relative humidity levels at the same operation temperature of 300°C. The sensitivity of the Au-NPs functionalized sensor reaches its maximum of 365% at 50% rH. The sensitivity of the sensor decreases to its minimum of 283% at 75% rH. From these measurements the response time and recovery time are calculated in average over all three relative humidity levels according to the deliberations of section 1.2.1. The response time for the Au-NPs functionalized gas sensor is 4.3 min, whereas the recovery time is 4.4 min. In case of the pristine CuO gas sensor the maximum in sensitivity 28% is reached at 50% rH. Again a drop in sensitivity to 18% at 75% is observed. The response time for the pristine gas sensor is 3.7 min, whereas the recovery time is 11.1 min. Both

sensors exhibit a slight dependence on the relative humidity level. However, the dependence is less pronounced in the case of the Au-NPs functionalized CuO gas sensor.

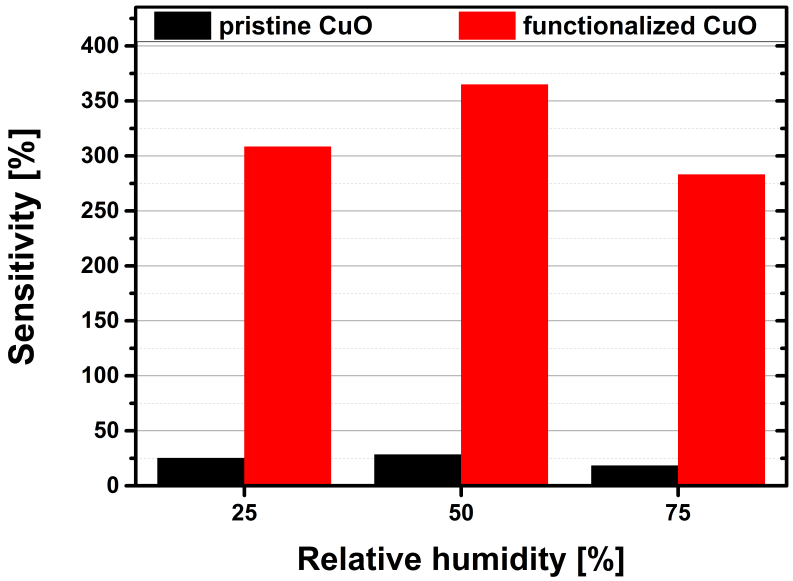

Figure 5.5.: Comparison of the pristine (black) and the Au-NPs functionalized (red) gas sensors sensitivities towards a CO_2 concentration of 2000 ppm at relative humidity levels of 25%, 50% and 75% and an operation temperature of 300°C.

CO measurements

Although the main objective for the development of this gas sensor is the measurement of CO_2 the cross selectivity of the sensor is an important issue, which has to be evaluated. Since the application of this CO_2 gas sensor is indoor air quality monitoring the determination of carbon monoxide (CO) cross selectivity is of highest importance. Figure 5.6 shows the resistance of the Au-NPs functionalized CuO gas sensor over time upon exposure to four CO concentrations at three relative humidity levels. The comparison of the gas sensors sensitivities towards CO_2 and CO are done in figure 5.7. Herein,

the gas sensors' sensitivities towards the highest concentrations of CO_2 (2000 ppm) and of CO (200 ppm) are compared. Additionally, the sensitivities are presented depending on three relative humidity levels (25%, 50%, 75%). Considering cross selectivity the CO measurements are conducted at the same operation temperature as is the optimal operation temperature for CO_2 measurements, hence 300°C. From figure 5.5 the highest sensitivity for CO is 86% at 50% rH. Similar to the CO_2 case the sensitivity decreases to 56% at 75%.

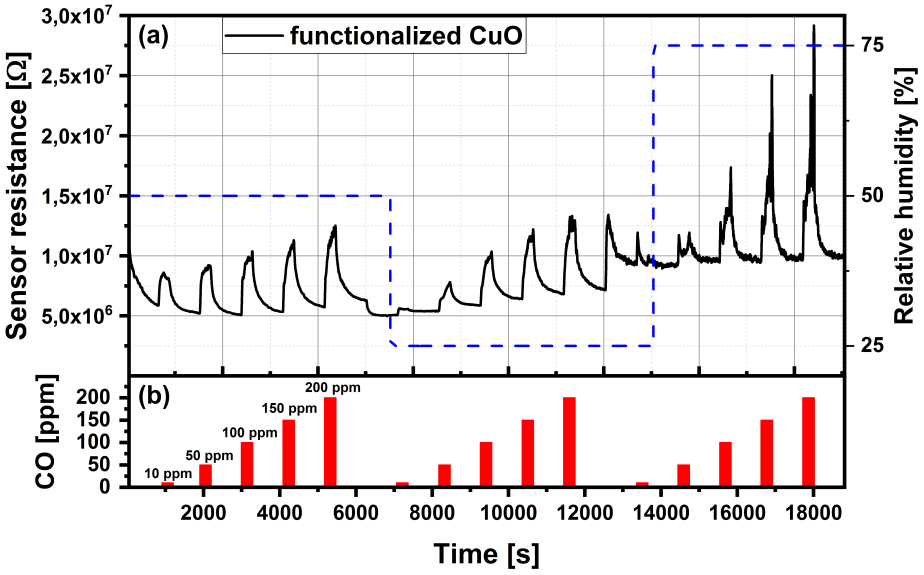

Figure 5.6.: (a) CO measurements of Au-NPs functionalized CuO thin film gas sensors at an operation temperature of 300°C and rH levels of 25%, 50% and 75%. (b) CO gas concentrations: 10 ppm, 50 ppm, 100 ppm, 150 ppm and 200 ppm.

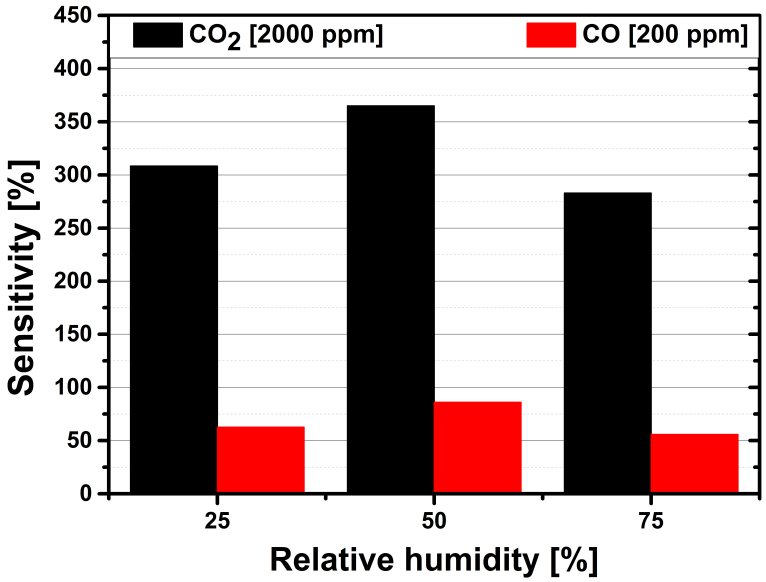

Figure 5.7.: Comparison of Au-NPs functionalized gas sensor towards the highest concentration of CO_2 (2000 ppm) and CO (200 ppm) at relative humidity levels of 25%, 50% and 75%.

5.2.2. SB: ZnO Measurements

The zinc oxide nanowire array was fabricated according to the process flow in chapter 3 (process parameters: tab.2.8). The nanowire array is evaluated for two different test gases: CO and HCMix (acetylene, ethane, ethene and propene). The HCMix is used as a reference for VOC testing. The sensor evaluation followed the measurement routine in section 5.1. The tested operation temperatures are 300°C, 325°C and 350°C. No reasonable results could be derived from the measurements done at the two lower temperatures. The entire sensor evaluation for CO and HCMix sensitivity was done at 350°C. The relative humidity levels in the measurement routine were set to 25%, 50% and 75%.

CO measurements

The zinc oxide nanowire arrays' sensitivity towards CO was tested at four gas concentrations: 10 ppm, 33 ppm, 58 ppm and 100 ppm. Each CO concentration was applied for a duration of 5 min. In between the gas concentrations a duration of 15 min was chosen for the gas sensors recuperation. Figure 5.8 depicts the resistance of the ZnO nanowire array gas sensor over time upon exposure to four CO concentrations and three relative humidity levels at an operation temperature of 350°C. Figure5.8 (a) shows the sensor resistance (black) as a function of time, gas exposure and changes in relative humidity levels (blue). In part (b) of figure 5.8 the sequence of CO gas concentrations as a function of time is shown. The resistance of the NW array decreases upon gas exposure. Since CO is a reducing gas the observed resistance change of the NW array corresponds to the predicated behaviour described in the ionosorption model for n-type gas sensors.
Figure 5.10 (a) shows the sensitivity values towards the highest CO concentration (100 ppm) as a function of relative humidity. At 25% rH the sensitivity reaches a value of 58%. Increasing the relative humidity to 50% slightly changes the sensitivity to 56%. Only at higher rH levels of 75% the sensitivity drops to 37%. The average response time of the ZnO NW array for this measurement is 4.8 min. The average recovery time reaches a value of 14.2 min.

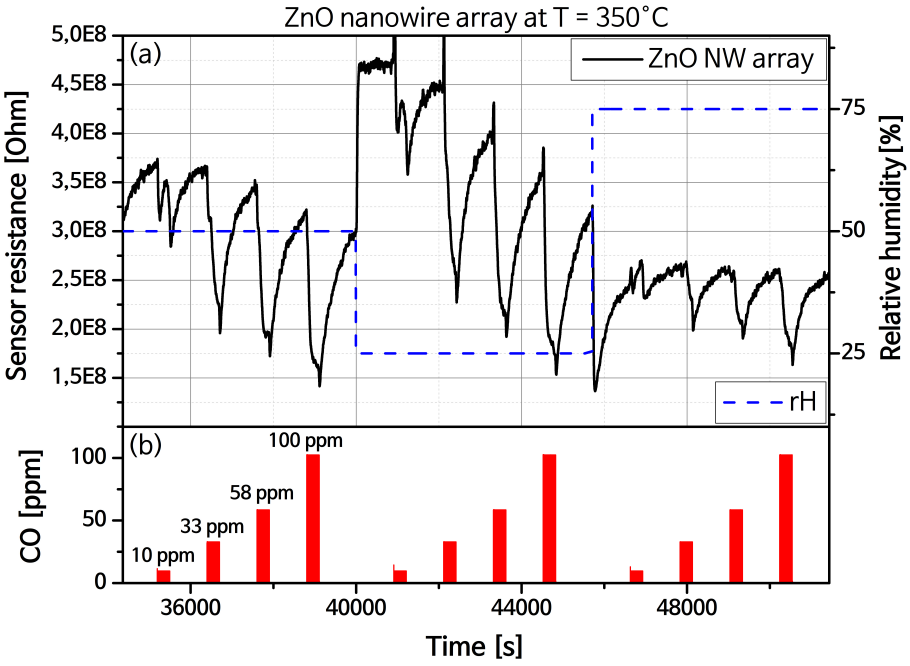

Figure 5.8.: ZnO nanowire array. (a) Sensor resistance (black) as a function of time at $T_{operation}$ = 350°C. The relative humidity levels 25%, 50% and 75% are depicted by a dashed blue line. (b) Gas pulse sequence of four CO concentrations (10 ppm, 33 ppm, 58 ppm and 100 ppm).

HC-mix measurements

The sensitivity evaluation of the ZnO NW array is done at four different HCMix concentrations: 10 ppm, 70.1 ppm, 130.1 ppm and 200.2 ppm. The durations for gas exposure and recuperation are maintained as for the CO measurements. Figure 5.9 shows the HCMix measurement at an operation temperature of 350°C. Fig.5.9 (a) shows the sensor resistance (black) as a function of time, gas concentration and relative humidity (blue). Fig.5.9 (b) depicts the HCMix gas concentrations as a function of time. The author presumes that the overshoot of the gas sensors resistance upon gas exposure is related to an overshoot in the gas pulse. This occurs during the adjustment of the true gas concentration by the mass flow controller. In figure 5.10 (b) the ZnO NW arrays' sensitivity towards the highest HCMix concentration

(200.2 ppm) is shown as a function of the relative humidity. At the lowest rH level of 25% the sensitivity is 43%. The sensitivity decreases by 4% to a rH level of 50% and further decreases by 6% at rH 75%. The average response time for the HCMix measurements is 6 min, whereas the average recovery time is roughly 13 min.

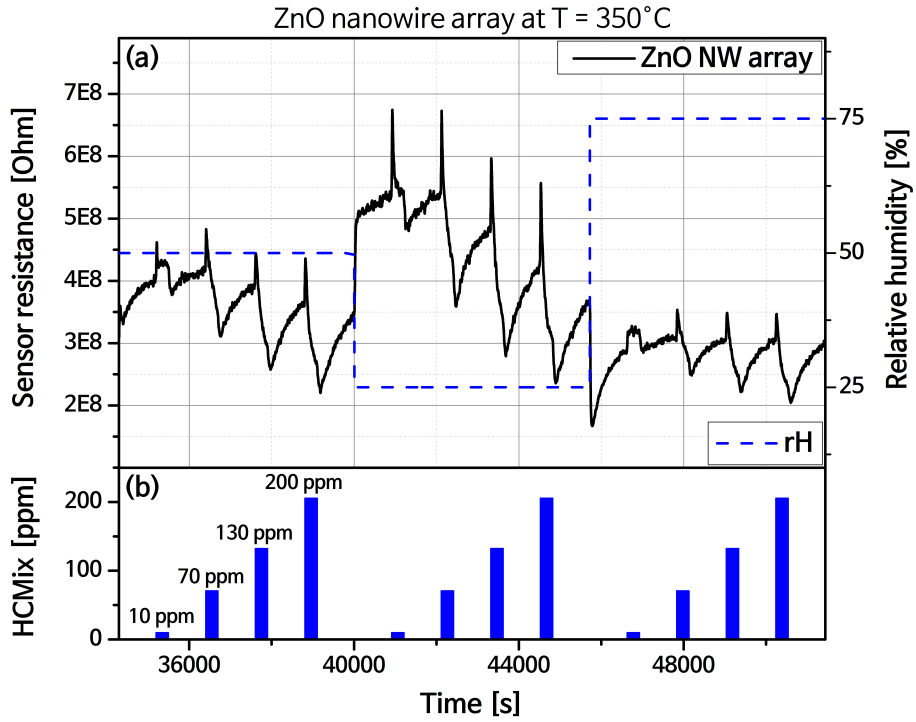

Figure 5.9.: ZnO nanowire array. (a) Sensor resistance (black) and relative humidity (blue) as a function of time at $T_{operation}$ = 350°C. (b) Gas pulse sequence of four HCMix concentrations (10 ppm, 70.1 ppm, 130.1 ppm and 200.2 ppm).

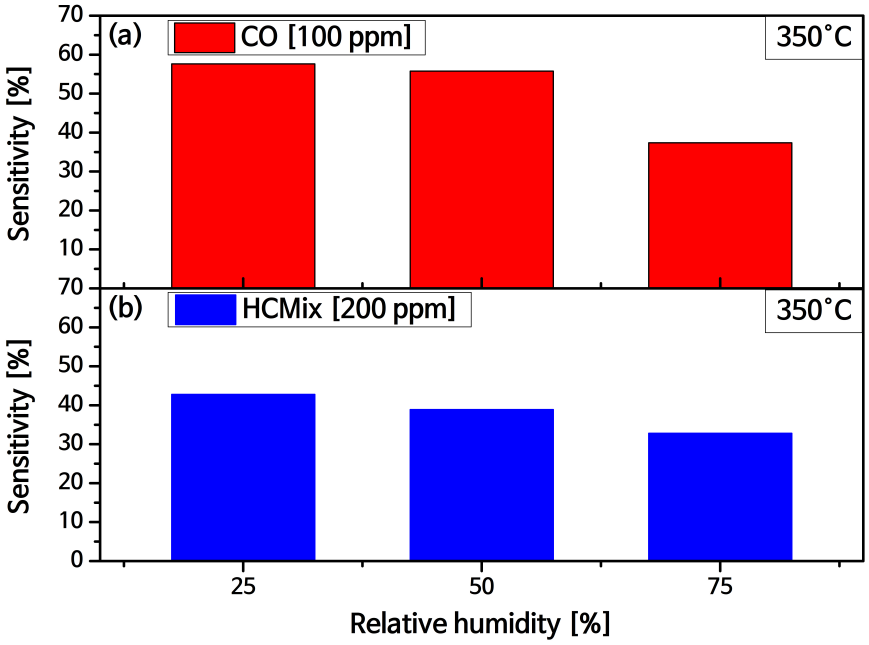

Figure 5.10.: ZnO NW arrays' sensitivities towards the highest concentration of (a) CO (100 ppm) and (b) HCMix (200.2 ppm) at relative humidity levels: 25%, 50% and 75%.

5.3. MPW3: CMOS integrated SnO_2 Gas Sensors

In section 3.2 two CMOS chips, which are used in this work, namely MPW3 and MPW4 are introduced. The MPW3 chip is a CMOS chip including two microhotplates with different geometries. Previous MPW iterations resulted in the definition of these two microhotplate geometries. The SnO_2 layer deposition is done according to section 3.2.2. Hereby, the SnO_2 gas sensor is functionalized with Au nanoparticles by thermal evaporation of a thin gold layer and consecutive annealing resulting in gold island growth, hence Au nanoparticles. The gas sensor was evaluated for three different test gases: CO, HCMix (see section 1.3.3) and ethanol. Ethanol was used to test the

gas sensors cross-selectivity. Additionally, two relative humidity levels were chosen to determine the gas sensors humidity dependence. The gas sensor evaluation was done at two different operation temperatures: 300°C and 400°C. This section is based on [15].

CO measurements

For the determination of the SnO_2 gas sensors CO sensing capabilities a series of five different CO concentrations are chosen: 7 ppm, 20 ppm, 40 ppm, 80 ppm and 160 ppm. Every single CO concentration is applied for a duration of 50 min. The entire CO concentration sequence is executed at a constant relative humidity level. Two relative humidity levels are investigated for the CO sensing: 45% rH and 73% rH. This results in the execution of two entire CO sequences per operation temperature. The relative humidity levels are set to compare the gas sensors response to lower and higher humidity levels. Figure 5.11 depicts the entire CO measurement of the Au-NPs functionalized SnO_2 gas sensor at an operation temperature of 300°C. The upper part of fig. 5.11 shows the sensor resistance as a function of time. The sensor resistance changes in dependence of the gas concentration or the relative humidity level. The lower part of fig. 5.11 shows the applied CO gas concentrations. Figure 5.12 shows the same measurement as seen in figure 5.12 at an operation temperature of 400°C.

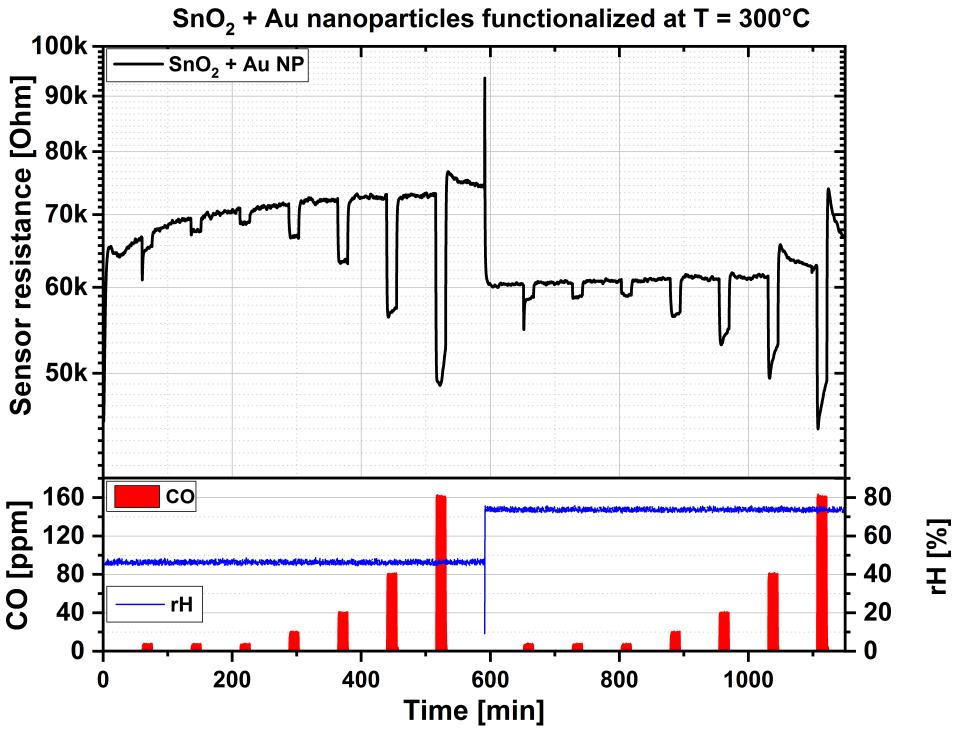

Figure 5.11.: CO measurement of the CMOS integrated Au-NPs functionalized SnO_2 thin film gas sensor at an operation temperature of 300°C. CO levels: 7 ppm, 20 ppm, 40 ppm, 80 ppm and 160 ppm. rH levels: 45% rH and 73% rH.

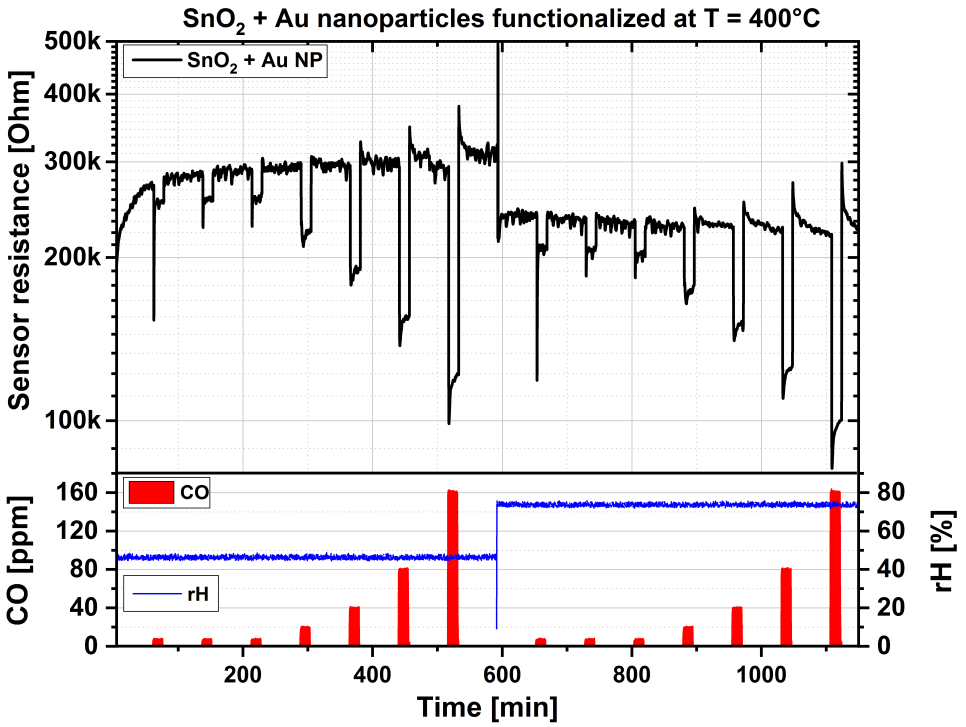

Figure 5.12.: CO measurement of the CMOS integrated Au-NPs functionalized SnO_2 thin film gas sensor at an operation temperature of 400°C. CO levels: 7 ppm, 20 ppm, 40 ppm, 80 ppm and 160 ppm. rH levels: 45% rH and 73% rH.

A comparison of the highest applied CO concentration of 160 ppm measured at the two temperatures 300°C and 400°C in dependence of a lower and higher relative humidity level is shown in figure 5.13 (a). At 300°C and 45% rH the sensitivity of the gas sensor reaches 28%. With increasing relative humidity the sensitivity decreases to 22% at 73% rH. The average response and recovery time for the sensor at this operation temperature is 46s and 50 s respectively. At 400°C and 45% rH the sensitivity increases to 59% compared to the operation temperature of 300°C. Again, a slight dependence on relative humidity can be observed at the higher operation temperature. The sensors sensitivity decreases to 56% at 73% rH. The increase in operation temperature results in a decrease of the average response time to 8s as well as of the average recovery time to 12s. The repeatability of the CMOS integrated Au-NPs functionalized SnO_2 gas sensor is tested by applying a

low CO concentration of 7 ppm three times consecutively. This is done at the same operation temperatures and relative humidity levels as described above. Figure 5.13 (b) depicts the sensors sensitivity towards 7 ppm CO at 300°C and 400°C as well as the relative humidity levels 45% rH and 73% rH. At 300°C and low rH (45%) the sensitivity is 2.5%. Consecutive measurements result in a deviation of $\pm$0.5% in sensitivity. At the higher rH (73%) the sensitivity increases slightly to 2.7%. The deviation remains $\pm$0.5% in sensitivity. By increasing the operation temperature to 400°C the low relative humidity level exhibits an increase in sensitivity to a value of 9%. Hereby, the deviation is $\pm$1.9% in sensitivity. Going to the higher relative humidity level results in an increase in sensitivity. The sensor sensitivity reaches 13% with a deviation of $\pm$1.4%.

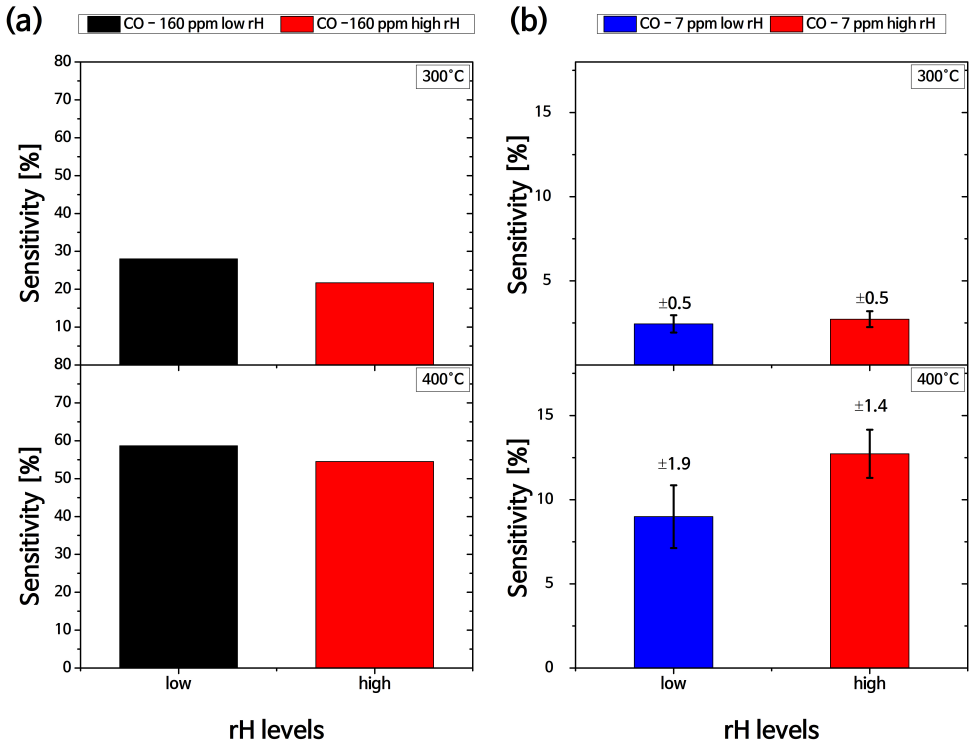

Figure 5.13.: (a) Comparison of the CMOS integrated Au-NPs functionalized SnO_2 thin film gas sensors' sensitivity towards a CO concentration of 160 ppm at 300°C and 400°C at a low rH (45%) and a high rH (73%). (b) Comparison of three repetitions of a CO concentration of 7 ppm at conditions described in (a).

VOC measurements

The Au-NPs functionalized SnO_2 gas sensor is evaluated for its sensitivity towards VOC by exposure to a HCMix and ethanol. In this case both test gases HCMix and ethanol are only evaluated at a single concentration of 50 ppm each. The sensors are tested as for the CO case at operation temperatures of 300°C and 400°C. The relative humidity levels at 300°C are 31% and 84%. Whereas, the relative humidity levels at 400°C are 25% and 78%. Although, the relative humidity levels are not identical for the

300°C and 400°C a trend for lower and higher relative humidity levels can be derived. Figures 5.14 and 5.15 show the sensor evaluation at 300°C and 400°C respectively. The upper part of both figures shows the time dependent sensor resistance as it changes upon test gas exposure. The lower part shows the sequence of ethanol gas pulses as well as the HCMix gas pulses. Three ethanol gas pulses (50 ppm) are followed by three HCMix pulses (50 ppm). This sequence is applied for the lower and higher relative humidity levels.

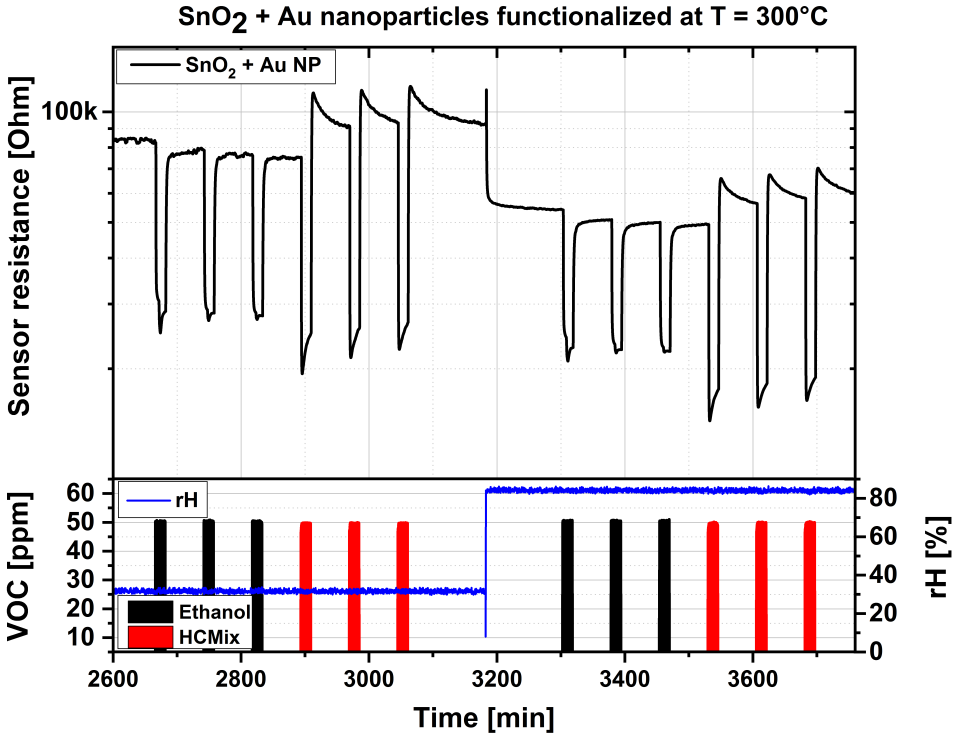

Figure 5.14.: HCMix and ethanol measurements of the CMOS integrated Au-NPs functionalized SnO_2 thin film gas sensor at an operation temperature of 300°C. HCMix and ethanol: 50 ppm. rH levels: 31% rH and 84% rH.

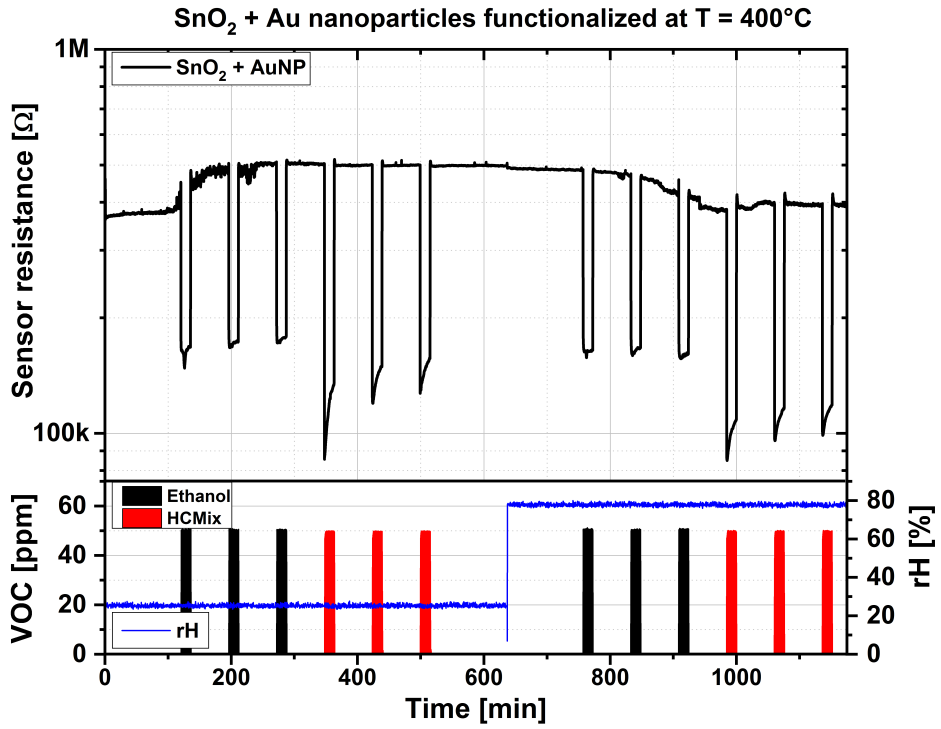

Figure 5.15.: HCMix and ethanol measurements of the CMOS integrated Au-NPs functionalized SnO_2 thin film gas sensor at an operation temperature of 400°C. HCMix and ethanol: 50 ppm. rH levels: 25% rH and 78% rH.

Figure 5.16 shows the change of the sensors sensitivity in dependence of relative humidity for ethanol (a) and HCMix (b). In the case of ethanol (fig.5.16 (a)) at the operation temperature of 300°C and the lower relative humidity level (31%) the sensor sensitivity reaches 64% with a deviation of ±1%. The sensitivity decreases at the higher relative humidity level (84.1%) to 56% with a deviation of ±1.3%. The average response and recovery time are 65s and 316s respectively. Increasing the operation temperature to 400°C yields a slightly lower sensitivity at the lower relative humidity level (25%) of 62%. The deviation increases to a value of ±3.7%. The higher relative humidity level (85%) results in marginal increase in sensitivity to 62% with a deviation of ±2.3%. The increased operation temperature leads to a decrease of the average response and recovery time to 19s and 25s respectively. Figure 5.16 (b) shows the corresponding case of HCMix. Beginning at the operation

temperature of 300°C and the low relative humidity level (31%) a sensitivity value of 70% obtained. The deviation of sensitivity is ±2.8%. The sensitivity slightly decreases to 67% with a deviation of ±1.8% at the high relative humidity level (84%). The average response and recovery time for HCMix at 300°C is 13s and 66s respectively. The higher operation temperature of 400°C at a lower relative humidity level (25%) results in the equivalent sensitivity value of 70%. Even the deviation is comparable with a value of ±2.5%. At this temperature the change to the higher relative humidity level (78%) leaves the sensitivity at 70%. Only the deviation reduced to a value of ±0.8%. At 400°C the average response and recovery time decrease to 8s and 17s respectively. A summary of all average response and recovery times is shown in table 5.1.

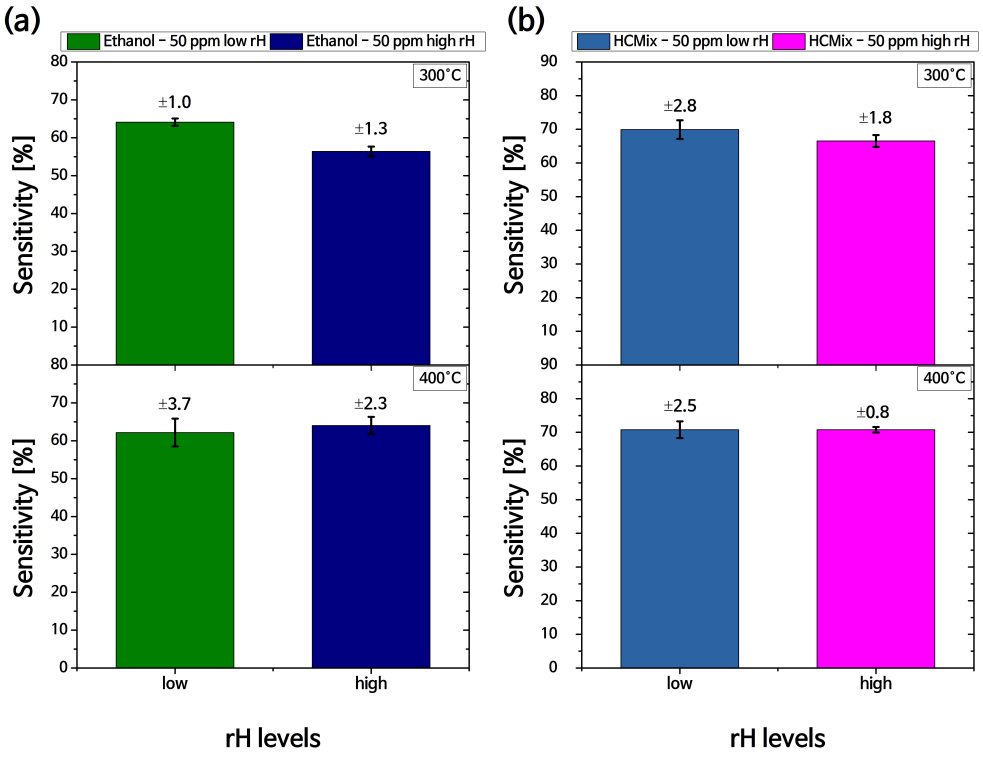

Figure 5.16.: Comparison of the CMOS integrated Au-NPs functionalized SnO_2 thin film gas sensors' sensitivity towards an (a) ethanol concentration and a (b) HCMix concentration of 50 ppm at 300°C with low rH (31%) and a high rH (84%) and 400°C with low rH (25%) and a high rH (78%).

Table 5.1.: Average response and recovery times of the CMOS integrated Au-NPs functionalized SnO_2 thin film gas sensor measurements of CO, HCMix and ethanol. Both quantities are calculated at each operation temperature. The calculation is done according to the deliberation of section 1.2.1.

Gas pwa-sulse	$\mathbf{T}_{operation}$ [°C]	**Avg.response time** [s]	**Avg.recovery time** [s]
CO [160 ppm]	300	46	50
CO [160 ppm]	400	8	12
HCMix [50 ppm]	300	13	66
HCMix [50 ppm]	400	8	17
Ethanol [50 ppm]	300	65	316
Ethanol [50 ppm]	400	19	25

6. Discussion and Outlook

6.1. Discussion

6.1.1. CuO thin film gas sensor

The CuO thin film gas sensors evaluated in section 5.2.1 are fabricated by thermal oxidation process, which is already published by our group in [18]. The oxidation process of metallic copper as discussed in section 2.2.2 results in the formation of Cu_2O (cuprous oxide) and CuO (cupric oxide). The Raman measurements shown in figure 4.14 identify the oxidized copper oxide as CuO. Chen et al.[235] shows that in general the thermal oxidation of metallic copper results in the formation of three phase system comprised of Cu, Cu_2O and CuO. Furthermore, an oxidation temperature of 400°C and higher would lead to CuO nanowire formation, which is shown by Xu et al.[234]. On the CuO thin film gas sensor surface only few nanowires can be found. The base material for Xu's oxidation experiments are copper foils. In comparison to the copper foils, the structured copper layer, which is used for the fabrication of the CuO thin film gas sensors, contains much less material for oxidation compared to the bulk material of Xu. Additionally the method of fabrication of the base material (copper) has an influence on the micro structure and on the oxidation process, which is in accordance with the findings of Popovski et al.[239]. The deviation of Xu's findings might be attributed to the relatively small copper volume and the fabrication method of the copper layer (thermal evaporation). Furthermore, the gap between the copper structures is additional space for the expanding oxide. This additional space can reduce the stress and strain, which is increasing during oxidation. Since stress is a primary factor for the growth of CuO nanowires a relief of stress can inhibit their formation. Figure 4.13 shows the surface of

the oxidized copper structure. The gaps between the copper structures are bridged by the copper oxide. A continuous copper oxide layer is formed. The occurrence of single nanowires on the surface suggests that during the oxidation process multiple copper phases are formed. During the extended duration of the oxidation cuprous oxide is converted to cupric oxide. Adilov et al.[240] investigated the conversion of cuprous oxide to cupric oxide at various temperatures and found that at 400°C and higher a total conversion can occur. This is in agreement with the Raman investigation, which found only CuO as stated above.

CO_2 gas sensing: Most metal oxides used for gas sensing show little to no sensitivity towards CO_2. CuO is an exception, which has been reported in [185] [231]. This is in agreement with the findings in this work. The pristine CuO gas sensor in figure 5.2 shows moderate sensitivity towards multiple CO_2 concentrations. Herein, the pristine CuO gas sensor exhibits its highest sensitivity to the maximum CO_2 concentration of 2000 ppm at 50% rH and an operation temperature of 350°C at 35%. This value is comparable to sensitivities shown in literature [231] [241].
The ionosorption model, which is the standard model for metal oxide interaction with gas molecules in gas sensors doesn't include a basic mechanism that describes the interaction of the CuO surface and the CO_2 molecules. Tanvir et al.[185] proposes a surface reaction on CuO nanoparticles, which induces a structural change in the material that can be measured. Herein, the surface reaction is dependent on humidity. Tanvir et al.[185] describes the formation of malachite and azurite on the surface of CuO. Although, the formation of copper carbonate would be an obvious choice as well, thermodynamically malachite and azurite are more stable. Equations 6.1 and 6.2 are proposed chemical reactions leading to the formation of these hydroxycarbonates.

Malachite:

$$2CuO_{(s)} + CO_{2(aq)} + H_2O_{(l)} \rightleftharpoons Cu_2(OH)_2CO_{3(s)} \tag{6.1}$$

Azurite:

$$3CuO_{(s)} + 2CO_{2(aq)} + H_2O_{(l)} \rightleftharpoons Cu_3(OH)_2(CO_3)_{2(s)} \tag{6.2}$$

In [185] it is stated that the occurrence of CO_2 can either be in gaseous or solved in aqueous form on the CuO surface. It is assumed that CO_2 is solved in aqueous form. Table 6.1 shows the Gibbs free energy of each component in equations 6.1 and 6.2. The calculations of the Gibbs free energy of formation for malachite and azurite are done according to Tanvir et al.[185]. Furthermore, this section is taken from the publication of this works author [238]. First the standard Gibbs free energy for the formation of a compound is calculated. This is done according to equation 6.3.

$$\Delta_R G^0 = \sum \Delta_f G^0_{product} - \sum \Delta_f G^0_{educt} \tag{6.3}$$

Herein, $\Delta_R G^0$ is the change of the standard Gibbs free energy of the examined chemical reaction at standard conditions. Standard conditions refer to a temperature of 298.15 K and a pressure of 1 bar. $\sum \Delta_f G^0_{product}$ is the sum over all standard Gibbs free energies of the products. $\sum \Delta_f G^0_{educt}$ is the sum over all standard Gibbs free energies of the educts.
Since the gas sensor is exposed to a certain CO_2 concentration the partial pressure of CO_2 has to be considered in the Gibbs free energy. The following two equations describe the deviation of the change of standard Gibbs free energy of a specific reaction at varying pressures. Equation 6.4 describes this deviation for malachite, whereas equation 6.5 describes the deviation for azurite.

$$\Delta_R G = \Delta_R G^0 + RTln(p_{CO_2})^{-1} \tag{6.4}$$

$$\Delta_R G = \Delta_R G^0 + RTln(p_{CO_2})^{-2} \tag{6.5}$$

$\Delta_R G$ is the change of Gibbs free energy of formation at a partial pressure varying from standard conditions. $\Delta_R G^0$ is the change of the standard Gibbs free energy of the examined chemical reaction at standard conditions.

Standard conditions refer to a temperature of 298.15 K and a pressure of 1 bar. R is the gas constant (R = 8.314 $\frac{J}{K \cdot mol}$). T is the temperature. p_{CO_2} is the partial pressure of CO_2.
The calculations are done for a CO_2 concentration of 400 ppm at 298.15 K. The results are shown in table 6.2 below.

Table 6.1.: Gibbs free energy of formation for educts and products of malachite and azurite formation at 298.15 K and 1 bar.

Compounds	**Literature**	$\Delta_f \mathbf{G}^0[\frac{kJ}{mol}]$ **at 298.15 K**
CuO	[242]	-127.6
$CO_{2(aq)}$	[185]	-385.99
H_2O	[242]	-237.34
$Cu_2(OH)_2CO_{3(s)}$ (malachite)	[242]	-906.2
$Cu_3(OH)_2(CO_{3(s)})_{2(s)}$ (azurite)	[242]	-1439.13

Table 6.2.: Gibbs free energy for the reactions shown in equation 6.1 (malachite) and 6.2 (azurite) at 400 CO_2, 298.15 K and 1 bar.

Compounds	**CO_2 [ppm]**	$\Delta_f \mathbf{G}^0[\frac{kJ}{mol}]$ **at 298.15 K**
Malachite: $Cu_2(OH)_2CO_{3(s)}$	400	-127.6
Azurite: $Cu_3(OH)_2(CO_3)_{2(s)}$	400	-385.99

It is known that both compounds, malachite and azurite, are insulating materials. The formation of these materials on the gas sensor surface would on one hand side reduce the possibility of oxygen adsorption to the surface and on the other hand side change the resistance of the material. On exposure to CO_2 the resistance of the gas sensor increases. As already stated above, the ionosorption model cannot explain this behaviour. A further indication for the formation of malachite and azurite on the gas sensor surface is

the optimal operation temperature, which is found to be 300°C. Investigations concerning the thermal stability of malachite and azurite have been conducted by Seguin[243]. Herein, both materials are investigated by DTA measurements. In these DTA measurements it is concluded, that malachite dissociates between 310°C to 420°C. Azurite dissociates between 295°C and 395°C. Since azurite is dissociating during the optimal operation temperature, it can be concluded that it only plays a minor role to the sensing mechanism. The drop in sensitivity between 350°C and 400°C also support the role of malachite for the sensing mechanism. It has been noted here, that further investigation have to be conducted to determine the existence or amount of malachite on the CuO gas sensor surface.
The enhancement of the gas sensors' sensitivity found by applying Au-NPs is shown in figure 5.2. Herein, a direct comparison of the pristine and Au-NPs functionalized CuO thin film is depicted. In section 1.4 the two mechanism for the enhancement of gas sensors' sensitivities are discussed: chemical sensitization and electronic sensitization. In the case of Au-NPs the chemical sensitization mechanism can be seen as the contributing mechanism. Since Au-NPs don't tend to oxidise at the environmental conditions set during gas sensing electronic sensitization can be neglected. It is assumed that the Au-NPs act as active sites for the adsorption of CO_2 onto the surface, thereby increasing the amount available for the formation of malachite. Yang et al.[244] reported in their findings that on an CeO_x/TiO_2 substrate decorated with Au-NPs the amount of CO_2 is increased. At the current state of this research further material compositions as Au/CuO NPs, which could be formed during the operation at 400°C cannot be excluded. The stability of this Au-NPs functionalized CuO gas sensor is currently under investigations. The drop coating process used for the deposition of the Au-NPs limits the reproducibility of the gas sensor. Therefore, other deposition methods as ink-jet printing have to be determined for their applicability.

Cross-selectivity: In section 5.2.1 the cross-sensitivity of the Au-NPs functionalized CuO gas sensor is evaluated. Hereby, the sensor is tested for its sensitivity towards carbon monoxide. Figure 5.7 shows a direct comparison of the highest CO_2 (2000 ppm) and CO (200 ppm) concentrations at three different relative humidity levels. It can by argued that the difference in

concentration, tenfold, would always lead to different results. Although, this is true the base application for this gas sensor is indoor air quality monitoring. Since the daily mean value for CO is 30 ppm [245], concentrations as high as 200 ppm are well outside of the normal operation range for indoor applications. However, this cross-selectivity test shows that even at this high concentrations the sensitivity of this gas sensor towards normal CO_2 concentrations still exceeds the CO signal. Optimal operations of this gas sensor in environments containing both gases would be ensured by implementing an additional gas sensor showing a high sensitivity towards CO and non towards CO_2. Such a sensor would be the SnO_2 gas sensor presented in this work.

6.1.2. ZnO nanowire array gas sensor

In contrast to other oxide materials, which are used for gas sensor fabrication, the process of thermal oxidation of zinc leads to additional precautions in comparison to those other materials, like copper. The choice of electrode material for example greatly influences the thermal oxidation process of zinc. In most of our gas sensors a layered system of gold and titanium (adhesive material) is being used as electrode material. Only for a few ZnO NW array gas sensors the oxidation process has been successfully completed. In those samples, where the oxidation process was unsuccessful, the oxidation was hindered by a process seen in figure 6.1. In this figure the zinc layer is marked with an orange rectangle. The zinc layer consists of several small squares and two larger rectangles each on one side, which are connected to the gold electrodes. At the overlap between zinc and gold electrodes a reaction occurs. This reaction spreads along the electrode and leads to a partial swelling and delamination of the electrode. The author assumes that an intermetallic phase between zinc and gold is formed. Within this work no following investigations have been done to verify this assumption.

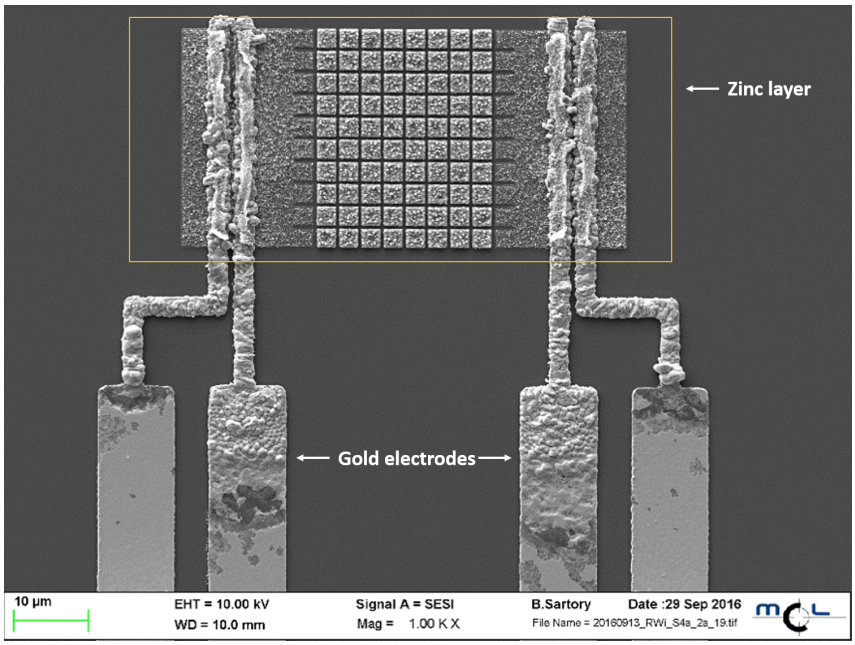

Figure 6.1.: SEM picture of a fail thermal oxidation of ZnO nanowires. Parts of the gold electrodes form a intermetallic phase with the zinc during thermal oxidation, thereby hindering the formation of zinc oxide nanowires.

CO measurements: Figure 5.8 (see section5.2.2) the ZnO NW array is evaluated for various CO concentrations. It can be seen for each gas concentration that the gas sensors' resistance is far from reaching a state of saturation during gas exposure. This is an indicator for a relatively slow gas sensing reaction. In figure 5.10 (a) the sensitivity values for the highest CO concentrations at the three rH levels is shown at an operation temperature of 350°C. The sensitivity of the ZnO NW array gas sensor decreases constantly from the lower rH level to the highest rH level. The above mentioned slow sensing reaction is supported by the average response and recovery times which are 4.8 min and 14.2 min respectively.

HCMix measurements: The entire evaluation of the ZnO NW gas sensors' response towards various HCMix concentrations is shown in figure 5.9. The gas sensors exhibits the same behaviour, which has been observed in the CO

measurement. Upon HCMix exposure the gas sensor doesn't reach a saturation state during the duration of the gas pulse. This indicates a slow reaction between the sensor surface and the HCMix. For the lowest HCMix concentration the gas sensor seems to change its n-type conduction behaviour and switches to p-type behaviour upon gas exposure. This behaviour is only observed for the HCMix measurement. The HCMix react as a reducing gas on the gas sensor. An explanation for the change in conduction could be that during the interaction between the HCMix components and the sensor surface a new component is formed. This new component reacts as an oxidizing gas, hence the sensor would seem to exhibit p-type conduction. Furthermore, it cannot be excluded, that the formation of this oxidizing component occurs at higher HCMix concentrations as well. The remaining components of the HCMix could react as a reducing gas. Therefore, the HCMix measurements shown in figure 5.9 (a) could be a superposition of both reactions. Figure 5.10 (b) shows the dependency of the sensitivity towards the maximum HCMix concentration (200 ppm) to three rH levels. It can be seen that higher rH levels reduce the sensors' sensitivity by a few percentage.
To substantiate these assumptions made above further investigations on this material system have to be made. So far these are only assumptions.

6.1.3. SnO_2 thin film gas sensor

In section 4.1 SnO_2 thin films deposited with the spray pyrolysis set-up used for the production of the CMOS integrated SnO_2 gas sensors in section 5.3 are investigated. These investigations are done to ensure repeatable deposition quality. By investigating the SnO_2 thin film with x-ray reflectometry (XRR), figure 4.2, and atomic force microscopy (AFM), figure 4.1, the layer roughness is determined. Since XRR uses a larger area during the measurement than AFM the value gained by XRR is used with higher confidence. The roughness of SnO_2 layers deposited by this method is around 0.55 nm. A following TEM investigation confirms the polycrystalline structure of the SnO_2 layers (fig.4.3).
The sensing mechanism applicable for both CO and HCMix can be described by the ionosorption model (see section 1.2.2).

CO measurement: A summarized view of the CO measurement can be seen in figure 5.13 (a) and (b). In part (a) of this figure the gas sensors' sensitivity towards the highest CO concentration 160 ppm is shown for a low and a high relative humidity level. The upper part of figure 5.13 (a) shows the sensitivity at 300°C, whereas the lower part shows the sensitivity at 400°C. In direct comparison it can be seen that the increase in temperature results in an increase in sensitivity by a factor of two. The influence of the relative humidity level is independent on the operation temperature. The reason for the increased sensitivity is described in the ionosorption model. Since the adsorbed oxygen ion density is a function of temperature [246] more oxygen species are available for the CO molecules to react to. A higher reaction rate leads to a higher sensitivity. In figure 5.13 (b) the repeatability of low gas concentration (7 ppm) measurements is investigated. As for the case in (a) the evaluation has been done for the same two operation temperatures. At 300°C the sensitivity towards CO is rather small. A higher rH leads to a small increase in sensitivity. For both rH levels the sensitivity can be measured repeatedly within only 0.5%. By increasing the operation temperature to 400°C the sensitivity is as in the case of the higher concentration doubled. The dependence to higher rH levels doesn't change. With the increase in sensitivity the variation in the repeatability increases as well to values of 1.9% and 1.4%. Additionally, in table 5.1 the average response and recovery time of the highest CO concentration is shown for both operation temperatures. Both times show the same behaviour as the sensors' sensitivity. By increasing the operation temperature the average response and recovery time are nearly decrease by a factor of 5.

HCMix and ethanol measurement: In the case of HCMix and ethanol measurements no variations in concentrations have been done. A single concentration for both test gases of 50 ppm was introduced to investigate the repeatability of the gas sensor measurements. The summary of this experiments is depicted in figure 5.16. Figure 5.16 (a) shows the evaluation of the ethanol measurements. The upper part shows the operation temperature of 300°C. Again the sensor is tested at a lower and a higher rH level. At this operation temperature the sensor shows a lower sensitivity at the higher rH level. The variation in sensitivity is similar on both rH levels. At 400°C the sensitivity doesn't increase in comparison to the lower operation

temperature. But the dependence in humidity is strongly reduced. Furthermore, the increase in temperature results in an increase of the variation in sensitivity between repeated measurements. The evaluation of the HCMix measurements is shown in figure 5.16 (b). As for the case of ethanol at the operation temperature of 300°C a dependence on the rH level is evident. This dependency is strongly reduced at the operation temperature of 400°C. The variation in sensitivity at the lower rH level is similar for both operation temperatures.
The average response and recovery times for ethanol and HCMix measurements show the same trend as for CO (see table 5.1). An increase in operation temperature results in each case in a reduction of both response and recovery time. A dramatic decrease in the average recovery time is seen for ethanol. Here the recovery time shortens from more than 5 min to less than a half minute, when changing the operation temperature from 300°C to 400°C.

6.1.4. Spray pyrolysis of other metal oxides

In addition to the spray pyrolysis of SnO_2 thin films, which are an established metal oxide for gas sensing, two new materials are investigated for their possible integration into our process flow for gas sensor fabrication. These two materials as discussed in previous chapters are CuO and ZnO.

CuO thin film: The integration of CuO thin films deposited by spray pyrolysis enables the fabrication of pn-junctions. As reported in literature [148] pn-junctions could increase the oxygen adsorption on the sensors surface, hence increase sensitivity. In section 4.2 the results of the CuO spray pyrolysis experiments are shown. The EDX spectrum in figure 4.7 and the XRD spectrum in figure 4.8 clearly show that the material deposited by spray pyrolysis is indeed CuO. The FIB cut depicted in figure 4.12 provides a picture of a homogeneous thin film. Although, this might be true and even encouraging, on top of this layer micrometer sized grown structures are found. These structures are statistically distributed on the CuO film. Investigations of this structures indicate that they are made of CuO and are a by-product of the spray pyrolysis process (see fig.4.9). So far no solution

was found to reduce the growth of these structures. Therefore, deposition of an aqueous copper nitrate solution cannot be used for the process flow established for SnO_2 thin films. Since the material cannot be deposited and processed (photolithography and etching), an evaluation of its gas sensing capabilities isn't possible at the moment.

ZnO thin film: The results of the ZnO spray pyrolysis experiments are shown in section 4.4. The optimal spraying solution for the deposition is a zinc acetate solved in a water/ethanol mixture of 1:3. At a deposition temperature of 400°C a homogeneous ZnO layer has been deposited (figure 4.21). The EDX spectrum in figure 4.23 indicates the occurrence of ZnO. The AFM measurement in figure 4.24 shows that the ZnO thin film is smooth with a roughness of only 3.7 nm. So far only a successful deposition can be shown here. The integration into the process flow is an ongoing work. Furthermore, the evaluation of the gas sensing capabilities of zinc oxide deposited by spray pyrolysis is depending on the integration work and is therefore ongoing as well.

6.2. Outlook

MPW4 gas sensor integration: In section 3.2 two different CMOS gas sensor platforms are presented. Results of the SnO_2 gas sensor integration on MPW3 are shown in section 5.3. In [247] E. Lackner shows the successful integration of spray pyrolysed SnO_2 on MPW4, and characterizes these sensors. In the dissertation of J. Krainer [248] WO_3 nanowire networks are integrated onto this CMOS platform by ink-jet printing. Hereby, the WO_3 nanowires are chemically synthesized in a separate process. So far the integration of the copper oxide nanowire array as well as copper oxide thin film gas sensors hasn't been achieved reliably. First results are encouraging, but the deposition process as well as the oxidation process still have to be further investigated to reach a higher degree of reproducible sensor response. The issue of zinc oxide nanowire array gas sensor integration on MPW4 is currently under investigations. Since the electrode material of the MPW4 chip is platinum, less interactions between the zinc and the

platinum are expected during the thermal oxidation process as compared to gold electrodes. This assumption will be validated in future investigations. Following the successful integration of CuO and ZnO is the reliable and repeatable deposition of various nanoparticles (mono-, bi- or tri-metallic). Two approaches, which have been applied in our group for nanoparticles deposition namely, ink-jet printing and sputter deposition, will be used on a larger scale. The overall goal of the sensor material (MOX and nanoparticles) integration is to obtain a device capable of qualitatively distinguish certain unknown gas mixtures. The MPW4 CMOS chip as a platform for different gas sensor materials would provide the possibility to fabricate a gas sensor array with up to 16 different gas sensitive materials. If chosen accordingly the sensitivities of those different gas sensors could span a vector room of gas sensitivities, which would allow to precisely differentiate numerous gases or even gas mixtures. Figure 6.2 depicts a fully processed MPW4 gas sensor bonded on an evaluation PCB. For now only single materials have been integrated.

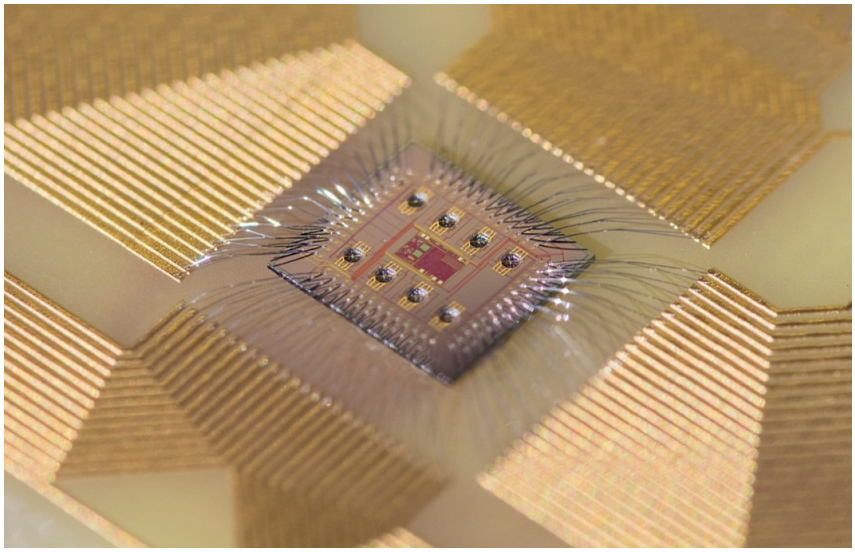

Figure 6.2.: Picture of a fully processed MPW4 gas sensor chip (8 micro hotplates) bonded on a PCB for evaluation.

3D stacked gas sensors: Gas sensors, which are fully integrated onto CMOS platform equipped with operation circuitry enable simple testing of the gas sensors under real life conditions. Within the MSP project it has been shown that the 3D-integration of gas sensors based on the MPW4 on a CMOS platform is feasible.
The circuitry integrated into the CMOS platform chip has been designed by Fraunhofer IIS for operating different sensor elements. In the case of the MPW4 gas sensors only one microhotplate, containing two sensor elements, can be operated by this chip. Within the full platform chip (size 20 x 20 mm) 20 so called base units are integrated, where each unit can operate one of the various sensor applied in the MSP project or as stated above in the case of the MPW4 one microhotplate plus two sensor layers.
To achieve our goal of parallel operation of all 16 gas sensors integrated on a single MPW4 chip, eight base units are required. A platform chip containing an array of eight base units would be required for operating a full sensor set enabled by the MPW4 chip. Both the MPW4 gas sensor chip as well as the platform chip have been specifically designed and fabricated for 3D-integration employing TSV technology. This has been performed within the MSP project.

Temperature modulated operation: Although gas sensors integrated on microhotplates have a low power consumption, a reduction of power always leads to longer battery lives, which makes gas sensors more attractive in Internet of Things (IoT) applications. The main power consumption of these gas sensors is attributed to the heating of the MOX material. Operating gas sensors in the regimes described by the ionosorption model heating is inevitable. In standard gas sensor operation the gas sensor is heated constantly for the entire gas measurement. A solution for this problem is the operation of the gas sensors at specific temperatures for a specific duration. This is called pulsed operation. The main drawback of pulsed operation is that the sensor cannot reach its equilibrium state, which is necessary for a reliable gas sensor reading. A different approach is temperature modulated operation (TMO), which is being tested within our group. The major difference between pulsed and TM operation is that the evaluation of the gas sensors' response is done after a temperature jump form a higher temperature to a lower temperature. According to [246] a

higher temperature results in a higher ionosorbed oxygen density on the sensor surface. This oxygen density is preserved, when the sensor is cooled down. Higher oxygen densities result in more oxygen ions and test gas molecules interactions, hence sensitivity. Since the sensor doesn't need to be operated at the higher temperature level constantly the power consumption for the overall measurement is reduced. A combination of operation CMOS and MPW4 CMOS, as described in the previous paragraph, would greatly benefit from this TM operation and increase its attractiveness for the IoT market.

MultiSensor Platfrom (MSP) Project: In this paragraph the major outcomes of the MultiSensor Platform (MSP) project are summarized. The majority of the research done in this thesis has been done within the MSP project.
One of the projects main goals was indoor air quality monitoring. Hereby, the constant monitoring of carbon dioxide (CO_2) as well as humidity was chosen as main quantities to adjust settings for HVAC systems. Prior to the MSP project various approaches have already tried to incorporate multiple sensors into a single device and were even made ready for the market. Some of these devices are:

- SAMSUNG SmartThings [249]
- AEOTEC MultiSensor 6 [250]
- Kenttix - Multisensor DOOR [251]
- Bosch BME680 [252]

Dating back to the beginning of the MSP project these sensor systems weren't integrated on CMOS technology and furthermore lacked wireless connectivity.
The vision of this project was to establish a manufacturing chain to 3D integrate multiple sensor devices on a single CMOS platform (see fig.6.3).

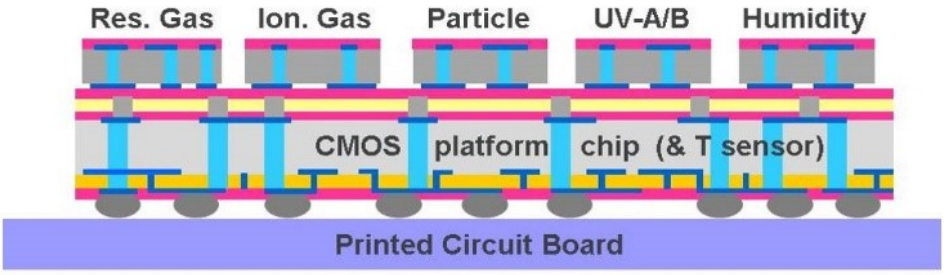

Figure 6.3.: Schematic drawing of the envisioned MSP demonstrator device.

The 3D integration by TSV technology leads to the reduction of the footprint of each sensor device. Furthermore, TSVs replace the commonly applied wire-bonding connection technology. Within the project various sensor devices were set to be developed by project partners for the final integration onto a CMOS platform chip. Following is a list of sensor devices, which were meant for the final integration.

- MPW4 gas sensor device chips for gas sensing of various gases were integrated. The materials applied were SnO_2 (thin film), CuO (nanowire arrays), ZnO and WO_3 (nanowire network). These gas sensors were sensitized with (bi)metallic nanoparticles.
- Graphene oxide deposited onto a CCMOS (Cambridge CMOS Sensors Ltd) microhotplate was employed as a humidity sensor.
- A GaN/AlGaN 2D-electron gas sensor for NO_2 was used. Furthermore, a GaN-on-Si based microhotplate was developed to operate the NO_2 gas sensor.
- Fine dust sensor based on a hybrid MEMS-FBAR based micro sensor system was further developed.
- UV-A/B sensor based on SiC technology was developed.
- A visible light sensor with near photopic responsivity was employed.
- For people or flame detection a thermopile based IR sensor was developed.
- A photovoltaic energy harvester based on black-Si, IDES back electrodes and Al_2O_3 as double sided passivation was developed.
- A piezoelectric energy harvester based on transparent, flexible and thin PVDF films was developed.

- An electronic platform chip onto which the sensor devices are stacked and connected via TSV technology was developed.
- A microcontroller based on SoC technology to improve the current state of the art (2017), tenfold.

During the entirety of the project progress has been made on all sensor technologies, which were investigated in this project. In addition a wireless communication module was included in the ultra-low-power microcontroller, which was part of the final MSP demonstrator but not part of the CMOS platform chip. Only three technologies weren't able to reach the final technology readiness level (TRL) to be integrated onto the final demonstrator: the photovoltaic energy harvester, the piezoelectric energy harvester and the fine dust particle sensor. Furthermore, the UV A/B sensor as well as the GaN-based NO_2 gas sensor didn't reach the TSV integration level. As a result both connection technologies, TSV and wire-bonding, were applied within the demonstrator.
A bottle neck process for the realisation of this multi-sensor device was the overmolding process. Hereby, a film-assisted molding technology was applied. With this technology the entire demonstrator with its extremely challenging topography and fragile structures, was successfully overmolded. In figure 6.4 (a) the overmold tool used for the MSP demonstrator is shown. Figure 6.4 (b) shows the product of the overmold process. Areas, which need direct access to the environment (e.g. gas sensitive material) are left untouched.

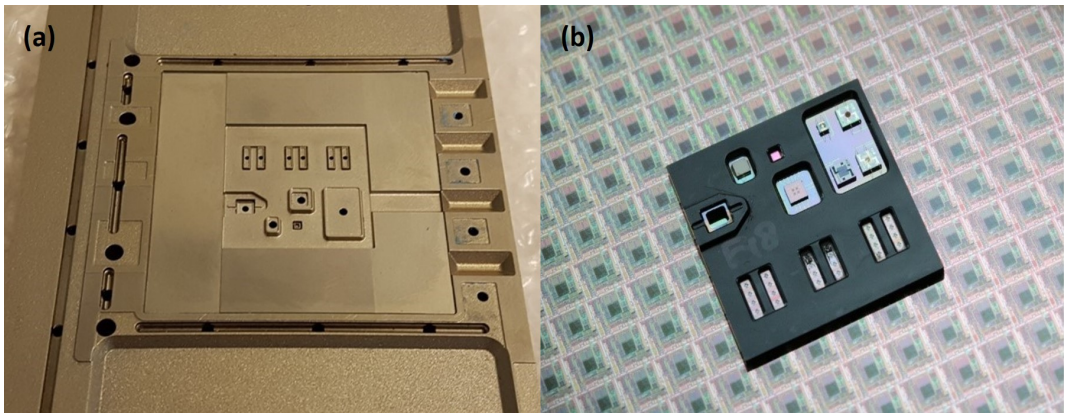

Figure 6.4.: (a) Overmold tool fabricated for the application on the MSP demonstrator. (b) Overmolded MSP demonstrator chip prior to assembly on evaluation PCB.

The sensors which made it to the MSP demonstrator are as follows:

- Three MPW4 CMOS chips containing 48 metal oxide gas sensors on 24 different microhotplates for CO, CO_2 and VOC gas sensing.
- One GaN/AlGaN 2D-electron gas detector build on an GaN-on-Si microhotplate for NO_2 gas sensing.
- One graphene oxide humidity sensor.
- A pre-calibrated temperature sensor.
- A UV A/B sensor based on SiC technology.
- A visible light sensor with near photopic responsivity.
- A silicon based thermopile infra-red sensor.
- Two gas metal oxide gas sensors on a SiN microhotplate for CO and VOC gas sensing.
- A SnO_2 nanowire based gas sensor for O_3 gas sensing.

Figure 6.5 depicts a detailed description of all employed sensors, which were stacked on the MSP demonstrator platform chip and overmolded. In its final form the MSP demonstrator was planned as a wearable. Figure 6.6 (a) shows the packaged device, which can be worn as a wristband. The interior of the packaged device is seen in figure 6.6 (b). Therein, the multi-sensor platform with a micro-controller with wireless connectivity can be seen. The resulting device is a low power device, which to the knowledge of the author is a worldwide unique device.

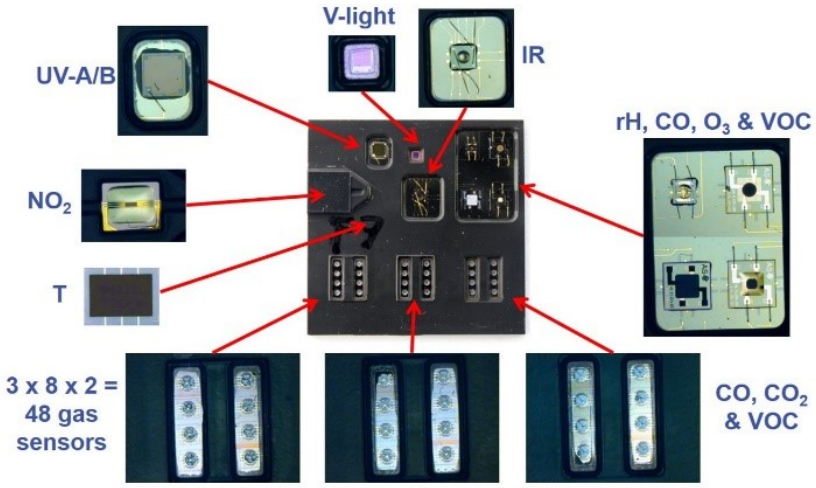

Figure 6.5.: Detailed depiction of the all sensor directly integrated on the CMOS platform chip. Sensor types: 53 gas sensors targeting rH, O_3, CO, CO_2, VOC and NO_2, 3 optical sensors measuring UV-A/B, infrared light (IR, thermopile) and visible light (V-light), 1 temperature sensor.

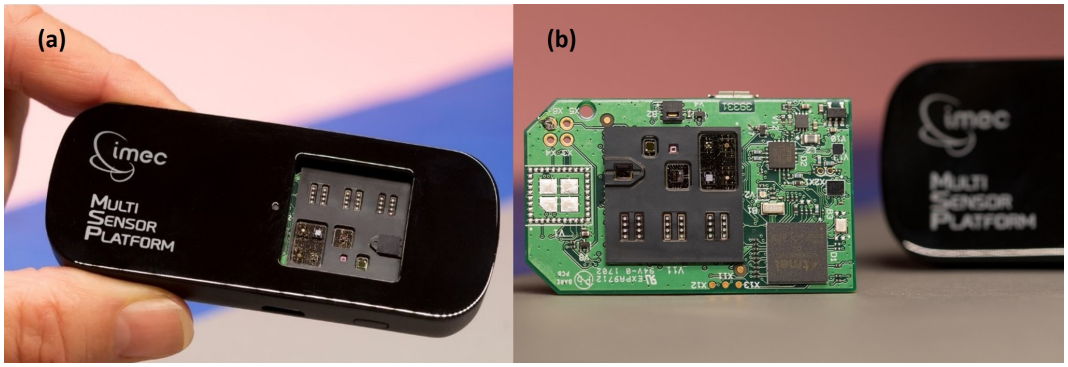

Figure 6.6.: (a) Picture of the final MSP demonstrator: a wearable wristband device. (b) PCB of MSP demonstrator including multi-sensor platform, micro-controller with wireless connectivity.

The central achievement of the MSP project was to establish a full manufacturing chain ranging from sensor processing, to device stacking up to the overmolding process of the final 3D-integrated device. Alongside this project goal the sensor development has been affected greatly, as can be

seen following the example of the CO_2 gas sensor development done within this work. The application of the MSP device or its underlying process experience can influence multiple areas of life. Within its intended area, indoor air quality monitoring a massive reduction in energy can be achieved in respect to HVAC systems. The devices capabilities can also be expanded towards outdoor air quality monitoring as well. Hereby, its multiple sensors can be used to achieve more reliable air quality measurements and even warn its wearer if he or she is exposed to elevated levels of air pollutants. Furthermore, gathered environmental data can be shared with others. This data can be used for pollution mapping and provide means for the population to avoid polluted areas.
The first step to bring this vision into the world would be a miniaturization of the CMOS platform chip as well as expanding its capability to operate an entire MPW4 gas sensor chip, hence 16 gas sensors. In case both CMOS chips could be fabricated with the same footprint a wafer-to-wafer bonding process would be feasible. Hereby, one wafer contains only MPW4 gas sensor chips, whereas wafer 2 only contains the improved CMOS platform chip. After both wafers are stacked upon each other, bonded and connected via TSV technology. A consecutive overmolding process (”wafer level molding”), followed by a dicing step would conclude this manufacturing chain resulting in a single, fully operable MPW4 gas sensor array. Furthermore, this gas sensor array would provide the basis for the wide spread of gas sensors applicable in numerous markets.

Appendix A.

List of chemicals

Table A.1.: Chemicals used for fabrication of the spray pyrolysis solutions.

No.	Name	Formula	Grade	Supplier
(1)	Tin (IV) chloride pentahydrate	$SnCl_4 \cdot 5H_2O$	$\geq$ 98%	Sigma-Aldrich
(2)	Ethyl acetate	$CH_3COOC_2H_5$	$>$ 99.5%	Carl Roth
(3)	Copper chloride dihydrate	$CuCl_2 \cdot 2H_2O$	ACS reagent,$\geq$ 99%	Sigma-Aldrich
(4)	Copper acetate monohydrate	$Cu(COOH_3) \cdot H_2O$	ACS reagent,$\geq$ 99%	Carl Roth
(5)	Copper nitrate trihydrate	$Cu(NO_3)_2 \cdot 3H_2O$	puriss. pa, 99% – 104%	Sigma-Aldrich
(6)	Ethanol	C_2H_5OH	Gradient grade LC	Merck
(7)	Aceton	CH_3COCH_3	$\geq$ 99.7% Ph.Eur., reinst	Carl Roth
(8)	Zinc acetate dihydrate	$Zn(COOCH_3)_2 \cdot 2H_2O$	ACS reagent $\geq$ 99.5%	Carl Roth

Continued on next page

Table A.1 – *Continued from previous page*

No.	Name	Formula	Grade	Supplier
(9)	Hydrochloric acid	HCl	ACS reagent 37%	Sigma-Aldrich
(10)	Isopropanol (2-Propanol)	C_3H_7OH	LC-MS-Grade $\geq$ 99.95%	Carl Roth

Appendix B.

Materials and tools

Tables B.1 and B.3 list most of the tools, materials and service providers used for the fabrication and evaluation of gas sensing materials. Table B.2 lists all test gases used for gas sensor evaluation at the Material Center Leoben (MCL).

Table B.1.: Tools used for the fabrication and evaluation of the thin films.

Label	Manufacturer	Description
White light reflectometer	Filmetrics a KLA company	Type: F40-NSR
Light microscope	Carl Zeiss AG	Axio Scope.A1
Electron beam lithography	Raith GmbH (utilized at University of Graz)	eLine Plus
Thermal evaporation	Leybold GmbH	Univex Evaporator 450
Wire bonding	F&K DELVOTEC Bondtechnik GmbH	Wirebonder 5550 (gold wires)
Mass flow controllers	Bronkhorst High-Tech B.V	various models
Source measure unit	Tektronix Inc.	Keithley 2400
Voltage source	Thurlby Thandar Instruments	PL330P
Digital multimeter	Keysight technologies	34401A

Table B.2.: Test gases used for gas sensor evaluation at gas measurement set-up (MCL).

Test gas	**Manufacturer**	**Description**
Carbon monoxide (CO)	Linde Gas GmbH	CO (900 ppm) + N_2 (rest of bottle volume)
Carbon dioxide (CO_2)	Linde Gas GmbH	CO_2 (2.5 Vol.%) + N_2 (rest of bottle volume)
Hydrocarbon mixture (HCMix)	Linde Gas GmbH	acetylene (500 ppm) + ethane (500 ppm) + ethene (500 ppm) + propene (500 ppm) + N_2 (rest of bottle volume)

Table B.3.: Materials and service providers used for the fabrication of gas sensors

Label	**Manufacturer/Service Provider**	**Description**
Metals (thermal evaporation)	MaTecK - Material-Technologie & Kristalle GmbH	Cu, Zn, Ti
Mikroheater	Delta-R GmbH AG	Pt6.8
Thermocouple	Delta-R GmbH AG	Pt100
Thermal conductive adhesive	T-E-Klebetechnik	Ceramabond 865
Electrode deposition	Siemens AG (Munich)	deposition of Au and Pt electrodes onto MPW4 chips
Silicon release etch	memsstar Limited	XeF_2 release etch of MPW3 and MPW4 chips

Appendix C.

Instruments for characterization

Instrument description for SEM and Raman characterization is taken from [238]. The instrument description of XRR is based on [253].

Scanning Electron Beam Microscopy: The scanning electron microscopy (SEM) investigation was done on an Auriga® -CrossBeam® Workstation (Carl Zeiss Microscopy GmbH) with an acceleration voltage of 10 keV. The surface investigations at high magnification and the elemental mapping were done on a ZEISS GeminiSEM 450 at 3 keV and 5 keV.

Raman Spectroscopy: The Raman spectrum was measured with LabRAM HR800 from Horiba Jobin Yvon. A green (514.5 nm) Ar-ion laser in backscattering geometry was used as an excitation source. The analysis of the Raman signal was performed with a grating (1800 g/mm), whereas the signal detection was done by a multichannel CCD.

Atomic force microscope (AFM): The AFM measurements presented in this work are done on DME (Danish Micro Engineering), model 2770. This AFM can be applied as an option for FE-SEMs.

X-ray reflectivity (XRR): The instrument used for x-ray reflectivity measurements is a PANalytical EMPYREAN Reflectometer. The x-ray radiation is generated in the x-ray tube with a copper anode. The radiation emitted at the CuKα line has a wavelength of 0.15418 nm. The beam emitted from the primary side (radiation source) is collimated by a multilayer mirror. The detection at the secondary side is performed by a PANalytical PIXcel 3D detector. Before entering the detector the beam passes through the receiving slit (Soller slit). The software X'Pert Reflectivity 1.3 is employed for the fitting of the XRR data.

X-ray diffration (XRD): X-ray diffraction was performed with an PANalytical EMPYREAN diffractometer using a sealed X-ray tube with a copper anode. On the primary side, a multilayer X-ray mirror was used for monochromatisation and to generate a parallel beam in combination with a divergence slit of 1/8° and a fixed beam mask of 4 mm. On the secondary side, a 7.5 mm anti-scatter slit and 0.02 rad Soller slit were used with a PANalytical PIXcel 3D detector acting as a one-dimensional detector with 255 active channels.

Transmission electron microscopy (TEM): The TEM pictures shown in this work were done at the Austrian Centre for Electron Microscopy and Nanoanalysis (FELMI). The pictures were made with a FEI Tecnai F20 by FEI Company (Thermo Fischer Scientific Inc.).

Appendix D.

Scientific paper

At the end of this thesis the publication ”CuO Thin Films Functionalized with Gold Nanoparticles for Conductometric Carbon Dioxide Gas Sensing” is attached. The contributions of the authors are as follows. The overall concept of the underlying work was done by Robert Wimmer-Teubenbacher and Anton Köck. The nanoparticles used for the functionalization of the CuO thin film were provided by Jan Steffen Niehaus and Oeznur Tokmak. The gas sensors were fabricated by Robert Wimmer-Teubenbacher. The various gas measurements were done by Robert Wimmer-Teubenbacher, Florentyna Sosada-Ludwikowska and Bernat Zaragoza Travieso. The presented Raman measurement was done by Marco Deluca. The evaluation of the measurements were done by Robert Wimmer-Teubenbacher, Florentyna Sosada-Ludwikowska, Marco Deluca and Stefan Defregger. All authors contributed to the writing process of this publication.

Appendix E.

Patent

In course of this thesis the author contributed to two patents. The first patent is already granted, whereas the second patent was filed.

The first patent: "Sensor arrangement for determining and optionally measuring a concentration of several gases and process for producing a sensor arrangement."
Austrian patent number: AT519492B1
Filed on: 22^{th} December, 2016
Granted on: 15^{th} March, 2019

The second patent: "Verfahren zur Herstellung eines Sensors und hiermit hergestellter Sensor."
Austrian patent application number: A 50377/2018
Filed on: 4^{th} May, 2018

List of Figures

1.1. Publication search on ”metal oxides” on Web of Science. Period: 1988-2018 [12] 21
1.2. Rutile crystal structure of tin dioxide (SnO_2). Taken from [81]. 23
1.3. Monoclinic crystal structure of copper (II) oxide (CuO). Taken from [111]. 25
1.4. Hexagonal (wurtzite) crystal structure of zinc oxide (ZnO). Taken from [133]. 27
1.5. Resistance change of an n-type metal oxide gas sensor upon exposure to a reducing gas. $R_{response}$ is 90% of the R_{gas} resistance value. $t_{response}$ is the time the gas sensor needs to reach $R_{response}$, after the onset of the gas pulse. $R_{recovery}$ is the resistance value 10% below the R_{air} resistance value. $t_{recovery}$ is the time the gas sensor needs to reach $R_{recovery}$, after the end of the gas pulse. 30
1.6. Temperature dependent occurrence of oxygen ion species. Ambient oxygen $O_{2(gas)}$ adsorbs to surfaces sites S by physisorption forming $O_{2(phys)}$, which dissociates at higher temperatures. Below 200 °C molecular ionic oxygen species O_2^- is predominate. Above 200 °C atomic ionic oxygen species (O^-, O^{2-}) are mainly available. According to Barsan et al.[136]. 34

1.7. Ionosorbed oxygen induces surface states on the n-type MOX surface resulting in a band bending of the electronic structure and formation of a depletion layer. Bulk: conduction band $E_{C,b}$, valence band $E_{V,b}$, χ electron affinity, ϕ work function, $\Delta\phi$ band bending. Surface: conduction band $E_{C,S}$, valence band $E_{V,S}$, donor level $E_{d,S}$, surface charge Q_{SS}, ionosorbed oxygen species $O^{-\alpha}_{\beta S}$, ambient oxygen $O_{2(gas)}$, physisorbed oxygen $O_{2(phys)}$. Bulk/surface: vacuum energy E_{vac}, Fermi level E_F. z_0 dimension of depletion layer. According to Barsan et al.[136]. 36
1.8. (a) Space charge layers formed at the surface of three consecutive MOX grains as a result of ionosorbed oxygen. (b) At the grain boundaries of the three grains a Schottky double potential is formed. The height of the potential barrier is eV_S. The three control mechanisms for electron conduction through MOX materials: (c) grain boundary control $D >> 2L_d$, (d) neck control $D \sim 2L_d$ and (e) grain control $D < 2L_d$ (D grain size, L_d space charge layer thickness). According to Yamazoe et al.[139]. 39
1.9. Ionosorbed oxygen induces surface states on the p-type MOX surface resulting in a band bending of the electronic structure and formation of accumulation layer. Energy levels: vacuum energy E_{vac}, conduction band E_C, Fermi level E_F, acceptor level E_A, valence band E_V. χ is the electron affinity, ϕ the work function and $\Delta\phi$ is the band bending. The ionosorbed oxygen states are entitled as $O^{-\alpha}_{\beta S}$. The physisorption of gaseous oxygen $O_{2(gas)}$ to form physisorbed oxygen $O_{2(phys)}$ is marked by an arrow. z_0 defines the dimension of the accumulation layer. According to Barsan et al. [142]. 41
1.10. Grain boundary of a p-type material depicting the double Schottky potential and the accumulation layer. qV_S is the barrier height of the double Schottky potential. The accumulation layer is shown as a highly concentrated hole area beneath the double Schottky potential. Energy levels: E_F is the fermi level, E_A is the acceptor level, E_V is the valence band. According to Barsan et al.[142]. 41

1.11. (a) n-type MOX grains with electron depletion layer (grey) formed by ionosorption of oxygen. Electron depletion layer possesses a high electrical resistance R_{High}. The semiconducting core (orange) of the grains has a low electrical resistance R_{Low}. (b) p-type MOX grains with hole accumulation layer (green) formed by ionosorption of oxygen. Hole accumulation layer posseses a low electrical resistance R_{Low}. The insulating core (dark grey) has a high electrical resistance R_{High}. Between both n-type and p-type grains a double Schottky potential barrier is formed. According to Kim et al.[141] . . . 43
1.12. (a) Percolation path of majority charge carrier (electrons) through two n-type MOX grains (blue arrow). Left side: Ionosorption of oxygen at the MOX surface leading to the formation of an electron depletion layer. Right side: Chemical reaction of ionosorbed oxygen O^- and CO resulting in CO_2, thereby changing the thickness of the electron depletion layer. (b) Equivalent circuit scheme depicting the total resistance as a serial circuit. The total resistance is the sum of the resistance of the electron depletion layer and the semiconducting core. According to Kim et al.[141] 44
1.13. (a) Percolation path of majority charge carrier (holes) through two p-type MOX grains (blue arrow). Left side: Ionosorption of oxygen at the MOX surface leading to the formation of a hole accumulation layer. Right side: Chemical reaction of ionosorbed oxygen O^- and CO resulting in CO_2, thereby changing the thickness of the hole accumulation layer. (b) Equivalent circuit scheme depicting the total resistance as a parallel circuit. The total resistance is the reverse sum of the reverse resistance of the hole depletion layer and the reverse resistance of the semiconducting core. According to Kim et al.[141] 46
1.14. Energy levels of two surface states. Energy levels: E_D bulk donor level, E_A bulk acceptor level, E_{S1} and E_{S2} surface acceptor levels. Energies: ΔE_G band gas energy, ΔE_D ionisation energy for donor levels, ΔE_A ionisation energy from bulk acceptor level. According to Henshaw et al.[145] 50

1.15. Cross-section of a metal oxide nanowire with diameter D_{NW}. (a) No oxygen is adsorbed to the nanowire surface. The conduction channel diameter $D_{channel}$ is equal to the nanowire diameter. (b) Ambient oxygen is ionosorbed at the nanowire surface. At the surface a depletion layer is formed with thickness L_d. The diameter of the conduction channel is decreased as result of the formed depletion layer. (c) Upon exposure to a test gas (reducing gas) a chemical reaction between test gas and ionosorbed oxygen occurs, resulting in the increase of the conduction channels diameter. According to Miller et al.[148] 54
1.16. Conduction path across multiple nanowires with diameter D_{NW}. The electrons move along the nanowires longitudinal axis as well as across nanowire junctions (yellow line). The two major contributions to the total electrical resistance are nanowire resistance (eq.1.24) and nanowire junction resistance (eq.1.7). According to Miller et al.[148] 55
1.17. (a) Double Schottky potential of a nanowire homo-junction (n-type MOX material) at ambient atmosphere V_{Air}. (b) Double Schottky potential after exposure to a reducing test gas V_{Gas}. The thickness of the depletion layer L_d at the nanowire junction is shown as a grey rectangle. Energy levels: E_C is the conduction band, E_F is the Fermi level and E_V is the valance band. According to Miller et al.[148] 56
1.18. Effect of nanoparticle functionalization on a nanowire surface. (a) Formation of an electron depletion layer at the boundary between nanoparticle and nanowire (Schottky barrier). (b) Electronic sensitization: the metallic nanoparticle M reacts with a test gas. Additional charges necessary for the chemical reaction are drawn from the nanowire. The depletion layer is extended (c) Chemical sensitization: the metallic nanoparticle M acts as a catalyst. Reaction products spill over to the nanowire surface. The spilled over products interact with the nanowire surface extending the electron depletion layer. The extension of the depletion layer is called spill over zone. According to Kolmakov[146] 58

1.19. Division of gases into eight groups according to their properties to interact with a sensor surface. Gases with similar surface reactions are grouped. Furthermore, the groups are classified by decreasing first ionization potential and increasing proton affinity. Taken from Krivetskiy et al.[177, chapter 3] 60
1.20. Atmospheric carbon dioxide concentration over the last 10 years (May 2008 - April 2019)[192]. The modulation of the concentration over a single year is a result of the seasonal change of the CO_2 concentration in the atmosphere. 70
1.21. Spillover process at the surface of a Pd metal nanoparticle by the example of oxygen dissociation. Gaseous oxygen ($O_{2(gas)}$) is dissociated at the Pd surface. The products (O_S) spill over to the MOX surface and form ionosorbed oxygen species (O_S^-, O_{2S}^-). According to Korotcenkov [208]. 78
1.22. Spillover zones encircling Pd metal particles on a tin dioxide surface. According to Korotcentkov et al. [209]. 79
1.23. Comparison of pristine and functionalized tin dioxide grain upon oxygen and test gas exposure. Upper: (Left) Pristine tin dioxide exposed to oxygen. The ionosorbed oxygen results in the formation of an electron depletion layer, with thickness L_d. The areas marked with dashed line represent the semiconducting core of the tin dioxide grain. (Right) After exposure to a reducing gas all ionosorbed oxygen species are removed. The electron depletion layer is gone. Lower: (Left) Tin dioxide functionalized with palladium exposed to oxygen results in a thicker depletion layer and the oxidation of Pd. (Right) After exposure to a reducing gas PdO is reduced to Pd and the electron depletion is gone. According to Yamazoe[139]. 81

2.1. Deposition of droplets as a function of increasing substrate temperature. Process (A): the droplets impinge on the substrate surface. Process (B) the precipitate impinges on substrate surface and decomposes (non uniform deposition). Process (C) the melted and vaporized precipitate chemically reacts with the substrate surface (continuous deposition). Process (D) the powdery target material is deposited on the substrate surface (low adhesion). According to Vigui et al.[212]). 87
2.2. Spray pyrolysis: Three possible trajectories during film growth. (1) Direct impact of droplets onto the substrate surface. A part of the droplets contribute to the film formation. The other part of the droplets is either formed to powder after passing the deposition area (2) or vented (3). According to Sears et al.[226]) 92
2.3. Set-up of a two-fluid spray pyrolysis set-up. Right side: Hotplate with the substrate on top. Left side: Spraying nozzle has three feeds for N_2 carrier gas, compressed air and spraying solution reservoir. The flow from the carrier gas and spraying solution reservoir are mixed in the nozzle. The compressed air is used to start and stop the spraying process. According to Mutinati [24]) 92
2.4. Cross-section of an air atomizing nozzle from Spraying Systems Co. / model: Quickmist 1/4QMJ [227] before (a) and during the spraying process (b). In (a) the needle blocks the flow from the liquid inlet into the fluid cap. Only nitrogen from the air inlet can pass through the nozzle exit (blue cone). In (b) the needle is retracted leading to the mixture of spraying liquid and nitrogen in the fluid cap and an atomization of the mixture through the nozzle exit (green/blue cone). . . 94
2.5. Air cap types for the air atomizing nozzle Quickmist 1/4QMJ [227]. 94
2.6. PRÄZITHERM High temperature hotplate with control unit [228] 96
2.7. Schematic representation of a full spray pyrolysis cycle. (Left) Procedure applied to start the MOX deposition on a substrate. (Center) MOX deposition of thin film. (Right) Procedure followed after the MOX deposition. 97

2.8. Electron beam lithography design of copper oxide nanowire array [29]. 108
2.9. Electron beam lithography design of zinc oxide nanowire array [29]. 108
2.10. Multilayer system formed during the thermal oxidation of a copper foil. (a) $T_{oxidation} \leq 300^{\circ}C$ growth promoted by grain boundary diffusion. (b) $T_{oxidation} \approx 400^{\circ}C$ - $700^{\circ}C$ growth promoted by sub-boundary diffusion. (c) $T_{oxidation} \geq 800^{\circ}C$ growth promoted by lattice diffusion. According to Xu et al.[234] 111
2.11. Growth mechanism of copper oxide nanowires during thermal oxidation. Formation of a multilayer system of Cu, Cu_2O, CuO and CuO nanowires. The nanowire growth is driven by diffusion of copper ions (red dots) along the grain boundaries of Cu_2O and CuO. On the CuO surface CuO nanowires are formed. A continuous flux of copper ions ensures the further growth of the CuO nanowires with oxygen from the ambient atmosphere. According to Chen et al.[235] 112
2.12. Growth mechanism of zinc oxide nanowires during thermal oxidation. (a) Hexagonal crystal structure of metallic zinc layer before oxidation (top view and side view). (b) Formation of zinc oxide layer and zinc oxide nanowire seeds during thermal oxidation. (c) The zinc oxide nanowire growth is fed by a flux of zinc ions from the subsiding zinc layer to the surface, where the oxidation occurs. According to Zhao et al.[236] 115

3.1. Process steps for electrode system fabrication. 118
3.2. Process flow for thin film gas sensor fabrication for silicon based gas sensors. 119
3.3. Process flow for nanowire array gas sensor fabrication for silicon based gas sensors. 120
3.4. The five process steps of gas sensor assembly and conditioning. 122

3.5. Final product of silicon based gas sensor fabrication. (a) Camera picture of the evaluation PCB with the attached gas sensor stack. The gas sensors itself are wire bonded (Au wires) to the PCB. (b) Optical microscope picture of a single gas sensor on the sensor stack. The gas sensor is made of the electrode system and the gas sensitive material (CuO thin film). 123
3.6. Scanning electron microscope picture of a microhotplate showing the spider structure and the etched cavity beneath it. This mircohotplate is part of a MPW4 CMOS chip. The two rectangles on the membrane are two gas sensing layers (SnO_2). Each gas sensing layer is contacted with four electrodes enabling a 4 wire measurement. 126
3.7. Schematic representation of a cross-section of the membrane stack with its general layer composition. 126
3.8. Process flow of (a) thin film gas sensor fabrication on MPW3 CMOS chip and (b) nanowire array gas sensor fabrication on MPW4 CMOS chip. 132
3.9. Schematic representation of the gas system of the gas measurement set-up. The upper three blocks define the gas intake. Two test gases can be set individually. Each test gas block is made of three mass flow controller to provide precise test gas concentrations. The block background gas defines the overall adjustment of the relative humidity level by mixing dry and water enriched air. A relative humidity sensor positioned before the test chamber is used in a feedback loop configuration with the background gas to ensure precise relative humidity levels. 134
3.10. Schematic representation of the electrical system of the gas measurement set-up. The four blocks surrounding the test chamber define different measurement devices needed to measure the gas sensors resistance, to apply voltage to the heater and to measure the heaters temperature via thermocouple. In the case of the MPW3 chip an additional device is needed to release the ESD protection. 135

4.1. Camera picture and AFM measurement of a SnO_2 thin film sample. 139

4.2. X-ray reflectivity measurement of a SnO_2 thin film. 139
4.3. Transmission electron microscope investigation of SnO_2 thin films on a CMOS microhotplate (left) and on a silicon substrate (right). 140
4.4. Microscope picture of a silicon substrate coated with a cupric oxide thin film. The CuO thin film was deposited at a deposition temperature of 400°C. 142
4.5. Scanning electron microscope picture of a cupric oxide thin film at 300 x magnification. A single pillar structure (height, width: several μm) is marked with a white circle. 143
4.6. Scanning electron microscope picture of a cupric oxide thin film at 3000x magnification. 144
4.7. Energy-dispersive x-ray spectrum of the cupric oxide thin film fabricated at a deposition temperature of 400°C. 145
4.8. X-ray diffraction pattern of a CuO thin film prepared by spray pyrolysis. The black pattern shows the measured pattern. The blue pattern is the reference pattern taken from the Inorganic Crystal Structure Database (ICSD) of cupric oxide with the reference code 010-080-0076. The reference pattern is marked with the Miller indices of crystallographic lattice planes found for cupric oxide. The two silicon peaks from the lattice plane (400) are attributed to the silicon substrate. 146
4.9. (a) Magnified CuO pillar structure (inset) on CuO thin films deposited by spray pyrolysis. (b) EDX spectrum of the area marked by the red dot on the pillar structure. 147
4.10. AFM measurement of a cupric oxide thin film deposited by spray pyrolysis at a deposition temperature of 300°C. (Right) Topography of an area of 2 x 2 μm. (Left) Linescan over a length of 2 μm marked by blue arrow in picture. 148
4.11. AFM measurement of a cupric oxide thin film deposited by spray pyrolysis at a deposition temperature of 400°C.(Right) Topography of an area of 2 x 2 μm. (Left) Linescan over a length of 2 μm marked by blue arrow in picture. 148
4.12. Focussed ion beam cut of a cupric oxide layer deposited on silicon substrate with an silicon dioxide layer on top. SEM pictures of the layer system with additional layer thickness measurement of CuO and SiO_2 layers. 150

4.13. SEM picture of the thermally oxidised copper structures. Oxidation temperature 400°C. 152
4.14. Raman spectrum of the thermally oxidised copper structures forming a continuous copper oxide layer (see fig.4.13). The copper structures are oxidized at 400°C. 152
4.15. SEM investigation of CuO surface decorated with gold nanoparticles. The insert shows a TEM image of a single gold nanoparticle. 154
4.16. Elemental mapping of the CuO surface decorated with Au nanopartilces (Area 4 μm x 4μm / E = 5 keV). (a) Au elemental map, (b) Cu elemental map, (C) O elemental map and (d) Si elemental map. 154
4.17. Energy-dispersive x-ray spectrum of a single Au nanoparticle on the CuO surface recorded at 5 keV. 155
4.18. Light microscopy picture of zinc oxide thin film deposited by spray pyrolysis at 400°C. Precursor solution: zinc acetate in ethanol. 156
4.19. Light microscopy picture of zinc oxide thin film deposited by spray pyrolysis at 400°C. Precursor solution: zinc acetate in water. 157
4.20. Light microscopy picture of zinc oxide thin film deposited by spray pyrolysis at 400°C. Precursor solution: zinc acetate in mixture of water and ethanol (1:3) 157
4.21. SEM picture of a zinc oxide layer at a magnification of 300x. Precursor solution: zinc acetate in water/ethanol mixture. Deposition temperature: 400°C. Structures visible on picture: a dot like structure showing a density variation, a pin hole and mounds. The mounds are either fragments of the layer or areas of extended growth. 158
4.22. SEM picture of a zinc oxide layer at a magnification of 30000x. Precursor solution: zinc acetate in water/ethanol mixture. Deposition temperature: 400°C. The fine structure of the layer consists close packed elongated islands. 159
4.23. Energy-dispersive x-ray spectrum of the zinc oxide thin film on a silicon / silicon dioxide substrate (top layer, thickness: 300 nm). Layer composition: zinc, oxygen and silicon. 160

4.24. AFM measurement of a zinc oxide thin film deposited by spray pyrolysis at 400°C. Topography of an area of 2 μm x 2 μm. 160

5.1. Measurement routine for gas sensor evaluation. (I) Three different operation temperature levels are applied. At each operation temperature (II) three relative humidity (rH) levels are set and at each rH level (III) four different gas concentrations are applied. 162
5.2. (a) CO_2 measurements of pristine and Au-NPs functionalized CuO thin film gas sensors at an operation temperature of 300°C and rH levels of 25%, 50% and 75%. (b) CO_2 gas concentrations: 250 ppm, 500 ppm, 100 ppm, 1500 ppm and 2000 ppm. 164
5.3. CO_2 measurement of pristine CuO thin film gas sensor at operation temperatures of 300°C, 350°C and 400°C and relative humidity levels of: (a) 25% (b) 50% (c) 75%. (d) CO_2 gas pulse with a concentration of 2000 ppm. 165
5.4. CO_2 measurement of Au-NPs functionalized CuO thin film gas sensor at operation temperatures of 300°C, 350°C and 400°C and relative humidity levels of: (a) 25% (b) 50% (c) 75%. (d) CO_2 gas pulse with a concentration of 2000 ppm. . . 166
5.5. Comparison of the pristine (black) and the Au-NPs functionalized (red) gas sensors sensitivities towards a CO_2 concentration of 2000 ppm at relative humidity levels of 25%, 50% and 75% and an operation temperature of 300°C. 167
5.6. (a) CO measurements of Au-NPs functionalized CuO thin film gas sensors at an operation temperature of 300°C and rH levels of 25%, 50% and 75%. (b) CO gas concentrations: 10 ppm, 50 ppm, 100 ppm, 150 ppm and 200 ppm. 168
5.7. Comparison of Au-NPs functionalized gas sensor towards the highest concentration of CO_2 (2000 ppm) and CO (200 ppm) at relative humidity levels of 25%, 50% and 75%. 169

5.8. ZnO nanowire array. (a) Sensor resistance (black) as a function of time at $T_{operation}$ = 350°C. The relative humidity levels 25%, 50% and 75% are depicted by a dashed blue line. (b) Gas pulse sequence of four CO concentrations (10 ppm, 33 ppm, 58 ppm and 100 ppm). 171
5.9. ZnO nanowire array. (a) Sensor resistance (black) and relative humidity (blue) as a function of time at $T_{operation}$ = 350°C. (b) Gas pulse sequence of four HCMix concentrations (10 ppm, 70.1 ppm, 130.1 ppm and 200.2 ppm). 172
5.10. ZnO NW arrays' sensitivities towards the highest concentration of (a) CO (100 ppm) and (b) HCMix (200.2 ppm) at relative humidity levels: 25%, 50% and 75%. 173
5.11. CO measurement of the CMOS integrated Au-NPs functionalized SnO_2 thin film gas sensor at an operation temperature of 300°C. CO levels: 7 ppm, 20 ppm, 40 ppm, 80 ppm and 160 ppm. rH levels: 45% rH and 73% rH. 175
5.12. CO measurement of the CMOS integrated Au-NPs functionalized SnO_2 thin film gas sensor at an operation temperature of 400°C. CO levels: 7 ppm, 20 ppm, 40 ppm, 80 ppm and 160 ppm. rH levels: 45% rH and 73% rH. 176
5.13. (a) Comparison of the CMOS integrated Au-NPs functionalized SnO_2 thin film gas sensors' sensitivity towards a CO concentration of 160 ppm at 300°C and 400°C at a low rH (45%) and a high rH (73%). (b) Comparison of three repetitions of a CO concentration of 7 ppm at conditions described in (a). 178
5.14. HCMix and ethanol measurements of the CMOS integrated Au-NPs functionalized SnO_2 thin film gas sensor at an operation temperature of 300°C. HCMix and ethanol: 50 ppm. rH levels: 31% rH and 84% rH. 179
5.15. HCMix and ethanol measurements of the CMOS integrated Au-NPs functionalized SnO_2 thin film gas sensor at an operation temperature of 400°C. HCMix and ethanol: 50 ppm. rH levels: 25% rH and 78% rH. 180

5.16. Comparison of the CMOS integrated Au-NPs functionalized SnO_2 thin film gas sensors' sensitivity towards an (a) ethanol concentration and a (b) HCMix concentration of 50 ppm at 300°C with low rH (31%) and a high rH (84%) and 400°C with low rH (25%) and a high rH (78%). 182

6.1. SEM picture of a fail thermal oxidation of ZnO nanowires. Parts of the gold electrodes form a intermetallic phase with the zinc during thermal oxidation, thereby hindering the formation of zinc oxide nanowires. 190
6.2. Picture of a fully processed MPW4 gas sensor chip (8 micro hotplates) bonded on a PCB for evaluation. 195
6.3. Schematic drawing of the envisioned MSP demonstrator device. 198
6.4. (a) Overmold tool fabricated for the application on the MSP demonstrator. (b) Overmolded MSP demonstrator chip prior to assembly on evaluation PCB. 200
6.5. Detailed depiction of the all sensor directly integrated on the CMOS platform chip. Sensor types: 53 gas sensors targeting rH, O_3, CO, CO_2, VOC and NO_2, 3 optical sensors measuring UV-A/B, infrared light (IR, thermopile) and visible light (V-light), 1 temperature sensor. 201
6.6. (a) Picture of the final MSP demonstrator: a wearable wrist-band device. (b) PCB of MSP demonstrator including multi-sensor platform, micro-controller with wireless connectivity. . 201

List of Tables

1.1. Typical metal oxide materials and morphologies used for gas sensing. 21
1.2. Material properties and crystallographic parameters of tin dioxide (SnO_2) [79] [50] [80]. 23
1.3. Material properties and crystallographic parameters of cupric oxide (CuO) [79] [85] [111]. 24
1.4. Material properties and crystallographic parameters of zinc oxide (ZnO) [79]. 26
1.5. Fabrication methods for metal oxide nanowires [150]: 59
1.6. Organic compounds subdivided into four classes by WHO (Table according to Seifert [194]): 72

2.1. List of various spray pyrolysis methods [212]. 88
2.2. Parameters of spray pyrolysis set-up for SnO_2 thin film deposition. 98
2.3. Different copper salts and solvents investigated for applicability of spray pyrolysis process for CuO. 100
2.4. Final parameters of spray pyrolysis set-up for CuO thin film deposition. 102
2.5. Final parameters of spray pyrolysis set-up for ZnO thin film deposition. 103
2.6. Parameters of a standard photolithography resist. 106
2.7. Parameters for cupric oxide nanowire array or cupric oxide thin film fabrication. 113
2.8. Parameters for zinc oxide nanowire array fabrication. 116

3.1. Direct comparison of both CMOS chips MPW3 and MPW4. . 129

5.1. Average response and recovery times of the CMOS integrated Au-NPs functionalized SnO_2 thin film gas sensor measurements of CO, HCMix and ethanol. Both quantities are calculated at each operation temperature. The calculation is done according to the deliberation of section 1.2.1. 183

6.1. Gibbs free energy of formation for educts and products of malachite and azurite formation at 298.15 K and 1 bar. 187
6.2. Gibbs free energy for the reactions shown in equation 6.1 (malachite) and 6.2 (azurite) at 400 CO_2, 298.15 K and 1 bar. . 187

A.1. Chemicals used for fabrication of the spray pyrolysis solutions. 203

B.1. Tools used for the fabrication and evaluation of the thin films. 205
B.2. Test gases used for gas sensor evaluation at gas measurement set-up (MCL). 206
B.3. Materials and service providers used for the fabrication of gas sensors 206

Curriculum Vitae

Personal data

Name Robert Wimmer-Teubenbacher (née Teubenbacher)
Date of birth June 4^{th}, 1982
Place of birth Bruck an der Mur
Nationality Austria

Education

2014 - present
Doctoral program Physics
Graz University of Technology, Austria
2011 - 2013
Master program Technical Physics
Graz University of Technology, Austria
2004 - 2011
Bachelor program Technical Physics
Graz University of Technology, Austria

Career

2014 - present
Material Center Leoben Forschung GmbH, Austria
Department of Materials for Microelectronics
PhD student / Research staff
2013
Austrian Academy of Sciences, Austria
Space Research Institute
Master student
2011
Graz University of Technology, Austria
Solid State Physics Department
Bachelor student
2009- 2012
Spar Market Teubenbacher, Austria
Temporary help

Publication list

Conference contributions

1. Robert Wimmer-Teubenbacher, J. Krainer, E. Lackner, F. Sosada-Ludwikowska, K. Rohracher, E. Wachmann, K. Poulsen, J.S. Niehaus, and A. Köck. CMOS Integrable CuO Nanowire Array Gas Sensors Enhanced by Au - Nanoparticles for Humidity Independent Gas Sensing. *materialstoday: Proceedings*, 4(7):7149–7154, 2017
2. Robert Wimmer-Teubenbacher, E. Lackner, J. Krainer, S. Steinhauer, and A. Köck. Gas Sensor Devices based on CuO- and ZnO- Nanowires directly synthesized on silicon substrate. *MRS Advances*, 1(13):817–823, 2016
3. Robert Wimmer-Teubenbacher, S. Steinhauer, O. von Sicard, E. Magori, J. Siegert, K. Rohracher, C. Gspan, W. Grogger, and A. Köck. Gas Sensing Characterisation of CMOS Integrated Nanocrystalline SnO_2 – Au Thin Films. *materialstoday: Proceedings*, 2(8):4295–4301, 2015
4. J. Krainer, M. Deluca, E. Lackner, Robert Wimmer-Teubenbacher, F. Sosada-Ludwikowska, C. Gspan, K. Rohracher, E. Wachmann, and A. Köck. CMOS Integrated Tungsten Oxide Nanowire Networks for ppb-level H_2S Sensing. *Procedia Engineering*, 168:272–275, 2016
5. E. Lackner, J. Krainer, Robert Wimmer-Teubenbacher, F. Sosada-Ludwikowska, C. Gspan, K. Rohracher, E. Wachmann, and A. Köck. CMOS Integrated Nanocrystalline SnO_2 Gas Sensors for CO Detection. *Procedia Engineering*, 168:297–300, 2016
6. E. Lackner, J. Krainer, Robert Wimmer-Teubenbacher, F. Sosada-Ludwikowska, M. Deluca, C. Gspan, K. Rohracher, E. Wachmann, and A. Köck. Carbon monoxide detection with CMOS integrated thin film SnO_2 gas sensor. *materialstoday: Proceedings*, 4(7):7128–7131, 2017

7. J. Krainer, M. Deluca, E. Lackner, Robert Wimmer-Teubenbacher, F. Sosada-Ludwikowska, C. Gspan, K. Rohracher, E. Wachmann, and A. Köck. Hydrogen sulphide detection by CMOS integrated tungsten oxide nanowire networks. *materialstoday: Proceedings*, 4(7):7132–7136, 2017
8. F. Sosada-Ludwikowska, Robert Wimmer-Teubenbacher, and A. Köck. Dry process of transferring MOx nanowires used for gas sensing applications. *materialstoday: Proceedings*, 7(3):930–933, 2019

Journal contribution

1. Robert Wimmer-Teubenbacher, F. Sosada-Ludwikowska, B. Zaragoza Travieso, S. Defregger, O. Tokmak, J.S. Niehaus, M. Deluca, and A. Köck. CuO Thin Films Functionalized with Gold Nanoparticles for Conductometric Carbon Dioxide Gas Sensing. *Chemosensors*, 6(4):56, 2018

Bibliography

[1] J. Meurig Thomas. Sir Humphry Davy and the coal miners of the world: a commentary on Davy (1816) 'An account of an invention for giving light in explosive mixtures of fire-damp in coal mines'. *Philisophical Transactions A*, 373, 2015.

[2] K. Eschner. The Story of the Real Canary in the Coal Mine. [Online; accessed 6-May-2019], 2016.

[3] T. Seiyama, A. Kato, K. Fujiishi, and M. Nagatani. A new detector for gaseous components using semiconductive thin films. *Analytical Chemistry*, 34(11):1502–1503, 1962.

[4] N. Taguchi. Method for making a gas-sensing element, December 1971. US Patent 3,625,756.

[5] B.R. Eggins. *Chemical Sensors and Biosensors*, volume 28. John Wiley & Sons, 2008.

[6] C.-D. Kohl and T. Wagner. *Gas Sensing Fundamentals*. Springer, 2014.

[7] E. Comini, G. Faglia, and G. Sberveglieri. *Solid State Gas Sensing*, volume 20. Springer Science & Business Media, 2008.

[8] J.A. Duffy. Ionic- Covalent Character of Metal and Nonmetal Oxides. *The Journal of Physical Chemistry A*, 110(49):13245–13248, 2006.

[9] A.D. McNaught and A. Wilkinson. *Compendium of Chemical Terminology*, volume 1669. Blackwell Science Oxford, 1997.

[10] A.F. Holleman and E. Wiberg. *Lehrbuch der Anorganischen Chemie*. Walter de Gruyter GmbH & Co KG, 102 edition, 2007.

[11] J.A. Rodríguez and M. Fernández-García. *Synthesis, properties, and applications of oxide nanomaterials*. John Wiley & Sons, 2007.

[12] Web of Science -"metal oxide" publication search for the last 30 years (1988-2018).

[13] S. Ramanathan. *Thin film metal-oxides*. Springer, 2010.

[14] E. Lackner, J. Krainer, R. Wimmer-Teubenbacher, F. Sosada, C. Gspan, K. Rohracher, E. Wachmann, and A. Köck. CMOS integrated nanocrystalline SnO_2 gas sensors for CO detection. *Procedia Engineering*, 168:297–300, 2016.

[15] R. Wimmer-Teubenbacher, S. Steinhauer, O. von Sicard, E. Magori, J. Siegert, K. Rohracher, C. Gspan, W. Grogger, and A. Köck. Gas Sensing Characterisation of CMOS Integrated Nanocrystalline SnO_2–Au Thin Films. *Materials Today: Proceedings*, 2(8):4295–4301, 2015.

[16] V. Galstyan, E. Comini, C. Baratto, G. Faglia, and G. Sberveglieri. Nanostructured ZnO chemical gas sensors. *Ceramics International*, 41(10):14239–14244, 2015.

[17] N.B. Tanvir, O. Yurchenko, E. Laubender, and G. Urban. Investigation of low temperature effects on work function based CO_2 gas sensing of nanoparticulate CuO films. *Sensors and Actuators B: Chemical*, 247:968–974, 2017.

[18] S. Steinhauer, E. Brunet, T. Maier, G.C. Mutinati, A. Köck, O. Freudenberg, C. Gspan, W. Grogger, A. Neuhold, and R. Resel. Gas sensing properties of novel CuO nanowire devices. *Sensors and Actuators B: Chemical*, 187:50–57, 2013.

[19] B. Urasinska-Wojcik, T.A. Vincent, M.F. Chowdhury, and J.W. Gardner. Ultrasensitive WO_3 gas sensors for NO_2 detection in air and low oxygen environment. *Sensors and Actuators B: Chemical*, 239:1051–1059, 2017.

[20] J. Krainer, M. Deluca, E. Lackner, R. Wimmer-Teubenbacher, F. Sosada, C. Gspan, K. Rohracher, E. Wachmann, and A. Köck. CMOS integrated

tungsten oxide nanowire networks for ppb-level H_2S sensing. *Procedia engineering*, 168:272–275, 2016.

[21] M. Pavan, S. Rühle, A. Ginsburg, D.A. Keller, H.-N. Barad, P.M. Sberna, D. Nunes, R. Martins, A.Y. Anderson, A. Zaban, and E. Fortunato. TiO_2/Cu_2O all-oxide heterojunction solar cells produced by spray pyrolysis. *Solar Energy Materials and Solar Cells*, 132:549–556, 2015.

[22] S. Mathur, T. Ruegamer, N. Donia, and H. Shen. Functional metal oxide coatings by molecule-based thermal and plasma chemical vapor deposition techniques. *Journal of nanoscience and nanotechnology*, 8(5):2597–2603, 2008.

[23] D.W. Lee and B.R. Yoo. Advanced metal oxide (supported) catalysts: Synthesis and applications. *Journal of Industrial and Engineering Chemistry*, 20(6):3947–3959, 2014.

[24] G.C. Mutinati. *3D-CMOS integrable gas sensor device based on nanocrystalline tin dioxide films*. PhD thesis, Technische Universität Wien, Oktober 2013.

[25] E. Brunet, T. Maier, G.C. Mutinati, S. Steinhauer, A. Köck, C. Gspan, and W. Grogger. Comparison of the gas sensing performance of SnO_2 thin film and SnO_2 nanowire sensors. *Sensors and Actuators B: Chemical*, 165(1):110–118, 2012.

[26] B. Cheng, J.M. Russell, W. Shi, L. Zhang, and E.T. Samulski. Large-scale, solution-phase growth of single-crystalline SnO_2 nanorods. *Journal of the American Chemical Society*, 126(19):5972–5973, 2004.

[27] Z.R. Dai, J.L. Gole, J.D. Stout, and Z.L. Wang. Tin oxide nanowires, nanoribbons, and nanotubes. *The Journal of Physical Chemistry B*, 106(6):1274–1279, 2002.

[28] K.S. Khashan, A.I. Hassan, and A.J. Addie. Characterization of CuO thin films deposition on porous silicon by spray pyrolysis. *Surface Review and Letters*, 23(05):1650044, 2016.

[29] S. Steinhauer. *Gas Sensing Properties of Metal Oxide Nanowires and their CMOS Integration*. PhD thesis, Technische Universität Wien, August 2014.

[30] A. Umar, A.A. Alshahrani, H. Algarni, and R. Kumar. CuO nanosheets as potential scaffolds for gas sensing applications. *Sensors and Actuators B: Chemical*, 250:24–31, 2017.

[31] M. Suchea, S. Christoulakis, K. Moschovis, N. Katsarakis, and G. Kiriakidis. ZnO transparent thin films for gas sensor applications. *Thin solid films*, 515(2):551–554, 2006.

[32] E.R. Waclawik, J. Chang, A. Ponzoni, I. Concina, D. Zappa, E. Comini, N. Motta, G. Faglia, and G. Sberveglieri. Functionalised zinc oxide nanowire gas sensors: Enhanced NO_2 gas sensor response by chemical modification of nanowire surfaces. *Beilstein journal of nanotechnology*, 3(1):368–377, 2012.

[33] R. Kumar, O. Al-Dossary, G. Kumar, and A. Umar. Zinc oxide nanostructures for NO_2 gas-sensor applications: a review. *Nano-Micro Letters*, 7(2):97–120, 2015.

[34] S. Öztürk, N. Kılınç, and Z.Z. Öztürk. Fabrication of ZnO nanorods for NO_2 sensor applications: Effect of dimensions and electrode position. *Journal of Alloys and Compounds*, 581:196–201, 2013.

[35] L. Shi, A.J.T. Naik, J.B.M. Goodall, C. Tighe, R. Gruar, R. Binions, I. Parkin, and J. Darr. Highly sensitive ZnO nanorod-and nanoprism-based NO_2 gas sensors: size and shape control using a continuous hydrothermal pilot plant. *Langmuir*, 29(33):10603–10609, 2013.

[36] M.M.H. Bhuiyan, T. Ueda, T. Ikegami, and K. Ebihara. Gas sensing properties of metal doped WO_3 thin film sensors prepared by pulsed laser deposition and DC sputtering process. *Japanese journal of applied physics*, 45(10S):8469, 2006.

[37] H. Long, W. Zeng, and H. Zhang. Synthesis of WO_3 and its gas sensing: a review. *Journal of Materials Science: Materials in Electronics*, 26(7):4698–4707, 2015.

[38] X. Gao, X. Su, C. Yang, F. Xiao, J. Wang, X. Cao, S. Wang, and L. Zhang. Hydrothermal synthesis of WO_3 nanoplates as highly sensitive cyclohexene sensor and high-efficiency MB photocatalyst. *Sensors and Actuators B: Chemical*, 181:537–543, 2013.

[39] J. Krainer, M. Deluca, E. Lackner, R. Wimmer-Teubenbacher, F. Sosada, C. Gspan, K. Rohracher, E. Wachmann, and A. Köck. CMOS integrated tungsten oxide nanowire networks for ppb-level H_2S sensing. *Procedia engineering*, 168:272–275, 2016.

[40] F. Yang and Z. Guo. Engineering NiO sensitive materials and its ultra-selective detection of benzaldehyde. *Journal of colloid and interface science*, 467:192–202, 2016.

[41] A. Kasikov, A. Gerst, A. Kikas, L. Matisen, A. Saar, A. Tarre, and A. Rosental. Pt coated Cr_2O_3 thin films for resistive gas sensors. *Open Physics*, 7(2):356–362, 2009.

[42] M. Zhao, H. Zhu, J. Zhang, M. Li, and Z. Cai. Synthesis and gas sensor application of nanostructure Cr_2O_3 hollow spheres. *IOP Conference Series: Materials Science and Engineering*, 207:012030, 06 2017.

[43] S. Vladimirova, V. Krivetskiy, M. Rumyantseva, A. Gaskov, N. Mordvinova, O. Lebedev, M. Martyshov, and P. Forsh. Co_3O_4 as p-type material for CO sensing in humid air. *Sensors*, 17(10):2216, 2017.

[44] J. Wöllenstein, M. Burgmair, G. Plescher, T. Sulima, J. Hildenbrand, H. Böttner, and I. Eisele. Cobalt oxide based gas sensors on silicon substrate for operation at low temperatures. *Sensors and Actuators B: Chemical*, 93(1-3):442–448, 2003.

[45] A. Yadav, A. Lokhande, J.H. Kim, and C.D. Lokhande. Enhanced sensitivity and selectivity of CO_2 gas sensor based on modified La_2O_3 nanorods. *Journal of Alloys and Compounds*, 723:880–886, 2017.

[46] A. Yadav, V. Lokhande, R. Bulakhe, and C. D. Lokhande. Amperometric CO_2 gas sensor based on interconnected web-like nanoparticles of La_2O_3 synthesized by ultrasonic spray pyrolysis. *Microchimica Acta*, 184(10):3713–3720, 2017.

[47] J. Huotari and J. Lappalainen. Nanostructured vanadium pentoxide gas sensors for SCR process control. *Journal of Materials Science*, 52(4):2241–2253, 2017.

[48] A. Dhayal Raj, T. Pazhanivel, P. S. Kumar, D. Mangalaraj, D. Nataraj, and N. Ponpandian. Self assembled V_2O_5 nanorods for gas sensors. *Current Applied Physics*, 10(2):531–537, 2010.

[49] Y. Suda, H. Kawasaki, J. Namba, K. Iwatsuji, K. Doi, and K. Wada. Properties of palladium doped tin oxide thin films for gas sensors grown by PLD method combined with sputtering process. *Surface and Coatings Technology*, 174:1293–1296, 2003.

[50] S.O. Kucheyev, T.F. Baumann, P.A. Sterne, Y.M. Wang, T. Van Buuren, A.V. Hamza, L.J. Terminello, and T.M. Willey. Surface electronic states in three-dimensional SnO_2 nanostructures. *Physical Review B*, 72(3):035404, 2005.

[51] A. Walsh, J.L.F. Da Silva, and S.-H. Wei. Origins of band-gap renormalization in degenerately doped semiconductors. *Physical Review B*, 78(7):075211, 2008.

[52] R.E. Presley, C.L. Munsee, C.H. Park, D. Hong, J.F. Wager, and D.A. Keszler. Tin oxide transparent thin-film transistors. *Journal of Physics D: Applied Physics*, 37(20):2810, 2004.

[53] T. Minami. Transparent conducting oxide semiconductors for transparent electrodes. *Semiconductor science and technology*, 20(4):S35, 2005.

[54] H.J. Snaith and C. Ducati. SnO2-based dye-sensitized hybrid solar cells exhibiting near unity absorbed photon-to-electron conversion efficiency. *Nano letters*, 10(4):1259–1265, 2010.

[55] A. Birkel, Y.-G. Lee, D. Koll, X. Van Meerbeek, S. Frank, M.J. Choi, Y.S. Kang, K. Char, and W. Tremel. Highly efficient and stable dye-sensitized solar cells based on SnO_2 nanocrystals prepared by microwave-assisted synthesis. *Energy & Environmental Science*, 5(1):5392–5400, 2012.

[56] K. Sekizawa, H. Widjaja, S. Maeda, Y. Ozawa, and K. Eguchi. Low temperature oxidation of methane over Pd catalyst supported on metal oxides. *Catalysis Today*, 59(1-2):69–74, 2000.

[57] S.S. Mulla, S.S. Chaugule, A. Yezerets, N.W. Currier, W.N. Delgass, and F.H. Ribeiro. Regeneration mechanism of $Pt/BaO/Al_2O_3$ lean NOx trap catalyst with H_2. *Catalysis Today*, 136(1-2):136–145, 2008.

[58] H. Widjaja, K. Sekizawa, and K. Eguchi. Low-temperature oxidation of methane over Pd supported on SnO_2-based oxides, 1999.

[59] T. Takeguchi, O. Takeoh, S. Aoyama, J. Ueda, R. Kikuchi, and K. Eguchi. Strong chemical interaction between PdO and SnO_2 and the influence on catalytic combustion of methane. *Applied Catalysis A: General*, 252(1):205–214, 2003.

[60] P.G. Harrison, N.C. Lloyd, and W. Daniell. The nature of the chromium species formed during the thermal activation of chromium-promoted tin (IV) oxide catalysts: an EPR and XPS study. *The Journal of Physical Chemistry B*, 102(52):10672–10679, 1998.

[61] G.C. Bond, L.R. Molloy, and M.J. Fuller. Oxidation of carbon monoxide over palladium–tin (IV) oxide catalysts: an example of spillover catalysis. *Journal of the Chemical Society, Chemical Communications*, 01 1975.

[62] T. H. Rogers, C. S. Piggot, W. H. Bahlke, and J. M. Jennings. The catalytic oxidation of carbon monoxide. *J. Am. Chem. Soc.*, 43(9):1973–1982, 1921.

[63] P.G. Harrison, N.C. Lloyd, W. Daniell, C. Bailey, and W. Azelee. Evolution of microstructure during the thermal activation of chromium-promoted tin (IV) oxide catalysts: an FT-IR, FT-Raman, XRD, TEM, and XANES/EXAFS study. *Chemistry of materials*, 11(4):896–909, 1999.

[64] F. Solymosi and J. Kiss. Adsorption and reduction of NO on tin (IV) oxide doped with chromium (III) oxide. *Journal of Catalysis*, 54(1):42–51, 1978.

[65] S. Das and V. Jayaraman. SnO_2: A comprehensive review on structures and gas sensors. *Progress in Materials Science*, 66:112–255, 2014.

[66] M. Batzill and U. Diebold. The surface and materials science of tin oxide. *Progress in surface science*, 79(2-4):47–154, 2005.

[67] L. Jiang, G. Sun, Z. Zhou, S. Sun, Q. Wang, S. Yan, H. Li, J. Tian, J. Guo, B. Zhou, and Q. Xin. Size-controllable synthesis of monodispersed SnO_2 nanoparticles and application in electrocatalysts. *The Journal of Physical Chemistry B*, 109(18):8774–8778, 2005.

[68] O. Lupan, L. Chow, G. Chai, A. Schulte, S. Park, and H. Heinrich. A rapid hydrothermal synthesis of rutile SnO_2 nanowires. *Materials Science and Engineering: B*, 157(1-3):101–104, 2009.

[69] S.-Z. Kang, Y. Yang, and J. Mu. Solvothermal synthesis of SnO_2 nanoparticles via oxidation of Sn^{2+} ions at the water–oil interface. *Colloids and Surfaces A: Physicochemical and Engineering Aspects*, 298(3):280–283, 2007.

[70] M. Zervos and A. Othonos. A systematic study of the nitridation of SnO_2 nanowires grown by the vapor liquid solid mechanism. *Journal of Crystal Growth*, 340(1):28–33, 2012.

[71] H. Huang, O.K. Tan, Y.C. Lee, M.S. Tse, J. Guo, and T. White. In situ growth of SnO_2 nanorods by plasma treatment of SnO_2 thin films. *Nanotechnology*, 17(15):3668, 2006.

[72] C. Velásquez, F. Rojas, M.L. Ojeda, A. Ortiz, and A. Campero. Structure and texture of self-assembled nanoporous SnO_2. *Nanotechnology*, 16(8):1278, 2005.

[73] N. Zamand, A.N. Pour, M.R. Housaindokht, and M. Izadyar. Size-controlled synthesis of SnO_2 nanoparticles using reverse microemulsion method. *Solid State Sciences*, 33:6–11, 2014.

[74] Y. Wang, J.Y. Lee, and T.C. Deivaraj. A microemulsion-based preparation of tin/tin oxide core/shell nanoparticles with particle size control. *Journal of Materials Chemistry*, 14(3):362–365, 2004.

[75] A.B. Bhise, D.J. Late, P. Walke, M.A. More, I.S. Mulla, V.K. Pillai, and D.S. Joag. A single In-doped SnO_2 submicrometre sized wire as a field emitter. *Journal of Physics D: Applied Physics*, 40(12):3644, 2007.

[76] S. Luo, J. Fan, W. Liu, M. Zhang, Z. Song, C. Lin, X. Wu, and P.K. Chu. Synthesis and low-temperature photoluminescence properties of SnO_2 nanowires and nanobelts. *Nanotechnology*, 17(6):1695, 2006.

[77] S. Chacko, M.J. Bushiri, and V.K. Vaidyan. Photoluminescence studies of spray pyrolytically grown nanostructured tin oxide semiconductor thin films on glass substrates. *Journal of Physics D: Applied Physics*, 39(21):4540, 2006.

[78] F. Paraguay-Delgado, W. Antúnez-Flores, M. Miki-Yoshida, A. Aguilar-Elguezabal, P. Santiago, R. Diaz, and J.A. Ascencio. Structural analysis and growing mechanisms for long SnO_2 nanorods synthesized by spray pyrolysis. *Nanotechnology*, 16(6):688, 2005.

[79] Haynes, W.M. and Lide, D.R. and Bruno, T.J., editor. *Handbook of Chemistry and Physics*. CRC Press (Taylor & Francis Group), 97th edition, 2017.

[80] Wikipedia. Tin(IV) Oxide — Wikipedia, the free encyclopedia. `https://en.wikipedia.org/wiki/Tin(IV)_Oxide`, 2019. [Online; accessed 15-May-2019].

[81] Wikipedia. Rutil — Wikipedia, the free encyclopedia. `http://de.wikipedia.org/w/index.php?title=Rutil&oldid=185701767`, 2019. [Online; accessed 18-March-2019].

[82] A.S. Zoolfakar, R.A. Rani, A.J. Morfa, A.P. O'Mullane, and K. Kalantar-Zadeh. Nanostructured copper oxide semiconductors: a perspective on materials, synthesis methods and applications. *Journal of Materials Chemistry C*, 2(27):5247–5270, 2014.

[83] D. Gopalakrishna, K. Vijayalakshmi, and C. Ravidhas. Effect of annealing on the properties of nanostructured CuO thin films for enhanced ethanol sensitivity. *Ceramics international*, 39(7):7685–7691, 2013.

[84] J.S. Ahn, R. Pode, and K.B. Lee. Stoichiometric p-type Cu_2O thin films prepared by reactive sputtering with facing target. *Thin Solid Films*, 623:121–126, 2017.

[85] D. Tahir and S. Tougaard. Electronic and optical properties of Cu, CuO and Cu_2O studied by electron spectroscopy. *Journal of physics: Condensed matter*, 24(17):175002, 2012.

[86] T. Minami, Y. Nishi, T. Miyata, and J.-i. Nomoto. High-efficiency oxide solar cells with ZnO/Cu_2O heterojunction fabricated on thermally oxidized Cu_2O sheets. *Applied Physics Express*, 4(6):062301, 2011.

[87] K.P. Musselman, A. Wisnet, D.C. Iza, H.C. Hesse, C. Scheu, J.L. MacManus-Driscoll, and L. Schmidt-Mende. Strong efficiency improvements in ultra-low-cost inorganic nanowire solar cells. *Advanced Materials*, 22(35):E254–E258, 2010.

[88] O. Akhavan and E. Ghaderi. Cu and CuO nanoparticles immobilized by silica thin films as antibacterial materials and photocatalysts. *Surface and Coatings Technology*, 205(1):219–223, 2010.

[89] M. Paschoalino, N.C. Guedes, W. Jardim, E. Mielczarski, J.A. Mielczarski, P. Bowen, and J. Kiwi. Inactivation of E. coli mediated by high surface area CuO accelerated by light irradiation > 360 nm. *Journal of Photochemistry and Photobiology A: Chemistry*, 199(1):105–111, 2008.

[90] B. Wang, X.-L. Wu, C.-Y. Shu, Y.-G. Guo, and C.-R. Wang. Synthesis of CuO/graphene nanocomposite as a high-performance anode material for lithium-ion batteries. *Journal of Materials Chemistry*, 20(47):10661–10664, 2010.

[91] L. Ji, Z. Lin, M. Alcoutlabi, and X. Zhang. Recent developments in nanostructured anode materials for rechargeable lithium-ion batteries. *Energy & Environmental Science*, 4(8):2682–2699, 2011.

[92] O. Akhavan, H. Tohidi, and A.Z. Moshfegh. Synthesis and electrochromic study of sol–gel cuprous oxide nanoparticles accumulated on silica thin film. *Thin Solid Films*, 517(24):6700–6706, 2009.

[93] R. Neskovska, M. Ristova, J. Velevska, and M. Ristov. Electrochromism of the electroless deposited cuprous oxide films. *Thin Solid Films*, 515(11):4717–4721, 2007.

[94] W. Hu, K. Manabe, T. Furukawa, and M. Matsumura. Lowering of operational voltage of organic electroluminescent devices by coating indium-tin-oxide electrodes with a thin CuO_x layer. *Applied physics letters*, 80(15):2640–2641, 2002.

[95] S. Kim, K. Hong, K. Kim, I. Lee, and J.-L. Lee. Phase-controllable copper oxides for an efficient anode interfacial layer in organic light-emitting diodes. *Journal of Materials Chemistry*, 22(5):2039–2044, 2012.

[96] M. Hara, T. Kondo, M. Komoda, S. Ikeda, J.N. Kondo, K. Domen, M. Hara, K. Shinohara, and A. Tanaka. Cu_2O as a photocatalyst for overall water splitting under visible light irradiation. *Chemical Communications*, pages 357–358, 1998.

[97] Z. Zheng, B. Huang, Z. Wang, M. Guo, X. Qin, X. Zhang, P. Wang, and Y. Dai. Crystal faces of Cu_2O and their stabilities in photocatalytic reactions. *The Journal of Physical Chemistry C*, 113(32):14448–14453, 2009.

[98] C.-L. Chu, H.-C. Lu, C.-Y. Lo, C.-Y. Lai, and Y.-H. Wang. Physical properties of copper oxide thin films prepared by dc reactive magnetron sputtering under different oxygen partial pressures. *Physica B: Condensed Matter*, 404(23-24):4831–4834, 2009.

[99] A.R. Rastkar, A.R. Niknam, and B. Shokri. Characterization of copper oxide nanolayers deposited by direct current magnetron sputtering. *Thin Solid Films*, 517(18):5464–5467, 2009.

[100] T. Ghodselahi, M.A. Vesaghi, A. Shafiekhani, A. Baghizadeh, and M. Lameii. XPS study of the Cu@ Cu_2O core-shell nanoparticles. *Applied Surface Science*, 255(5):2730–2734, 2008.

[101] C.R. Crick and I.P. Parkin. CVD of copper and copper oxide thin films via the in situ reduction of copper (II) nitrate a route to conformal superhydrophobic coatings. *Journal of Materials Chemistry*, 21(38):14712–14716, 2011.

[102] Y. Tan, X. Xue, Q. Peng, H. Zhao, T. Wang, and Y. Li. Controllable fabrication and electrical performance of single crystalline Cu_2O nanowires with high aspect ratios. *Nano Letters*, 7(12):3723–3728, 2007.

[103] M. Cao, C. Hu, Y. Wang, Y. Guo, C. Guo, and E. Wang. A controllable synthetic route to Cu, Cu_2O, and CuO nanotubes and nanorods. *Chemical Communications*, 9:1884–1885, 2003.

[104] L. Armelao, D. Barreca, M. Bertapelle, G. Bottaro, C. Sada, and E. Tondello. A sol–gel approach to nanophasic copper oxide thin films. *Thin solid films*, 442(1-2):48–52, 2003.

[105] S.C. Ray. Preparation of copper oxide thin film by the sol–gel-like dip technique and study of their structural and optical properties. *Solar energy materials and solar cells*, 68(3-4):307–312, 2001.

[106] K.P. Muthe, J.C. Vyas, S.N. Narang, D.K. Aswal, S.K. Gupta, D. Bhattacharya, R. Pinto, G.P. Kothiyal, and S.C. Sabharwal. A study of the CuO phase formation during thin film deposition by molecular beam epitaxy. *Thin solid films*, 324(1-2):37–43, 1998.

[107] J. Li, Z. Mei, D. Ye, H. Liang, Y. Liu, and X. Du. Growth of single-crystalline Cu_2O (111) film on ultrathin MgO modified α-Al_2O_3 (0001) substrate by molecular beam epitaxy. *Journal of Crystal Growth*, 353(1):63–67, 2012.

[108] M. Kawwam, F.H. Alharbi, T. Kayed, A. Aldwayyan, A. Alyamani, N. Tabet, and K. Lebbou. Characterization of CuO(111)/MgO(100) films grown under two different PLD backgrounds. *Applied Surface Science*, 276:7–12, 2013.

[109] Y. Fu, H. Lei, X. Wang, D. Yan, L.-H. Cao, G. Yao, C. Shen, L. Peng, Y. Zhao, Y. Wang, and W. Wu. Fabrication of two domain Cu_2O (011) films on MgO (001) by pulsed laser deposition. *Applied Surface Science*, 273:19–23, 2013.

[110] R.K. Bedi and I. Singh. Room-temperature ammonia sensor based on cationic surfactant-assisted nanocrystalline CuO. *ACS applied materials & interfaces*, 2(5):1361–1368, 2010.

[111] Wikipedia. Copper(II) oxide — Wikipedia, the free encyclopedia. https://en.wikipedia.org/wiki/Copper(II)_oxide, 2019. [Online; accessed 15-May-2019].

[112] P. Uikey and K. Vishwakarma. Review of zinc oxide (ZnO) nanoparticles applications and properties. *International Journal of Emerging Technology in Computer Science & Electronics*, 21(2):239, 2016.

[113] R.J.D. Tilley. *Understanding Solids: The Science of Materials*. John Wiley & Sons, Ltd, 2004.

[114] A. Kołodziejczak-Radzimska and T. Jesionowski. Zinc oxide from synthesis to application: a review. *Materials*, 7(4):2833–2881, 2014.

[115] A.B.G. Lansdown and A. Taylor. Zinc and titanium oxides: promising UV-absorbers but what influence do they have on the intact skin? *International journal of cosmetic science*, 19(4):167–172, 1997.

[116] M. Mirhosseini and F.B. Firouzabadi. Antibacterial activity of zinc oxide nanoparticle suspensions on food-borne pathogens. *International Journal of Dairy Technology*, 66(2):291–295, 2013.

[117] M.Y. Guo, M.K. Fung, F. Fang, X.Y. Chen, A.M.C. Ng, A.B. Djurišić, and W.K. Chan. ZnO and TiO_2 1D nanostructures for photocatalytic applications. *Journal of Alloys and Compounds*, 509(4):1328–1332, 2011.

[118] S.-M. Lam, J.-C. Sin, A.Z. Abdullah, and A.R. Mohamed. Degradation of wastewaters containing organic dyes photocatalysed by zinc oxide: a review. *Desalination and Water Treatment*, 41(1-3):131–169, 2012.

[119] Z.H. Lim, Z.X. Chia, M. Kevin, A.S.W. Wong, and G.W. Ho. A facile approach towards ZnO nanorods conductive textile for room temperature multifunctional sensors. *Sensors and Actuators B: Chemical*, 151(1):121–126, 2010.

[120] Z. Mao, Q. Shi, L. Zhang, and H. Cao. The formation and UV-blocking property of needle-shaped ZnO nanorod on cotton fabric. *Thin Solid Films*, 517(8):2681–2686, 2009.

[121] A. Das, D.-Y. Wang, A. Leuteritz, K. Subramaniam, H.C. Greenwell, U. Wagenknecht, and G. Heinrich. Preparation of zinc oxide free, transparent rubber nanocomposites using a layered double hydroxide filler. *Journal of Materials Chemistry*, 21(20):7194–7200, 2011.

[122] L. Ibarra, A. Marcos-Fernandez, and M. Alzorriz. Mechanistic approach to the curing of carboxylated nitrile rubber (XNBR) by zinc peroxide/zinc oxide. *Polymer*, 43(5):1649–1655, 2002.

[123] C.-H. Lu and C.-H. Yeh. Emulsion precipitation of submicron zinc oxide powder. *Materials Letters*, 33(3-4):129–132, 1997.

[124] T. Tsuzuki and P.G. McCormick. ZnO nanoparticles synthesised by mechanochemical processing. *Scripta Materialia*, 44(8-9):1731–1734, 2001.

[125] Ö.A. Yıldırım and C. Durucan. Synthesis of zinc oxide nanoparticles elaborated by microemulsion method. *Journal of Alloys and Compounds*, 506(2):944–949, 2010.

[126] Y.-d. Wang, C.-l. Ma, X.-d. Sun, and H.-d. Li. Preparation of nanocrystalline metal oxide powders with the surfactant-mediated method. *Inorganic Chemistry Communications*, 5(10):751–755, 2002.

[127] P. Li, Y. Wei, H. Liu, and X.-k. Wang. Growth of well-defined ZnO microparticles with additives from aqueous solution. *Journal of solid state chemistry*, 178(3):855–860, 2005.

[128] J. Xu, Q. Pan, Y. Shun, and Z. Tian. Grain size control and gas sensing properties of ZnO gas sensor. *Sensors and Actuators B: Chemical*, 66(1-3):277–279, 2000.

[129] Z.M. Khoshhesab, M. Sarfaraz, and Z. Houshyar. Influences of Urea on Preparation of Zinc Oxide Nanostructures Through Chemical Precipitation in Ammonium Hydrogencarbonate Solution. *Synthesis and Reactivity in Inorganic, Metal-Organic, and Nano-Metal Chemistry*, 42(10):1363–1368, 2012.

[130] M. Ristić, S. Musić, M. Ivanda, and S. Popović. Sol–gel synthesis and characterization of nanocrystalline ZnO powders. *Journal of Alloys and Compounds*, 397(1-2):L1–L4, 2005.

[131] D. Chen, X. Jiao, and G. Cheng. Hydrothermal synthesis of zinc oxide powders with different morphologies. *Solid State Communications*, 113(6):363–366, 1999.

[132] J.J. Schneider, R.C. Hoffmann, J. Engstler, A. Klyszcz, E. Erdem, P. Jakes, R.-A. Eichel, L. Pitta-Bauermann, and J. Bill. Synthesis, characterization, defect chemistry, and FET properties of microwave-derived nanoscaled zinc oxide. *Chemistry of Materials*, 22(7):2203–2212, 2010.

[133] Wikipedia. Zinc oxide — Wikipedia, the free encyclopedia. `https://en.wikipedia.org/wiki/Zinc_oxide`, 2019. [Online; accessed 15-May-2019].

[134] N. Yamazoe, K. Shimanoe, and C. Sawada. Contribution of electron tunneling transport in semiconductor gas sensor. *Thin Solid Films*, 515(23):8302–8309, 2007.

[135] G. Korotcenkov. *Handbook of Gas Sensor Materials: Properties, Advantages and Shortcomings for Applications Volume 2: New Trends and Technologies*, volume 2. Springer International Publishing Switzerland, 1 edition, 2014.

[136] N. Barsan and U. Weimar. Conduction model of metal oxide gas sensors. *Journal of electroceramics*, 7(3):143–167, 2001.

[137] G. Korotcenkov. *Handbook of Gas Sensor Materials: Properties, Advantages and Shortcomings for Applications Volume 1: Conventional Approaches*, volume 1. Springer International Publishing Switzerland, 1 edition, 2013.

[138] E. Roduner. Size matters: why nanomaterials are different. *Chemical Society Reviews*, 35(7):583–592, 2006.

[139] N. Yamazoe. New approaches for improving semiconductor gas sensors. *Sensors and Actuators B: Chemical*, 5(1-4):7–19, 1991.

[140] M. Hübner, C.E. Simion, A. Tomescu-Stănoiu, S. Pokhrel, N. Bârsan, and U. Weimar. Influence of humidity on CO sensing with p-type CuO thick film gas sensors. *Sensors and Actuators B: Chemical*, 153(2):347–353, 2011.

[141] H.-J. Kim and J.-H. Lee. Highly sensitive and selective gas sensors using p-type oxide semiconductors: Overview. *Sensors and Actuators B: Chemical*, 192:607–627, 2014.

[142] N. Barsan, C. Simion, T. Heine, S. Pokhrel, and U. Weimar. Modeling of sensing and transduction for p-type semiconducting metal oxide based gas sensors. *Journal of electroceramics*, 25(1):11–19, 2010.

[143] D.E. Williams and P.T. Moseley. Dopant effects on the response of gas-sensitive resistors utilising semiconducting oxides. *Journal of Materials Chemistry*, 1(5):809–814, 1991.

[144] D.E. Williams. Semiconducting oxides as gas-sensitive resistors. *Sensors and Actuators B: Chemical*, 57(1-3):1–16, 1999.

[145] G.S. Henshaw, D.H. Dawson, and D.E. Williams. Selectivity and composition dependence of response of gas-sensitive resistors. Part 2. Hydrogen sulfide response of $Cr_{2-x}Ti_xO_{3+y}$. *Journal of Materials Chemistry*, 5(11):1791–1800, 1995.

[146] A. Kolmakov. Some recent trends in the fabrication, functionalisation and characterisation of metal oxide nanowire gas sensors. *International Journal of Nanotechnology*, 5(4-5):450–474, 2008.

[147] E. Comini and G. Sberveglieri. Metal oxide nanowires as chemical sensors. *Materials Today*, 13(7-8):36–44, 2010.

[148] D.R. Miller, S.A. Akbar, and P.A. Morris. Nanoscale metal oxide-based heterojunctions for gas sensing: a review. *Sensors and Actuators B: Chemical*, 204:250–272, 2014.

[149] I.-S. Hwang and J.-H. Lee. Gas sensors using oxide nanowire networks: An overview. *Journal of Nanoengineering and Nanomanufacturing*, 1(1):4–17, 2011.

[150] E. Comini, C. Baratto, G. Faglia, M. Ferroni, A. Ponzoni, D. Zappa, and G. Sberveglieri. Metal oxide nanowire chemical and biochemical sensors. *Journal of Materials Research*, 28(21):2911–2931, 2013.

[151] A. Parretta, M.K. Jayaraj, A. Di Nocera, S. Loreti, L. Quercia, and A. Agati. Electrical and optical properties of copper oxide films prepared by reactive RF magnetron sputtering. *physica status solidi (a)*, 155(2):399–404, 1996.

[152] Z.W. Chen, J.K.L. Lai, and C.H. Shek. Nucleation mechanism and microstructural assessment of SnO_2 nanowires prepared by pulsed laser deposition. *Physics Letters A*, 345(4-6):391–397, 2005.

[153] K. Hong, M. Xie, R. Hu, and H. Wu. Synthesizing tungsten oxide nanowires by a thermal evaporation method. *Applied physics letters*, 90(17):173121, 2007.

[154] O. Tigli and J. Juhala. ZnO nanowire growth by physical vapor deposition. In *2011 11th IEEE International Conference on Nanotechnology*, pages 608–611. IEEE, 2011.

[155] L. Wang, X. Zhang, S. Zhao, G. Zhou, Y. Zhou, and J. Qi. Synthesis of well-aligned ZnO nanowires by simple physical vapor deposition on c-oriented ZnO thin films without catalysts or additives. *Applied Physics Letters*, 86(2):024108, 2005.

[156] H. Choi and S.-H. Park. Seedless growth of free-standing copper nanowires by chemical vapor deposition. *Journal of the American Chemical Society*, 126(20):6248–6249, 2004.

[157] I. Sayago, M.J. Fernández, J.L. Fontecha, M.C. Horrillo, and J.P. Santos. Synthesis and characterization of SnO_2 nanowires grown by CVD for application as gas sensors. In *2015 10th Spanish Conference on Electron Devices (CDE)*, pages 1–4. IEEE, 2015.

[158] B.S. Thabethe, G.F. Malgas, D.E. Motaung, T. Malwela, and C.J. Arendse. Self-catalytic growth of tin oxide nanowires by chemical vapor deposition process. *Journal of Nanomaterials*, 2013:66, 2013.

[159] T. Abuzairi, B.-R. Huang, and T.-C. Lin. Synthesis of Tungsten Oxide Nanowires onto ITO Glass Using T-CVD. *Makara Journal of Technology*, 17(3):103–106, 2014.

[160] L.V. Podrezova, S. Porro, V. Cauda, M. Fontana, and G. Cicero. Comparison between ZnO nanowires grown by chemical vapor deposition and hydrothermal synthesis. *Applied Physics A*, 113(3):623–632, 2013.

[161] P.-C. Chang, Z. Fan, W.-Y. Tseng, J. Hong, W.-A. Chiou, and G.J. Lu. Characterization ZnO Nanowires Synthesized by Vapor Trapping CVD Method. *Microscopy and Microanalysis*, 10(S02):390–391, 2004.

[162] A. Li, H. Song, J. Zhou, X. Chen, and S. Liu. CuO nanowire growth on Cu_2O by in situ thermal oxidation in air. *CrystEngComm*, 15(42):8559–8564, 2013.

[163] X. Jiang, T. Herricks, and Y. Xia. CuO nanowires can be synthesized by heating copper substrates in air. *Nano Letters*, 2(12):1333–1338, 2002.

[164] D. Wei, Y. Shen, M. Li, W. Liu, S. Gao, L. Jia, C. Han, and B. Cui. Synthesis and characterization of single-crystalline SnO_2 nanowires. *Journal of Nanomaterials*, 2013:20, 2013.

[165] D. Chen, P. Xie, S. Deng, N. Xu, and J. Chen. Preparation of tungsten oxide nanowires by thermal oxidation method for large area cold cathode application. In *2015 IEEE International Vacuum Electronics Conference (IVEC)*, pages 1–2. IEEE, 2015.

[166] O. Martínez, V. Hortelano, J. Jiménez, J.L. Plaza, S. De Dios, J. Olvera, E. Diéguez, R. Fath Allah, J.G. Lozano, T. Ben, D. González, and J. Mass. Growth of ZnO nanowires through thermal oxidation of metallic zinc films on CdTe substrates. *Journal of Alloys and Compounds*, 509(17):5400–5407, 2011.

[167] C. Florica, N. Preda, A. Costas, I. Zgura, and I. Enculescu. ZnO nanowires grown directly on zinc foils by thermal oxidation in air: Wetting and water adhesion properties. *Materials Letters*, 170:156–159, 2016.

[168] B. Vidhyadharan, I.I. Misnon, R.A. Aziz, K.P. Padmasree, M.M. Yusoff, and R. Jose. Superior supercapacitive performance in electrospun copper oxide nanowire electrodes. *Journal of Materials Chemistry A*, 2(18):6578–6588, 2014.

[169] A. Khalil, M. Jouiad, M. Khraisheh, and R. Hashaikeh. Facile synthesis of copper oxide nanoparticles via electrospinning. *Journal of Nanomaterials*, 2014:80, 2014.

[170] Y. Wang, B. Liu, S. Xiao, X. Wang, L. Sun, H. Li, W. Xie, Q. Li, Q. Zhang, and T. Wang. Low-temperature H_2S detection with hierarchical Cr-doped WO_3 microspheres. *ACS applied materials & interfaces*, 8(15):9674–9683, 2016.

[171] T. Krishnamoorthy, M.Z. Tang, A. Verma, A.S. Nair, D. Pliszka, S.G. Mhaisalkar, and S. Ramakrishna. A facile route to vertically aligned electrospun SnO_2 nanowires on a transparent conducting oxide substrate for dye-sensitized solar cells. *Journal of Materials Chemistry*, 22(5):2166–2172, 2012.

[172] F.A. Ofori, F.A. Sheikh, R. Appiah-Ntiamoah, X. Yang, and H. Kim. A simple method of electrospun tungsten trioxide nanofibers with enhanced visible-light photocatalytic activity. *Nano-micro letters*, 7(3):291–297, 2015.

[173] W.-Y. Wu, J.-M. Ting, and P.-J. Huang. Electrospun ZnO nanowires as gas sensors for ethanol detection. *Nanoscale research letters*, 4(6):513, 2009.

[174] G. Zhang and N. Liu. A novel method for massive synthesis of SnO_2 nanowires. *Bulletin of Materials Science*, 36(6):953–960, 2013.

[175] S. Rajagopal, H.-M. Lee, K. Lee, and C.-K. Kim. Hydrothermal synthesis of one-dimensional tungsten oxide nanostructures using cobalt ammonium sulfate as a structure-directing agent. *Korean Journal of Chemical Engineering*, 30(10):1833–1835, 2013.

[176] J.B. Shim, H. Chang, and S.-O Kim. Rapid hydrothermal synthesis of zinc oxide nanowires by annealing methods on seed layers. *Journal of Nanomaterials*, 2011:25, 2011.

[177] M.A. Carpenter, S. Mathur, and A. Kolmakov. *Metal oxide nanomaterials for chemical sensors*. Springer Science & Business Media, 2012.

[178] X. Xu, P. Zhao, D. Wang, P. Sun, L. You, Y. Sun, X. Liang, F. Liu, H. Chen, and G. Lu. Preparation and gas sensing properties of hierarchical flower-like In_2O_3 microspheres. *Sensors and Actuators B: Chemical*, 176:405–412, 2013.

[179] K. Großmann, S. Wicker, U. Weimar, and N. Barsan. Impact of Pt additives on the surface reactions between SnO_2, water vapour, CO and H_2: An operando investigation. *Physical Chemistry Chemical Physics*, 15(44):19151–19158, 2013.

[180] V. Galstyan, E. Comini, I. Kholmanov, A. Ponzoni, V. Sberveglieri, N. Poli, G. Faglia, and G. Sberveglieri. A composite structure based on reduced graphene oxide and metal oxide nanomaterials for chemical sensors. *Beilstein journal of nanotechnology*, 7(1):1421–1427, 2016.

[181] H.-J. Freund and M.W. Roberts. Surface chemistry of carbon dioxide. *Surface Science Reports*, 25(8):225–273, 1996.

[182] J. Baltrusaitis, J. Schuttlefield, E. Zeitler, and V.H. Grassian. Carbon dioxide adsorption on oxide nanoparticle surfaces. *Chemical Engineering Journal*, 170(2-3):471–481, 2011.

[183] G.F. Fine, L.M. Cavanagh, A. Afonja, and R. Binions. Metal oxide semi-conductor gas sensors in environmental monitoring. *sensors*, 10(6):5469–5502, 2010.

[184] T. Ishihara, K. Kometani, Y. Mizuhara, and Y. Takita. Mixed oxide capacitor of CuO-$BaTiO_3$ as a new type CO_2 gas sensor. *Journal of the American Ceramic Society*, 75(3):613–618, 1992.

[185] N.B. Tanvir, O. Yurchenko, C. Wilbertz, and G. Urban. Investigation of CO_2 reaction with copper oxide nanoparticles for room temperature gas sensing. *Journal of Materials Chemistry A*, 4(14):5294–5302, 2016.

[186] A. Gurlo, N. Bârsan, and U. Weimar. Gas sensors based on semiconducting metal oxides. In *Metal Oxides*, pages 694–749. CRC Press, 2005.

[187] O. Badr and S.D. Probert. Carbon monoxide concentration in the Earth's atmosphere. *Applied Energy*, 49(2):99–143, 1994.

[188] US EPA (Environmental Protection Agency). Carbon Monoxide's Impact on Indoor Air Quality.

[189] D.N. Bateman. Carbon monoxide. *Medicine*, 40(3):115–116, 2012.

[190] S.H. Hahn, N. Barsan, U. Weimar, S.G. Ejakov, J.H. Visser, and R.E. Soltis. CO sensing with SnO_2 thick film sensors: role of oxygen and water vapour. *Thin Solid Films*, 436(1):17–24, 2003.

[191] A. Zima. *Development of highly sensitive nano-gassensors based on nanocrystalline tin dioxide thin films and single-crystalline tin dioxide nanowires*. PhD thesis, Technische Universität Wien, November 2009.

[192] H. Shaftel, R. Jackson, and L. Tenenbaum. Climate Change: Vital Signs of the Planet: Carbon Dioxide.

[193] R. Boos, B. Damberger, P. Hutter, M. Kundi, H. Moshammer, P. Tappler, F. Twrdik, and P. Wallner. Bewertung der Innenraumluft: Physikalische Faktoren, Kohlenstoffdioxid als Lüftungsparameter, 2006.

[194] B. Seifert. Richtwerte für die Innenraumluft Die Beurteilung der Innenraumluftqualität mit Hilfe der Summe der flüchtigen organischen Verbindungen (TVOC-Wert). *Bundesgesundheitsblatt-Gesundheitsforschung-Gesundheitsschutz*, 42(3):270–278, 1999.

[195] US EPA (Environmental Protection Agency). Technical Overview of Volatile Organic Compounds.

[196] M.J. Mendell. Indoor residential chemical emissions as risk factors for respiratory and allergic effects in children: a review. *Indoor air*, 17(4):259–277, 2007.

[197] T. Salthammer. Very volatile organic compounds: an understudied class of indoor air pollutants. *Indoor Air*, 26:25–38, 2016.

[198] C. Höckelmann and F. Jüttner. Volatile organic compound (VOC) analysis and sources of limonene, cyclohexanone and straight chain

aldehydes in axenic cultures of Calothrix and Plectonema. *Water Science & Technology*, 49:47–54, 2004.

[199] H. Demirtepe, L. Melymuk, M.L. Diamond, L. Bajard, Š. Vojta, R. Prokeš, O. Sáňka, J. Klánová, L. Palkovičová Murínová, D. Richterová, V. Rašplová, and T. Trnovec. Linking past uses of legacy SVOCs with today's indoor levels and human exposure. *Environment International*, 127:653–663, 2019.

[200] E.G. Gregorich, M.H. Beare, U.F. Kim, and J.O. Skjemstad. Chemical and Biological Characteristics of Physically Uncomplexed Organic Matter. *Soil Science Society of America Journal*, 70:975–985, 2006.

[201] C.-H. Lin, W.-C. Chang, and X. Qi. Growth and characterization of pure and doped SnO_2 films for H_2 gas detection. *Procedia Engineering*, 36:476–481, 2012.

[202] A.J. Haider, S.S. Shaker, and A.H. Mohammed. A study of morphological, optical and gas sensing properties for pure and Ag doped SnO_2 prepared by pulsed laser deposition (PLD). *Energy Procedia*, 36:776–787, 2013.

[203] N. Murata, T. Suzuki, M. Kobayashi, F. Togoh, and K. Asakura. Characterization of Pt-doped SnO_2 catalyst for a high-performance micro gas sensor. *Physical chemistry chemical physics*, 15(41):17938–17946, 2013.

[204] A. Chen, S. Xia, Z. Ji, J. Xi, H. Qin, and Q. Mao. Effects of Cu doping on the structure, electronic and optical properties of SnO_2 thin films by spray pyrolysis: An experimental and density functional study. *Surface and Coatings Technology*, 322:120–126, 2017.

[205] G. Korotcenkov, V. Brinzari, and I. Boris. (Cu, Fe, Co, or Ni)-doped tin dioxide films deposited by spray pyrolysis: doping influence on film morphology. *Journal of materials science*, 43(8):2761–2770, 2008.

[206] R.A. Bennett, P. Stone, and M. Bowker. Scanning tunnelling microscopy studies of the reactivity of the TiO_2 (110) surface: Re-oxidation and the thermal treatment of metal nanoparticles. *Faraday Discussions*, 114:267–277, 1999.

[207] A. Kolmakov, D.O. Klenov, Y. Lilach, S. Stemmer, and M. Moskovits. Enhanced gas sensing by individual SnO_2 nanowires and nanobelts functionalized with Pd catalyst particles. *Nano letters*, 5(4):667–673, 2005.

[208] G. Korotcenkov. Gas response control through structural and chemical modification of metal oxide films: state of the art and approaches. *Sensors and Actuators B: Chemical*, 107(1):209–232, 2005.

[209] G. Korotcenkov, V. Brinzari, Y. Boris, M. Ivanov, J. Schwank, and J. Morante. Influence of surface Pd doping on gas sensing characteristics of SnO_2 thin films deposited by spray pirolysis. *Thin Solid Films*, 436(1):119–126, 2003.

[210] G. Sharma, D. Kumar, A. Kumar, A.-M. Ala'a, D. Pathania, M. Naushad, and G.T. Mola. Revolution from monometallic to trimetallic nanoparticle composites, various synthesis methods and their applications: a review. *Materials Science and Engineering: C*, 71:1216–1230, 2017.

[211] P.S. Patil. Versatility of chemical spray pyrolysis technique. *Materials Chemistry and physics*, 59(3):185–198, 1999.

[212] J.C. Viguie and J. Spitz. Chemical vapor deposition at low temperatures. *J. Electrochem. Soc*, 122(4):585–588, 1975.

[213] L. Filipovic, S. Selberherr, G.C. Mutinati, E. Brunet, S. Steinhauer, A. Köck, J. Teva, J. Kraft, J. Siegert, and F. Schrank. Methods of simulating thin film deposition using spray pyrolysis techniques. *Microelectronic Engineering*, 117:57–66, 2014.

[214] A. Juma, I.O. Acik, A.T. Oluwabi, A. Mere, V. Mikli, M. Danilson, and M. Krunks. Zirconium doped TiO_2 thin films deposited by chemical spray pyrolysis. *Applied Surface Science*, 387:539–545, 2016.

[215] S. Edinger, J. Bekacz, M. Richter, R. Hamid, R.A. Wibowo, A. Peić, and T. Dimopoulos. Influence of the acetic acid concentration on the growth of zinc oxide thin films prepared by spray pyrolysis of aqueous solutions. *Thin Solid Films*, 594:238–244, 2015.

[216] J. Liu, Y. Lu, X. Cui, Y. Geng, G. Jin, and Z. Zhai. Gas-sensing properties and sensitivity promoting mechanism of Cu-added SnO_2 thin films deposited by ultrasonic spray pyrolysis. *Sensors and Actuators B: Chemical*, 248:862–867, 2017.

[217] E. Zaleta-Alejandre, J. Camargo-Martinez, A. Ramirez-Garibo, M.L. Pérez-Arrieta, R. Balderas-Xicohténcatl, Z. Rivera-Alvarez, M. Aguilar-Frutis, and C. Falcony. Structural, electrical and optical properties of indium chloride doped ZnO films synthesized by Ultrasonic Spray Pyrolysis technique. *Thin Solid Films*, 524:44–49, 2012.

[218] S. Pisduangdaw, J. Panpranot, C. Methastidsook, C. Chaisuk, K. Faungnawakij, P. Praserthdam, and O. Mekasuwandumrong. Characteristics and catalytic properties of Pt–Sn/Al_2O_3 nanoparticles synthesized by one-step flame spray pyrolysis in the dehydrogenation of propane. *Applied Catalysis A: General*, 370(1-2):1–6, 2009.

[219] L. Mädler, H.K. Kammler, R. Mueller, and S.E. Pratsinis. Controlled synthesis of nanostructured particles by flame spray pyrolysis. *Journal of Aerosol Science*, 33(2):369–389, 2002.

[220] C.R. Bickmore, K.F. Waldner, R. Baranwal, T. Hinklin, D.R. Treadwell, and R.M. Laine. Ultrafine titania by flame spray pyrolysis of a titanatrane complex. *Journal of the European Ceramic Society*, 18(4):287–297, 1998.

[221] W. Siefert. Corona spray pyrolysis: a new coating technique with an extremely enhanced deposition efficiency. *Thin Solid Films*, 120(4):267–274, 1984.

[222] W. Siefert. Properties of thin In_2O_3 and SnO_2 films prepared by corona spray pyrolysis, and a discussion of the spray pyrolysis process. *Thin solid films*, 120(4):275–282, 1984.

[223] S.G. Kim, J.Y. Kim, and H.J. Kim. Deposition of MgO thin films by modified electrostatic spray pyrolysis method. *Thin solid films*, 376(1-2):110–114, 2000.

[224] U. Lafont, A. Anastasopol, E. Garcia-Tamayo, and E. Kelder. Electrostatic spray pyrolysis of LiNio.5Mn1.5O4 films for 3D Li-ion microbatteries. *Thin Solid Films*, 520(9):3464–3471, 2012.

[225] M. Miki-Yoshida and E. Andrade. Growth and structure of tin dioxide thin films obtained by an improved spray pyrohydrolysis technique. *Thin Solid Films*, 224(1):87–96, 1993.

[226] W.M. Sears and M.A. Gee. Mechanics of film formation during the spray pyrolysis of tin oxide. *Thin solid films*, 165(1):265–277, 1988.

[227] Spraying Systems Co. Automatic & Air Atomizing Spray Nozzles, 2017.

[228] Harry Gestigkeit Gmbh. Präzitherm: High temperature hot plate of TITANIUM up to 600 degree celcius for continuous operation. Technical report, Harry Gestigkeit GMBH (Fabrik für Labor-Apparate), Düsseldorf, 2017.

[229] E. Brunet. *Fabrication of tin oxide nanowire gas sensors*. PhD thesis, Technische Universität Wien, März 2014.

[230] T. Arai. The study of the optical properties of conducting tin oxide films and their interpretation in terms of a tentative band scheme, 1960.

[231] C. Abdelmounaïm, Z. Amara, A. Maha, and D. Mustapha. Effects of molarity on structural, optical, morphological and CO_2 gas sensing properties of nanostructured copper oxide films deposited by spray pyrolysis. *Materials Science in Semiconductor Processing*, 43:214–221, 2016.

[232] J. Ghose and A. Kanungo. Studies on the thermal decomposition of $Cu(NO_3)_2 \cdot 3H_2O$. *Journal of Thermal Analysis and Calorimetry*, 20(2):459–462, 1981.

[233] C.-C. Lin and Y.-Y. Li. Synthesis of ZnO nanowires by thermal decomposition of zinc acetate dihydrate. *Materials Chemistry and Physics*, 113(1):334–337, 2009.

[234] C.H. Xu, C.H. Woo, and S.Q. Shi. Formation of CuO nanowires on Cu foil. *Chemical Physics Letters*, 399(1-3):62–66, 2004.

[235] M. Chen, Y. Yue, and Y. Ju. Growth of metal and metal oxide nanowires driven by the stress-induced migration. *Journal of Applied Physics*, 111(10):104305, 2012.

[236] C.X. Zhao, Y.F. Li, J. Zhou, L.Y. Li, S.Z. Deng, N.S. Xu, and J. Chen. Large-scale synthesis of bicrystalline ZnO nanowire arrays by thermal oxidation of zinc film: growth mechanism and high-performance field emission. *Crystal Growth & Design*, 13(7):2897–2905, 2013.

[237] L. Debbichi, M.C. Marco de Lucas, J.F. Pierson, and P. Kruger. Vibrational properties of CuO and Cu_4O_3 from first-principles calculations, and Raman and infrared spectroscopy. *The Journal of Physical Chemistry C*, 116(18):10232–10237, 2012.

[238] R. Wimmer-Teubenbacher, F. Sosada-Ludwikowska, B. Zaragoza Travieso, S. Defregger, O. Tokmak, J.S. Niehaus, M. Deluca, and A. Köck. CuO Thin Films Functionalized with Gold Nanoparticles for Conductometric Carbon Dioxide Gas Sensing. *Chemosensors*, 6(4):56, 2018.

[239] G. Fritz-Popovski, F. Sosada-Ludwikowska, A. Köck, J. Keckes, and G. Maier. Study of CuO Nanowire Growth on Different Copper Surfaces. *Scientific reports*, 9(1):807, 2019.

[240] Sh.R. Adilov, V.P. Afanaciev, I.N. Kashkul, S.E. Kumekov, N.V. Mukhin, and E.I. Terukov. Studying the composition and structure of films obtained by thermal oxidation of copper. *Glass Physics and Chemistry*, 43(3):272–275, 2017.

[241] T. Ishihara, M. Higuchi, T. Takagi, M. Ito, H. Nishiguchi, and Y. Takita. Preparation of CuO thin films on porous $BaTiO_3$ by self-assembled multibilayer film formation and application as a CO_2 sensor. *Journal of Materials Chemistry*, 8(9):2037–2042, 1998.

[242] Richard A Robie. Thermodynamic propertiesof minerals and related subsances at 298.15 K (25.0°C) and one atmosphere (1.013 bars) pressure and at higher temperatures. *US Geol. Surv. Bull.*, 1259, 1968.

[243] M.K. Seguin. Thermogravimetric and differential thermal analysis of malachite and azurite in inert atmospheres and in air. *The Canadian Mineralogist*, 13(2):127–132, 1975.

[244] X. Yang, S. Kattel, S.D. Senanayake, J.A. Boscoboinik, X. Nie, J. Graciani, J.A. Rodriguez, P. Liu, D.J. Stacchiola, and J.G. Chen. Low Pressure CO_2 Hydrogenation to Methanol over Gold Nanoparticles Activated on a CeO_x/TiO_2 Interface. *Journal of the American Chemical Society*, 137(32):10104–10107, 2015.

[245] Bundesministerium für Digitalisierung und Wirtschaftsstandort. Bundesrecht konsolidiert: Gesamte Rechtsvorschrift für Grenzwerteverordnung 2018, Fassung vom 27.02.2019.

[246] C. Schultealbert, T. Baur, A. Schütze, S. Böttcher, and T. Sauerwald. A novel approach towards calibrated measurement of trace gases using metal oxide semiconductor sensors. *Sensors and Actuators B: Chemical*, 239:390–396, 2017.

[247] E. Lackner. *Optimization of CMOS integrated tin oxide gas sensors using metallic and bimetallic nanoparticles*. PhD thesis, Technische Universität Graz, Juni 2017.

[248] J. Krainer. *Fabrication of CMOS Integrated Gas Sensor Devices Based on Tungsten Oxide Nanowires*. PhD thesis, Technische Universität Graz, Juni 2017.

[249] SmartThings Inc. Samsung smartthings. `https://www.smartthings.com/`, 2019. [Online; accessed 9-April-2019].

[250] Aeotec Inc. Aeotec multisensor 6. `https://aeotec.com/z-wave-sensor`, 2019. [Online; accessed 9-April-2019].

[251] Kentix GmbH. Kentix multisensor-door. `https://kentix.com/de/product/multisensor-door/`, 2018. [Online; accessed 9-April-2019].

[252] Bosch Sensortec GmbH. Bosch bme680. `https://www.bosch-sensortec.com/bst/products/all_products/bme680`, 2019. [Online; accessed 9-April-2019].

[253] M. Dohr, H.M.A. Ehmann, A.O.F. Jones, I. Salzmann, Q. Shen, C. Teichert, C. Ruzié, G. Schweicher, Y.H. Geerts, R. Resel, M. Sferrazza, and O. Werzer. Reversibility of temperature driven discrete layer-by-layer formation of dioctyl-benzothieno-benzothiophene films. *Soft Matter*, 13:2322–2329, 2017.

[254] Robert Wimmer-Teubenbacher, J. Krainer, E. Lackner, F. Sosada-Ludwikowska, K. Rohracher, E. Wachmann, K. Poulsen, J.S. Niehaus, and A. Köck. CMOS Integrable CuO Nanowire Array Gas Sensors Enhanced by Au - Nanoparticles for Humidity Independent Gas Sensing. *materialstoday: Proceedings*, 4(7):7149–7154, 2017.

[255] Robert Wimmer-Teubenbacher, E. Lackner, J. Krainer, S. Steinhauer, and A. Köck. Gas Sensor Devices based on CuO- and ZnO- Nanowires directly synthesized on silicon substrate. *MRS Advances*, 1(13):817–823, 2016.

[256] Robert Wimmer-Teubenbacher, S. Steinhauer, O. von Sicard, E. Magori, J. Siegert, K. Rohracher, C. Gspan, W. Grogger, and A. Köck. Gas Sensing Characterisation of CMOS Integrated Nanocrystalline SnO_2 – Au Thin Films. *materialstoday: Proceedings*, 2(8):4295–4301, 2015.

[257] J. Krainer, M. Deluca, E. Lackner, Robert Wimmer-Teubenbacher, F. Sosada-Ludwikowska, C. Gspan, K. Rohracher, E. Wachmann, and A. Köck. CMOS Integrated Tungsten Oxide Nanowire Networks for ppb-level H_2S Sensing. *Procedia Engineering*, 168:272–275, 2016.

[258] E. Lackner, J. Krainer, Robert Wimmer-Teubenbacher, F. Sosada-Ludwikowska, C. Gspan, K. Rohracher, E. Wachmann, and A. Köck. CMOS Integrated Nanocrystalline SnO_2 Gas Sensors for CO Detection. *Procedia Engineering*, 168:297–300, 2016.

[259] E. Lackner, J. Krainer, Robert Wimmer-Teubenbacher, F. Sosada-Ludwikowska, M. Deluca, C. Gspan, K. Rohracher, E. Wachmann, and A. Köck. Carbon monoxide detection with CMOS integrated thin film SnO_2 gas sensor. *materialstoday: Proceedings*, 4(7):7128–7131, 2017.

[260] J. Krainer, M. Deluca, E. Lackner, Robert Wimmer-Teubenbacher, F. Sosada-Ludwikowska, C. Gspan, K. Rohracher, E. Wachmann, and

A. Köck. Hydrogen sulphide detection by CMOS integrated tungsten oxide nanowire networks. *materialstoday: Proceedings*, 4(7):7132–7136, 2017.

[261] F. Sosada-Ludwikowska, Robert Wimmer-Teubenbacher, and A. Köck. Dry process of transferring MOx nanowires used for gas sensing applications. *materialstoday: Proceedings*, 7(3):930–933, 2019.

[262] Robert Wimmer-Teubenbacher, F. Sosada-Ludwikowska, B. Zaragoza Travieso, S. Defregger, O. Tokmak, J.S. Niehaus, M. Deluca, and A. Köck. CuO Thin Films Functionalized with Gold Nanoparticles for Conductometric Carbon Dioxide Gas Sensing. *Chemosensors*, 6(4):56, 2018.

chemosensors

MDPI

Article

CuO Thin Films Functionalized with Gold Nanoparticles for Conductometric Carbon Dioxide Gas Sensing

Robert Wimmer-Teubenbacher [1,*], Florentyna Sosada-Ludwikowska [1], Bernat Zaragoza Travieso [1], Stefan Defregger [1], Oeznur Tokmak [2], Jan Steffen Niehaus [2], Marco Deluca [1] and Anton Köck [1]

[1] Materials Center Leoben Forschung GmbH, A-8700 Leoben, Austria; florentyna.sosada-ludwikowska@mcl.at (F.S.-L.); bernat.zaragoza-travieso@mcl.at (B.Z.T.); stefan.defregger@mcl.at (S.D.); marco.deluca@mcl.at (M.D.); anton.koeck@mcl.at (A.K.)

[2] Fraunhofer-Institut für Angewandte Polymerforschung IAP-CAN, D-20146 Hamburg, Germany; oeznur.tokmak@iap.fraunhofer.de (O.T.); jan.steffen.niehaus@iap.fraunhofer.de (J.S.N.)

* Correspondence: robert.wimmer-teubenbacher@mcl.at; Tel.: +43-3842-4592-234

Received: 28 August 2018; Accepted: 21 November 2018; Published: 22 November 2018

Abstract: Metal oxides (MOx) are a well-established material for gas sensing. MOx-based gas sensors are sensitive to a wide variety of gases. Furthermore, these materials can be applied for the fabrication of low-cost and -power consumption devices in mass production. The market of carbon dioxide (CO_2) gas sensors is mainly dominated by infra-red (IR)-based gas sensors. Only a few MOx materials show a sensitivity to CO_2 and so far, none of these materials have been integrated on CMOS platforms suitable for mass production. In this work, we report a cupric oxide (CuO) thin film-based gas sensor functionalized with gold (Au) nanoparticles, which exhibits exceptional sensitivity to CO_2. The CuO-based gas sensors are fabricated by electron beam lithography, thermal evaporation and lift-off process to form patterned copper (Cu) structures. These structures are thermally oxidized to form a continuous CuO film. Gold nanoparticles are drop-coated on the CuO thin films to enhance their sensitivity towards CO_2. The CuO thin films fabricated by this method are already sensitive to CO_2; however, the functionalization of the CuO film strongly increases the sensitivity of the base material. Compared to the pristine CuO thin film the Au functionalized CuO film shows at equal operation temperatures (300 °C) an increase of sensitivity towards the same gas concentration (e.g., 2000 ppm CO_2) by a factor of 13. The process flow used to fabricate Au functionalized CuO gas sensors can be applied on CMOS platforms in specific post processing steps.

Keywords: metal oxides; gas sensors; CuO; CO_2; CMOS integration

1. Introduction

Natural emissions of carbon dioxide CO_2 in Earth's atmosphere can be referenced to the carbon cycle. Man-made or anthropogenic CO_2 emissions can be mainly attributed to the combustion of fossil fuels in transport, industry, and electricity [1]. Over the last two centuries the carbon dioxide concentration has risen from an average value of approximately 280 ppm [2] (pp. 4–6) to a value about 411 ppm [3]. Apart from this alarming trend, CO_2 has a significant direct impact to human health and thus plays an important role for indoor air quality monitoring. The main source of the indoor CO_2 concentration is the metabolism of the occupants, who continuously exhale a steady amount of CO_2, that is added to the base global CO_2 concentration, setting the lower level for the indoor concentration. An elevated indoor CO_2 level causes significant symptoms for humans: reduction of mental concentration, fatigue, headache, and dizziness [4]. Extreme conditions, such

as agricultural silo accidents, can even lead to death. Application of CO_2 gas sensors in heating, ventilation, and air conditioning systems (HVAC) improves indoor air quality and thus the comfort for its occupants. Moreover, precise control of HVAC by air quality monitoring sensors—in particular, CO_2 sensors—would strongly reduce the overall energy consumption of those systems. According to Nassif [5] the energy consumption of regular HVAC systems can be potentially decreased by 25% by switching to intelligent CO_2 controlled HVACs, which would have a great impact on the global CO_2 emissions and thus the outdoor CO_2 levels. Currently available commercial CO_2 gas sensors, which measure the CO_2 concentration directly, are mostly based on optical (infra-red) detection [6] employing an IR emitter and a detector with a specific absorption length in between. The advantages of these sensors are their precision, resolution, and robustness. The disadvantages are their size (several cm), high power consumption and comparatively high cost. At research level a lot of effort is put into the exploitation of new approaches for optical CO_2 sensors [7,8], in particular with respect to miniaturization. Employment of wave-guides and integration on silicon or even CMOS devices might reduce size and power consumption; however, the optical principle requires a minimum absorption length, which prevents significant miniaturization. A promising alternative to optical sensors are conductometric chemical sensors. A variety of established sensors already exist on the market, which can detect various target gases, such as CO, H_2 or Volatile Organic Compounds (VOCs).

In literature various material types exhibiting sensitivity towards CO_2 are reported: metal organic framework [9], nascion [10], perovskite [11], solid electrochemical type [12]. The most prominent class of materials for gas sensing are metal oxide materials, which exhibit high sensitivity towards numerous gases, but in general hardly any to CO_2. For the following metal oxides a sensitivity to CO_2 has been reported: Gd-doped CeO_2 [13], Pd-doped La_2O_3 [14], nano-particulate CuO films [15,16] and $BaTiO_3$-CuO films [17]. However, up to now no electrical sensor capable to directly detect CO_2 is available as a commercial product.

In this work, we present CuO thin film sensors fabricated by thermal oxidation of patterned copper layers. The sensitivities of the pristine CuO sensors and sensors functionalized with gold (Au) nanoparticles have been evaluated towards CO_2 at different humidity levels. While the pristine CuO sensor has a maximum response of 32% at 350 °C, the Au functionalization of the CuO sensor leads to an exceptional increase of the response by a factor of 11 up to 365% at 300 °C. To our best knowledge this is one of the highest responses ever reported for a conductometric CO_2 sensor. Table A1 shows some of the highest CO_2 responses for metal oxide-based sensors in literature compared to this work. One of the most important features of our sensor device is that the entire process flow enables an integration on CMOS devices.

2. Materials and Methods

2.1. Gas Sensor Fabrication

The gas sensor is fabricated using a five-step process: (1) electrode deposition, (2) fabrication of a patterned copper (Cu) layer, (3) sensor stack assembly, (4) thermal oxidation and (5) nanoparticles functionalization. All the essential parameters of the fabrication process have been optimized to enable subsequent integration on CMOS devices.

1. The base substrate for fabricating the gas sensors is a silicon substrate with a thermal silicon oxide layer of 300 nm on top (SIEGERT WAFER GmbH). Gold electrodes are employed to electrically contact the CuO sensing film. The fabrication of the electrode system is done by photolithography with a positive photoresist (AZ®MIR701, Microchemicals, EVG 620 Mask aligner) and thermal evaporation (Univex Evaporator 450 by Leybold GmbH) of 5 nm thick titanium layer and a gold layer of 200 nm thickness as electrode material. The lift-off process is realized by submerging the substrate in acetone for a duration of 12 h (see Table A2 in appendix for the applied process parameters). The geometry of the electrode system is designed to enable four-point measurement (see Figure 1b) and to ensure precise electrical resistance measurements.

2. In the second step the Cu-films are deposited on top of the Ti/Au electrode system. For this a 60 µm by 25 µm structure is exposed by electron beam lithography (Raith eLINE plus, positive electron beam resist AR-P 672.08, ALLRESIST GmbH) into the resist. The structure itself is subdivided into six strips, which are separated by a distance of 2.25 µm. After resist development, a Ti adhesion layer (thickness 5 nm) and a Cu layer (thickness 500 nm) are deposited by thermal evaporation (Univex Evaporator 450, Leybold GmbH). The lift-off process is realized by submerging the entire substrate in acetone for 4 h.
3. In the third step the assembly of the gas sensor stack is performed. Metal oxide gas sensors need to be operated at higher temperatures (200 °C–400 °C). Therefore, the sensor stack, containing the substrate with Ti/Au electrode system and the Cu layer (as precursor for CuO), must be merged with a heater and a thermocouple. The heater consists of two Pt 6.8 elements (Delta-R GmbH) connected in series; a Pt100 element (Delta-R GmbH) is used as the thermocouple to monitor operation temperature. The sensors are glued with both heater elements and thermocouple to a sensor system with thermoconductive adhesive (Aremco Ceramabond 865, Aremco Products Inc.). The final device is soldered, and wire bonded to a custom-made printed circuit board (PCB) as shown in Figure 1a.
4. The fourth step addresses the thermal oxidization of the Cu metal layer, which is performed in situ in the gas measurement set-up (GMS). The atmospheric condition in the GMS is provided by synthetic air (Linde Gas GmbH) with relative humidity level (rH) of 50%. For a duration of six hours the gas sensor is heated at a constant temperature of 400 °C, which results in oxidation of the Cu layer. The entire Cu metal layer is oxidized to form a continuous CuO film.
5. The sensor fabrication is finalized in the fifth step by functionalizing the CuO film with Au nanoparticles (Au-NPs). This is performed by stepwise drop coating a volume of 5 µL of an aqueous Au-NPs solution (CANdot® Series G, c = 100 µg Au/mL, Fraunhofer IAP-CAN) onto the sensor surface. To ensure a fast evaporation of the solvent during nanoparticles deposition, the sensor is heated up to 85 °C. This is repeated several times; each consecutive step is started once the solvent is evaporated.

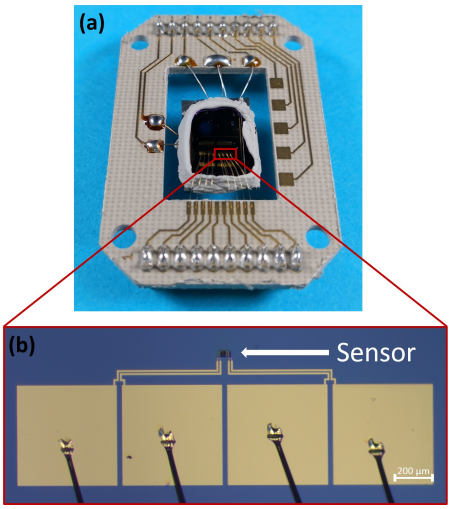

Figure 1. (**a**) Evaluation board with soldered heater and thermocouple and wire bonded gas sensor stack. (**b**) Wire bonded gas sensors with electrode system.

2.2. Sensitivity Calculation and Data Evaluation

The gas sensors sensitivity is determined by Equation (1). Herein, the resistance of the gas sensors in synthetic air is R_{air}, whereas the highest resistance value during gas exposure is R_{gas}. The sensitivity is a measure of the gas sensors' response towards a specific target gas at a specific concentration, humidity level and the operation temperature of the gas sensor.

$$S[\%] = \frac{(R_{gas} - R_{air})}{R_{air}} \cdot 100 \quad (1)$$

2.3. Scanning Electron Beam Microscopy

The scanning electron microscopy (SEM) investigation was done on an Auriga®-CrossBeam® Workstation (Carl Zeiss Microscopy GmbH) with an acceleration voltage of 10 keV. The surface investigations at high magnification and the elemental mapping were done on a ZEISS GeminiSEM 450 at 3 keV and 5 keV.

2.4. Raman Spectroscopy

The Raman spectrum was measured with LabRAM HR800 from Horiba Jobin Yvon. A green (514.5 nm) Ar-ion laser in backscattering geometry was used as an excitation source. The analysis of the Raman signal was performed with a grating (1800 g/mm), whereas the signal detection was done by a multichannel CCD.

2.5. Gas Measurements Set-Up

The GMS used in this work is a custom-made system capable of chemical sensor evaluation in a controlled and adjustable mixture of gases. The GMS consists of two parts: the gas atmospheric part and the electrical evaluation part.

The gas atmospheric part shown in Figure A1a enables precise control of the concentrations of two different test gases and the relative humidity (rH) levels of the background gas. Since the goal is to simulate an ambient atmosphere, synthetic air (20% O_2, 80% N_2, Linde Gas GmbH) is used as background gas. The background gas is set by two mass flow controllers (type: EL-FLOW, Bronkhorst High-Tech B.V.). The first mass flow controller is providing dry air, whereas the second mass flow controller is providing wet air, formed by bubbling part of the synthetic air through a container filled with deionized water. The two outputs of the dry and wet air are mixed to provide specific rH levels in the range of 10%–90% rH, which is measured using a commercial, humidity sensors (type: AFK-E, KOBOLD Holding Gesellschaft m.b.H.). Similar to the background gas the flows of each of the two test gases are set by three independent mass flow controllers (type: EL-FLOW, Bronkhorst High-Tech B.V.) to provide a wide adjustable range of concentrations. Each of these three mass flow controllers is calibrated for a specific concentration range to provide precision and range for varying test plan requirements. The background gas and the test gases are mixed before being introduced into the measurement chamber, which is an air-tight sealed stainless steel tube holding a volume of approximately 80 cm^3. Our specific GMS is designed for a constant flow of 1000 sccm to ensure an optimal gas injection into the measurement chamber. The gas is flowing parallel to the sensor surface. The sensor stack (see Figure 1) has a comparatively high thermal mass and no cooling effect was observed. Moreover, the Pt100 element provides a feedback loop to keep the sensor stack at a constant temperature.

The electrical evaluation part of the GMS (see Figure A1b) is designed for measuring the electrical resistance of the gas sensor, for operating the heater and for measuring the operation temperature of the entire sensor stack via voltage measurement of the thermocouple. The gas sensor resistance is measured by employing a source measure unit (type: 2400 SourceMeter SMU, Keithley). The heater is operated by a voltage source (type: PL330P, Thurlby Thandar Instruments). The voltage measurement of the thermocouple is done by a digital multimeter (type: 34401A, Keysight technologies). Both parts of the GMS are joined by a LabView program, wherein specific test plans can be defined.

3. Results

3.1. Copper Oxide Characterization

The evaluation of the gas sensitive copper oxide film was done by SEM and Raman spectroscopy. Figure 2a shows the oxidized surface of the copper structures. The initial Cu strips can still be seen suggestively as vertical lines; however, thermal oxidation results in swelling of the Cu structures, the gaps between the separated Cu stripes are closed, electrically connected and a continuous film of copper oxide is formed. The oxidation parameters ($T_{Oxidation}$ = 400 °C/rH = 50%/t = 6 h) were chosen to result in the formation of a CuO film instead of CuO nanowires. Figure 3 shows a representative SEM image of the sensor surface, where the bright spots indicate the Au-NPs. A TEM picture of a Au-NP having an average diameter of 20 nm is shown in the insert. The SEM image shows both single Au-NPs on the CuO surface as well as agglomerated Au-NPs. To analyze the material composition and confirm the materials responsible for the chemical sensing mechanism at the sensor's surface, an elemental mapping has been performed in the 4 µm × 4 µm section of the sensor surface as shown in Figure 3. The elemental mapping was done for four elements and is presented in Figure 4: (a) gold Au, (b) copper Cu, (c) oxygen O and (d) silicon Si. The contrast of each color corresponds to the occurrence of the element. The SEM picture shows multiple nanoparticles on the sensor surface, high contrast. The Au elemental map clearly shows the highest contrast for Au at the same bright structures, which are shown in Figure 3 as Au-NPs. In both the Cu and the O elemental maps voids can be clearly seen at the location of these Au-NPs. Figure 4d presents the elemental mapping of Si, where the occurrence of Si is a result of silicon diffusion during the oxidation process. Figure 5 shows an EDX of one of the Au-NPs, which clearly indicates that these nanoparticles are made of Au.

The identification of the copper oxide state (CuO or Cu_2O) was performed by Raman spectroscopy. CuO possesses 12 phonon modes due to the presence of four atoms in the primitive unit cell. Factor group analysis gives [18]:

$$\Gamma_{vibr} = A_g + 2B_g + 4A_u + 5B_{u'} \quad (2)$$

of which only the three A_g and B_g modes are Raman-active. The Raman spectrum of CuO presents a strong A_g mode at 296 cm^{-1} and two B_g modes at 346 cm^{-1} and 631 cm^{-1}. These modes involve only the vibrations of oxygen atoms in the direction of the b-axis of the unit cell for A_g and perpendicular to the b-axis for B_g modes [18]. Figure 2b presents the Raman spectrum measured on the thermally oxidized film. The assignment of the Raman modes confirms that only CuO (one A_g mode and two B_g modes compatible with the positions reported in literature) is present—other copper oxide species cannot be evidenced from the measured spectrum. Cu_2O and Cu_4O_3, in fact, present distinctive modes at 150 cm^{-1}, 220 cm^{-1} and 541 cm^{-1}, respectively [18], which were not detected on the oxidized CuO film.

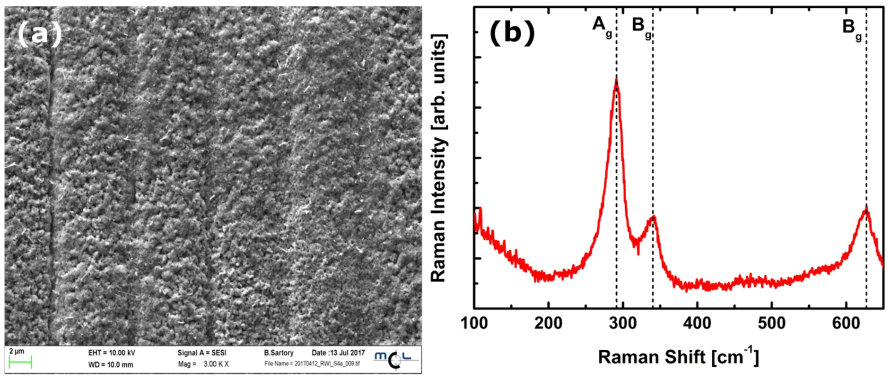

Figure 2. (**a**) SEM picture of the thermally oxidized CuO film. (**b**) Raman spectrum of the thermally oxidized CuO film.

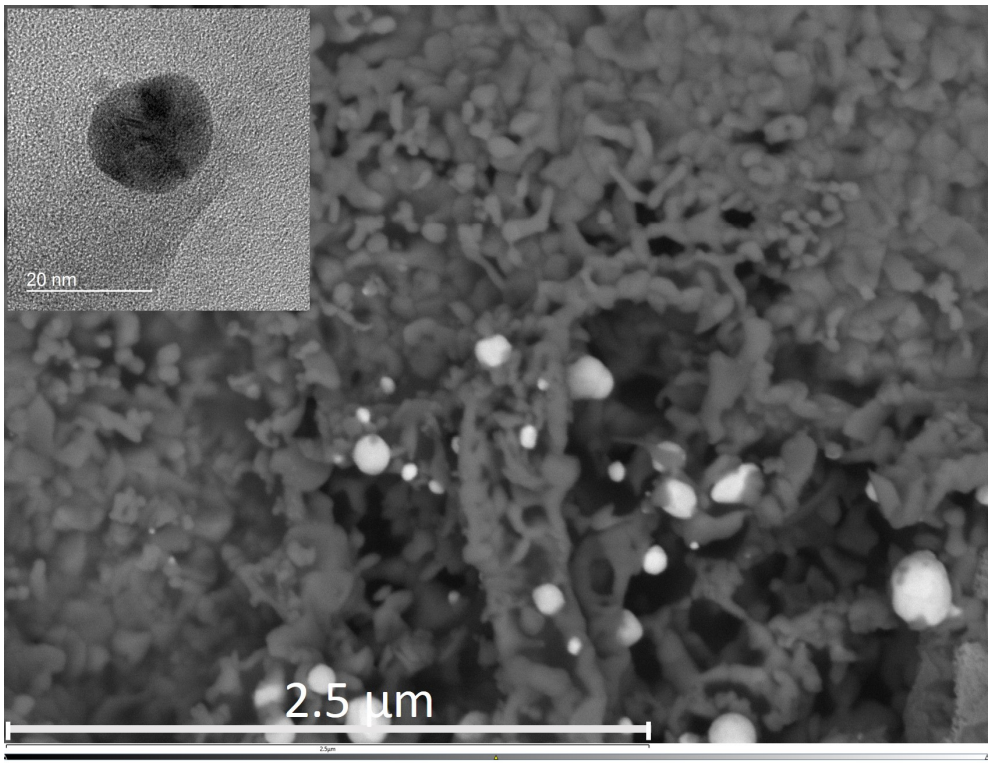

Figure 3. SEM image of the investigated sensor surface area containing Au nanoparticles. The insert shows a TEM image of a single nanoparticle.

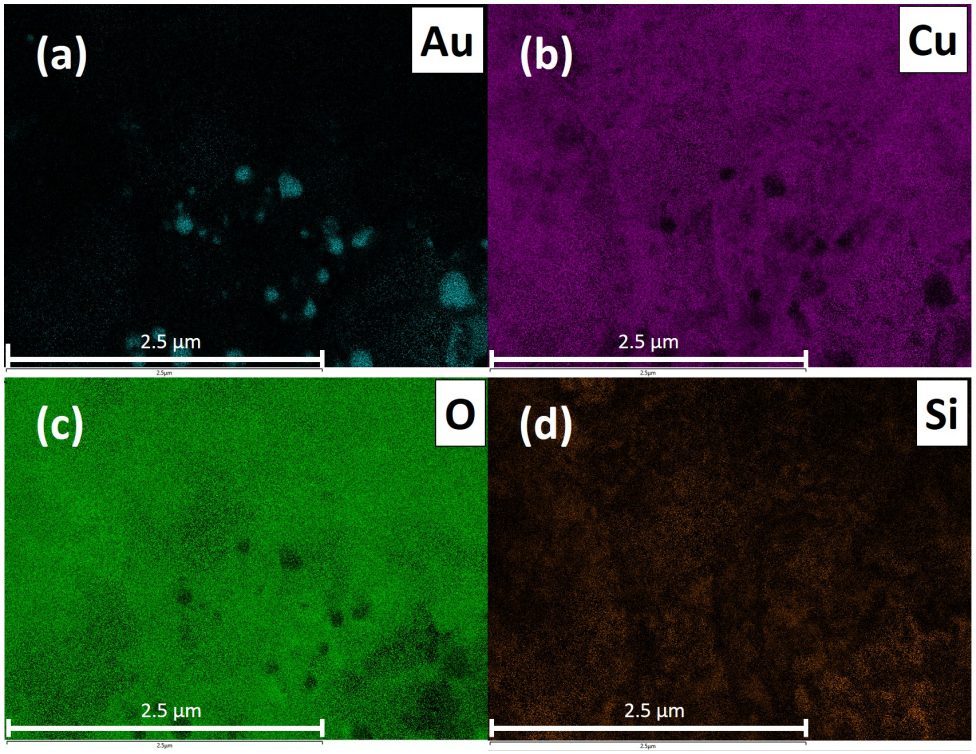

Figure 4. Elemental mapping of a 4 µm × 4 µm section on the copper oxide surface with 5 keV (primary beam energy). (**a**) Au elemental map, (**b**) Cu elemental map, (**c**) O elemental map and (**d**) Si elemental map.

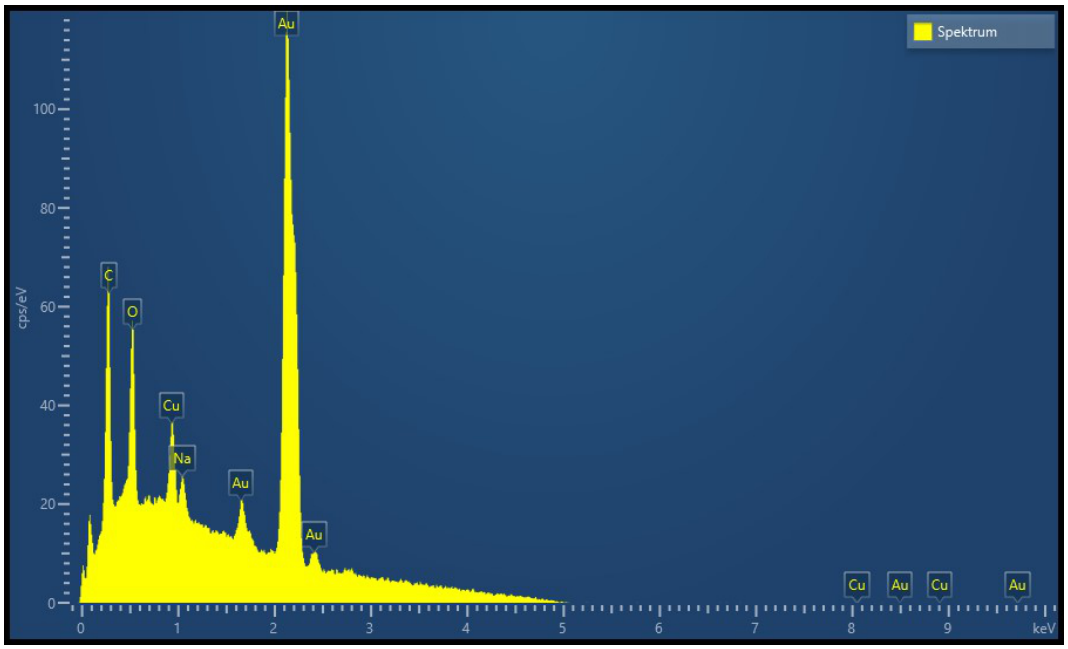

Figure 5. EDX spectrum of a single nanoparticle on the copper oxide surface at 5 keV.

3.2. Carbon Dioxide Measurements of a Pristine and Functionalized Gas Sensor

The CO_2 measurements were performed in the GMS (see Section 2.5). The evaluation of the gas sensors' performance towards CO_2 was done following this measurement plan: the gas sensor was operated at three different temperatures (300 °C, 350 °C, 400 °C) and for each operating temperature three rH levels (25%, 50%, 75%) were set. Within each rH level a series of CO_2 gas pulses (single pulse duration: 5 min) with various concentrations (250 ppm, 500 ppm, 1000 ppm, 1500 ppm and 2000 ppm) were applied to meet the general demands of indoor air quality monitoring. Figure 6 shows the sensor resistances of the pristine (not functionalized with nanoparticles) and the Au-NPs functionalized CuO sensors responding to different concentrations of CO_2 at 300 °C operation temperature. Herein, it can be seen that the base resistance of the functionalized sensor decreases by a factor of 2 compared to the pristine sensor. The pristine CuO sensor exhibits a small response to CO_2 (maximum 28%), which decreases with increasing rH level. The response of the functionalized CuO sensor is 13 times higher and reaches a maximum of 365%. The response increases linearly with the CO_2 concentration. To the best of our knowledge this is one of the highest reported sensitivities of a conductometric CO_2 sensor. For clear comparison the gas sensor performance of the pristine and Au-NPs functionalized CuO sensors to a CO_2 concentration of 2000 ppm are shown in Figures 7 and 8, respectively, for three different operation temperatures (300 °C, 350 °C, 400 °C) and three different rH levels (25%, 50%, 75%). The sensitivities are normalized in accordance with Equation (1).

Figure 7 depicts the CO_2 gas measurement of a pristine CuO gas sensor towards a single CO_2 gas pulse of 2000 ppm. In this figure the gas sensor response for all three sensor operation temperatures is shown for constant relative humidity levels of (a) 25%, (b) 50% and (c) 75%. Figure 7d depicts the CO_2 gas pulse of 2000 ppm. The sensitivity of the pristine CuO gas sensor reaches a maximum of 32% at an operation temperature of 350 °C and a rH-level of 50%.

Figure 8 shows the sensitivity of the Au-NPs functionalized CuO gas sensor. Please note that the sensitivity scale of Figure 8 is expanded by a factor of ten as compared to the scale of Figure 7. The functionalized CuO gas sensor reaches a maximum of 365% at an operation temperature of 300 °C and at a rH-level of 50%. The maximum sensitivity is a factor of 11 higher than that of the pristine sensor at its optimal, operation temperature of 350 °C. The response of the Au-NPs functionalized CuO sensor decreases with increasing temperature (350 °C) and drops drastically at 400 °C operation temperature.

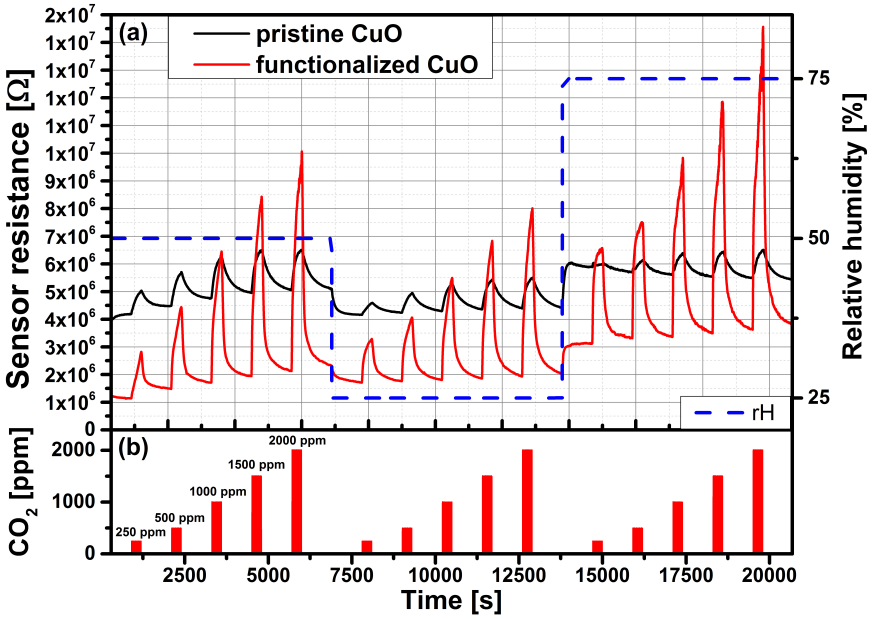

Figure 6. (**a**) Carbon dioxide measurement of the pristine and functionalized CuO gas sensors at an operation temperature of 300 °C and rH levels of 25%, 50% and 75%. (**b**) CO_2 gas pulses: 250 ppm, 500 ppm, 100 ppm, 1500 ppm and 2000 ppm.

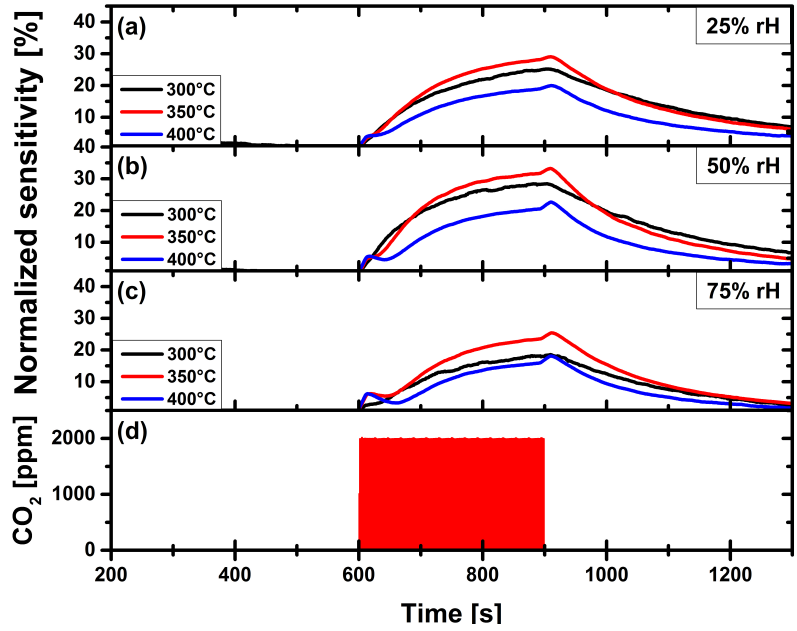

Figure 7. Carbon dioxide measurement of pristine CuO gas sensor, at operation temperatures 300 °C, 350 °C and 400 °C, at constant relative humidity levels of: (**a**) 25%. (**b**) 50%. (**c**) 75%. (**d**) Applied gas pulse of 2000 ppm CO_2.

In Figure 9 the maximum sensitivities of the pristine sensor and the Au-NPs functionalized sensor to a CO_2 concentration of 2000 ppm are compared for the different relative humidity levels (25%, 50%, 75%) at the same operation temperature of 300 °C. The functionalized sensor has a maximum sensitivity of 365% at 50% rH, which decreases down to 283% at 75% rH. Its average response time is 4.3 min with an average recovery time of 4.4 min. The pristine sensor has a maximum sensitivity of 28% at 50% rH, which decreases down to 18% at 75% rH. The average response time for the pristine sensor

is 3.7 min, whereas the its average recovery time is 11.1 min. At the same operation temperature of 300 °C the sensitivity of the Au-NPs functionalized sensor is even increased by a factor of 13 compared to the pristine sensors' sensitivity. While both types of sensors exhibit a certain cross-sensitivity to water, this sensitivity drop is much less in the case of the functionalized sensor. Functionalization with Au-NPs thus not only increases the sensitivity, but also decreases cross-sensitivity to humidity.

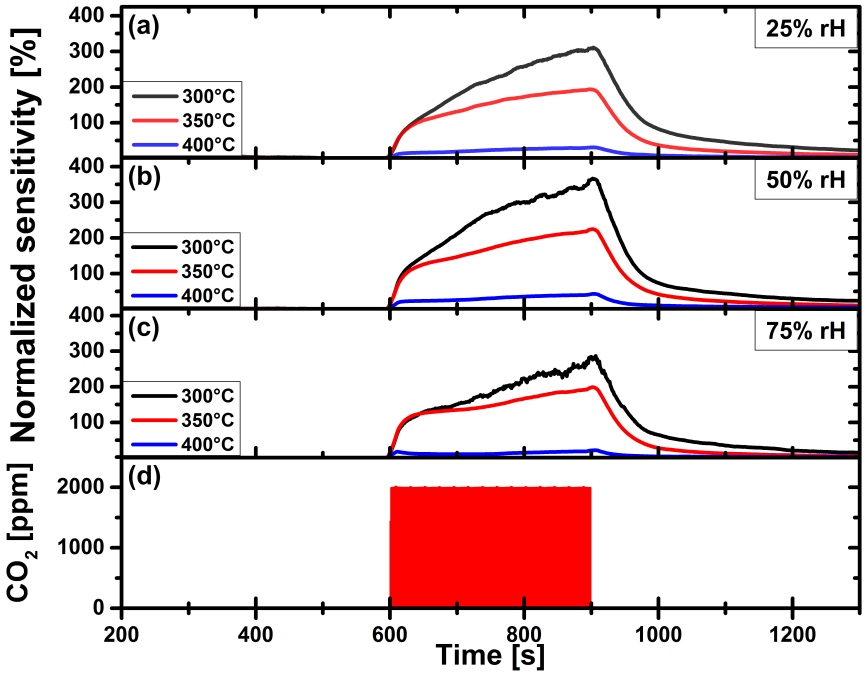

Figure 8. Carbon dioxide measurement of gold nanoparticles functionalized CuO gas sensor, at operation temperatures 300 °C, 350 °C and 400 °C, at constant relative humidity levels of: (**a**) 25%. (**b**) 50%. (**c**) 75%. (**d**) Applied gas pulse of 2000 ppm CO_2.

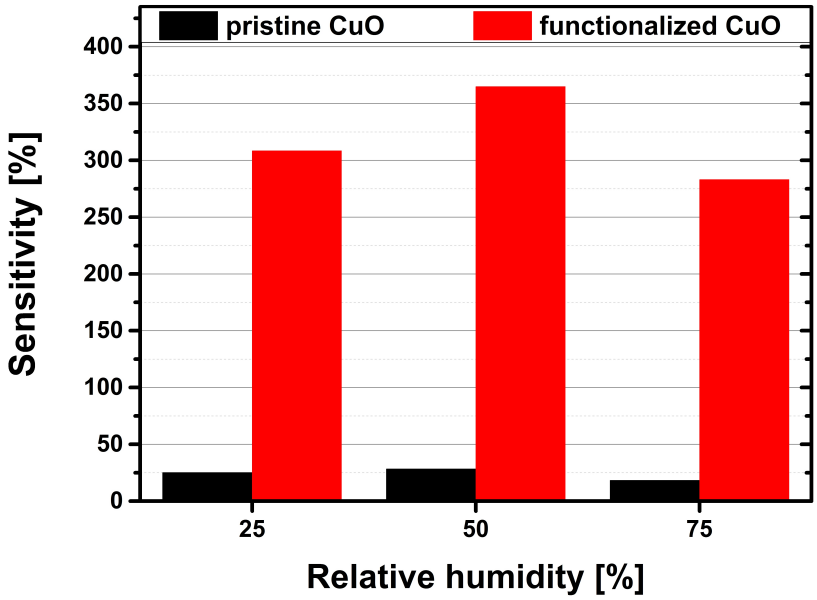

Figure 9. Comparison of the pristine (black bars) and the Au-NPs functionalized (red bars) gas sensors sensitivities towards a 2000 ppm CO_2 gas pulse at relative humidity levels of 25%, 50% and 75% at an operation temperature of 300 °C.

3.3. Carbon Monoxide Measurements

Cross selectivity is an important issue for chemical sensors. Our sensor developments are focused on indoor air quality monitoring, where detection of carbon monoxide (CO) is important for safety reasons. CO is a color- and odorless gas, which is highly toxic. Incomplete combustion of natural gas in gas appliances, such as boilers, gas fires, or gas cookers can lead to people being exposed to CO in their homes or at work place. Prolonged exposure to CO in case of a defect heating system, for example, can eventually be fatal. The maximum permitted work place concentration value for CO is 30 ppm [19] in Germany. Thus, the sensitivity of the Au-NPs functionalized CuO-based sensors has been also evaluated towards CO. Figure 10 shows the sensitivity of the Au-NPs functionalized CuO-based gas sensor towards CO_2 and CO. The CuO-based sensors show a response of less than 5% at CO concentrations around 20 ppm. Thus, to achieve a relevant response, the concentration of CO has been increased up to 200 ppm, which is compared with the response to a CO_2 concentration of 2000 ppm. The sensor temperature is set to 300 °C, since this is the optimum operation temperature for both test gases. Furthermore, the sensitivities have been evaluated for three different relative humidity levels (25%, 50%, 75%).

The sensitivity of the gas sensor towards CO reaches its maximum of 86% at 50% rH. At 75% rH the sensitivity to CO decreases to 56%. The average response time for the CO measurement is 3 min, whereas the average recovery time is 10 min. The direct comparison of the Au-NPs functionalized sensors' sensitivity to the maximum concentrations of CO_2 and of CO at 50% rH shows that the CO_2 sensitivity is roughly 4 times higher than the CO sensitivity. Figure 10 clearly shows that the CuO-based sensor exhibits a much higher sensitivity towards CO_2 which is enough to discriminate between the two different target gases.

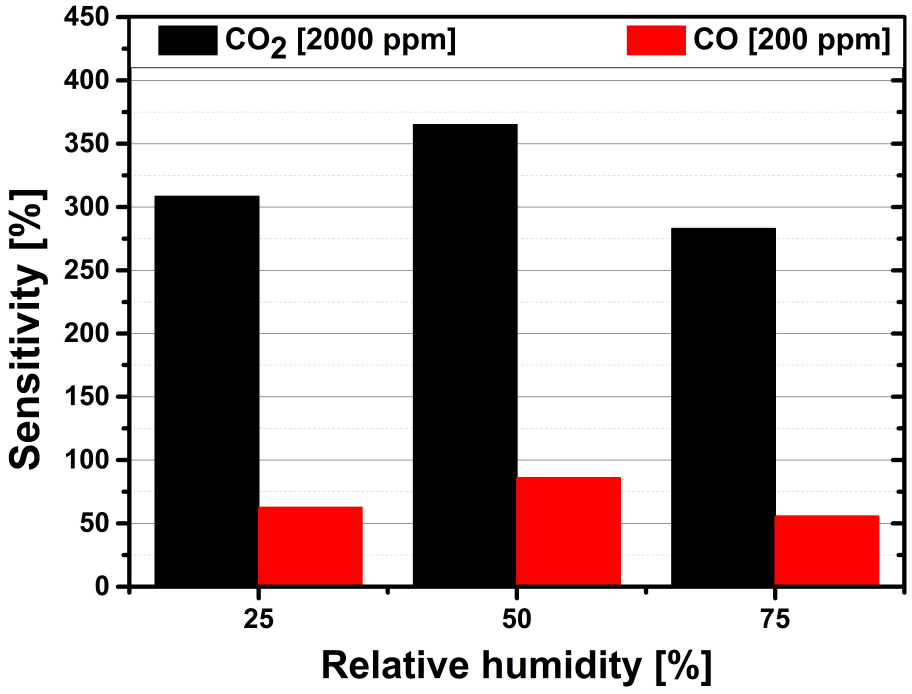

Figure 10. Comparison of the Au-NPs functionalized gas sensors sensitivities towards a 2000 ppm CO_2 gas pulse (black bars) and a 200 ppm CO gas pulse (red bars) at relative humidity levels of 25%, 50% and 75% at an operation temperature of 300 °C.

4. Discussion and Conclusions

The CuO films used within this work are formed during an in situ thermal oxidation process [20]. It is well established that metallic Cu predominately oxidizes into cuprous oxide (Cu_2O) or cupric oxide (CuO). As proven by Raman spectroscopy, in case of our sensors the thermal oxidation resulted in CuO. According to Chen et al. [21] copper oxidizes by forming a multi-layer system of metallic Cu, Cu_2O and CuO. Xu et al. [22], who investigated the thermal oxidation of Cu foils, found that oxidation temperatures of 400 °C and higher would result in the formation of CuO nanowires. In our case, however, only a few CuO-NWs have been found on the thermally oxidized Cu structures. The employed Cu structures have a smaller lateral dimension and thickness, and thus much less volume than a bulk material. Furthermore, the Cu-layers have been deposited by thermal evaporation method. Both specific features—small Cu volume and evaporation method—could lead to a deviation from Xu's findings. The authors presume the gaps between the Cu stripes provide additionally lateral room for the thermal copper oxide to expand. Thereby, the built-up of strain or stress in the Cu structure, which are strong driving forces for the growth of CuO-NWs during oxidation, is to a large extent avoided. As a result, the formation of the CuO nanowires could be inhibited.

The SEM investigation show (Figure 2a) that the gaps between the copper structures are bridged by the expanding CuO. We conclude that the thermal oxidation process results first in a multi-layer of Cu, Cu_2O and CuO [21], which is subsequently fully converted to CuO during the six hours oxidation. This is in accordance with the work of Adilov et al. [23], who found that Cu_2O films heated to a temperature of 400 °C and above would transform into CuO. This assumption is fully supported by Raman spectroscopy measurement, where no peaks for Cu- and Cu_2O-phases have been found on our sensing films.

It has already been reported in literature that CuO is sensitive to carbon dioxide [16,24]. The results in Figure 7 show that the maximum sensitivity of our pristine CuO sensor exposed to a CO_2 concentration of 2000 ppm at 50% rH and an operation temperature of 350 °C is 35%. This supports findings in literature and can be compared to CuO-based sensors reported by Abdelmounaim et al. [24] and Ishihara et al. [25].

A potential surface reaction explaining the interaction between the target gas CO_2 and the sensing material CuO (NPs) has been described by Tanvir et al. [16]. A key reactant of this reaction is humidity. The authors of [16] presume that the CuO-NPs' surface reacts with CO_2 and H_2O forming either malachite or azurite, since these reactions are thermodynamically more favorable than the formation of copper carbonate ($CuCO_3$). Equations (3) and (4) display the formation equations of these two hydroxycarbonates. Furthermore, Tanvir et al. [16] presume that CO_2 can either be available on the surface in its gaseous phase or solvated in water. Table 1 shows the Gibbs free energy for the formation of malachite and azurite at 400 ppm CO_2 at 298.15 K. Equations (A1), (A2) and (A3) and literature values (Table A4) used for the calculations of the values in Table 1 can be found in the appendix. Since malachite and azurite are both insulators the formation of those compounds on the sensor surface would result in a resistance increase. This sensing mechanism deviates from the established ionosorption model, where adsorbed ionic oxygen species on the sensor surface interact with the test gas resulting in resistance change of the sensor.

$$2CuO_{(s)} + CO_{2(aq)} + H_2O_{(l)} \rightleftharpoons Cu_2(OH)_2CO_{3(s)} \quad (3)$$

$$3CuO_{(s)} + 2CO_{2(aq)} + H_2O_{(l)} \rightleftharpoons Cu_3(OH)_2(CO_3)_{2(s)} \quad (4)$$

Table 1. Gibbs free energy of the malachite and azurite reaction (Equations (3) and (4)) at 298.15 K at 400 ppm of CO_2.

Hydroxycarbonate	CO_2 [ppm]	$\Delta_R G$ [$\frac{kJ}{mol}$] at 298.15 K
malachite [$Cu_2(OH)_2CO_{3(s)}$]	400	−8.3
azurite [$Cu_3(OH)_2(CO_3)_{2(s)}$]	400	−8.2

The decrease in sensor sensitivity at temperatures exceeding the optimal operation temperature of 300 °C can be connected to the formation of malachite or azurite too. Seguin [26] investigated the dissociation of malachite and azurite by DTA measurements. Seguin found that the malachite dissociates in a temperature window of 310 °C to 420 °C, whereas azurite dissociates between 290 °C to 395 °C. Therefore, the authors presume that malachite is mainly responsible for the sensing mechanism at the optimal operation temperature. Furthermore, the dissociation of malachite and azurite at these temperatures explains the decrease in sensitivity at the investigated operation temperatures of 350 °C and 400 °C.

The dramatic increase of the sensitivity to CO_2 has been achieved by functionalizing the pristine CuO film with Au-NPs. According to Korotcenkov [27] nanoparticles deposited onto a MOx surface in general change the sensitivity of a metal oxide gas sensor either by chemical sensitization or electronic sensitization. The authors presume that the interface of metal oxide and gold nanoparticles provide additional active cites for the adsorption of CO_2. A similar process was reported by Yang et al. [28], where the base material was a CeO_x/TiO_2 substrate on which Au nanoparticles were deposited. As a result, the adsorption of CO_2 increased. In our case, the increased CO_2 adsorption could lead to a rise in malachite formation, thereby increasing the sensors' sensitivity. However, at the moment we do not understand this interaction mechanism yet. We cannot exclude chemical surface reactions such as diffusion of Au into the CuO and resulting alloy of Au–CuO hybrid NPs or similar effects, which might arise due to the high operation temperature up to 400 °C. Detailed analysis of the Au-NPs functionalized CuO surface with respect to potentially new alloys or phases are presently under investigation in order to clarify the surface reaction process for the Au-NPs functionalized CuO film.

The lifetime of the CO_2 sensor has been tested over more than 2 weeks in DC-operation and a degradation of the sensor performance has been observed, which the authors mainly attribute to structural changes of the functionalization. As is obvious from Figure 3, the Au nanoparticles seem to agglomerate over time, which might be responsible for a reduced response. Another issue is the adhesion of the CuO-layer on the Si-substrate. Although the chosen patterns (Cu stripes) release part of the stress/strain during thermal oxidation, reliable adhesion is still a problem. Optimization of the process technology steps (variation of gap width between Cu stripes, Cu-thickness etc.) is in progress. Concerning repeatability, the process technology used in this work to functionalize the CuO surface with the Au nanoparticles is drop-coating. Since this method has limits concerning reproducibility, more precise technologies for deposition such as ink-jet printing will be employed in the future to ensure repeatable Au-coverage.

The issue of cross-sensitivity is investigated by the evaluation of the Au-NPs functionalized sensors' sensitivity towards carbon monoxide. Figure 10 clearly shows that the sensor exhibits a higher sensitivity towards CO_2. Although the maximum concentrations, which are compared in Figure 10 are not equivalent, this comparison reflects practical requirements for indoor air quality monitoring. CO_2 concentration can easily exceed 2000 ppm in closed rooms, which can be detected by the CuO-based sensor even in case of extremely high CO concentration of 200 ppm. For detection of CO concentrations well below 100 ppm SnO_2-based gas sensors can be employed. A combination of the CuO-based CO_2 sensor and a SnO_2-based sensor would thus be a proper choice for air quality as well as safety issues. In case of a HVAC system monitored by such a sensor combination, the HVAC would immediately blow in fresh air.

In conclusion, it has been shown that CuO formed by in situ thermal oxidation and functionalized with gold nanoparticles exhibits a high sensitivity towards CO_2. Direct comparison of the pristine and Au-NPs functionalized CuO sensor shows a sensitivity increase by a factor 13 (comparison: CO_2 2000 ppm, rH 50%, operation temperature 300 °C). Compared to the sensitivity values of various MOx gas sensors found in literature (see Table A1), the gas sensor introduced in this work exhibits one of the highest sensitivities towards CO_2, at lower temperatures. The process flow of our Au-NPs functionalized CuO gas sensor enables integration on CMOS-based microhotplates.

5. Patents

The fabrication procedure and the CO_2 sensor with the specific sensing material are subject-matter of Austrian patent application no. A 50377/2018 filed on May 4, 2018.

Author Contributions: The concept of the presented work has been elaborated by R.W.-T. and A.K.; J.S.N. and O.T. provided the Au-NPs for the sensor fabrication process; the gas sensors were fabricated by R.W.-T.; the gas measurements were conducted by R.W.-T., F.S.-L. and B.Z.T.; the Raman measurement was done by M.D.; the evaluation of the measurements was done by R.W.-T., F.S.-L., M.D. and S.D.; all authors contributed to the writing process.

Funding: This work was funded in part by the Sevenths Framework Programme for Research and Technological Development of the European Union as part of the MSP - Multi-Sensor Platform for Smart Building Management [No. 611887] and the ECSEL project IOSense [GA. No. 692480, FFG No. 6054961].

Acknowledgments: The authors want to thank Günther Maier for valuable discussion during the writing process. Furthermore, the authors want to thank Bernhard Sartory for the SEM investigations.

Conflicts of Interest: The authors declare no conflict of interest.

Abbreviations

The following abbreviations are used in this manuscript:

MOx	Metal oxide
CO_2	Carbon dioxide
CMOS	Complementary metal oxide semiconductor
CuO	Cupric oxide
Cu_2O	Cuprous oxide
HVAC	Heating, ventilation and air conditioning
rH	Relative humidity
ppm	Parts per million
Au-NP	Gold nanoparticles
GMS	Gas measurement set-up

Appendix A. Supplementary Information

Appendix A.1. Metal Oxide-Based Carbon Dioxide Gas Sensors

Table A1. CO_2 responses of various metal oxide materials reported in literature.

Material	$T_{operation}$ [°C]	Response $\frac{R_{gas}}{R_{air}}$	CO_2 [ppm]	Reference
La_2O_3/SnO_2	400	3.6	2000	[29]
LaOCl	260	3.4	2000	[30]
LaOCl-functionalized SnO_2 nanowires	400	5.6	2000	[31]
Au-NPs functionalized CuO	300	4.7	2000	this work

Appendix A.2. Photolithography

Table A2. Process parameters for the fabrication of gold electrodes.

(1) Photolithography	
Positive photoresist	AZ®MIR701 (Microchemicals GmbH)
Spin-coating speed [rpm]	4000
Spin-coating duration [s]	35
Annealing temperature [°C]	90
Annealing duration [s]	60
Developer	AZ®MIF726 (Microchemicals GmbH)
Development duration [s]	30
Stopper	deionized water
Stopper duration [s]	120
(2) Thermal Evaporation	
Adhesion layer	titanium
Adhesion layer thickness [nm]	5
Primary layer	gold
Primary layer thickness [nm]	200
(3) Lift-Off	
Solvent	acetone
Duration [h]	12

Appendix A.3. Electron Beam Lithography

Table A3. Process parameters for the fabrication of the CuO thin film functionalized with Au nanoparticles.

(1) Electron Beam Lithography	
Positive PMMA resist	AR-P 672.08 (ALLRESIST GmbH)
Spin-coating speed [rpm]	2000
Spin-coating duration [s]	60
Annealing temperature [°C]	180
Annealing duration [s]	300
Developer	AR600-55 (ALLRESIST GmbH)
Development duration [s]	15
Stopper	AR600-60 (ALLRESIST GmbH)
Stopper duration [s]	60
(2) Thermal Evaporation	
Adhesion layer	titanium
Adhesion layer thickness [nm]	5
Primary layer	copper
Primary layer thickness [nm]	500
(3) Lift-Off	
Solvent	acetone
Duration [h]	4
(4) Thermal Oxidation	
Oxidation temperature [°C]	400
Oxidation duration [h]	6
Relative humidity [%]	50
(5) Au Nanoparticles Depositon	
Deposition volume [µL]	40
Deposition temperature [°C]	85

Appendix A.4. Equations for Gibbs Free Energy Calculation

The equations used for calculations were taken form the work of Tanvir et al. [16].

1. Standard Gibbs free energy for the formation of a compound:

$$\Delta_R G^0 = \sum \Delta_f G^0_{product} - \sum \Delta_f G^0_{educt} \quad \text{(A1)}$$

$\Delta_R G^0$: Change of the standard Gibbs free energy of the examined chemical reaction at standard conditions. Standard conditions refer to a temperature of 298.15 K and a pressure of 1 bar.
$\sum \Delta_f G^0_{product}$: Sum over all standard Gibbs free energies of the products.
$\sum \Delta_f G^0_{educt}$: Sum over all standard Gibbs free energies of the educts.

2. Gibbs free energy at varying pressures (malachite):

$$\Delta_R G = \Delta_R G^0 + RT \ln (p_{CO_2})^{-1} \quad \text{(A2)}$$

3. Gibbs free energy at varying pressures (azurite):

$$\Delta_R G = \Delta_R G^0 + RT \ln (p_{CO_2})^{-2} \quad \text{(A3)}$$

$\Delta_R G$: Change of Gibbs free energy of formation at a partial pressure varying from standard conditions.
$\Delta_R G^0$: Change of the standard Gibbs free energy of the examined chemical reaction at standard conditions. Standard conditions refer to a temperature of 298.15 K and a pressure of 1 bar.
R: Gas constant. R = 8.314 $\frac{J}{K \cdot mol}$
T: Temperature.
p_{CO_2}: Partial pressure of CO_2.

4. Gibbs free energy of formation for educts and products envolved in the formation of malachite and azurite (standard conditions):

Table A4. Gibbs free energy of formation for educts and products of malachite and azurite formation at 298.15 K and 1 bar.

Compounds	$\Delta_f G^0$ [$\frac{kJ}{mol}$] at 298.15 K
CuO [32]	−127.6
$CO_{2(aq)}$ [16]	−385.99
H_2O [32]	−237.34
$Cu_2(OH)_2CO_{3(s)}$ [malachite] [32]	−906.2
$Cu_3(OH)_2(CO_3)_{2(s)}$ [azurite] [32]	−1439.13

Appendix A.5. Gas Measurement Set-Up

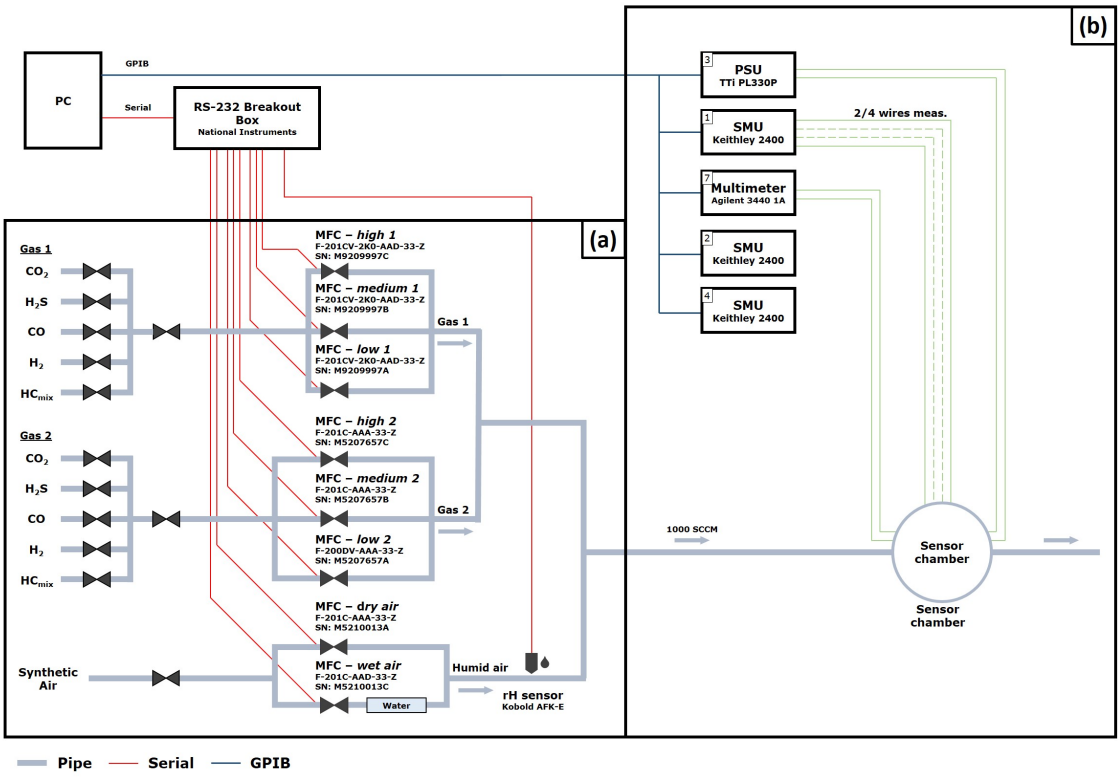

Figure A1. Gas measurement set-up: (**a**) gas atmospheric part, (**b**) electrical evaluation part.

References

1. Pachauri, R.K.; Allen, M.R.; Barros, V.R.; Broome, J.; Cramer, W.; Christ, R.; Church, J.A.; Clarke, L.; Dahe, Q.; Dasgupta, P.; et al. *Climate Change 2014: Synthesis Report. Contribution of Working Groups I, II and III to the Fifth Assessment Report of the Intergovernmental Panel on Climate Change*; IPCC: Geneva, Switzerland, 2014; p. 28.
2. Ahn, J.; Brook, E.J.; Mitchell, L.; Rosen, J.; McConnell, J.R.; Taylor, K.; Etheridge, D.; Rubino, M. Atmospheric CO_2 over the last 1000 years: A high-resolution record from the West Antarctic Ice Sheet (WAIS) Divide ice core. *Glob. Biogeochem. Cycles* **2011**, *26*. [CrossRef]
3. Recent Monthly Average Mauna Loa CO_2, 2018. Available online: https://www.esrl.noaa.gov/gmd/ccgg/trends/index.html (accessed on 18 July 2018).
4. Seppänen, O.A.; Fisk, W.J.; Mendell, M.J. Association of Ventilation Rates and CO_2 Concentrations with Health andOther Responses in Commercial and Institutional Buildings. *Indoor Air* **1999**, *9*, 226–252. [CrossRef] [PubMed]
5. Nassif, N. A robust CO_2-based demand-controlled ventilation control strategy for multi-zone HVAC systems. *Energy Build.* **2012**, *45*, 72–81. [CrossRef]
6. Raum-Luftqualitätsfühler QPA10.. QPA20.., 2005. Available online: https://hit.sbt.siemens.com/RWD/DB/DE/de/Assets/39693.pdf (accessed on 18 July 2018).
7. Ratterman, M.; Shen, L.; Klotzkin, D.; Papautsky, I. Carbon dioxide luminescent sensor based on a CMOS image array. *Sens. Actuators B Chem.* **2014**, *198*, 1–6. [CrossRef]
8. Wang, J.; Wen, Z.; Yang, B.; Yang, X. Optical carbon dioxide sensor based on fluorescent capillary array. *Results Phys.* **2017**, *7*, 323–326. [CrossRef]
9. Pentyala, V.; Davydovskaya, P.; Ade, M.; Pohle, R.; Urban, G. Carbon dioxide gas detection by open metal site metal organicframeworks and surface functionalized metal organic frameworks. *Sens. Actuators B Chem.* **2016**, *225*, 363–368. [CrossRef]

10. Lorenc, P.; Strzelczyk, A.; Chachulski, B.; Jasinski, G. Properties of Nasicon-based CO_2 sensors with $Bi_8Nb_2O_{17}$ reference electrode. *Solid State Ion.* **2015**, *271*, 48–55. [CrossRef]
11. Wang, X.; Qin, H.; Sun, L.; Hu, J. CO_2 sensing properties and mechanism of nanocrystalline $LaFeO_3$ sensor. *Sens. Actuators B Chem.* **2013**, *188*, 965–971. [CrossRef]
12. Lee, J.; Choi, N.J.; Lee, H.K.; Kim, J.; Lim, S.; Kwon, J.; Lee, S.; Moon, S.; Jong, J.; Yoo, D. Low power consumption solid electrochemical-type micro CO_2 gas sensor. *Sens. Actuators B Chem.* **2017**, *248*, 957–960. [CrossRef]
13. Abouda, A.; Al-Keleshb, H.; El Roubyc, W.; Farghalic, A.; Hamdedeinc, A.; Khedrc, M. CO_2 responses based on pure and doped CeO_2 nano-pellets. *J. Mater. Res. Technol.* **2018**, *7*, 14–20. [CrossRef]
14. Yadav, A.; Lokhande, A.; Kim, J.H.; Lokhande, C. Enhanced sensitivity and selectivity of CO_2 gas sensor based on modified La_2O_3 nanorods. *J. Alloys Compd.* **2017**, *723*, 880–886. [CrossRef]
15. Tanvir, N.; Yurchenko, O.; Laubender, E.; Urban, G. Investigation of low temperature effects on work function based CO_2 gas sensing of nanoparticulate CuO films. *Sens. Actuators B Chem.* **2017**, *247*, 968–974. [CrossRef]
16. Tanvir, N.; Yurchenko, O.; Wilbertz, C.; Urban, G. Investigation of CO_2 reaction with copper oxide nanoparticles for room temperature gas sensing. *J. Mater. Chem. A* **2016**, *4*, 5294–5302. [CrossRef]
17. Herran, J.; Mandayo, G.; Castano, E. Semiconducting $BaTiO_3$-CuO mixed oxide thin films for CO_2 detection. *Thin Solids Films* **2009**, *517*, 6192–6197. [CrossRef]
18. Debbichi, L.; Marco de Lucas, M.; Pierson, J.; Krüger, P. Vibrational Properties of CuO and Cu_4O_3 from First-Principles Calculations, and Raman and Infrared Spectroscopy. *J. Phys. Chem.* **2012**, *116*, 10232–10237. [CrossRef]
19. Deutsche Forschungsgemeinschaft. *MAK– und BAT–Werte–Liste 2013: Maximale Arbeitsplatzkonzentrationen und Biologische Arbeitsstofftoleranzwerte. Mitteilung 49*; Wiley VCH Verlag GmbH & Co. KGaA: Weinheim, Germany, 2013; p. 93, doi:10.1002/9783527675135.
20. Steinhauer, S.; Brunet, E.; Maier, T.; Mutinati, G.; Köck, A. Suspended CuO nanowires for ppb level H_2S sensing in dry and humid atmosphere. *Sens. Actuators B Chem.* **2013**, *186*, 550–556. [CrossRef]
21. Chen, M.; Yue, Y.; Ju, Y. Growth of metal and metal oxide nanowires driven by the stress-induced migration. *J. Appl. Phys.* **2012**, *111*, 104305. [CrossRef]
22. Xu, C.H.; Woo, C.H.; Shi, S.Q. Formation of CuO nanowires on Cu foil. *Chem. Phys. Lett.* **2004**, *399*, 62–66. [CrossRef]
23. Adilov, S.R.; Afanaciev, V.P.; Kashkul, I.N.; Kumekov, S.E.; Mukhin, N.V.; Terukov, E.I. Studying the Composition and Structure of Films Obtained by Thermal Oxidation of Copper. *Glass Phys. Chem.* **2017**, *43*, 272–275. [CrossRef]
24. Abdelmounaïm, C.; Amara, Z.; Maha, A.; Mustapha, D. Effects of molarity on structural, optical, morphological and CO_2 gas sensing properties of nanostructured copper oxide films deposited by spray pyrolysis. *Mater. Sci. Semicond. Process.* **2016**, *43*, 214–221. [CrossRef]
25. Ishihara, T.; Higuchi, M.; Takagi, T.; Ito, M.; Nishiguchi, H.; Takita, Y. Preparation of CuO thin films on porous $BaTiO_3$ by self-assembled multibilayer film formation and application as a CO_2 sensor. *J. Mater. Chem.* **1998**, *8*, 2037–2042. [CrossRef]
26. Seguin, M. Thermogravimetric And Differential Thermal Analysis Of Malachite And Azurite In Inert Atmospheres And In Air. *Can. Mineral.* **1975**, *13*, 127–132.
27. Korotcenkov, G. *Handbook of Gas Sensor Materials*, 1st ed.; Springer-Verlag New York: New York, NY, USA, 2013; pp. 273–279.
28. Yang, X.; Kattel, S.; Senanayake, S.; Boscoboinik, J.; Nie, X.; Graciani, J.; Rodriguez, J.; Liu, P.; Stacchiola, D.; Chen, J.G. Low Pressure CO_2 Hydrogenation to Methanol over Gold Nanoparticles Activated on a CeO_x/TiO_2 Interface. *J. Am. Chem. Soc.* **2015**, *137*, 10104–10107. [CrossRef] [PubMed]
29. Iwata, T.; Matsuda, K.; Takahashi, K.; Sawada, K. CO_2 Sensing Characteristics of a La_2O_3/SnO_2 Stacked Structure with Micromachined Hotplates. *Sensors* **2017**, *17*, 2156. [CrossRef] [PubMed]
30. Marsal, A.; Dezanneau, G.; Cornet, A.; Morante, J. A new CO2 gas sensing material. *Sens. Actuators B Chem.* **2003**, *95*, 266–270. [CrossRef]

31. Trung, D.; Toan, L.; Hong, H.; Lam, T.; Trung, T.; Hieu, N. Selective detection of carbon dioxide using LaOCl-functionalized SnO_2 nanowires for air-quality monitoring. *Talanta* **2012**, *88*, 152–159. [CrossRef] [PubMed]
32. Robie, R.; Waldbaum, D. Thermodynamic properties of minerals and related substances at 298.15 K (25.0 °C) and one atmosphere (1.013 bars) pressure and at higher temperatures. Available online: https://pubs.er.usgs.gov/publication/b1259 (accessed on 22 November 2018).